Material and Process Characterisation of PolyEtherKetone for EOSINT P800 High Temperature Laser Sintering

Submitted by

Rachel Jane Trimble

to the University of Exeter as a thesis for the degree
of Doctor of Philosophy in Engineering, December 2017.

I certify that all material in this thesis which is not my own work has been identified and that no material has previously been submitted and approved for the award of a degree by this or any other University.

.....
Rachel Jane Trimble

Abstract

Laser Sintering (LS) is a powder based Additive Manufacturing (AM) technology capable of producing near-net shape objects from 3D data. The benefits of LS include almost unlimited design freedom and reduced material waste, however the number of commercially available materials are limited, with materials traditionally being optimised for the process using a trial and error method and material development being led by previous research into polyamide (PA). There is a desire for greater material choice in LS, particularly high performance polymers.

The EOSINT P800 by AM systems manufacturer EOS GmbH is the first commercially available high temperature laser sintering (HT-LS) system capable of working high performance polymers; a PolyEtherKetone (PEK) known by the trade name HP3 PEK is the first material offered by EOS for use with the system. This research project undertakes to characterise the EOSINT P800 and HP3 PEK material with different thermal histories. Experimental work focusses on establishing material properties such as size and shape, crystallinity and decomposition. Characterisation of coalescence behaviour and comparison with theoretical models for viscous sintering is presented as a less experimentally intensive method of understanding how a material will behave during the LS process. A map of temperatures inside the powder bed in the EOSINT P800 is created for the first time and compared with output from on-board temperature sensors in the system, demonstrating the thermal distribution within the bed during building, and explaining differences between as-received and used powder.

The results demonstrate that material and process characterisation methods are useful for understanding how and why a high temperature laser sintering

material behaves the way it does. The behaviour of HP3 PEK observed during experimental work indicates that guidelines based on LS of PA are too restrictive as indicators of suitability for LS and newer systematic approaches are potentially better suited for qualification of HT-LS polymers. The novel method for mapping thermal distribution inside the LS system documented here shows the limitations of current hardware to effectively process high performance polymers. Overall, the finding of this research project is that understanding of material and process cannot be considered in isolation but combined have the potential to reduce the amount of trial and error required during qualification of new materials and increase the range and variety of polymers available for LS and HT-LS.

"I believe in the future. It is wonderful because it stands on what has been achieved."

- Sergei Korolev

Acknowledgements

First and foremost, my thanks to my supervisors Oana Ghita & Ken Evans for giving me this opportunity, for challenging and guiding me and for patiently bearing with me during my writing up.

From my time in Exeter, my thanks to Paul Brookbank and Andy McLauchlin for teaching me how to do almost everything, for use of your textbooks and for answering all my stupid questions, of which there have been many. Thanks also to Tommy Shyng, Lesley Wears and James Beard for help with experimental work. Thanks to Richard Davies, James Bradbury, Ed James for teaching me the ins and outs of the P800. Thank you to Silvia Berretta for everything; being a friend, a research partner and a (much needed and greatly appreciated) thesis critic. I am also grateful to Alwyn Pryse at EOS, who taught me a lot during his time as the P800 service engineer, and subsequently helped me translate the log reports for the process chapter.

Particular thanks go to Clare Perryman, without whom I would have a spent a lot longer trying to figure out the maths for the theoretical modelling section. Thanks also to my various housemates over my time in Exeter, to Fran Edwards, and to Jimmy Trimble for your friendship.

Thanks to Elizabeth Stanway for your help with my LaTeX woes and for reminding me that PhDs are hard and to stop beating myself up. To other online friends there are too many to count, but thanks to Ella and Oli Matthews, Bethany Wilson, Jaci and AJ Fry, Richard Bennett, Mark Lawrence and Tami Jaggs and all of the PSB Informers, and Susan Doshi for helpful comments when I've been over-dramatic on social media. I should also probably thank Dutch Uncles (in

general.)

In Bristol, I am indebted to the Additive Manufacturing Centre at GKN Aerospace for their patience and encouragement. Everyone has helped in ways big and small, but specific thanks go to Tim Hope, Claire Scott and Nick Pearson. Maciej Mazur, thank you for continuing to call me Dr Trimble, even when I asked you not to, and for generally making me laugh every day. Kallia Sapountzi, I don't have words to express how grateful I am for your sunny smile and boundless enthusiasm and for your solidarity - thesis buddies together! To the rest of you, thanks for bearing with me and listening patiently to my complaints about lack of progress. There will be cake.

To my family at Zion United Church, your love and support have been little short of life-changing. Thank you in particular to Stephen Newell and P-j Charters, and also to Jane Crane, Helen & Mike Murphy and Lisa & Nick Smith.

To my friends and family that I have been neglecting, particularly Chris, James, Dave & Kez, I promise I'll see more of you now. I really haven't been avoiding you.

Lastly, I am eternally indebted to Russ Dallen, who has been there through every triumph and crisis and has faithfully mopped me up and made tea and never, ever given up the faith that this day would come. You've listened to my insane plans to get more work done, nagged far less than I really deserved when I was procrastinating and been incredibly patient when we've had to put things off that we'd far rather have been doing. I love you and this would not have been even remotely possible without you.

There have been many moments over the period it has taken me to complete this when I have wondered if I could really finish what I started. Most of the time I think the people around me have had more faith in me to complete this than I've had in myself. To every single person of whom that was true, thank you. Your belief has got me here.

Publications

O R Ghita, E James, **R Trimble**, K E Evans, *Physico-chemical behaviour of Poly (Ether Ketone) (PEK) in High Temperature Laser Sintering (HT-LS)*, Journal of Materials Processing Technology, Volume 214, Issue 4, April 2014, Pages 969 - 978, ISSN 0924-0136, http://dx.doi.org/10.1016/j.jmatprotec.2013.11.007

Contents

List of Figures

List of Tables

List of Abbreviations

AM	Additive Manufacturing
DSC	Differential Scanning Calorimetry
HT-LS	High Temperature Laser Sintering
LS	Laser Sintering
MFR	Melt Flow Rate
PA	Polyamide (Nylon)
PAEK	Poly Aryl Ether Ketone
PEEK	Poly Ether Ether Ketone
PEK	Poly Ether Ketone
PSD	Particle Size Distribution
SEM	Scanning Electron Microscopy
T_g	Glass Transition Temperature
TGA	Thermogravimetric Analysis
T_m	Melting Temperature
UV-Vis	UV-Visible Spectroscopy
XRD	X Ray Diffraction

Chapter 1

Introduction

1.1 Research Context & Objectives

Additive Manufacturing (AM) is a group of manufacturing technologies capable of producing near-net shape objects from 3D data. Parts can be built in a variety of materials including resins, plastics, metals, wax, ceramics and paper. Initially used for producing models and prototypes, in the last 25 years AM capabilities have expanded to include functional prototypes, tooling, moulds and end-use parts [1].

Of these technologies, the most commonly used for processing semi-crystalline thermoplastics is laser sintering (LS), which produces parts by selectively fusing thin layers of powder. Parts built using LS are fully dense with mechanical properties usually comparable with traditional processing methods [2]. The major advantages of LS over traditional processing methods are almost unlimited design freedom, elimination of tooling requirements and reduced material waste as powder remaining following building can be mixed in with the fresh powder and reused in subsequent builds [1–7].

The number of materials available are limited, consisting predominantly of polyamide and polyamide variants and there is a desire for more high performance materials with higher mechanical properties and higher working temperatures than polyamide can provide. The complexity of what is occurring in the materials and the LS system during the building process is a primary reason for the limited

material selection available, and typically optimisation of materials and machine parameters is undertaken by trial and error, which can be expensive and very time consuming [8, 9]. In recent years research has undertaken to find more systematic approaches to qualification based on understanding of the properties of the materials and the machines in order to process a more diverse range of materials [8, 10, 11].

The EOS EOSINT P800 is the first commercially available LS system capable of building parts in high temperature polymers and PolyEtherKetone (PEK) based material HP3 PEEK is the first material offered by EOS for use in the system; HP3 PEEK is subsequently referred to as HP3 PEK to avoid confusion with PEEK, which has different properties to PEK. There is interest in understanding the properties of HP3 PEK which make it suitable for high temperature laser sintering (HT-LS) in order to apply this knowledge to selection of other potential high temperature polymers, and to examine systematic approaches to qualification in order to identify new methodologies which may speed up development of new materials. Research already undertaken on HP3 PEK shows that powder removed from the P800 following building shows different properties from virgin and a thorough investigation would contribute to understanding of these differences and what is causing them [12].

Thus, the objectives of this thesis are as follows:

1. Use established systematic approaches and new methodologies to characterise both virgin and used HP3 PEK powder.

2. Characterise the EOSINT P800 in order to understand more about the system performance and how it enables sintering of high temperature polymers

3. Investigate what is occurring in the EOSINT P800 during building which may result in the properties seen in used powder.

It is anticipated that the outcomes of the work will contribute to investigation of new materials with similar properties.

1.2 Thesis Outline

A full outline of the structure of this thesis is given on the following page and a brief overview is given below:

The literature review in Chapter 2 presents the state of the art of PolyArylEtherKetone (PAEK) materials and their properties, the laser sintering (LS) process and development of PAEKs for use in LS, and sintering theory and the application of sintering models to polymers, including those used in LS.

Chapter 3 presents descriptions of the equipment and experimental methods used to undertake the experimental work in the following three chapters.

The experimental work is split into three sections covering material, coalescence and process characterisation:

- Chapter 4 presents results of characterisation of physical and intrinsic properties of HP3 PEK with differing thermal histories, specifically shape and size of powder particles, crystallinity and decomposition.
- Chapter 5 covers the characterisation of behaviour of HP3 PEK under application of heat using hot stage analysis, and calculation of and comparison with predictive sintering models.
- Chapter 6 regards the EOSINT P800 itself; a description of the heaters in use in the machine followed by experiments to measure the temperature inside the build chamber and comparison with temperatures measured by the sensors built into the P800.

The final chapters presents the conclusions from the experimental work along with both general and specific suggestions for future work to build on the knowledge gained from the current work.

Thesis Structure

Chapter 1	Introduction
Chapter 2	Literature Review • PolyArylEtherKetones (PAEKs) • Laser Sintering of Polymers • Sintering Theory
Chapter 3	Experimental Methods
Chapter 4	Material Characterisation • Particle Size & Shape • Crystallinity • Degradation • Stable Sintering Region
Chapter 5	Coalescence Characterisation • Investigation into Heating Rates • Isothermal Heating Tests • Dynamic Heating Tests • Used Powder • Coalescence Modelling
Chapter 6	Process Characterisation • Heater Schematic • Verification of Temperature Measuring Devices • Thermal Map
Chapter 7	Conclusions & Further Work

Chapter 2

Literature Review

2.1 Overview

This section covers literature relevant to the work undertaken during this study. The outline of this chapter in context with the rest of the work is given in Figure 2.1.

2.2 PolyArylEtherKetones

2.2.1 Introduction

A polymer is a material made up of a number of repeating chemical units called monomers [13]. The properties of a polymer such as its strength, ductility or chemical resistance are defined by the combination of monomers and how they are linked together [14]. Generally speaking, polymers are either thermoplastic or thermosetting. Thermoplastic polymers undergo deformation when melted but return to their original state when cooled. Thermosetting polymers undergo an irreversible chemical change when heated and do not return to their original state [15].

In the solid state, polymers are made up of many long chains of molecules. These can either be highly ordered, forming so-called crystalline regions, or disordered, forming amorphous regions [14]. Most polymers are a combination of these two

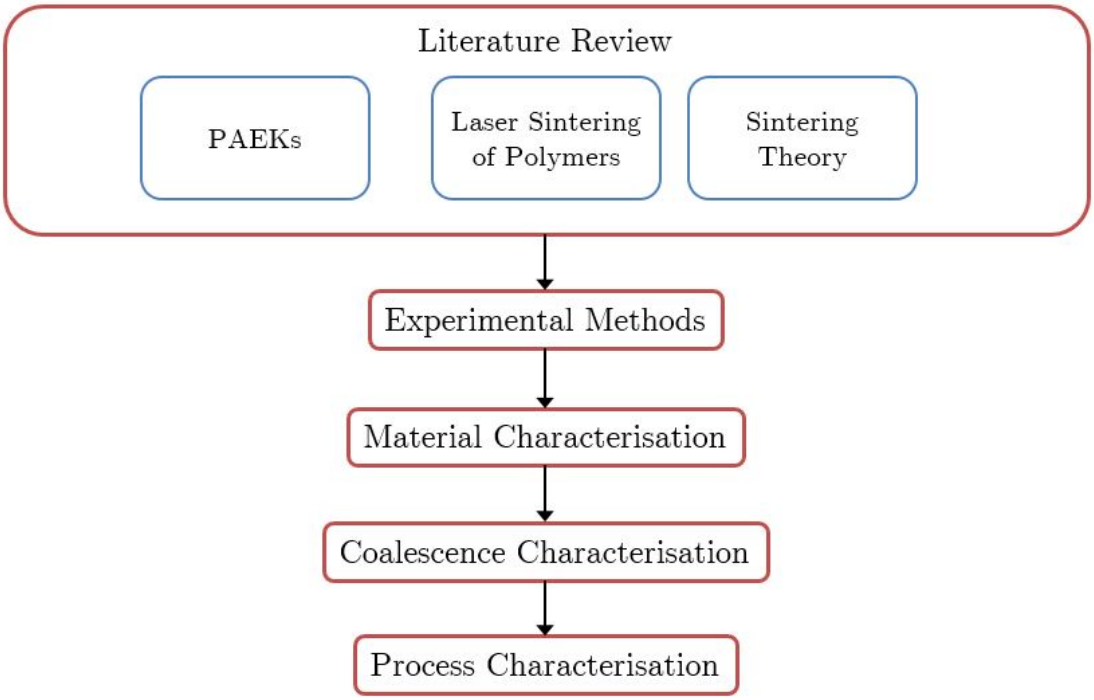

Figure 2.1: Overview of Literature Review Chapter in Context

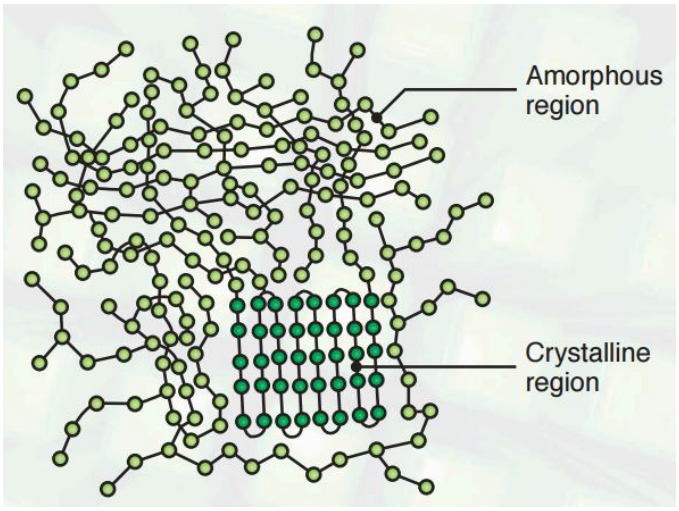

Figure 2.2: Amorphous and Crystalline Regions in a Polymer [16]

regions and are known as semi-crystalline. This structure is shown in Figure 2.2 [16].

PolyArylEtherKetones (PAEKs) are a family of semi-crystalline thermoplastics, developed for high working temperatures, high mechanical properties, good chemical resistance and ease of processing [17–21]. This makes them a good candidate to replace some metals in aerospace and automotive applications,

especially where reducing weight is desirable. Their high stiffness is an advantage in electronic applications [22]. PAEKs are also biocompatible and are used in spinal, orthopaedic and trauma implants [23].

In order to determine the limits of their potential and suitability for various applications, studies have been undertaken on their structure and behaviour. These will be covered in the following subsections.

Although many PAEK structures exist, PEEK and PEK are the most commonly used, and most literature is on the properties of PEEK [19,24]. However, for reasons which will be outlined, many studies on PEEK apply to other PAEKs also.

2.2.2 Chemical Structure

PAEKs are made up of phenyl rings connected by ether and keto linkages. Some PAEK structures are shown in Figure 2.3. Increasing the ketone content increases the glass transition (T_g) and melting temperature (T_m) of the polymer, from $T_g = 129$°C and $T_m = 324$°C for PEEEK to $T_g = 175$°C and $T_m = 392$°C for PEKK [20,25,26]. Keto linkages increase the stiffness of the molecule and improve the packing efficiency of the crystal structure, resulting in higher energy being required to break the structure down [27]. A comparison of the glass transition and melting temperature of a number of PAEKs is shown in Figure 2.4. Apart from increasing the stiffness, increasing the keto content does not change the unit cell parameters. Thus most PAEKs are very similar crystallographically, even though their transitions temperatures are very different [22].

2.2.3 Crystalline Morphology

The degree of crystallinity and the structure and quality of the crystalline region are highly dependant on processing methods. The crystalline morphology is responsible for many of the desirable properties in PAEKs and thus crystallisation kinetics are a much studied area [29].

Lovinger and Davis [30] found that when crystallised from a solution at low temperatures (below 215°C), PEEK has a spherulitic structure made up

Structure	Name	Ketone (%)
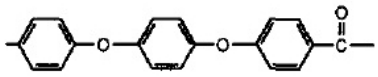	PEEK	33
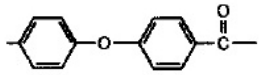	PEK	50
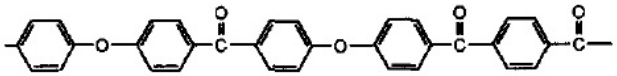	PEKEKK	60
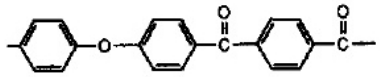	PEKK	67

Figure 2.3: Structures of PAEKs by ketone content [27]

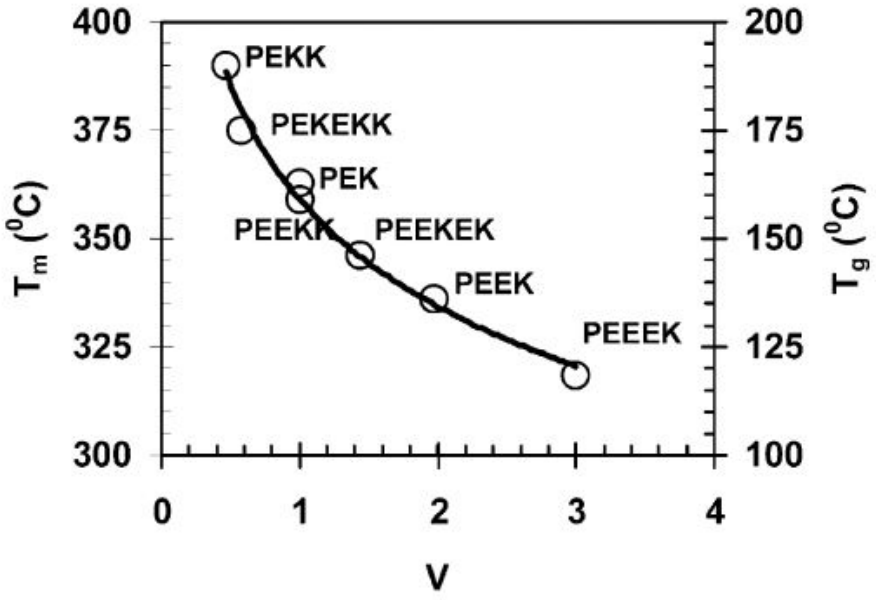

Figure 2.4: Comparison of melting and glass transition temperatures of PAEKs [28]

of long, narrow lamellae. The lamellae themselves are composed of very fine microcrystallites. As the crystallisation temperature is raised the lamellae grow thicker; at higher crystallisation temperatures there are fewer nucleation seeds and whilst crystal growth is slower the lamellae have more space to develop [31, 32]. Lamellar thickening can also occur during annealing at high enough temperature [33]. In a later study, Lovinger et al [34] found that at very high crystallisation temperatures (320°C and above) the lamellar structure was different; whereas at lower temperatures the spherulites were composed of individual lamellae, at high temperature they grew in bundles. These lamellar stacks were much stiffer than the individual lamellae and promoted a very high degree of order in the spherulites.

Waddon et al [35] compared the crystal structure of PEEK and PEK. They found that solution grown crystals of both confirmed the findings by Lovinger and Davis [30]. Waddon et al also obtained different results for different molecular weights when the thermal history and crystallisation conditions were the same; at lower molecular weight the spherulites were much larger than at higher molecular weight. However, they explained that spherulites grow around nuclei such as impurity particles, meaning that spherulite size is a reflection of the degree of purity of the polymer.

According to the Encyclopedia of Polymer Science and Engineering, "the natural grade of PEEK is ca 35% crystalline" [18]. However, the attainable percentage crystallinity is dependent on the rate of cooling from the melt; the slower the cooling rate, the higher the crystallinity [31]. Depending on processing conditions, % crystallinity varies between 0 and 40% [36] when measured using X Ray Diffraction (XRD), Differential Scanning Calorimetry (DSC) or density techniques. However, using Fourier Transform Infrared Spectroscopy (FTIR), Nguyen and Ishida [37] calculated much higher values when PEEK was slow cooled from very high temperature. They attributed this to differences in the crystalline structure being picked up the FTIR but not by other techniques. At lower crystallinity values FTIR and DSC were in good agreement.

Crystallinity can be increased post processing by annealing. Zimmermann

and Könnecke [20] found that increasing the annealing temperature resulted in a continuous increase in crystallinity until very close to the melting temperature. Bassett at al [38] investigated the effect of various annealing treatments on PEEK and were able to attain crystallinity values up to 60%. Chivers and Moore [39] found that high crystallinities were achieved by slow cooling, but also that the maximum attainable crystallinity was related to molecular weight; as molecular weight was increased, the maximum crystallinity decreased.

In order to calculate crystallinity the theoretical heat of fusion for a 100% crystalline polymer is required. Blundell and Osborn [40] calculated this to be 130 Jg^{-1} for PEEK and Zimmermann and Könnecke [20] reported that the same value was also valid for PEK and PEEKK. Furthermore, Blundell and Osborn [40] calculated the thermodynamic melting point of infinite perfect crystals to be 395°C. This theoretical value, which is much higher than the measured melting point of PEEK crystals is calculated from the Gibbs-Thomson equation which is used to correlate melting temperature with crystal dimensions [41].

Many studies have found that PAEKs display a double melting peak. There is some discussion over whether this is due to annealing effects producing crystals with a lower melting temperature (T_m) or whether more than one crystalline structure is present.

Gardner et al [27] found that a second structure was present in some solvent crystallised PAEKs and that increasing the keto content increased the amount present. Ho et al [17] obtained two different structures in PEKK using different crystallisation processes. They concluded that the tendency towards one crystal structure or the other was dependant on the cooling conditions; the more thermodynamically stable form I occurred at higher crystallisation temperatures where the crystals formed slowly due to fewer nucleation sites, whereas form II was more prevalent when the crystals formed very quickly.

Lee and Porter [42] studied cold-crystallised, annealed and melt-crystallised PEEK and concluded the lower melting peak was due to the thermal history as the lower T_m changed with the processing conditions. In a later study they showed that

samples which showed a double melting peak in DSC gave the same XRD pattern as those with a single peak, meaning that the crystal structure was the same for both [43]. Blundell and Osborn [40] and later Blundell alone [44] also attributed the lower melting peak to the processing conditions; both studies showed that the lower peak shifted in temperature as the annealing temperature was changed. Similar results for PEEK were published by Bassett et al [38] and for PEEKK by Wang et al [45]; overall the view that melting peaks are related to processing conditions is more prevalent in the literature.

The mechanical properties of PEEK are a result of its molecular weight and crystallinity. The tensile modulus and yield strength increase with increasing crystallinity; this is due to the stiffness of the more tightly packed chains and higher quality crystals [39]. However, Cebe at al [46] found that samples with the same degree of crystallinity showed different tensile properties depending on the rate of cooling; high quality crystals from slow cooling resulted in better tensile properties. The fatigue life is also increased by higher crystallinity [47]. Fracture toughness of PEEK is higher at higher molecular weight and low crystallinity; larger crystallites are more susceptible to fracture [39,48]. Tensile strength, tensile modulus and flexural strength are similar for PEEK, PEK and PEKEKK at room temperature [22].

In summary, the percentage crystallinity and the crystalline morphology are predominantly controlled by the heating and cooling regime to which the material is subjected; a high processing temperature and a slow cooling rate will result in both a high percentage crystallinity and high perfection crystals with large spherulites. Mechanical properties are influenced by the crystallinity, with various properties affected by either high or low crystallinity.

2.2.4 Thermal Stability

PAEKs were developed to have excellent thermal stability and high working temperatures, so much research has been undertaken on their behaviour at high temperature. Identifying how and why PAEKs degrade is the first step towards

avoiding such behaviours and increasing the range of their potential applications [49].

PEEK has a melting temperature of 343°C and PEK has a melting temperature of 373°C [15, 21, 50].

In general, PAEKs degrade when processed above their melting temperature, that is, their chemical structure is irreversibly changed in a manner which impacts negatively on certain properties of the processed material. Jonas and Legras [29] reported that degradation was noticeable in PEEK when heated in air at 385°C and under vacuum at 440°C. They suggested that processing PEEK automatically leads to degradation, even if the processing conditions are carefully chosen.

Lee and Porter [32] suggested that crosslinking begins during the early stages of melt annealing; crosslinking impedes the ability of a polymer to crystallise, which in turn negatively impacts tensile strength as this is achieved through high crystallinity, as explained in Section 2.2.3. Cebe [51] found that when PEEK was annealed above 319°C for 24 hours or more, crosslinking occurred and Day et al [52] observed the same behaviour when heating at 400°C. Commonly, studies have reported that the presence of an insoluble fraction when the material is dissolved in acid is evidence of crosslinking and this has been found by Hay and Kemmish [49], Jonas and Legras [29], Cebe [51] and Day et al [52]. Thompson and Farris [53] also reported an insoluble fraction but wrote that this alone is not conclusive evidence of crosslinking; they used Carbon 13 nuclear magnetic resonance to prove that crosslinking had occurred.

Crosslinking of PAEKs has been studied extensively as it occurs very early in the decomposition process and impacts on the achievable mechanical properties [49]. Several studies have deliberately caused crosslinking in order examine the effects. Banihashemi et al [54] found that crosslinking PEEK increased thermal stability, that is, the structure of the polymer became fixed and less susceptible to variation introduced by changes in the crystalline fraction as a result of shifting polymer chains. When Thompson and Farris [53] induced crosslinking in Hydroquinone PEEK (HDQPEEK) the glass transition temperature was increased from 143°C to

280°C. Chan and Venkatraman [55, 56] reported an increase in glass transition in PEEK crosslinked by the addition of elemental sulphur. Above the glass transition temperature, creep properties improved with amount of sulphur added; as the crystallinity of all the samples was similar this was attributed to crosslinking and morphological differences in the crystalline phase [55]. They also found that prior to being heat aged, the crystallisation rate increased as a result of lower molecular weight caused by chain scission. However, after heat ageing the crystallisation rate decreased as a result of crosslinking [56]. An increase in glass transition associated with increasing hold time and temperature was also found by Day et al [57].

When heated under vacuum, Hay and Kemmish [49] found that no change in molecular weight occurred in PEEK below 300°C, but when heated in air change was noted around 200°C. Discolouring occurred above 400°C and once cooled the crystallinity was reduced. Observing the material under a hot-stage microscope showed that nucleation and spherulite growth were reduced and in some areas no crystallisation took place. Jonas and Legras [29] too noted an increase in molecular weight in the early stages of degradation. Decreasing crystallisation was seen when melt temperature and hold time were increased, a behaviour also seen by Day et al [52].

Jonas and Legras [29] found that the amount of insoluble residue - and by extension the amount of crosslinking - present increased as the sample surface to volume ratio was increased. This effect was not seen when heating under vacuum. They concluded that degradation in air is more significant as the diffusion of oxygen into the surface of molten PEEK speeds up degradation.

Hay et al [49] found that PEEK degrades by random homolytic scission of the ether and carbonyl bonds in the chemical chain. This results either in hydrogen abstraction from adjacent polymer chains or crosslinks at the chain ends. Day et al [58] confirmed this process was occurring, although in their study they found slightly different degradation products, possibly as a result of different pyrolysis conditions.

When annealed at a temperature a couple of degrees below the melting point

for long periods of time (20-72 hours), Zhang and Zeng [59] found that the high temperature melting peak of PEEK far exceeded the melting temperature recorded during standard DSC scans. Beyond 46 hours annealing time, the melting temperature was higher than the theoretical melting temperature of perfect crystals calculated by Blundell and Osborn [40]. The XRD patterns showed this was not due to changes in the unit cell parameters of the samples. Two explanations were offered for this phenomenon; crosslinking had occurred which hindered the melting of the lamellae, or inaccuracy in the calculated value of the equilibrium melting point. They posited that crosslinking and recrystallisation were occurring at the same time when PEEK was annealed in air; crystallisation was occurring at the surface of the lamellae but crosslinking was occurring further away resulting in regions of both.

Analysis by thermogravimetric analysis (TGA) shows that mass loss begins at temperatures above 550°C [60, 61]. When the heating rate is increased, mass loss begins at higher temperatures [62]. Total mass loss is higher in an air atmosphere than in nitrogen; several studies found that when heated to 1000°C, a residue was always present following heating under nitrogen but in an air atmosphere mass loss was 100% [61–63]. Hay and Kemmish [49] reported that there were no significant differences between the decomposition characteristics of PEEK and PEK, therefore it can be assumed that the results of other studies are representative of PEK also.

Overall, the kinetics of decomposition in air are more complex than under nitrogen. The derivative of the decomposition curve in nitrogen or argon tends to show one peak suggesting a simple, one-stage weight loss [60,64]. Patel et al [65] identified a much smaller second decomposition step during heating in nitrogen which they attributed to cracking of material crosslinked during the heating regime. However, results for heating under air vary from study to study. When increasing the heating rate, Yao et al [61] found that the curves in air varied from one heating rate to another whilst tests undertaken under nitrogen did not; see Figure 2.5. Day et al [62] suggest that several reaction mechanisms are occurring when PEEK is heated in air and that transport of oxygen through the melt results in thermal

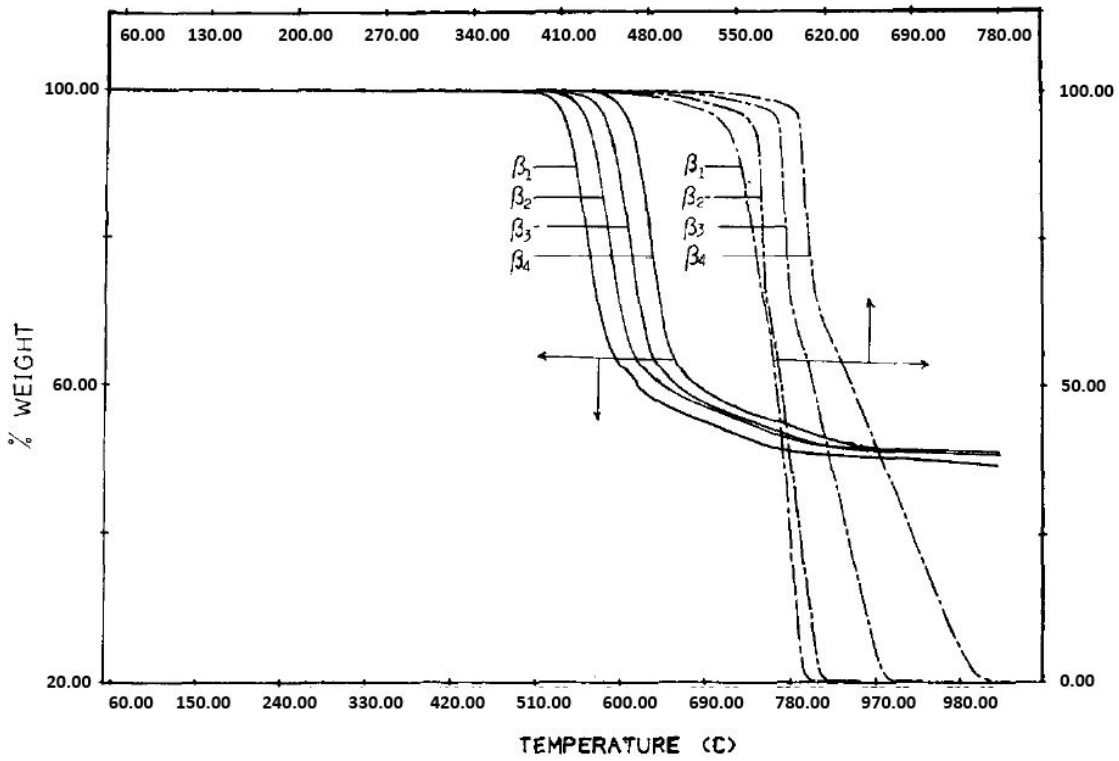

Figure 2.5: Variance in TGA Curves at different heating rates. Straight line denotes nitrogen atmosphere, dashed line denotes air. [61]

oxidative degradation. By contrast, a single reaction mechanism is responsible for decomposition under nitrogen.

In summary, it is important to work PEEK in an inert atmosphere when temperatures above the melting point are required in order to minimise oxidative degradation and ensure thermal stability.

2.3 Laser Sintering of Polymers

2.3.1 Introduction

Additive Manufacturing (AM) is a group of manufacturing technologies capable of producing near-net shape objects from 3D data. Parts can be built in a variety of materials including resins, plastics, metals, wax, ceramics and paper. Initially used for producing models and prototypes, in the last 25 years AM capabilities have expanded to include functional prototypes, tooling, moulds and end-use parts.

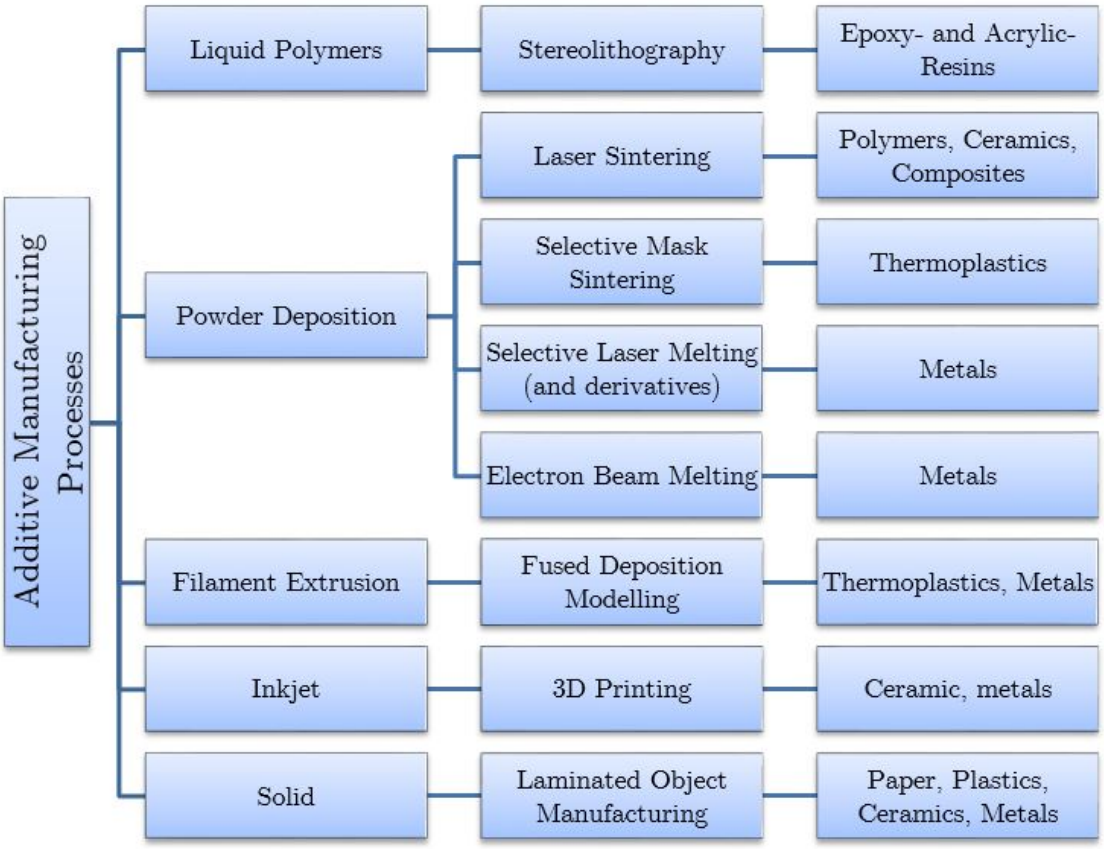

Figure 2.6: Overview of Additive Manufacturing Processes, Methods, Systems and Materials [7, 66]

Markets in which AM is used include aerospace, automotive, architecture, medicine and consumer products such as jewellery and furniture [1].

For the right applications, there are many advantages to AM over traditional subtractive manufacturing technologies. These include almost unlimited design freedom and the ability to build very complex and fully customised geometries, reduced material waste, faster component turnaround times and the elimination of tooling requirements for many applications [1–7].

Figure 2.6 gives an overview of commercially available additive manufacturing systems and materials, classified by material deposition methods.

The most commonly used AM technique for producing high quality semi-crystalline thermoplastic components is laser sintering (LS). This will be covered in more detail in this section.

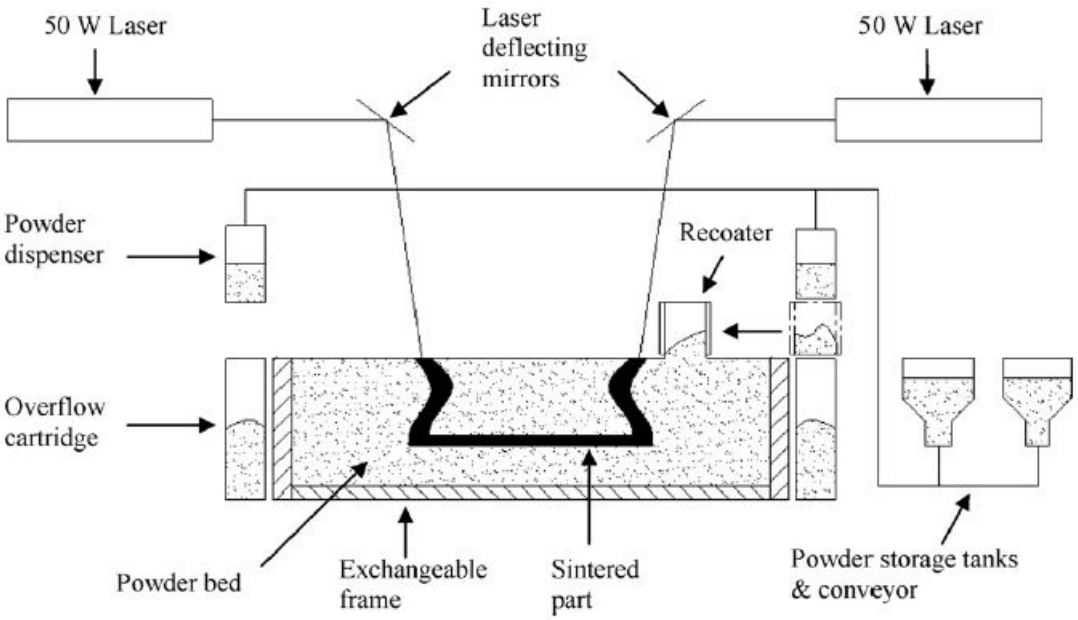

Figure 2.7: Schematic of the EOSINT P700 ([67])

2.3.2 Laser Sintering Process

Commercial laser sintering systems use varying designs of components such as powder dispensers and re-coaters but the principle is essentially the same [2]. A schematic of the interior of an EOSINT P700 is shown in Figure 2.7; the P700 has the largest build volume of any EOS polymer laser sintering system at 700 x 380 x 580mm and operates the same process as the P800, the first High Temperature Laser Sintering (HT-LS) system. The P800 is capable of processing PAEK materials and will be covered in Subsection 2.3.5.

Powder is stored in external hoppers and transported via a powder delivery system to the top of the machine, where it is held in dispensers located on either side of the build chamber prior to use; the powder delivery system continues to feed new powder in over the course of the build to ensure it does not run out. A simplified schematic of the laser sintering process is shown in Figure 2.8 and explained below.

1. 3D data such as a CAD file or model defines what the manufactured part is to look like.

2. This is exported as an STL file to a piece of software which slices the part into very small layers, typically 50-100μm.

3. Powder is delivered from the dispenser into the recoater, which spreads a layer of powder corresponding to the slice thickness onto the build platform. Any powder remaining in the recoater which has not been spread across the build platform is collected in overflow cartridges to either side of the build chamber to be removed later. The build chamber is pre-heated and then held at a temperature just below the melting point of the material which is determined during a calibration procedure undertaken during machine maintenance. A CO2 laser (3a) guided by mirrors selectively scans the cross section determined by the software. The un-sintered powder remains in place to support the consolidated cross section (3b).

4. Once the layer has been completed, the build platform moves down one layer (4c). A fresh layer of powder is spread across the build chamber (4d) and the new layer is sintered. As the new cross section is consolidated it bonds with the layer below to create a 3D part. This continues until the entire part has been built.

5. After the part has been cooled, the excess powder can be removed. Parts are often post processed to improve surface finish or mechanical properties.

The process takes place in a nitrogen atmosphere [68]. It is important to minimise air in the build chamber as degradation of the material occurs much quicker when there is oxygen present during heating [29]. The temperature of the machine and material is closely controlled throughout the build.

Theoretically, the surrounding unsintered LS powder can be reused as no physical changes in the powder result from being processed; this powder is counter-intuitively referred to as "used" [2]. In practise, the high temperatures result in changes in the thermal and mechanical properties of the powder. Pham et al [6] found that the molecular weight of PA2200 increases with time spent in the build chamber resulting in increased shrinkage of parts, reduced flowability

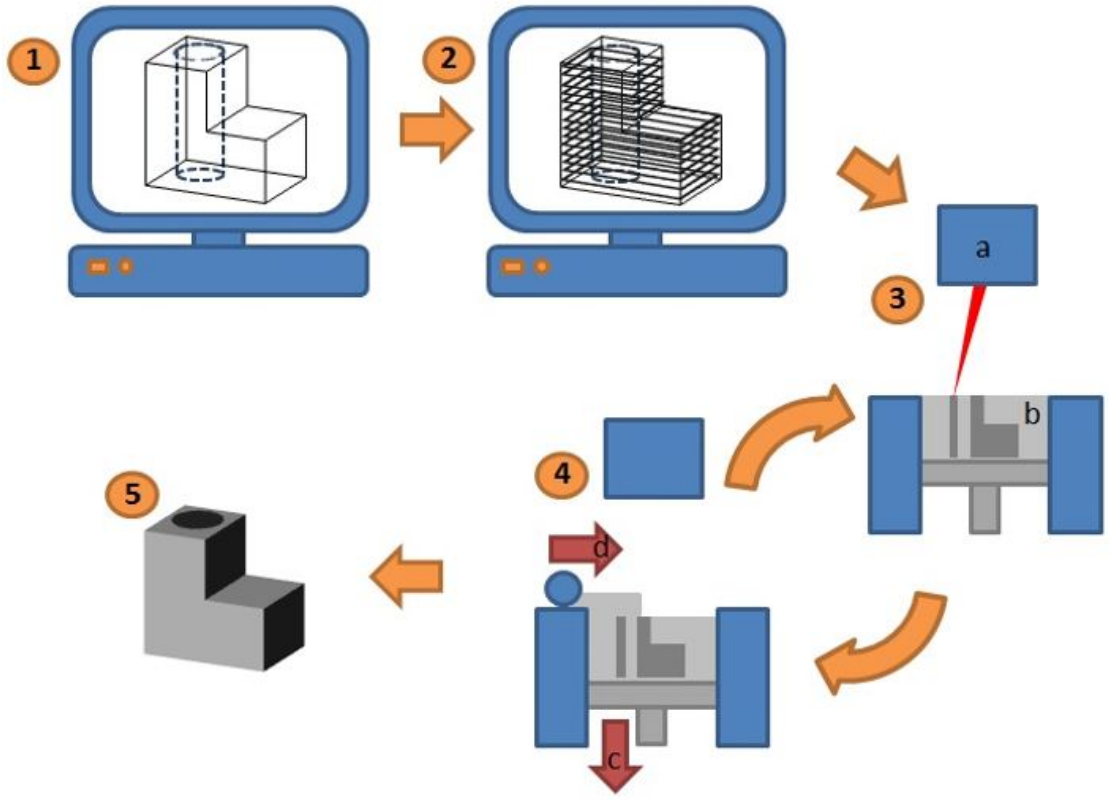

Figure 2.8: Schematic of the Laser Sintering Process

and a poor surface finish, referred to as "orange peel." The percentage of new (also called virgin) powder required to "refresh" used powder varies depending on the degradation of the powder and the machine in use. Industry standard tends towards 30-50% new powder in each build but the actual degradation of the powder is not taken into account. Several studies have used melt flow rate or melt flow index measurements of used powder with various thermal histories to quantify the degradation and thus produce more accurate mixing profiles for building consistent quality parts [6, 69, 70].

2.3.3 Materials

The polymeric materials commercially available for use with LS are shown in Figure 2.9. Generally speaking, any material which is available in powder form and tends to consolidate when heat is applied can be used in laser sintering [71]. Practically however, whether a material can be effectively sintered depends on several factors. The thermal processes involved are extremely complex and the machine set up must be determined according to the properties of each material, historically without investigating the behaviour of the material at a fundamental level [8]. The complexity involved in qualifying new materials for LS is one of the reasons why there are not more commercially available [2, 9].

Thermosetting materials are used as infiltrates for green parts and can also be sintered as part of a metal-thermoset mixture for creating metal parts. A few elastomer based materials are commercially available and are recommended for applications requiring excellent flexural properties such as shoe soles [72]. However, the vast majority of commercially available polymers are thermoplastics [2].

Both amorphous and semi-crystalline polymers can be processed with LS. Parts made from amorphous polymers tend to be porous with poor mechanical properties [2]. However, they also exhibit a much lower rate of shrinkage than semi-crystalline polymers, resulting in higher accuracy of parts. Amorphous polymers are often used in applications such as moulds and casting patterns where the high accuracy and porosity are an advantage [72].

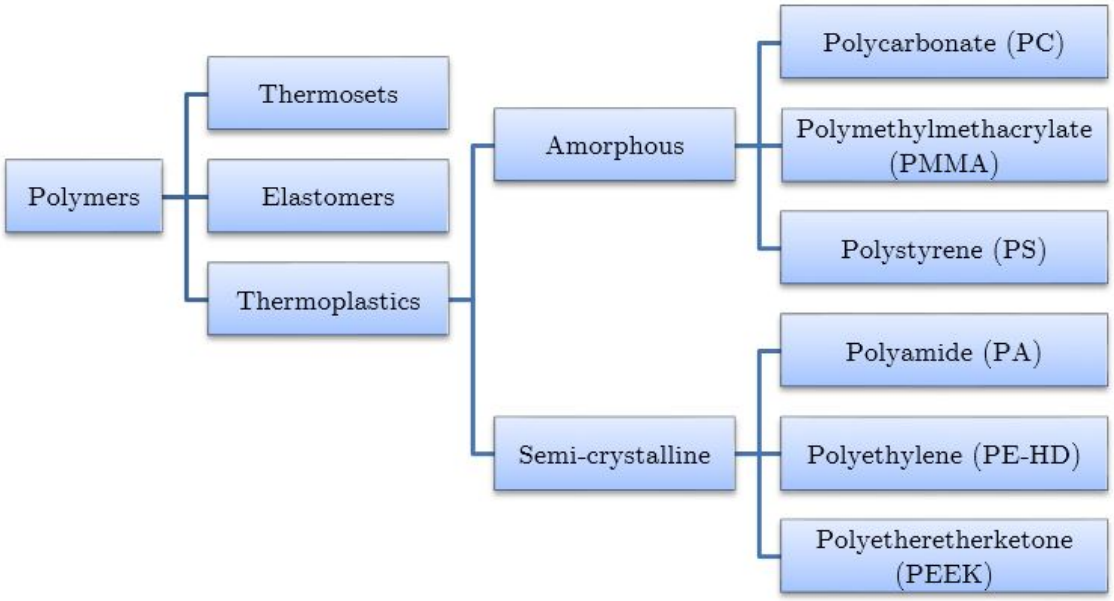

Figure 2.9: Commercially Available Polymers for Laser Sintering

Semi-crystalline polymers are more commonly used in LS as parts produced have good mechanical properties and high density. Most materials on the market are variants of polyamide (nylon). As such, most of the published research covers polyamide, however LS of other polymers is of significant interest and more literature is becoming available as the factors required to produce successful parts are better understood [73].

It is generally accepted that the key factors which govern successful sintering are [74]:

- Physical powder properties such as size, shape, particle size distribution and flowability.
- Thermal and rheological material properties such as glass transition temperature, melting temperature and viscosity.
- Machine process parameters including laser power, scan speed, processing temperatures and the cooling regime following building.
- Location and orientation of the part within the build chamber

The following sections cover these key factors.

2.3.4 Key Factors for Effective LS

2.3.4.1 Physical Powder Properties

The shape, size and flowability of powder affect how it is deposited on the build platform and how well it packs in the layer. Good compaction in the bed improves interaction between particles during sintering and will result in high density and good mechanical properties [75].

Generally, the closer the powder particles are to spherical, the better they will flow and therefore the better they will pack [76]. The shape of the powder is determined by how it is manufactured. For example, cryogenic fracture will tend towards irregular shapes which do not flow easily, resulting in deposition of an uneven layer [77]. Polyamide powder is commercially produced from polymerisation, resulting in more regular, spherical particles which have been shown to produce much better parts [2]. Mys et al [9] investigated ball milling, rotor milling and spray drying methods for producing polysulfone LS powders from pellets. They found that rotor milling and spray drying produced spherical particles, although the particles produced by spray drying were deemed very small ($26.1 \pm 12.8\,\mu m$).

Berretta et al [78] quantitatively investigated particle shape by analysing Scanning Electron Miscroscope (SEM) images of particles and classifying them according to Circularity and Roundness, that is, how close to a circular a particle is (where a perfectly circular particle has a value of 1) and how rounded the profile of the particle is (where very round particles have a value of 1 and those showing sharp edges and flake-like features are closer to 0.) They found that highly circular and round particles exhibited better flow behaviour. Several studies have attempted to sinter powder with non-spherical particles and have been unsuccessful or seen poor mechanical properties due to the poor flow behaviour of the material [2, 77, 79]. However, using discrete element method simulation and representative experimental tests on elongated particles, Haeri et al [80] demonstrated that the quality of a powder bed made up of non-spherical particles is also affected by the

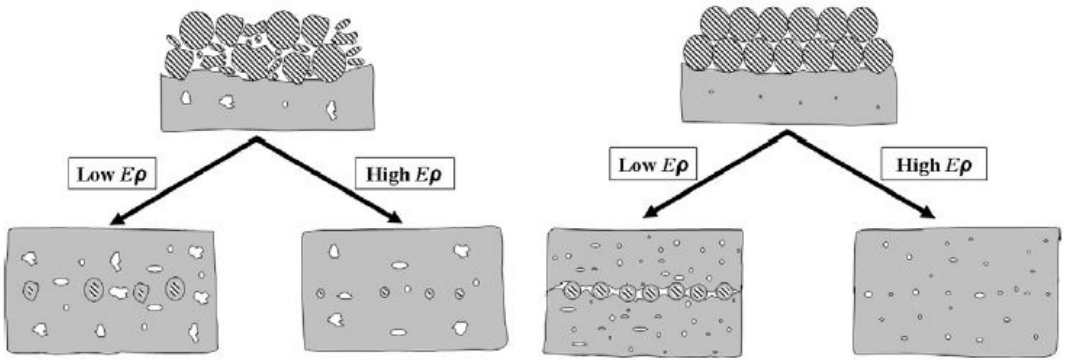

Figure 2.10: Influence of PSD on porosity at low and high energy input (E_ρ) for Duraform PA (left) and Innov PA (right) [82]

method used to spread the powder; this will be covered later in this section.

Small, fine particles will lead to high resolution and dimensional accuracy [81]. A good fraction of small particles will fill gaps between larger particles, resulting in better initial compaction. However, small particles require less energy to melt and will tend to sinter at a lower temperature to large particles. Too many small particles will tend to stick to each other and reduce the powder bed density. Schmid et al [73] found that a significant number of very small particles which led to cohesion reducing the flow of one of the powders they investigated, and Schultz at al [77] also saw that a large fraction of small particles led to bed porosity which negatively impacted mechanical properties. Furthermore, small particles can be disturbed from the powder bed by the protective gas flowing through the build chamber and can lead to a thin film of powder being deposited over various components of the machine itself [72].

The particle size distribution (PSD) is an important factor to consider. Dupin et al [82] found that a large fraction of small particles (8 µm) in Duraform PA led to lower porosity and better inter-layer bonding at low values of energy input than Innov PA which had a smaller median particle size (43 µm, compared to 60 µm) but fewer smaller particles. They attributed this to insufficient melting of particles at the bottom of the layer of Innov PA due to the uniformity of particle size and shape. However, at higher energy input, the Innov PA showed lower porosity and fewer unmelted particles, as shown in Figure 2.10.

In general, commercial powders have a narrow particle size distribution with a small number of small particles [75,81]. Ziegelmeier at al [83,84] saw an increase in packing density of TPU as the smaller particles were sifted out. It is important to note that they attributed this to the irregular particle shape of the smaller particles which hindered flow; the larger particles showed a smoother surface which flowed better. The recommended median particle size for polyamide 12 differs between authors [2,73,75,81] but a powder size too close to the layer height tends to result in particles segregating during deposition, which results in porosity in the final parts [2].

Flowability is a measure of how a material will flow under a specific set of conditions and is affected by particle size, shape and PSD as well as intrinsic material properties such a molecular weight and viscosity [85,86]. A powder with good flowability will tend to produce better parts because layers will be smooth and efficiently packed [2,77]. Flowability can be improved through use of additives with good flow properties [87–89] and by changing the powder properties through tempering [90,91]. The equipment used to spread the powder will also impact its flowability; Haeri et al [80] found that elongated particles of PA produced a better quality layer when spread with a roller rather than a blade recoater, and analysed the speed at which the material was spread as a factor. In a later paper, Haeri [92] showed using discrete element method that the blade recoater could be optimised such that at higher spreading speeds the bed packing was more efficient than was achievable at the same speed with a roller.

2.3.4.2 Thermal and Rheological Material Properties

Some of the key thermal properties of polymers which impact their effectiveness in LS are glass transition, melting and crystallisation temperatures, specific heat, thermal conductivity, molecular weight and viscosity [74, 81]. Of these, the most significant for semi-crystalline thermoplastics are melt and crystallisation temperatures as these define the operating temperature at which they are processed.

Semi-crystalline polymers exhibit a peak melting temperature at which melting of the majority of the crystals occurs; this is useful for laser sintering as it helps to identify the energy input required to result in consolidation of the material.

Similarly, semi-crystalline polymers show a peak temperature at which the majority of the recrystallisation occurs [93]. The packing efficiency of the crystal structure is determined by the speed at which the material is cooled from molten to below the glass transition temperature, at which point the structure is frozen and no further crystallisation takes place [31,32]. The rearrangement of polymer chains into this efficient packed crystalline structure is the reason why semi-crystalline polymers shrink as they cool; volumetric changes occur during crystallisation [74]. Controlling shrinkage and thus minimising distortion in parts is one of the main challenges when qualifying new materials for LS, particularly as the rate of shrinkage increases as the crystallinity increases [81].

In order to ensure effective sintering, most research states that there should be a significant difference between the melting temperature and the crystallisation temperature of the polymer; this is referred to as the processing window [2, 7, 72, 75, 81, 82, 94, 95]. The processing window can be determined from a differential scanning calorimetry (DSC) trace of the material and PA12 is an excellent example of a material with a wide processing window; an example is shown in Figure 2.11. There are two reasons why a wide processing window is recommended.

Firstly, the processing window dictates the temperature at which the material should be processed; a narrow processing window will have a very small temperature window in which the material can be effectively processed which as a result of the the number of parameters involved is extremely difficult to achieve [73]. Partee et al [96] found that the processing window for polycaprolactone was 2°C; below 46°C severe distortion prevented the deposition of subsequent layers while above 48°C the un-sintered powder bed began to fuse together which is detrimental to the recyclability of the powder and makes removing the parts difficult [2]. Other semi-crystalline materials with a small processing window include PA11 [11] and high density polyethylene [75]. There are far fewer commercial variants of these

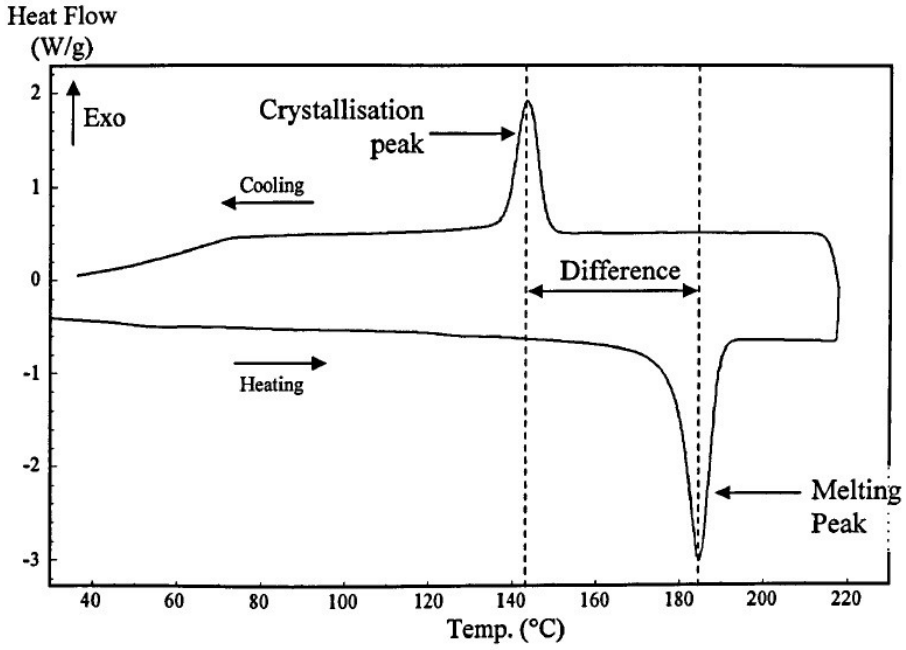

Figure 2.11: DSC Curve for Nylon-12 Power Showing Difference Between Melt and Crystallisation Temperatures [97]

polymers available compared to PA12.

Secondly, a wide processing window indicates that a material will stay in a liquid state for longer during processing before crystallising which reduces residual stresses which cause part warping. A wide process window ensures material is not also crystallising whilst it is melting, which reduces the likelihood of localised shrinkage due to differing crystal properties from one region of the melt to another [75, 97].

Not all research supports the necessity of a wide processing window, however. Wegner [98] determined the processing window for several different polymers and established that a large processing window did not necessarily result in good quality parts, but must be considered alongside other properties such as flowability.

Amorphous polymers do not show a distinct peak melting temperature and thus do not have a processing window. Whilst some authors have shown that these materials do not have good properties when laser sintered, others have been successful. Kruth et al [72] state that whilst the viscosity of amorphous polymers decreases with temperature, they do not flow as well as semi-crystalline polymers in the temperature range in which they are processed, which results in

poorer consolidation, higher porosity and poor mechanical properties. A study by Yan et al [99] to process amorphous polystyrene supports this claim as they found the tensile values of their LS samples to be substantially lower than fully dense polystyrene; they stated that porosity in the parts was the reason for this. However, Shi et al [100] found that once the correct processing parameters had been established, high impact polystyrene could be laser sintered to produce parts with good enough mechanical properties to meet the requirements for patterns for investment casting. Dadbakhsh et al [101] produced parts in a TPU elastomer with mechanical properties comparable with injection moulding and the material did not show a distinct melting range when measured using DSC; they found that the PSD and powder packing was the main factor in the mechanical results of their parts.

It has been established that several PAEK materials do not have a wide processing window and that the melting and crystallisation regions overlap, however fully dense structures with good mechanical properties are attainable [8, 12, 50, 90]. This will be covered in more detail in Section 2.3.5.

An alternative method proposed for establishing processing conditions for LS which takes into account the interaction of the intrinsic properties of materials is the "stable sintering region." The concept of the stable sintering region was introduced by Vasquez et al [10, 11]. The stable sintering region is defined as the temperature range in which optimised machine parameters will ensure complete material melting but without triggering decomposition of the material; the general principle is shown in Figure 2.12.

Rather than looking at just the processing window determined by differential scanning calorimetry, the method for determining the stable sintering region considers both the lower and upper limits for effective sintering by factoring in DSC and thermogravimetric analysis data; the stable sintering region established for PA12 is shown in Figure 2.13. The lower limit is the temperature at which DSC predicts the material is fully melted; this can be validated by using hot stage microscopy to visually confirm that the material is fully molten. The upper

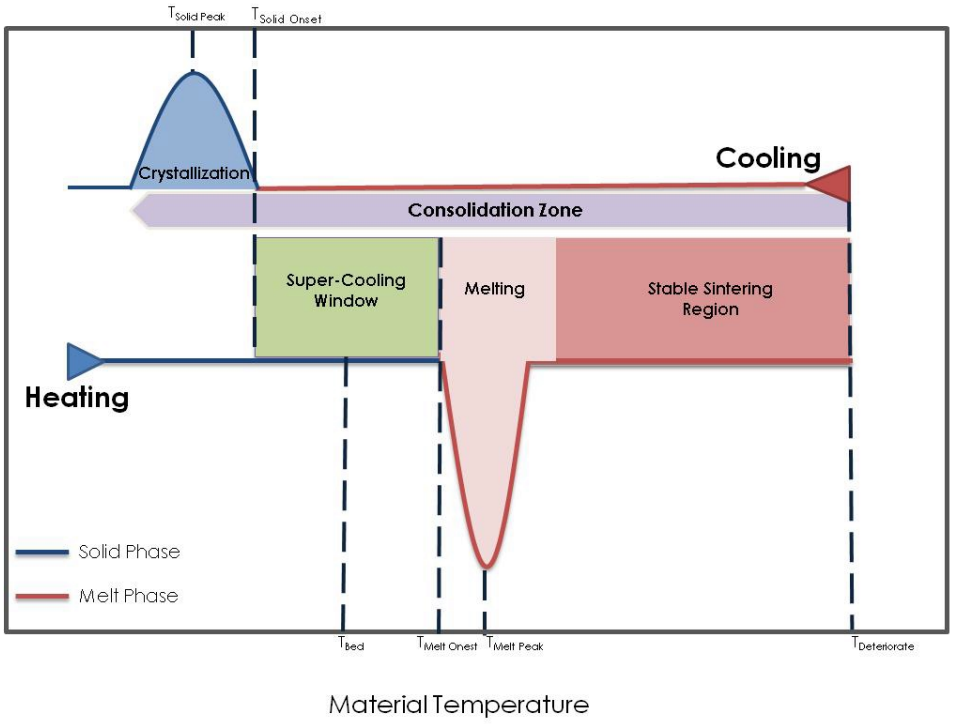

Figure 2.12: LS process window and stable sintering region proposed by Vasquez et al [11]

limit is defined by 1% mass loss using thermogravimetric analysis (TGA). One of the benefits of keeping the temperature below that at which 1% mass loss of the material occurs is that recyclability of the remaining unsintered powder is potentially improved. In a follow up paper [102] the authors validated that concept experimentally, showing that a variety of processing parameters could be chosen in line with the stable sintering region to produce good mechanical properties.

Berretta et al [8] used this approach to establish a stable sintering region for PEEK450PF, a PEEK material previously untested for LS. They found that the results predicted a very wide processing window, in contrast to the processing window predicted by DSC analysis alone.

The intrinsic properties of the material also affect whether it can be processed effectively using LS. The melt flow rate (MFR) is a "measure of the flow viscosity of a molten polymer [6]." A powder with a high MFR will typically have a small molecular weight and low viscosity which leads to good flow of the material when molten and thus parts with good properties, particularly surface finish. Conversely,

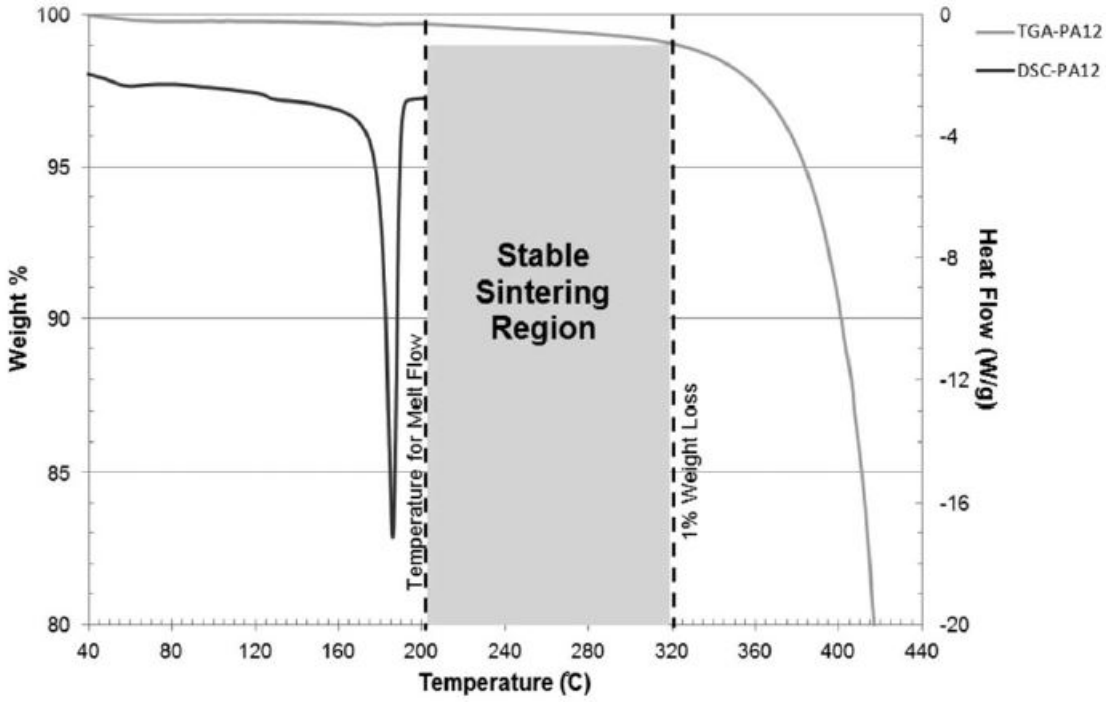

Figure 2.13: Stable sintering region of PA12 proposed by Vasquez et al [102]

a low MFR indicates high viscosity which tends towards poor flow when molten and a rough surface texture referred to as "orange peel". As the molecular weight of the powder will tend to increase during the build even when it is not being sintered, MFR can be used to measure material degradation [69]. This is particularly useful for determining how much powder can be reused.

Coalescence of the molten polymer is governed by viscosity and surface tension [103]. A low melt viscosity and low surface tension are desirable as these facilitate adequate coalescence which will result in high density in the parts [73]. However, a low viscosity will also result in increased shrinkage [104]. There will always be a compromise, therefore, between the various material properties if effective sintering is to occur.

In conclusion, there are many different material properties which affect how it will sinter. As all of these properties are interrelated, there is currently no one method which can be used to determine the suitability of a powder for LS; multiple complementary techniques must be employed in order to build up the full picture of how a material should be processed [105].

2.3.4.3 Machine and Part Set Up

There are many different ways a machine can be set up in order to sinter effectively and produce quality parts. Some, such as the type of laser used and whether the beam is continuous or pulsed will be set by the machine specification and cannot be changed by the user [106]. Others, such as the speed at which the laser passes over the surface of the powder (scan speed), the distance between successive parallel scan lines (hatch spacing) and the layer thickness can be changed according to the requirements of the component.

Machine manufacturers supply a range of combinations of parameters aimed at specific desired advantages such as high accuracy or achieving the highest mechanical properties [95]. It is not possible to achieve both to the highest standard. High mechanical properties require the part to have a high density and a high bed temperature is required to achieve this [107]. However, a high bed temperature is also associated with increased shrinkage which will reduce accuracy [2]. Therefore for most applications, a compromise on these desired qualities will be required.

The powder bed temperature is set to a temperature quite close to the melting temperature of the material which is determined during machine calibration. There are two main reasons for this. Firstly, pre-heating reduces the energy input required to tip the powder over its melting point to a liquid state in which it sinters. Secondly, it reduces the thermal gradient between the sintered powder and the un-sintered powder surrounding it. This reduces warpage as a result of stresses caused by the high temperature difference between the sintered part and the surrounding powder [2].

In order to compensate for the shrinkage which occurs as a result of the internal restructuring of the polymer chains during cooling, a scaling factor must be applied to the CAD file during build set up. The scaling factor is determined by building uncorrected test samples and measuring the deviation from the CAD file. The scaling factor is then applied before build, either manually by the operator setting up the build or automatically by the system software [108]. Following building

the machine must be left to cool as slowly as possible in order ensure that even shrinkage occurs.

The location of the part within the build volume can affect its final properties as it is difficult to uniformly heat the build chamber, resulting in parts of the build being held at different temperatures [107,109]. The proximity of parts to each other and the density of packing of parts will also affect the temperature distribution. Efficiently controlling the build is difficult because conditions inside the chamber change as a result of the number of varying parameters in effect, and commercial systems tend to show an uneven temperature distribution within the chamber [2].

Goodridge et al [2] mapped the temperature inside an EOS P390 machine and subsequently built and tested mechanical samples built in different locations around the machine to demonstrate how mechanical properties were affected. They found that samples built in the corners tended to have lower tensile strength than those built in the centre; this was consistent with the centre being the hottest part of the machine while the corner were far cooler (see Figure 2.14). Soe [67] investigated degree of part curling in an EOS P700 and found the surface of the powder showed the temperature in each of the four corners was different from each other while a large band across the centre of the bed was up to 7°C hotter than the lowest corner.

Bourell et al [110] used infrared imaging to identify the temperature range in their LS machine and also identified a difference of several degrees across the surface, which they point out is very significant as a difference of only 3-4°C can be the difference between the set powder bed temperature and the melting temperature of the material. They found the introduction of a multi-zone heater system significantly evened out the temperature distribution of the surface. Nelson et al [111] replaced the scanner in a DTM Sinterstation with a thermal imaging camera and also found a temperature variance of up to 7°C across the surface of the powder bed. Ghita et al [108] examined the shrinkage of PEK tensile samples according to their build location and produced a shrinkage map which showed that shrinkage was highest at the centre and lowest at the corners but also higher at the bottom of the build than at the top; they attributed this to thermal variation in the

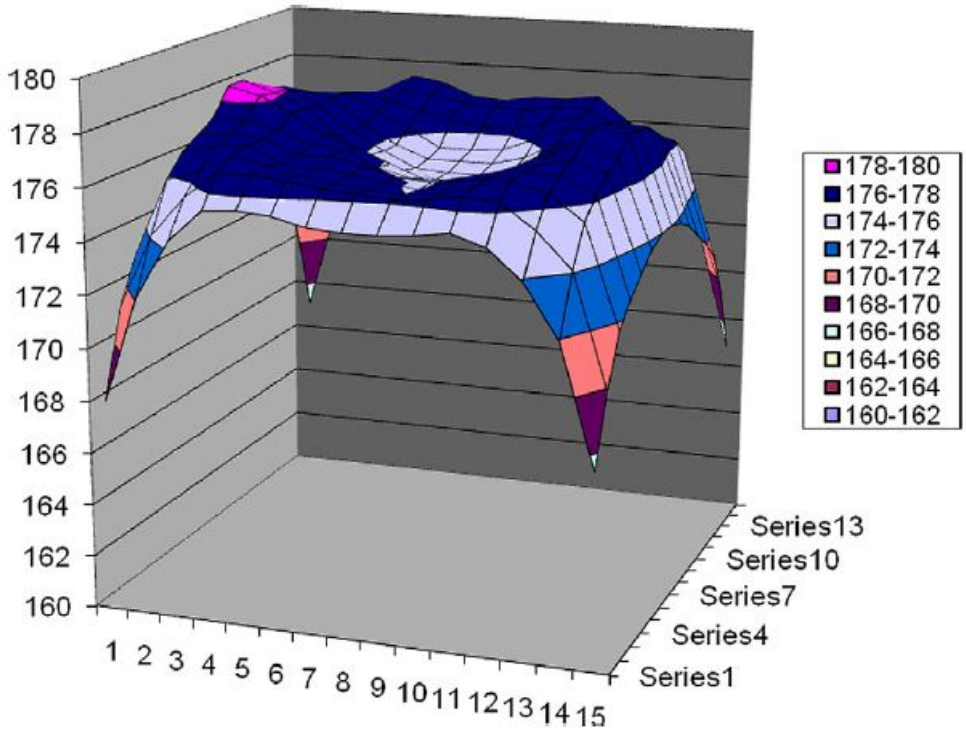

Figure 2.14: Temperature distribution measured in an EOS P390 [2]

build bed. The map of the Z-direction samples is very similar to the temperature distribution of the surface produced by Soe [67].

In order to create a comprehensive thermal map of an EOSINT P395, Josupeit and Schmid [112] drilled holes in the bottom of the frame and installed bars filled with thermocouples which then moved up through the build chamber as the build platform was lowered during building. Using Matlab they were able to generate extremely detailed 3D plots showing temperature distribution during cooling and draw conclusions about the state of the used powder as a result. Wegner and Witt [113] used wireless temperature loggers in the bottom of a build chamber and a thermal imaging system at the surface of the powder bed in order to compare the thermal distribution at both the top and bottom of the build chamber.

In-process monitoring and controlling of the temperature of the system has been proposed as the most effective way to ensure an even temperature distribution within the build chamber. To this end, studies have been undertaken to investigate methods of monitoring and adjusting the build whilst its in progress. Benda [114]

developed a system to keep the material temperature constant during sintering by detecting thermal emissions and adjusting the laser power accordingly. It was found that material was more uniformly sintered using this method. Some commercially available machines are beginning to include active in-process control which adjusts parameters such as laser power to keep the energy within the system constant. However this is not yet the norm [2].

Part orientation also affects mechanical properties; the layerwise building means the final parts are highly anisotropic in the z-direction. Gibson and Shi [74] found that tensile specimens built with a small cross section scanned in the x-y plane had higher tensile strength and density than those with a large cross section in the x-y plane. This is because the short scanning time required meant the temperature in the layer was more uniform.

In order to reduce the guesswork required to predict which parameters will lead to good results, some studies have undertaken to find theoretical ways to determine the best parameters [115]. Energy density is a measure of the amount of energy supplied to the powder bed over a given area and takes into account laser power, scan speed and hatch spacing [116]. Various studies have demonstrated that properties of parts such as density, Young's modulus and yield strength improve as energy density is increased [107, 117, 118]. Vasquez et al [119] for example looked into the effect of energy density on the properties of a thermoplastic polyurethane (TPU) which had not previously been used in laser sintering. They found that as energy density was increased they were able to achieve better mechanical properties than were observed in a similar commercial LS elastomer, enough to remove the requirement for a post sintering infiltration step.

Supplying too much energy, however, leads to degradation and a reduction in mechanical properties. Plotting the energy density against mechanical properties gives a clear indication of where this occurs; Figure 2.15 shows how Young's Modulus declines once a certain energy density value has been exceeded [68].

Starr et al [120] found that that energy density alone was not an accurate representation of the energy going into the material and developed the Energy

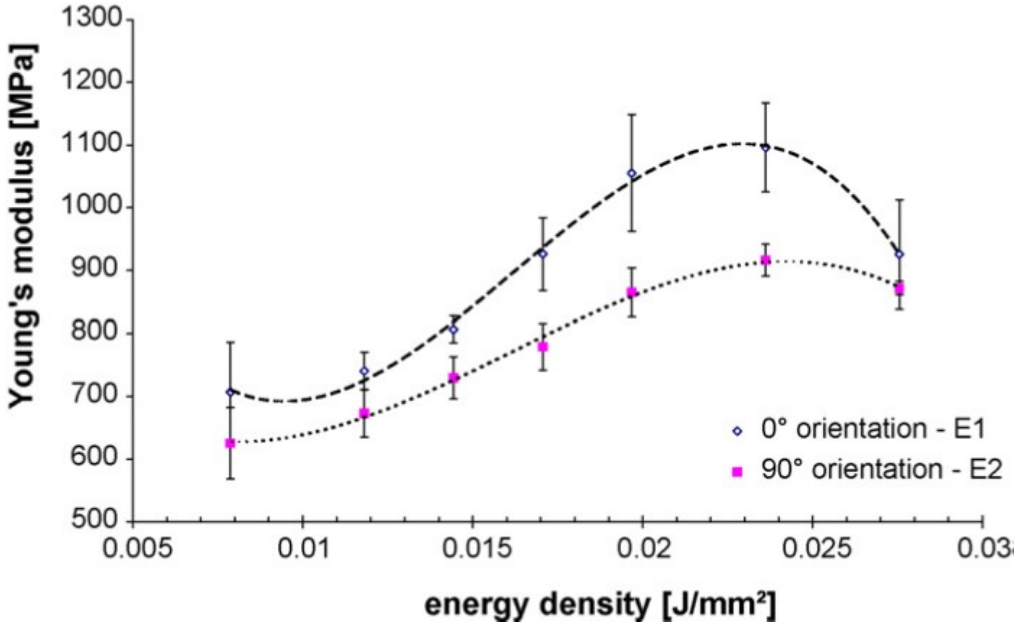

Figure 2.15: Young's modulus vs energy density for nylon-12 tensile bars [68]

Melt Ratio which takes into account the layer thickness and temperature of the powder bed during building. They found this dimensionless volumetric parameter was more accurate for a greater variety of layer thicknesses than energy density and suggested it could be used to compare results from different materials.

Sintering theory has also been examined as a more in depth way of predicting how powder particles will merge together when heated. This will be covered in Section 2.4.

2.3.5 Laser Sintering of PAEKs

The high mechanical properties of PAEKs and their broad spectrum of applications make them excellent candidates for laser sintering. However the higher melting temperature of PAEKs over other semi-crystalline polymers such as polyamide make them difficult to work with LS. As such, there is less research into LS of PAEKs compared to other polymers.

Whilst polyamide powder particles have a uniform near-spherical shape, the available PEEK tends to be irregular and studies found it difficult to deposit a homogeneous layer. Rechtenwald et al [4] found the layer thickness varied by up

to 15% across the x-axis of the layer and suggested that a different recoater was required from that used for polyamide. Woicke et al [89] successfully laser sintered PEEK powder with a carbon black additive on an experimental machine. Single layer specimens were good but as the number of layers was increased the parts began to distort. Schultz et al [77] investigated cryogenic mechanical alloying to produce a nylon 12/PEEK composite powder. Due to the powder morphology they had difficulty achieving a fully dense powder bed and the mechanical properties they achieved were lower than expected.

Distortion of parts can be attributed to thermal gradients caused by the high temperature difference between un-sintered powder and the sintered part [114]. Woicke et al [89] did not preheat the powder whereas Rechtenwald et al [4] modified the build platform so that a preheating temperature of 250°C could be achieved. They concluded that the powder should be just below the melting point for more effective sintering, as is the case with polyamide, and went on to develop an additional heating element in order to achieve this.

Using the additional heating element and by adding 1 wt% of carbon black to the PEEK power to improve flowability, multi-layer parts suitable for cell testing in vitro were built by Pohle et al [87] and von Wilmowsky et al [88]. Schmidt et al [121] went on to characterise the experimental set up. The process window required to build 100% dense parts was determined as a combination of energy density and pre-heating temperature. It was noted that whilst a large range of energy densities can produce dense parts, the pre-heating window is comparatively small if distortion in parts is to be avoided. Mechanical properties such as notched impact strength and maximum relative strength were found to be lower than traditionally manufactured parts due to residual porosity.

The only commercially available laser sintering system specifically designed to process PAEKs at the time of writing is the EOSINT P800. The machine is very similar to the EOSINT P760 in size and set up but has options for a reduced build chamber size as the un-sintered material forms a cake which maintain the integrity of the sides of the powder bed even when not physically supported [78]. Another

unique feature of the P800 is the post sintering step; following the sintering of each layer the surface of the build bed is exposed to heat for a further 12 seconds in order to ensure homogeneous coalescence across the layer [12]. The machine uses a powder optimised specifically for high temperature laser sintering (HT-LS) called HP3 PEEK. This name is a misnomer as the material is not PEEK but rather PEK. Therefore the material will be referred to as HP3 PEK from here on.

Analysis of the powder shows it to be generally less round than polyamide LS powders, with a higher angle of repose than polyamide suggesting different flow characteristics [78]. DSC analysis of the virgin powder shows that it does not have a processing window where the melting and crystallisation peaks do not overlap [12]. However, this does not affect its ability to form fully dense structures when laser sintered [122]. High resolution SEM of the powder shows that the particles are made up of clusters of micron sized particles containing submicron size fibrils [123].

Beard et al [122] built a small quantity of tensile specimens using 100% virgin HP3 PEK. SEM analysis of the fracture surface of the samples showed that the layering effect of the process was clearly visible but Micro-CT did not show up any voids or defects and the parts were fully dense. Analysis of the fracture surface by Wang et al [124] shows two distinct morphologies; layers of fully sintered structure with no visible particles, alternating with layers where individual particles are clearly present. This is similar to structure in PA-12 found by Zarringhalam et al [125] in which some particles do not fully melt but remain as nucleating "cores" which promote crystallisation.

Furthermore, the crystal morphology of the fracture surfaces show a hierarchical structure consisting of primary crystal blocks, a secondary structure of less ordered crystals and larger granular crystal blocks consisting of both primary and secondary structures [123].

In one study, Ghita et al [12] looked at the properties of the used powder. EOS do not recommend refreshing used HP3 PEK as is standard for other LS polymers, which given the high cost of the material is likely to inhibit widespread

adoption of the system [2]. The used powder showed a higher PSD compared with virgin, that is, there were larger particles present in used powder than in virgin resulting in a broader range overall, and reduced viscosity measurements showed a high insoluble fraction would could be the result of crosslinking during processing. The melting temperature and crystallinity of the used material were also much higher compared to the virgin powder. Building with a mixture of virgin and up to 30% used powder resulted in a 17% drop in tensile strength and a 16% drop in elongation at break. Hot stage analysis showed that the used particles did not melt when heated but were rather incorporated by the molten virgin material. The sintered parts showed higher porosity when used powder was incorporated but this was improved by increasing the laser power and it was concluded that with the right processing conditions, incorporation of used powder into the build could be achieved without significant detriment the to part quality.

Shrinkage across the build chamber was investigated by filling three quarters of a full size build with tensile samples in X, Y and X directions [108]. The study found shrinkage across all locations, suggesting that the scaling factor set during machine calibration was too low. Furthermore, shrinkage varied with location; shrinkage at the centre of the build was higher than at the corners and was also higher for samples built in the Z-direction than in X/Y. The tensile strength was stronger in the X and Y directions than the Z, which is typical for parts built in a layerwise fashion, but all results were lower than injection moulded samples. A difference in colour was also noted on the surface of the samples according to their location, with the darker samples being those which spent more time spent at higher temperature. When the crystallinity of the surface compared to the core of the samples was measured, the crystallinity was found to be lower in the darker samples than in the lighter, while the crystallinity inside the samples was the same regardless of location. The colour was attributed to degradation at the surface of the material, and this was confirmed by TGA analysis which showed the decomposition temperature of the darker samples was much lower than the for the cores.

Studies into using alternative PAEK powders in the EOSINT P800 have been broadly successful. Berretta et al have extensively investigated Victrex PEEK 450PF and PEEK 150PF for use in the P800 [8, 50, 78, 90, 126]. The powders were found to have angular shaped particles with highly irregular flaky structures and a much higher angle of repose than commercial LS grades which inhibited flow. The addition of fillers did improve flow somewhat [78], however tempering the material to produce more even shaped particles without the irregular surface structure was far more successful [50,90,126]. Samples were laser sintered using the tempered materials and tensile strength was found to increase with energy density, although the maximum achievable tensile strength was slightly lower than HP3 PEK samples for PEEK 450PF [50] and substantially lower for PEEK 150PF [90]. The post sintering step was found to be important for the bonding between layers although the surface roughness was found to increase as the duration of the post sintering step was increased.

Neither of the Victrex PEEK grades showed a processing window as has previously been suggested was necessary for effective LS [90]. However, the authors were able to establish a stable sintering region for PEEK 450PF which showed a wide temperature range in which the material could be processed without degradation [8]. The melt viscosity was found to affect the rate of sintering, and tensile strength was higher for the materials tested which had higher melt viscosities. By combining tensile strength, coalescence speed and MFI a region of overlap was found which recommends the material properties most desired in HT materials for effective sintering [90].

Some studies have also been undertaken on mixing PEK and PEEK with fillers and additives for use in the P800. Wang et al [124] investigated sintering a mixture of HP3 PEEK with glass beads. They found the glass beads improved the flow of the powder and resulted in an improvement in hardness, while tensile strength remained the same.

In another study the authors mixed PEEK 150PF with up to 7.5 wt.% graphite [127]. The addition of the graphite improved the absorption of heat which resulted

in better interlayer bonding but was detrimental to flowability. Whilst a small amount (up to 5 wt.%) improved mechanical strength compared with virgin PEEK 150PF, larger quantities resulted in a drop in tensile strength along with increased porosity and pore size.

Chen et al [128] manufactured composite PEK and PEEK powders incorporating carbon fibre and carbon black using two milling processes. Using rotary knife milling they were able to produce particles with a high value of circularity and roundness which showed an angle of repose comparable to HP3 PEK. Using hot stage microscopy they found that the coalescence process of the new powders was different to the commercially available LS powder but from the final results concluded that the powder had significant potential for use in the P800.

2.4 Sintering Theory

2.4.1 Introduction

Typically, materials are qualified for additive manufacturing processes experimentally by trial and error, with initial conditions set by the known material properties such as glass transition temperature, melting temperature, reflectivity and thermal conductivity. Qualification is a lengthy and often expensive process in terms of time spent turning the machine around, machine overheads, cost of material and so on.

One way to reduce the experimental requirement is to create theoretical models which describe aspects of material behaviour. These can then be used either as a starting point for experimental work, thus reducing guesswork required to find starting parameters, or to analytically predict how a material will behave under certain conditions. In the context of additive manufacturing, it is useful to model how the material behaves when heat is applied, as this can be used to determine how much heat is required and how long for in order to achieve fully dense parts with good mechanical properties.

The term sintering traditionally refers to heating particles together to form a

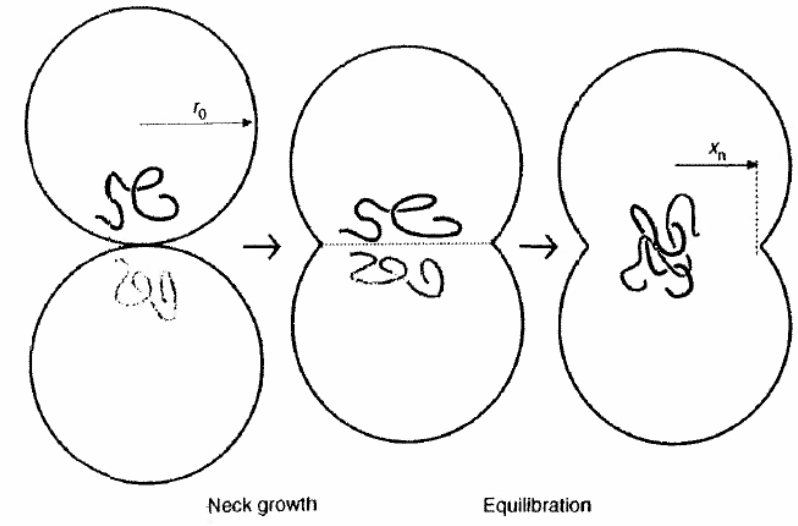

Figure 2.16: Stages of coalescence according to Mazur [130]

solid mass without bringing them to a melt [129]. As polymer coalescence requires heating beyond the glass transition or melting temperature the term sintering is incorrect. However, many publications use the word sintering interchangeably with coalescence and therefore it is now an accepted term for the melt-coalescence process [130]. Understanding the kinetics and mechanisms of the coalescence process is important because the final morphology and therefore the mechanical and physical properties of the final part can be influenced by what occurs during consolidation [131].

Sintering consists of several stages. The exact definition of what constitutes each stage differs between studies but is broadly as follows [130]. Figure 2.16 shows a graphical depiction of these stages:

1. Connections or "necks" form between particles which are in contact.

2. These necks grow, resulting in a change in the shape of the particles but the boundaries separating the internal structures remain intact.

3. The internal molecular structure of the particles relaxes, allowing reorganisation of the polymer chains and merging of the individual particles into one mass; this is known as equilibration.

Where the coalescence of multiple particles is concerned there is a further stage: The material shrinks and circular pores form which can be eliminated with continued densification [132–134]. This study is interested in the merging of two particles and therefore the formation and elimination of pores within a compact will not be covered further.

2.4.2 Frenkel and the Role of Viscous Flow

It is commonly accepted that the driving force in the coalescence of polymers is viscous flow caused by surface tension [103]. Frenkel was the first to derive a model which shows how viscosity and surface tension affect the development of the neck over time, as applicable to crystalline bodies (see Figure 2.17) [135, 136]

$$\frac{x}{a} = \left(\frac{3}{2}\frac{\Gamma t}{\mu a_0}\right)^{1/2} \tag{2.1}$$

where x is the radius of the neck between the particles, a_0 is the initial particle radius, t is time and Γ and μ are surface tension and viscosity respectively. Frenkel's model assumes that the neck growth increases linearly over time. It is only applicable to Newtonian flow and assumes the initial particle radius remains constant throughout. This restricts its validity to the early stages of coalescence.

2.4.3 Comparison of Frenkel with Experimental Results

The typical experimental procedure for observing coalescence is to place two particles of material in a temperature controlled chamber under a microscope and use time-lapse photography to take images as the temperature is changed [131]. Neck radius (x) and particle radius (a) are then measured from the images to calculate x/a, which is described as the dimensionless neck radius, or the coalescence or contact ratio. Following this, two methods of comparing with Frenkel's model appear in the literature. In the first, x/a of experimental results is plotted against time on a log-scale plot. If the resulting plot shows a linear relationship and the value of the slope is in agreement with Frenkel's theory, that

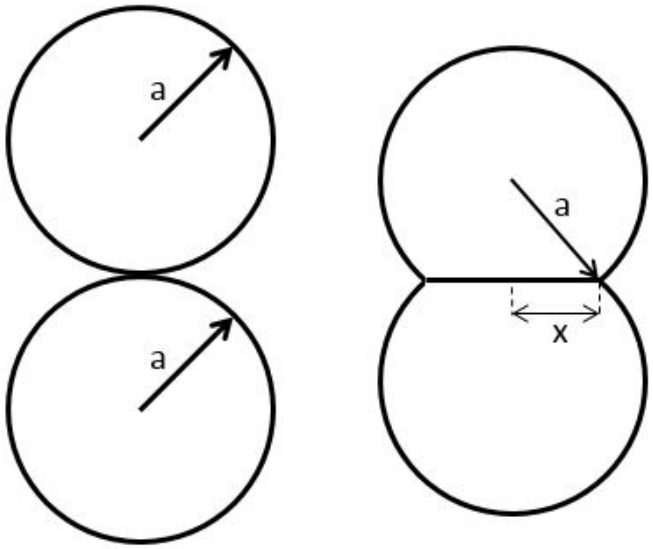

Figure 2.17: The evolution of shape of two spherical particles, according to Frenkel

is, approximately 0.5, then it is concluded that Frenkel's model holds correct for that material [137–139]. The second is to calculate the theoretical x/a curve for a material using the equation and then compare this with the x/a curve determined experimentally to see if they match [131, 134, 140].

Initially, the analysis was applied to the behaviour of metal powder systems. Several authors concluded that viscous flow alone could not account for the sintering behaviour of metal powders [141–143]. However, while investigating his own theory that diffusion was the dominant mechanism for glass particles, Kuczynski [144] found a linear relationship between the particle radius and the time held at high temperature and concluded that Frenkel's theory of viscous flow was true for this material. It should be noted that experimental results were not compared directly with theoretical curves. Rather the presence of a linear relationship between neck and particle radius against time was concluded as evidence that Frenkel's theory was correct [132].

Frenkel's model has been applied to polymers with some success. Rosenzweig and Narkis [137, 138] found sintering of polystyrene and PMMA spheres showed good agreement with Frenkel's theory, showing slopes of 0.56 and 0.53 respectively compared with the 0.5 predicted by Frenkel. Hornsby and Maxwell [139] found sintering of polypropylene beads to be in good agreement with Frenkel's model,

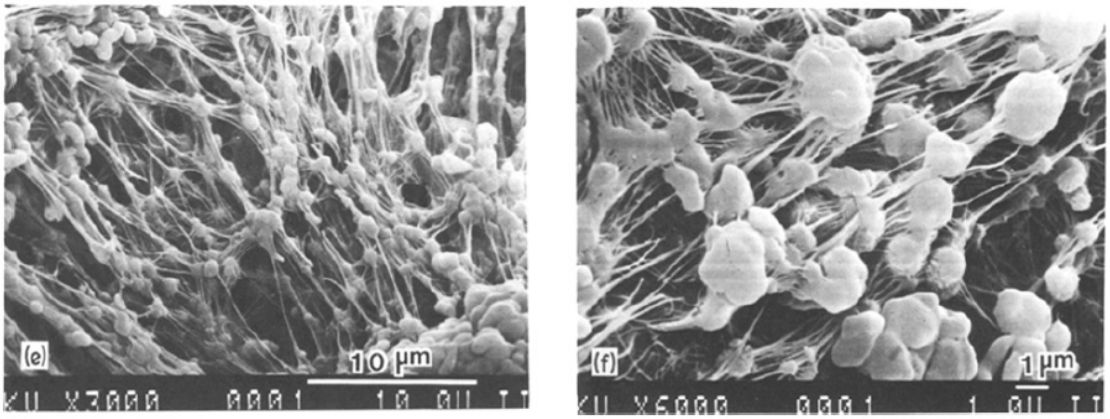

Figure 2.18: SEM micrographs of UHWMPE particles show complex morphology [145]

giving a slope of 0.48. They also assessed the effect of particle size, as smaller particles are known to sinter quicker due to their greater surface area. The gradient of the plotted curve from these results was 0.45, also in good agreement with Frenkel.

Siegmann et al [145] considered three types of polyethylene with different molecular weights and compared them with PMMA and polystyrene (PS). They anticipated that the higher the viscosity of the polymer the longer it would take to coalesce. They found the coalescence period for PMMA and PS matched up with literature but UHMWPE coalesced much quicker than the model predicted, in spite of its high viscosity. To explain their results, they considered the particle morphology. On closer inspection, the surface of the particles was found to be covered in small ($\sim$1μm) nodules connected by fine fibrils (see Figure 2.18). They concluded that the particle morphology was also an important factor in the sintering process and in some cases was more important than viscosity and surface tension.

Truss et al [146] attempted to overcome the very high melt viscosity of UHMWPE by processing it using cold compaction moulding, a process traditionally used to sinter metal powders by compacting the powder at a temperature slightly below the melting point. The viscosity of the material was so high that in theory no flow of the material should have been possible. They found that particles

with a fibrous morphology coalesced but similar grades without this structure did not. From Frenkel's equation they calculated the particle size which would lead to effective sintering taking into account the viscosity and concluded that the small fibres in the particles were the effective particle size, resulting in much faster coalescence than would otherwise be expected. When they annealed the powder to remove the fibrils the powder no longer sintered; the morphology was the driving factor in the process.

Frenkel's model assumes that the particles are perfect spheres. However, several authors have compared the model with irregular shapes of particles. Cutler and Henrichsen [147] considered the applicability of Frenkel's model to crushed glass, which has a considerably different morphology from a perfect sphere. They found the shrinkage to be significant when experimental temperature was reached, and the viscosity to be considerably higher than the data available from the manufacturer. They considered that crystalline materials would stray even further from the ideal model equation because the rate of shrinkage is not linear. Prado et al [148] also noted that sharp edges and particles without a shape factor of 1, that is, perfectly round, display increased densification rates which are not predicted by Frenkel's models.

Other authors have also proposed that factors besides viscosity and surface tension are important to the prediction of sintering time and behaviour. These include molecular inter-diffusion at the interface between the particles, [149], viscoelastic adhesive contact or curvature based forces at the neck of the two particles [150], and viscoelastic relaxation forces in the melt [151].

2.4.4 Modifications to Frenkel's Model

The simplicity of Frenkel's equation reduces the accuracy of the model in real powder systems [152]. Some authors have undertaken to modify the equation to deal with inconsistencies between theoretical and experimental results [132, 153, 154].

In the discussion of a paper by Shaler [143], Eshelby noted that Frenkel had

neglected to include incompressibility and was thus in violation of the continuity equation. His correction is as follows [155]:

$$\frac{x}{a} = \left(\frac{\Gamma t}{\mu a_0}\right)^{1/2} \tag{2.2}$$

The Frenkel/Eshelby equation is often used instead of, or as well as the Frenkel equation.

Kuczynski et al [153] developed a more general form of Frenkel's equation shown in Equation 2.3 which has been used to describe flows other than the Newtownian flow predicted by Frenkel:

$$\left(\frac{x^2}{a}\right)^n = F(T)t \tag{2.3}$$

where $F(T)$ is a function of temperature, and n is a temperature dependent constant which varies according to the melt flow behaviour. If the exponent n is equal to 1, the flow is Newtonian. When $n > 1$, the flow is non-Newtonian. Kuczynski et al [153] experimentally observed the sintering of PMMA spheres and showed that above a certain temperature, flow was non-Newtonian. Narkis [133] found a similar result for PMMA spheres except that non-Newtonian flow was observed at higher temperature than Kuczynski. Rosenzweig and Narkis [138] also examined the sintering of PMMA spheres but found the flow to be fully Newtonian and in contradiction to the findings of Kuczynski et al [153].

Hornsby and Maxwell [139] compared their results for polypropylene beads with Kuczynski's model and found an n value of 1 for all the temperatures they tested, confirming their earlier conclusion from comparison with Frenkel's model that flow was Newtonian. Hambir and Jog [156] found that UHMWPE showed a range of n values between 1.8 and 4.5, which they attributed to diffusion of polymer chains being the dominant mechanism rather than viscous flow.

Rosenzweig and Narkis [157] based their "round neck" approach on the Frenkel model, modifying it so that rather than a sharp corner at the intersection of the particle and neck radius a curved neck could be seen instead. They solved

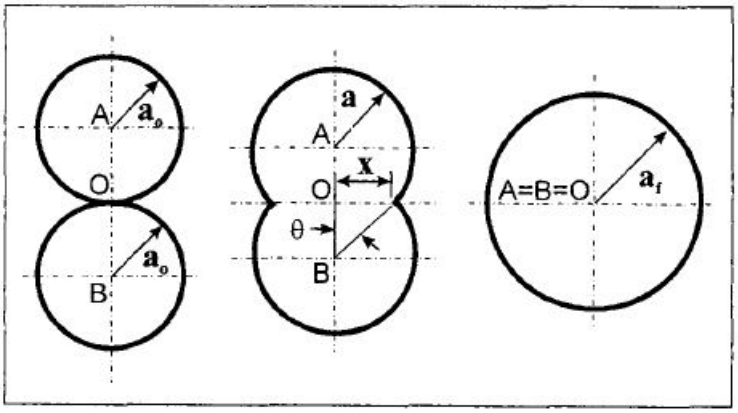

Figure 2.19: Shape evolution according to Pokluda et al [154]

their model numerically for polystyrene, finding their model to be a better fit for the experimental data than the Frenkel model, although they noted that a finite element method which could also account for the change in viscosity, surface tension and density as a function of time would be more accurate. They went on to develop this model [158] and comparison with experimental results for PMMA found it was in agreement for a small section of the sintering period.

Pokluda et al [154] went beyond the initial stages of coalescence and took into account the change of the particle radius over time in order to predict the complete coalescence process. The model was based on the balance of the work of surface tension and the viscous dissipation. Beginning with an assumption about the shape evolution of two particles which can be seen in Figure 2.19, they derived two equations to describe the evolution over time of the angle of intersection between the particle centre and the edge of the neck, and the change in the radius of the neck over time. These are given in Equations 2.4 and 2.5 respectively:

$$\theta' = \frac{\Gamma}{a_o \mu} \frac{2^{-5/3} cos(\theta) sin(\theta) [2 - cos(\theta)]^{1/3}}{[1 - cos(\theta)][1 + cos(\theta)]^{1/3}} \tag{2.4}$$

$$\frac{x}{a_f} = sin(\theta) \left(\frac{2}{[1 + cos(\theta)]^2 [2 - cos(\theta)]} \right)^{1/3} \tag{2.5}$$

where θ is the angle of intersection between the particle centre and the edge

of the neck, a_o and a_f are the initial particle radius and the final particle radius respectively and x is the radius of the neck.

Equation 2.4 was shown to be the numerical solution the Frenkel/Eshelby Equation (given in 2.2) once solved using an automatic step size Runge-Kutta-Fehlberg integration method to give a range of values with time. These values were then substituted into Equation 2.5 to give the corresponding change in particle radius and the results for both equations plotted.

They found the model was similar to Frenkel/Eshelby and Hopper's Model for the early stages of sintering but subsequently predicted a slower neck radius evolution.

They compared their model with several other models and were able to improve the fit to experimental data for various grades of polyethylene. However, application to other materials was not as successful [134]. Bellehumeur et al [149] applied the model to propylene ethylene copolymers and found the material coalesced far slower than the model predicted. This was attributed to rheological behaviour such as stress relaxation time which was unaccounted for by the model.

Bellehumeur [134] introduced more steps into the modified-Frenkel equation published by Pokluda et al [154] in order to account for viscoelastic behaviour, which it was hypothesised was the reason that the original model was unsuccessful. The viscoelastic model was found to be a better fit for the tested copolymer resins than the Pokluda et al model. Asgarpour et al [159] compared experimental results for polyvinylidene fluoride with Bellehumeur's model and found that it was in very good agreement for the sintering of two grains of material. However, when Perot and Maazouz [160] applied Bellehumeur's updated model to three commercial ethylene-propene copolymers used in rotational moulding they found the experimental data showed coalescence was much slower than the model predicted. Muller et al [161] compared the theory with several different materials and found it worked for some but not others, concluding that the model did not take into account all the factors which were important to the sintering of certain materials.

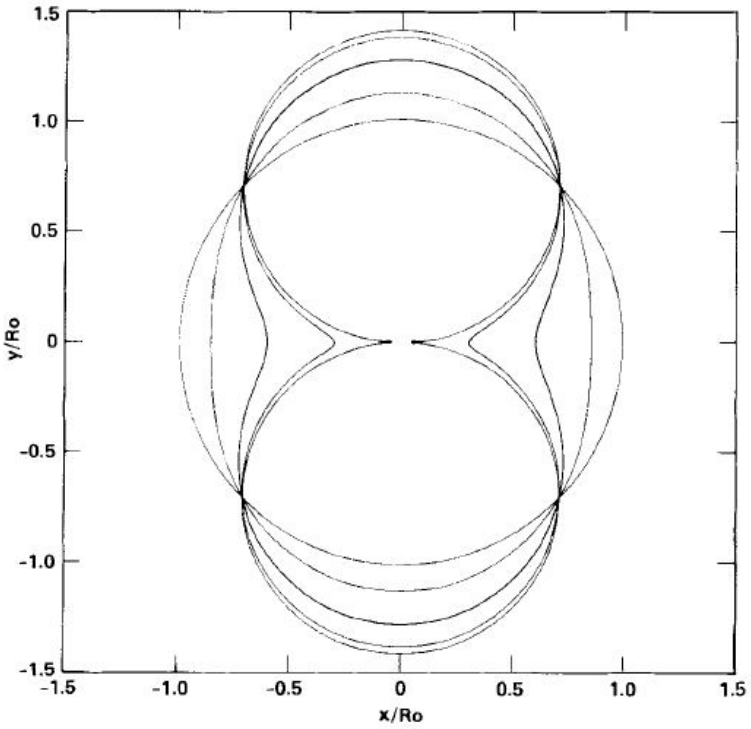

Figure 2.20: Shape evolution according to Hopper [162]

Hopper [162–164] considered the Frenkel's model as the basis for a more complete approximation of sintering. Hopper's approach was to consider how the shape of two equal cylinders changes throughout the coalescence as a result of surface tension and viscous flow, assuming that the contact of the two cylinders at the neck forms the shape of an inverse ellipse; see Figure 2.20.

The model employs an exact solution of the Navier-Stokes equations resulting in the following equations:

$$\frac{x}{a_f} = \frac{(1-\alpha)}{\sqrt{1+\alpha^2}} \tag{2.6}$$

$$\frac{\Gamma t}{\mu a_f} = \frac{\pi}{4} \int_{\alpha^2}^{1} \frac{1}{(\beta\sqrt{(1+\beta)}\mathrm{K}(\beta)} \mathrm{d}\beta \tag{2.7}$$

where a_f is the final particle radius and α is a number between 0 and 1; when $\alpha = 0$ the curve is a circle and as $\alpha \to 1$ the curve approaches the shape of

two circles. The function $K(\beta)$ is the complete elliptic integral of the first kind, a mathematical function defined by Gradshetyn and Ryzhik [165] for which the solution is:

$$K(\beta) = \int_0^1 [(1-\chi^2)(1-\beta\chi^2)]^{-1/2} \mathrm{d}\chi \tag{2.8}$$

where χ is a parameter of the elliptic integral ranging from 0 to 1. Bellehumeur et al [131] found Hopper's model to be more accurate than Frenkel and Frenkel/Eshelby when compared with experimental results for various rotational moulding polymers.

In summary, attempts to adapt Frenkel's model to better reflect the sintering of polymers show that it can be modified successfully for a specific material given a set of assumptions, but typically the modified models cannot then successfully be applied to other materials if the assumptions do not hold true for those materials also. Several authors have noted that the simplicity of Frenkel's model is one of the main reasons it remains the starting point for modelling of the sintering process [11, 161]. Kuczynski's modification is useful for identifying whether the flow is Newtonian or non-Newtonian. Models such as Hopper are useful as it describes the coalescence beyond the early stages but remains relatively simple to undertake.

Sintering of polymer particles involves complex thermodynamics and a simple model will be an approximation at best. Many studies have chosen to use numerical simulations in order to better capture the coalescence of polymeric materials [150, 166–169]. Numerical simulations are considered outside the scope of this investigation and therefore only analytical models are considered.

2.4.5 Theoretical Modelling and Laser Sintering

Whilst there is considerable research into the modelling of coalescence of polymers in general, there is substantially less research into the modelling of coalescence specifically for laser sintering polymers, and the application of theory to practical

situations is limited. Studies aimed at qualification of materials tend to focus on adjusting build parameters in order to improve build quality rather than focusing on more fundamental details such as how coalescence occurs. Research involving viscosity typically focuses on melt flow rate which is useful for establishing how effective a material will be when re-used during LS but authors note that it is a diagnostic tool and more comprehensive understanding of the material state is still desirable for improving recyclability of LS materials [2, 140].

Modelling laser sintering is difficult because of the changes in temperature that occur during the process which result in constantly changing viscosity and surface tension. Haworth et al [140] used Frenkel's approximation as a starting point for their research. They considered the relationship between viscosity, shear stress, surface energy and molecular weight for Nylon-12. They noted that pre-drying the powder was very important as water absorption reduced shear viscosity. Variations in the viscosity of virgin and used powder were considered as a function of molecular weight. The molecular weight in used powder was much higher than virgin as a result of degradation. They concluded that Frenkel's model could be used to predict how changing the percentage of used powder in the mix would affect the sintering time but did not directly correlate this with experimental data. They instead used the model to demonstrate that the increase in viscosity observed in used powder will affect sintering times when the percentage of used mixed with virgin for re-use is increased.

In an earlier paper the authors expressed uncertainty about the suitability of Frenkel's model as a predictive tool for LS materials; typically LS powders are an uneven size and shape with a wide particle size distribution. Furthermore, thermal gradients in the powder bed cause uneven temperature distribution making Frenkel's model an oversimplification of what is occurring during LS [170]. Frenkel's equation still has its uses in characterising materials for LS however, as surface tension and viscosity are both important factors in the coalescence of polymers, particularly semi-crystalline thermoplastics [171].

An important change required in order to apply Frenkel's method to LS

materials is the use of a dynamic heating rate. In traditional sintering materials are held for several hours at the same temperature. All the sintering models described in the previous sections cover isothermal heating of polymers, usually at a selection of different temperatures in order to compare how this affects rate of coalescence. By contrast, in LS extreme heat is applied to the material for a fraction of a second to very quickly tip it over the melting temperature; Vasquez [11] estimates that the heating rate of the LS process when applied to polyamide is approximately 22,000°C min^{-1}. In order for experimental work in a hot stage to be a suitable reflection of the LS process it makes sense to use a dynamic heating rate rather than holding at one temperature.

Rather than attempt to replicate the very fast heating rate in the LS machine which the hot stage was not capable of, Vasquez et al [171] used a heating rate of 10°C min^{-1} as this allowed them to use DSC traces undertaken at the same rate to identify the melting regions for each material. They used Frenkel's relationship between neck radius and particle radius to plot coalescence for each of their materials so they could compare melting behaviour. They suggested that hot stage microscopy of particles could be used as part of the screening process for potential new LS materials alongside other material characterisation methods such as DSC.

In summary, whilst Frenkel's model is cited often as the basis for understanding coalescence of LS materials, no work has been specifically undertaken to compare theoretical models with experimental results.

2.4.6 Theoretical Modelling of PolyEtherKetones

An approach based on on Bellehumeur et al's work [131] on quantifying coalescence was used by Berretta [90] to analyse coalescence behaviour of HP3 PEK compared with two grades of PEEK previously unqualified for LS. This was used as part of a wider investigation to identify desirable properties of HT polymers for LS but the prediction of theoretical modelling curves was not covered.

Brink et al [172] investigated cold compaction moulding of PEEK as a potential processing method which avoids the crosslinking reaction associated with high

temperature processing. They focussed on using small (submicron) particles to increase the surface area and therefore the surface free energy to drive the sintering and successfully formed dense compacts under some of the conditions tested. They reported good agreement between their experimental results and Frenkel's equation. By rearranging Frenkel's equation in conjunction with the plot from their experimental work, they were able to estimate the effect of particle size on sintering and found these estimations to be in good agreement with experimental work also. This was the only study which could be found which specifically covered theoretical modelling of the coalescence behaviour of PAEKs.

It would appear however, that no work to date has been undertaken to construct theoretical models of the coalescence behaviour of laser sintering PAEK materials.

2.5 Conclusions

PolyArylEtherKetones (PAEKs) are a family of high performance semi-crystalline thermoplastics, developed for high working temperatures, high mechanical properties, good chemical resistance and ease of processing. Properties such as tensile strength can be increased by increasing the percentage crystallinity through annealing or long slow cooling times from high temperature, however it believed that PAEKs begin to degrade when processed above their melting temperature, typically resulting in crosslinking of the polymer chains.

Additive Manufacturing (AM) is a group of manufacturing technologies capable of producing near-net shape objects from 3D data. Laser sintering (LS) is a powder based AM technology used for producing high quality components in semi-crystalline thermoplastics by selectively fusing powder layer by layer to generate 3D parts. Benefits of using LS over traditional manufacturing methods include increased design flexibility and reduced material waste as powder which has not been sintered can be reused.

Qualifying materials for LS can be challenging as the thermal processes involved are very complex and there are many factors which govern how successfully a material can be sintered. As a result there are still a limited number of materials

available. The physical properties of the powder such as size, shape and flowability as well as intrinsic properties such as viscosity and glass transition and melting temperature are all important when considering potential new LS materials. The LS process itself is governed by a number of machine build parameters but factors such as the location and orientation of components within the build chamber can impact their final properties.

Historically, how effective a material will be during LS has been analysed using thermal characterisation techniques such as differential scanning calorimetry, however recent research shows that some materials can be successfully sintered even without displaying characteristics previously thought necessary. As such, research is now seeking to find new, more general methods of identifying material suitability which take into account more of the material characteristics.

The build parameters which will produce good components must be determined for each material and a compromise between accuracy and mechanical properties is generally required. The temperature inside the powder bed is very important to the properties of the finished part; as a result of the number of parameters governing the sintering process it can be difficult to uniformly control temperature throughout the whole chamber which can result in warping, uneven shrinkage and even degradation of both parts and powder.

LS of PAEKs is a challenge because of their high melting temperature, however some experimental systems have been able to build parts and a system designed specifically for working with high temperature materials is commercially available. The EOS P800 is supplied with a PEK material known as HP3 and research shows that it produces 100% dense parts despite having different material characteristics from those traditionally thought necessary for successful sintering. However, reuse of the material is not recommended and studies into tensile samples show uneven shrinkage and discolouration across various locations in the build chamber.

Modelling of sintering behaviour provides another method of examining material properties and has the potential to reduce the trial and error required to find successful LS parameters, by identifying the temperature at which each

stage of coalescence occurs and predicting sintering behaviour based on known material properties. The most common theoretical model for sintering as a result of viscous flow is Frenkel. Frenkel's equation has been shown to be useful for predicting the early stages of sintering for many polymers. Several models have undertaken to improve upon Frenkel's method to predict the whole coalescence process, with varied success. Where Frenkel and related models do not compare well with experimental work it is typically because they are too simplistic to explain complex flow behaviour.

Some work has been undertaken on examining coalescence behaviour of LS materials, however this has not covered comparison of theoretical models with experimental work, and no previous work has considered application of theoretical models to LS PAEK materials.

Thus it has been identified that more work is still required to understand the most effective way to qualify new materials for laser sintering, particularly if qualification is to be based on a thorough knowledge of fundamental material characteristics rather than using an experimental trial and error approach. Modelling and prediction of coalescence behaviour has potential to be useful in this regard. The high temperature of PAEKs mean that understanding the thermal properties of both the material and the LS process are particularly important in order for them to be processed effectively.

Chapter 3

Experimental Methods

Investigation of HP3 PEK powder with different thermal histories and the EOSINT P800 high temperature laser sintering (HT-LS) system was undertaken using a number of characterisation methods. These can be categorised into three groups; a) characterisation of powder material, b) characterisation of melting behaviour and coalescence, and c) characterisation of the EOSINT P800 system and the HT-LS process.

This chapter covers the equipment and the experimental methods used to undertake the characterisation. For each technique, a description of the equipment used and the procedure followed for each experiment is included.

3.1 EOSINT P800 HT-LS System

The EOSINT P800 HT-LS system was as supplied and installed by EOS, and an internal view is shown in Figure 3.1, with a brief description of the numbered components listed below:

1. Optics chamber: contains the laser and associated systems
2. Left dispenser: one of two containers from which powder is dispensed into the system for building; a powder delivery system transports powder from a larger hopper stored outside the system into the dispensers as they are not large enough to contain all the powder required for a full size build

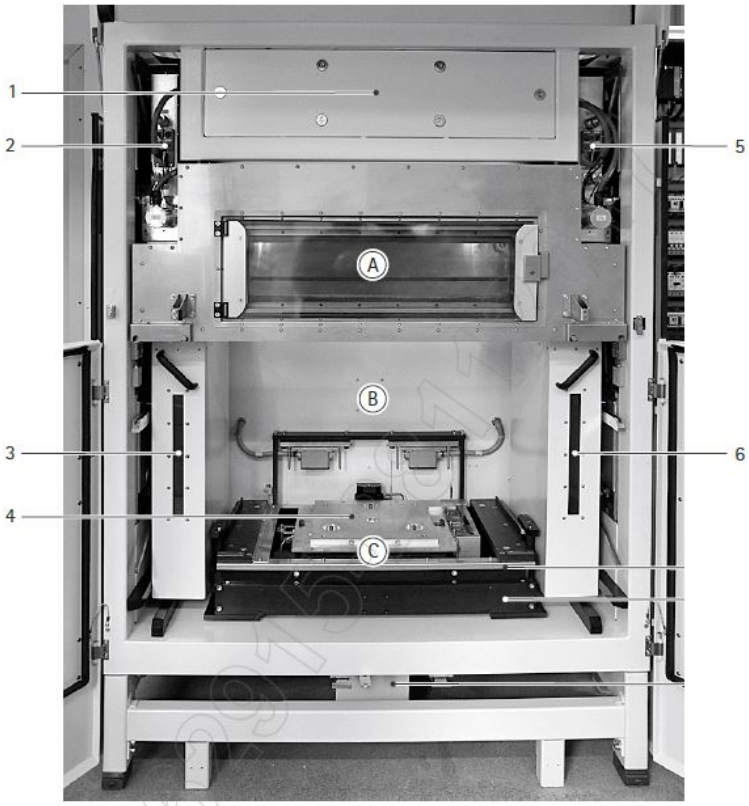

Figure 3.1: Internal view of EOSINT P800 HT-LS system [173]; A: Process chamber, B: Removal chamber, C: Z Axis system, individual numbers explained in Section 3.1

3. Left overflow bin: one of two containers in which the powder left over in the recoater following recoating is deposited for removal later
4. Building platform carrier: raises the build platform during building
5. Right dispenser: second of two containers of powder to be dispensed into the system during building
6. Right overflow bin: second of two containers for powder left over following recoating

A chamber referred to as the exchangeable frame is inserted into Area B, and is removed following building to a separate breakout station so that parts can be removed. The exchangeable frame consists of an outer frame which fits over Area C, and a non-fixed build platform which begins the build at the top of the frame and is moved down by set increments each layer in order for powder to be dispensed into the system.

The build chamber dimensions are 700 x 380 x 560 mm, and the material is sintered by two CO_2 lasers, one for each half of the chamber with a small overlap in the middle. The P800 employs a double blade recoater to spread each layer of powder; the recoater sweeps from one side of the process chamber to the other each layer, alternating between the left and right sides each layer, thus there are left and right dispensers and overflow bins. Not all powder dispensed is required for a given layer; any excess is deposited in the overflow bins where it remains during the rest of building for removal later. Powder which is not sintered remains in the build chamber around the parts until the building process is complete and is manually removed from around the parts in the break outstation.

3.2 Material

The material in all experiments was HP3 PEK, a fine powder supplied by EOS for use in the EOSINT P800 system. It is based on PolyEtherKetone and has a melting temperature of 372°C [174].

All powder was stored in temperature and humidity controlled conditions to prevent absorption of moisture and exposure to light and heat.

Several different thermal histories were investigated, these are as follows:

- Virgin: Brand new powder as supplied by EOS, not previously used in building.
- Overflow: Powder which has been spread across the surface of the build during recoating but which was not deposited as part of the layer, being instead deposited in overflow collection bins to to either side of the build chamber of the P800, as shown in Figure 3.1.
- Used: Powder which has been in the build chamber during building but which has not been directly exposed to the laser. All material still in powder state (e.g. not excessively agglomerated) is collected when the parts are broken out following building.

Figure 3.2: Location of used powder samples

Furthermore, there were four different states of used powder, as follows:

- Corner: Powder taken from the corner of the build chamber, furthest away from the centre.
- Mid: Powder taken from midway between the centre and the corner, darker in colour than corner powder.
- Centre: Powder taken from directly around the parts in the centre of the build. This powder is very dark in colour compared to all other used samples and would not be included in with other used powder for re-use but for comparison purposes may be useful.
- Sieved Mixed Powder: Almost all of the used powder (apart from the powder closest to the parts) is collected after each build and contained together. This means it includes powder from all locations around the build. It is sieved to get rid of large agglomerations and inclusions left from the build.

Samples for individual locations were taken during breakout at approximately halfway down the same 50mm height build consisting of closely packed tensile samples, from the locations shown in Figure 3.2. Sieved mixed used powder was taken from stored collected powder from multiple different builds.

3.3 Characterisation of Powder Material

Characterisation of powder was undertaken on all thermal histories, except where explicitly stated.

3.3.1 Particle Size & Shape

3.3.1.1 Scanning Electron Microscope

Scanning Electron Microscopy (SEM) is a technique used to take very high resolution images by scanning the surface of a sample with a focussed beam of high-energy electrons. Images of powder particles were taken at increasing magnifications using an FEI Nova NanoLab 600 scanning electron microscope. Powder was distributed in a thin even layer on a stub of metal covered with adhesive, and then coated with a 4nm gold coating to reduce surface charging. At least four images were taken at each magnification, and the whole surface of the sample was scanned visually before choosing sites which were representative for imaging.

3.3.1.2 Particle Size Distribution

Particle size distribution (PSD) analysis was undertaken to determine the range of particle sizes in a typical sample of each thermal history of powder. A Micromeritics Saturn Digisizer 5200 employing light scattering analysis was used. The powder was dispersed in 0.4% sodium hexametaphosphate; 6.7g sodium hexametaphosphate and 1.3g sodium hydrogen carbonate in 2 litres deionised water. A laser was shone through the suspension and a charge-coupled device detector collected a high resolution image of the scattering pattern from which the PSD was determined. Three repeats were taken for each sample.

PSD was undertaken on virgin, overflow and sieved mixed used powder only; unsieved powder would not be used in the build process as it could contain large agglomerations of particles which would adversely affect spreading and packing.

3.3.2 Crystallinity

3.3.2.1 Differential Scanning Calorimetry

Differential scanning calorimetry (DSC) is a thermal analysis technique which can be used to determine material properties such as melting temperature, glass transition temperature and crystallinity. A small sample of powder in a pan is subjected to a pre-determined heating regime. The energy required to maintain the regime is measured and compared to the energy required to subject an identical but empty pan to the same regime. The output is a quantitative measure of enthalpy change which is plotted against temperature to produce a graph. Thermal events such as melting and recrystallisation can be read from the features of the graph.

Tests were undertaken using a Mettler Toledo DSC821e. Samples of 10mg±0.8mg were placed in crimped aluminium pans with an empty pan used as a reference. Nitrogen gas at a flow rate of 50ml min^{-1} was used to protect the sample from oxidation. Virgin and overflow samples were cycled from 30°C to 400°C to 30°C at 10°C min^{-1}. Used powder was initially cycled to 400°C but it was established that full melting was not complete at this temperature; all subsequent samples of all thermal histories of used powder were cycled from 30°C to 440°C to 30°C at 10°C min^{-1}. At least five repeats were taken for each thermal history. Results were recorded using Mettler Toledo STARe software.

Results were analysed using both Mettler Toledo STARe software and OriginPro software. Both software packages contain features for determining peaks such as peak melting temperature (T_m) and peak re-crystallisation temperature (T_χ), as well as for calculating the area of endotherms and exotherms which could then be used to determine crystallinity.

Crystallinity (χ) was calculated for melting and recrystallisation by integrating the area of the enthalpy from the corresponding endo or exotherm using the following equation, as given by Blundell et al [175]:

$$\chi = \frac{\Delta h}{\Delta H_f} \tag{3.1}$$

where Δh is the enthalpy of the melting endotherm and ΔH_F is the enthalpy at theoretical 100% crystallinity. Blundell and Osborn calculated this value to be 130 kJ kg^{-1} for PEEK [40], and Tregub et al determined the value for PEK to be very similar [176].

3.3.2.2 X-Ray Diffraction

X-Ray Diffraction is a non-thermal method of identifying crystal properties of materials. An incident beam of monochromatic X-rays is directed at the sample and is scattered when it encounters crystal lattices in the material. The interactions of the reflected x-rays are recorded and produce patterns according to the crystal structure, which is unique to each material. The positions and intensity of peaks in the pattern can be used to identify crystal structure, specific phases and percentage crystallinity of a sample.

The sample was prepared by first grinding the powder using a pestle and mortar to ensure fine particles and in the case of used powder, to break down any remaining agglomerations of particles following sieving. Samples were then lightly compacted on a glass slide. XRD was performed using a Bruker D8 Advance X-Ray Diffractometer with a LynxEye detector, operating at 40kV voltage and 40mA current using CuK radiation (γ=0.1542nm) in the 2ϕ= 5°-50° range in 0.05° increments. Three repeats were performed for each sample. Results were recorded using Bruker DIFFRAC.Measurement.Suite.V4 software and were analysed in both DIFFRAC.EVA V4 software and Origin Pro software.

Percentage crystallinity is indicated by the area under each peak. A figure was determined by measuring the whole area of the graph and subtracting the amorphous peak. The amorphous fraction was determined by applying a baseline through the bottom points of each peak, as shown in Figure 3.3. The area under the line marked "amorphous baseline" corresponds to the amorphous fraction. To determine crystallinity Equation 3.2 was used.

$$\chi = \frac{\text{Total Area} - \text{Amorphous Fraction}}{\text{Total Area of Plot}} \times 100\% \tag{3.2}$$

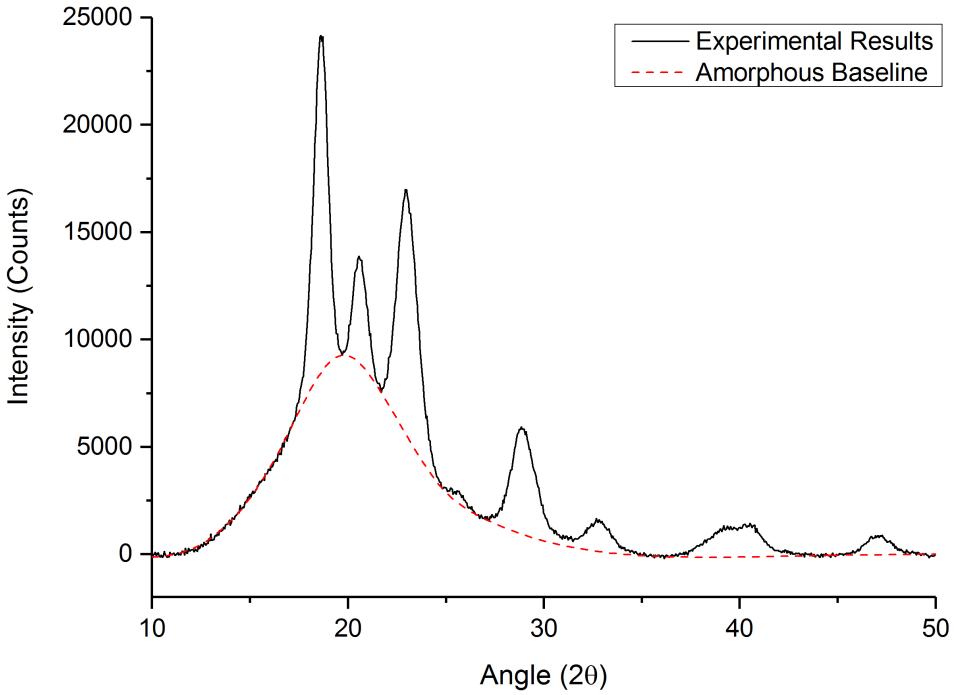

Figure 3.3: Calculating crystallinity from XRD trace

XRD was undertaken on virgin, overflow, mid used and sieved used mixed powder, as due to time constraints it was not possible to examine all thermal histories.

3.3.3 Degradation

3.3.3.1 Thermogravimetric analysis

Thermogravimetric analysis (TGA) is another thermal technique used to learn about properties of materials by subjecting them to a controlled temperature profile. As a material is heated it undergoes chemical changes such as absorption or loss of water, oxidation and decomposition. These chemical reactions result in a change of mass. In TGA, a sample weight is measured using very sensitive scales and any change in mass as temperature is increased is recorded. The resulting decomposition curve can be used to identify the temperature at which a material degrades and how it breaks down. In the context of analysing additive manufacturing materials, it can be used to identify the point at which degradation starts occurring and therefore the maximum temperature to which the material

should be subjected during building if it is to be reused in subsequent builds.

The TGA instrument used was a NETZSCH TG 209, and resulted were recorded using Proteus software, and analysed using OriginPro software. Samples were heated from 25 to 900°C at 10°C min^{-1}, and test were undertaken on virgin, overflow and mid used powder.

Ceramic pans were used for all tests; these were first cleaned by heating to 900°C and holding for five minutes to ensure any material residue from previous tests was burnt off. Before beginning a new series of tests and in between each set of two experiments, a correction run was undertaken. An empty pan was heated using the same temperature profile as the subsequent experiments and the results used to provide a correct baseline for the experiments. All samples weighed 10mg±0.2mg. Nitrogen gas at a flow rate of 50ml min^{-1} was used to protect the sample from oxidation. Three repeats were taken for each sample.

3.3.3.2 UV-Visible Spectroscopy

Following building in the P800, both built samples and the used powder showed varying degrees of discolouration. UV-Visible Spectroscopy quantifies change in colour by displaying it as a function of wavelength. A pre-determined range of wavelengths of light are shone onto a sample and the reflected light collected and displayed either as a function of the the light reflected or absorbed by the sample. If the identified wavelengths can be shown to correspond to specific thermal behaviour as identified by DSC and TGA, then it could offer a non-destructive method of identifying degradation.

The equipment used for UV-Visible Spectroscopy was an Ocean Optics DH2000 Deuterium-Halogen Light Source connected to an HR2000+ Spectrometer. The probe used was an R400-7-UV-Vis inserted into an RPH-1 Reflection Probe Holder.

The samples were 60mm x 10mm x 5mm bars, built on the P800 using the standard profile provided by EOS. Samples were built horizontally in the configuration shown in Figure 3.4. As the samples showed a colour change gradient from one end to the other, the colour of both ends was measured. To ensure that

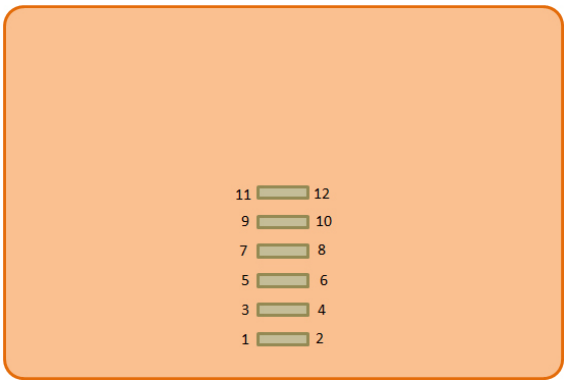

Figure 3.4: Location of samples for colour testing

colour was measured from the same position on each sample, the probe holder was held upside down and the sample placed such that the end fitted against a stop. During measurements the sample was weighted to ensure it fitted flush against the probe holder, thus reducing extraneous light.

Measurements were recorded using SpectraSuite software in Absorbance mode using an integration time of 450ms, 10 scans to average and boxcar width 5. Each measurement was run twice and the second set of results recorded. A minimum of three measurements was taken for each sample. The SpectraSuite software was also used to output the CIE Y value, known as luminance, for each sample.

3.4 Characterisation of Coalescence

3.4.1 Hot Stage Tests

Using a hot stage with an optical microscope allows the user to observe at magnification how a material changes visually as heat is applied. The sample is placed on a slide inside a sealed environment which can be very precisely controlled. The hot stage controller can then be programmed with a set heating and cooling profile, allowing the user to observe what is going on through the microscope. The purpose of the tests in the context of this work is two-fold; to understand more about the nature of the coalescence of HP3 PEK powder, and to compare coalescence plots with theoretical models as put forward by Frenkel,

Frenkel/Eshelby and Hopper (see Section 2.4).

The hot stage was a Linkam THMS600, connected to a Linkam TMS94 controller. Observations were made on a Bruker IRScope II in visual reflection mode. Initially, images were captured manually with a Sony CCD-IRIS Camera (model SSC-C350P), and viewed using Opus software. Dimensions were measured in pixels using Gimp 2 image editing software and converted to µm using a calibration guide.

Following the first set of dynamic tests, a new Dino-Eye Microscope Eyepiece Camera (model AM-423X) was used for the rest of the experimental work. Images could be captured either manually or automatically using the time-lapse function in DinoCapture 2.0. This software was also used for analysis and measurements of images.

All hot stage tests were undertaken on virgin powder only, apart from a small study on used powder; this is described separately in Section 3.4.1.5.

3.4.1.1 General Method

A thin layer of powder was scattered on a glass slide in the chamber of the hot stage. Due to the small size of the particles it was not possible to place them in the desired arrangement. Instead the layer of powder was carefully examined for particles which were in this placement following spreading. A pair of particles was considered suitable if they were both clearly visible (the magnification quite often made this difficult), approximately circular and there was little chance of surrounding particles being pulled into the melt during the test.

3.4.1.2 Dynamic Heating Tests

Initially a heating rate of 1°C min^{-1} was chosen; it was anticipated at this low heating rate the coalescence would occur slowly, allowing fpr in depth analysis. Images were taken manually every 5 minutes. However, at 400 °C, very little coalescence had been observed. The heating rate was subsequently increased each test to examine how heating rate affected coalescence; the heating rates tested were

1, 8, 10, 20, 60, 80 and 100°C min^{-1} and powder was heated to 400°C in each test. At least two repeats were undertaken for each heating rate.

All subsequent dynamic heating tests were undertaken at 100°C min^{-1}. It was decided that this very fast heating rate was desirable in order to more accurately simulate the heating taking place in the LS machine and to minimise oxidation of the sample due to the air atmosphere. All further analysis was undertaken as follows; the powder was heated from ambient temperature to 440 °C at 100°C min^{-1} and images were taken automatically every second once 370 °C had been reached. Ten repeats were undertaken at this heating rate.

3.4.1.3 Isothermal Heating Tests

The theoretical models chosen for comparison with experimental results predict sintering at a constant temperature. Although LS takes place using dynamic heating, isothermal tests were undertaken for better comparison with theory. Five hold temperatures were tested; 375°C, which is very close to the melting temperature of the powder, 380, 385, 390 and 395°C, at which it had been observed from the dynamic heating tests that significant coalescence had already occurred. The powder was heated from ambient temperature to the hold temperature point at 100°C min^{-1} and then held at the hold temperature for 20 minutes. Images were taken at regular intervals throughout the hold period.

From these tests, it was identified that the majority of coalescence occurred between 380 and 385 °C. A further test was undertaken at 381 °C to determine whether a "trigger" temperature existed at which isothermal heating would be sufficient to complete coalescence. Powder was heated as before but held at 381 °C for two hours. As significant coalescence had occurred before the hold point was reached, it was decided not to test any higher temperatures and instead to focus on dynamic heating.

3.4.1.4 Investigation of Adhesion Effects

To determine if adhesion to the glass slide affected the rate of coalescence, a series of tests were undertaken on glass slides coated with a non-stick material. Slides were sprayed with a thin layer of Molykote 321R, a carbon-based dry lubricant; as a result of the high temperature of the tests this was the only material found which was suitable. The slides were left to cure for at least 20 minutes in an air atmosphere before use in the hot stage. Ten repeats were undertaken from ambient temperature to 440 °C at 100°C min^{-1} as per the method outlined in Section 3.4.1.2 in order to allow direct comparison of results.

3.4.1.5 Used Powder

A small study was undertaken on used powder, as DSC results showed a melting curve for each of the thermal histories of used powder, but observation of the samples following DSC showed that distinct particles were still visible.

Tests were undertaken on corner, mid, centre and sieved mixed used powder. Two sets of tests were undertaken; in the first, the powder was heated to 440°C at 10°C min^{-1}, and in the second the powder was heated to 440°C at 100°C min^{-1}. These heating rates were chosen because the tests were undertaken on the Bruker microscope with no time lapse function and it was difficult to take images during the test at high heating rates; images were taken at regular intervals during the test at 10°C min^{-1}, and at ambient temperature and at 440°C for the 100°C min^{-1} heating rate test.

3.4.2 Measurements Required for Modelling

As HP3 PEK is a new material, viscosity values required for theoretical modelling were not available. Furthermore, it was decided that the theoretical model should be compared with dynamic heating results rather than isothermal and displayed as a function of temperature as well as time. This meant a range of values between 375°C and 440°C were required. As a result, it was necessary to experimentally determine to the viscosity of virgin HP3 at a range of temperatures.

Viscosity was measured using a Rosand Precision RH7-2 Twin Bore Capillary Rheometer. Capillary rheometry works by applying a force to molten material to push it through a bore and out through a capillary die. The pressure is measured as the material exits through the die and shear viscosity can be calculated from the resulting measurements. The mathematics of calculating viscosity from the data require the use of corrections; the Bagley correction in particular necessitates the use of two capillaries measuring two different pressure drops. The first die is used to obtain shear flow results, while the second - the "zero length" die - was used to obtain corrected values of shear viscosity. The corrections and subsequent calculation of viscosity data were done automatically by Flowmaster Control software, which was also used to control the rheometer.

Experiments were run using dies of length 16mm and 0mm and both diameter 1mm. A shear rate range of 50-1000s^{-1} was used. Tests were undertaken at 390, 395 and 400°C. Below 390°C the material would not melt sufficiently to be forced through the die, and 400°C was the physical limit of the equipment. The relationship between viscosity and temperature is described by the Arrhenius equation and this was used to find the rest of the values required:

$$\mu = \mu_0 e^{E_a/RT} \tag{3.3}$$

Where μ is viscosity, μ_0 is viscosity at a reference temperature, E_a is activation energy, R is the Universal Gas Constant and T is temperature.

Equation 3.3 can be rearranged to give the following expression:

$$\ln(\mu) = \frac{E_a}{R}\left(\frac{1}{T}\right) + \ln(\mu_0) \tag{3.4}$$

In this form, the Arrhenius expression describes the equation of a straight line in the form $y = ax + b$ where $\ln(\mu)$ and 1/T are known values, calculated from experimental data, E_a/R is the slope of the line and $\ln(\mu_0)$ is the intercept. Therefore $\ln(\mu)$ was against 1/T, and the equation of the slope used to calculate the extrapolated viscosity values.

3.5 Characterisation of EOSINT P800 and the HT-LS Process

Results from the material and coalescence characterisation showed differences between the properties of material with different thermal histories which may be explained by understanding the temperatures which are occurring in the P800 during building. Tests were undertaken to measure the temperatures inside the P800 and these were compared with output from the P800 built-in sensors.

3.5.1 Temperature Measuring Devices

Two types of temperature measuring equipment were used, thermocouples and button data loggers:

3.5.1.1 Thermocouple Temperature Probes

The thermocouples used were K type, made of nickel aluminium and nickel chrome with a maximum temperature of 450°C. The major drawback of thermocouple wire is that the temperature measurement is taken using a thermometer which must be kept well away from the high temperatures that the probe itself can withstand. This meant that while thermocouples were useful for measuring the temperature inside the chamber when no building was taking place, they were unsuitable for use during building as they would interfere with the action of the recoater.

Furthermore, the probe needed to be taped in place to stop it moving around. As the thermocouples were only used in tests up to a maximum temperature of 140°C, polyamide tape which was suitable up to 180°C was used to keep the probe in position. Lastly, thermocouple readings had to be taken manually, which made them very labour intensive for long tests.

	Ref	Test 1	Test 2	Test 3	Test 4	Test 5
% of "normal" temp	100%	27%	31%	34%	37%	38%
Process (°C)	368	100.0	115.0	125.0	135.0	140.0
Build (°C)	347	94	108	118	127	132
Frame (°C)	345	94	108	118	127	131

Table 3.1: Temperature profiles tested in P800 compared with set temperatures for building

3.5.1.2 Button Data Loggers

In order to test the temperature inside the powder during heating, button data loggers were used. Five SL55T-A data loggers by Signatrol with a maximum temperature of 140°C were used. This was the highest temperature measurable by a self-contained temperature logging unit that could be sourced. The loggers were initially connected to a PC via a USB interface and set to record once every 30 seconds with ±0.5°C accuracy. Text could be assigned to each logger so that the location it was used at could be identified later. As loggers were self-contained and only 17mm in diameter, they could be embedded in powder before a test began and built over as they did not interfere with the recoating action.

3.5.2 Experimental Heating Profile

The "low" temperature of the button data loggers meant that measuring the temperatures at which the P800 operates was not possible. It was therefore decided to test five temperature profiles representing a percentage of the working temperatures of the machine and attempt to linearly extrapolate the profile upwards to estimate the actual temperatures during building. The set temperature of three sets of heaters could be user-defined; the Process Chamber, the Build Platform, and the Exchangeable Frame. The profiles tested and their relation to the working temperature of the P800 are given in Table 3.1.

3.5.3 Validating Measuring Devices

The button data loggers were calibrated by the manufacturer but as they had previously been unused it was decided to check they were accurate. A thermocouple probe was taped to each of five data loggers. They were suspended in the centre of an oven and the temperature set to 135°C. Thermocouple readings were taken in turn; for five minutes, a reading was taken every 30 seconds so that ten results could be compared with logger data. This was repeated for each of the five loggers/thermocouples. An hour later, the heating was switched off and the same process repeated for each thermocouple during cooldown. This meant two sets of data were collected for each logger and the dynamic response to change in heat could be checked. The results showed that the thermocouples register changes in temperature more quickly than the loggers but generally they were in good agreement.

3.5.4 Stability of EOSINT P800 at "low" temperature

The P800 is designed to have a working temperature in excess of 345°C. The button data loggers were only usable up to 140°C. It was necessary therefore to first test whether the P800 build chamber was capable of maintaining lower temperatures than its intended purpose.

This test was undertaken in an empty build chamber. Five thermocouples were used; one in the centre of the build platform, and one taped in the centre of each side approximately 100mm below the zero position, approximately in the centre of the upper heating band. The build platform was dropped to 200mm below the zero position. Data loggers were placed in the four corners of the build platform, approximately 20mm away from the corner heaters, and one was placed in the centre; this is the same configuration which was used later in the simulated build tests. The locations of the thermocouples and loggers are shown in Figure 3.5.

The lowest temperature profile was set first (see Test 5 in Table 3.1). Once the set temperatures had been reached they were held for thirty minutes before

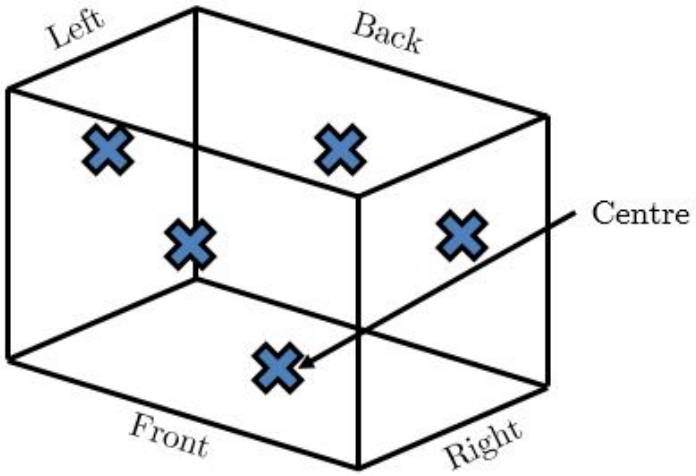

(a) Location of thermocouples during chamber low temperature validation test

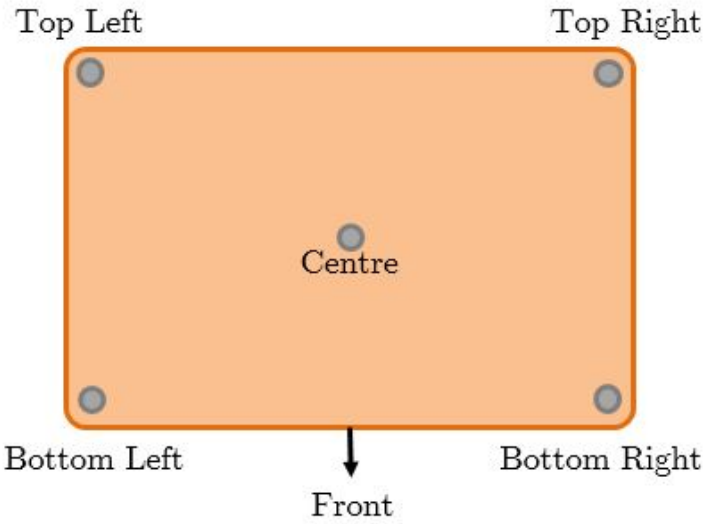

(b) Location of button data loggers during low temperature validation test and experimental builds with powder

Figure 3.5: Placement of thermocouples and loggers

changing the profile to the next. As only two thermometers were available only one thermocouple reading could be taken each minute. This meant that readings for each thermocouple were taken every five minutes. The temperatures output by the P800 software were recorded manually each minute from the PC display for comparison with data from the the thermocouples and data loggers.

Based on the results from this test, it was decided that the P800 was stable at each of the proposed heating profiles, and simulated builds involving powder could

proceed.

3.5.5 Heating During Build

With the build chamber heating profile and the loggers validated, tests were undertaken to examine heating during a simulated build. These tests were undertaken with used or overflow powder; as no actual parts were being built it was not necessary to use virgin.

The build platform was dropped to 20mm below zero position and the chamber filled with powder. The data loggers were pressed into the powder in the four corners and one in the centre, as shown in Figure 3.5b. The build platform was dropped a couple of mm and powder was spread over the loggers using the recoater. The temperatures for the process chamber, exchangeable frame and build platform were set according to the profiles given in Table 3.1, and the machine left for two hours to warm up.

The test consisted of building 90mm of layers with no exposure set so that no sintering took place. As the loggers were embedded in the powder, they moved down layer by layer with the build platform, recording the change in temperature as the z-height increased. The machine was left to cool overnight following each build and the loggers removed once the temperature was below 50°C. Each set temperature profile was run at least twice, and more if there were events such as build interruptions which could make comparison of the data challenging.

Data was exported from the loggers to OriginPro software for analysis. The temperatures from the P800 sensors were logged by the EOS PSW software used to control the system. The log files for each test were sent to EOS, who provided the temperature data for comparison with experimental data.

Chapter 4

Material Characterisation

4.1 Introduction

In the literature review the key characteristics of materials which are suitable for use in laser sintering were discussed, such as particle shape and size, particle size distribution, melting temperature and crystallinity. Determination of these properties form the backbone of almost all studies into new LS materials [2, 74, 75, 81, 101, 119]. As HP3 PEK is among the first commercially available PAEKs for LS, it makes sense to begin an investigation into its use in high temperature laser sintering with determination of its material characteristics. Furthermore, as used powder is not recommended for reuse in the P800, it is desirable to understand how the properties of used powder differ form virgin in order to understand what makes it unsuitable.

Therefore, the purpose of this chapter is to investigate the fundamental material properties of HP3 PEK powder, particularly those which are relevant to its processability as a material for laser sintering. Observations are combined with material analysis to provide an overview of virgin, overflow and used powder, their differences and similarities. An overview of the work in this chapter in context is give in Figure 4.1.

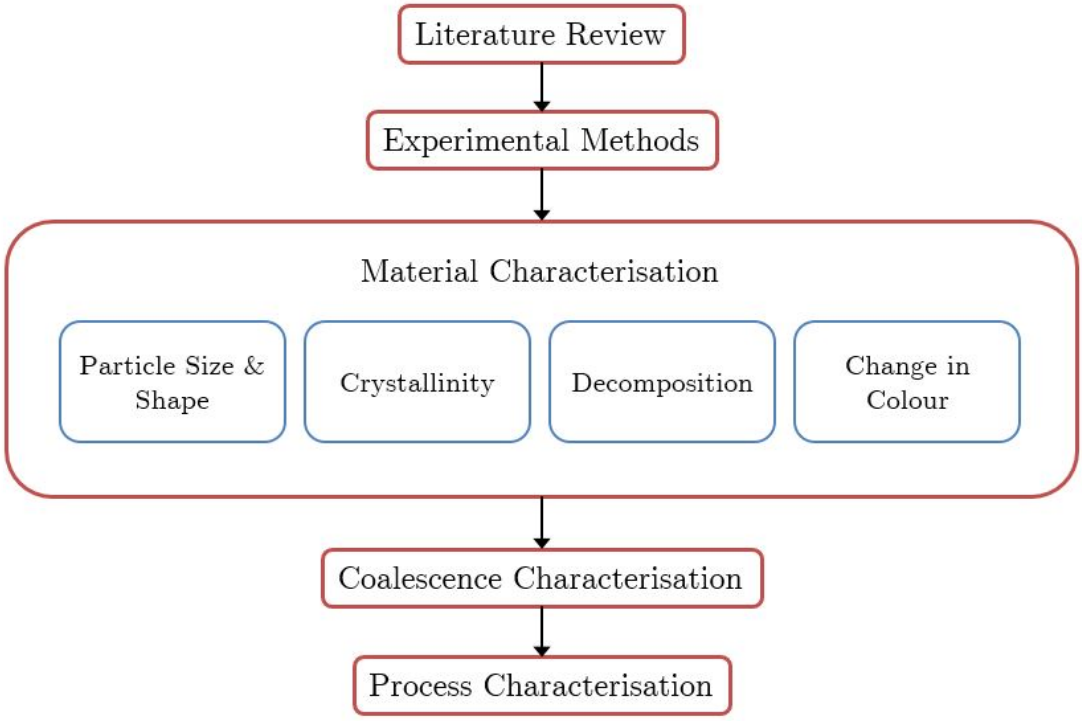

Figure 4.1: Overview of material characterisation chapter in context

4.2 Particle Size & Shape

Particle size and shape was examined by looking at very high magnification images taken using Scanning Electron Microscopy (SEM) and Particle Size Distribution analysis (PSD).

4.2.1 Scanning Electron Microscopy

Scanning Electron Microscopy (SEM) was undertaken to look at the shape of particles and to gain an insight into their structure. Whilst the shape of the particles affects how well they will pack together, the structure can affect the flow as surface irregularities such as flakes can cause the particles to mechanically lock together rather than flowing freely [126].

4.2.1.1 Virgin

SEM images for virgin powder are shown in Figure 4.2. At 500x magnification (4.2a), virgin powder particles are a mixture of round, oval and irregular shape particles of varying sizes, most of which which look smooth and solid. As the magnification is increased, it is apparent that some of the particles are cracked there are some very small particles attached to larger ones. At magnification 6500x and higher (Figures 4.2c-f), the surface of the particles is smooth in some regions but in other regions consists of bundles of short fibres or long, connected fibrous strands. The cracks in the particles are uneven around the edges. These images are in agreement with the results found for virgin HP3 PEK by Wang et al [123], who also noted short bundles of fibres. Using transmission electron microscopy they identified that the bundles of fibres are orientated in a preferred direction and are made up of arrays of connected granular blocks.

It is recommended that for good flowability and efficient packing resulting in effective sintering, particles should be close to spherical [2, 76]. Irregular shaped particles generally do not result in good packing [105]. Similarly, particles should be smooth and whole as surface irregularities can result in the particles attaching together during spreading which will reduce flowability; this has been clearly seen for other PAEK materials [126]. HP3 PEK powder shows a large proportion of oval and irregular shape particles which should theoretically result in diminished flow.

However, research has shown that 100% dense parts can be built in HP3 PEK [122] and that flow properties are close to or better than refreshed LS PA12 powder [126, 127]. Therefore in the case of HP3 PEK, the shape of the particles and the morphology at the surface do not adversely affect flowability. It is worth noting that a fibrous morphology is advantageous in a sintering material as it increases the contact surface area between particles allowing for faster merging to occur when heated, and has been shown to result in excellent sintering behaviour in other materials [145, 146]. In this respect, virgin HP3 PEK is well suited to laser sintering.

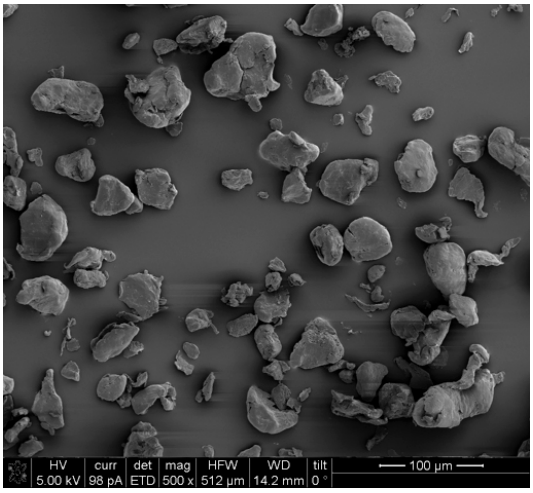

(a) Scale: 100 µm

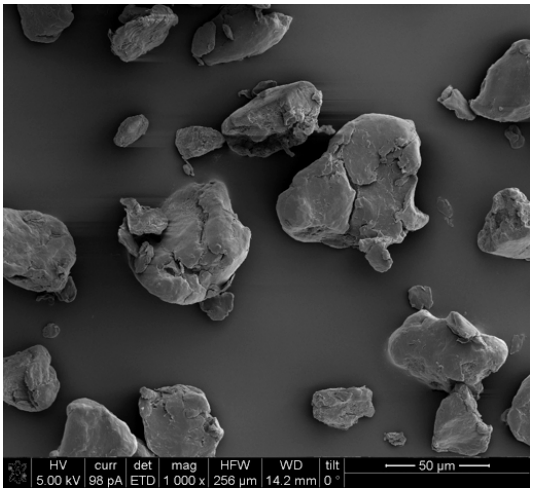

(b) Scale: 50 µm

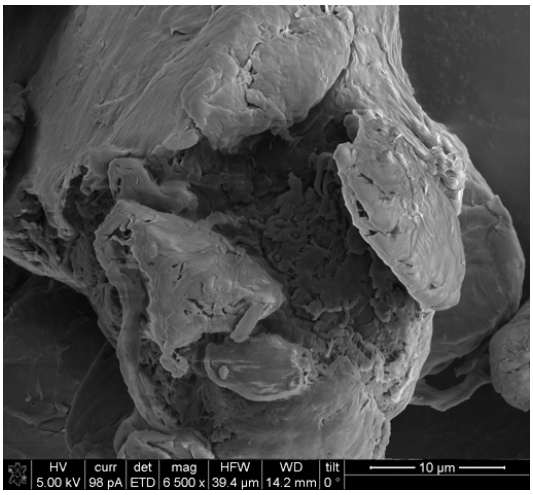

(c) Scale: 10 µm

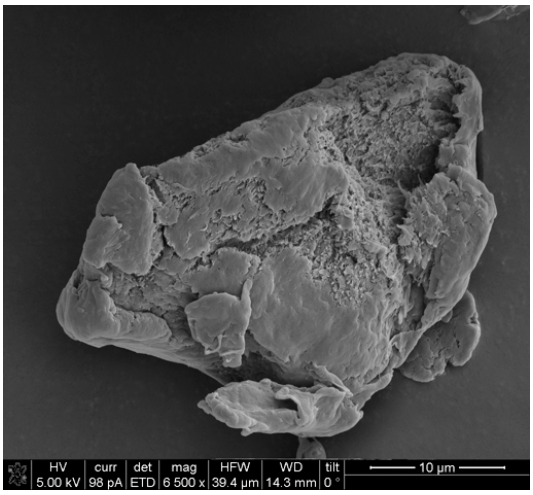

(d) Scale: 10 µm

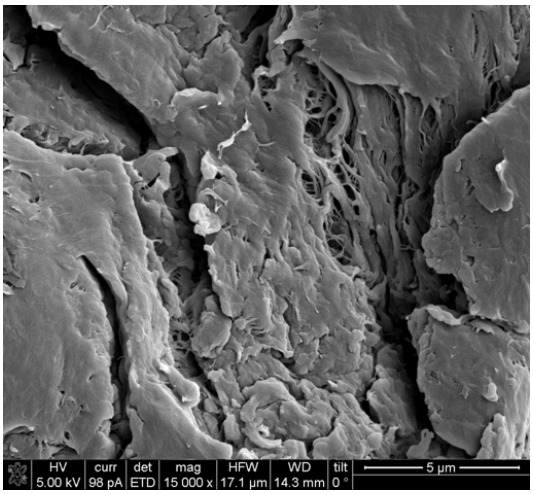

(e) Scale: 5 µm

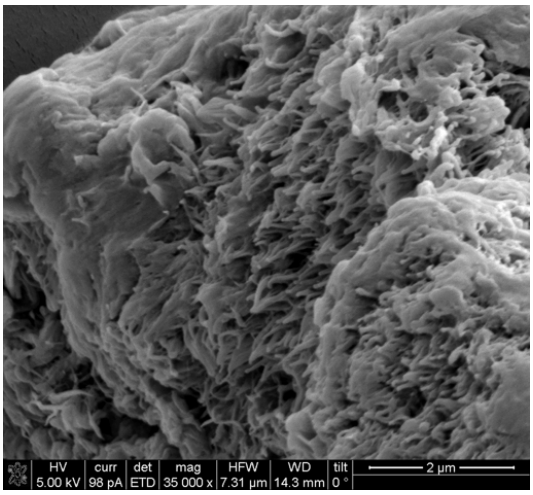

(f) Scale: 2 µm

Figure 4.2: SEM images of virgin PEK powder at increasing magnifications

4.2.1.2 Overflow

Images of overflow powder are shown in Figure 4.3.

At low magnification (Figures 4.3a-b), overflow particles do not look dissimilar to virgin particles; a combination of oval and irregular shaped particles of varying sizes. There appear to be fewer cracked particles, although there are more irregular and elongated particles. At higher magnifications (Figures 4.3c-d) the structure of overflow particles appear slightly different to virgin; the cracks in the surface have rounder edges. The fibrillar structure in Figures 4.3d and 4.3f have rounded ends and appear agglomerated. The short bundles present in Figure 4.3e are very similar to virgin at a similar magnification; however there is a region where the bundles are either substantially smaller or have shrunk; they are very short compared to other regions, with rounded ends. The temperature in the overflow chambers is not measured or controlled [personal communication, Nov 2017] so it not possible to say what temperature the powder is exposed to; however given the proximity of the overflow chambers to the build chamber it is not unreasonable to assume that some heat is radiated into the overflow powder. If this heat raises the temperature of the powder above its glass transition temperature then it would allow for restructuring of the polymer chains and may account for the change in shape observed in the overflow powder.

4.2.1.3 Used

SEM images were taken of four grades of used powder; powder taken from corner, mid and centre locations and sieved mixed. These are shown in Figures 4.4-4.7. It was of particular interest whether the location the powder was taken from had an effect on the shape and structure of the particles.

At low magnification, the images for all four grades are very similar to each other. The variety of shapes of the particles is as seen for virgin and overflow powder. Some agglomeration of particles has occurred, with some of the images showing small clusters of particles or small particle attached to larger ones; Figure 4.7b shows one large cluster in the sieved mixed powder. Particles from the corner

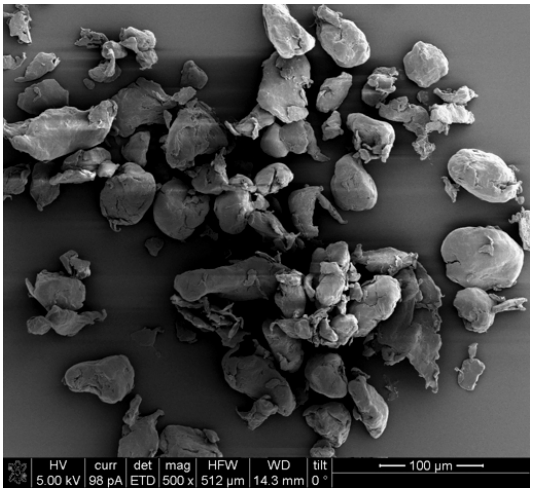

(a) Scale: 100 µm

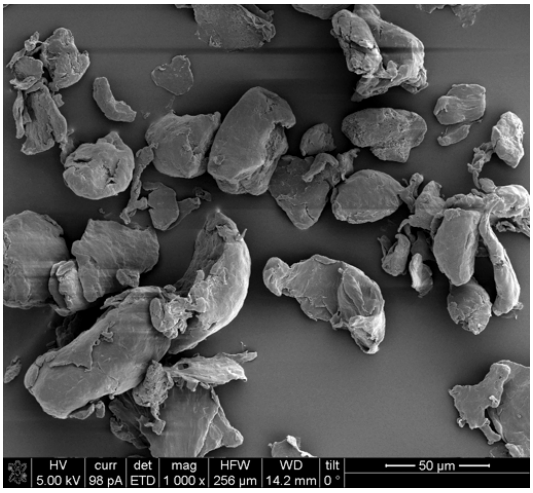

(b) Scale: 50 µm

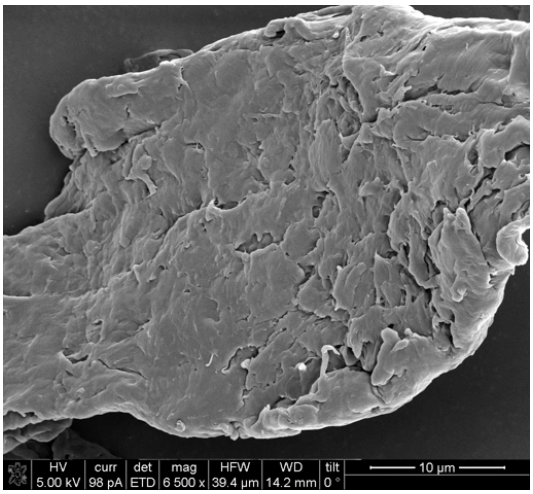

(c) Scale: 10 µm

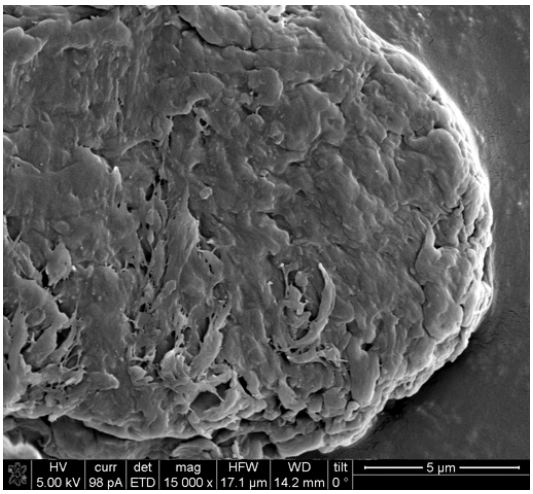

(d) Scale: 5 µm

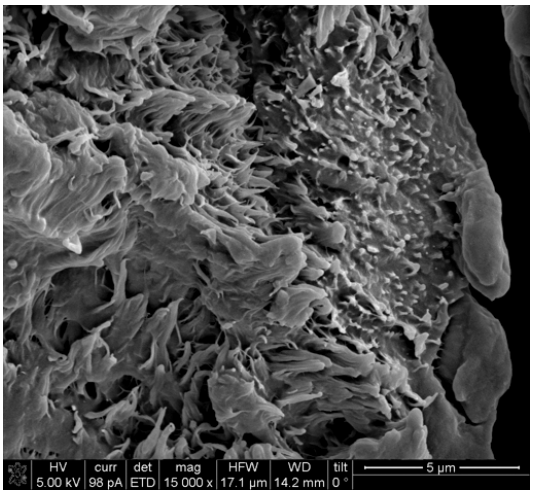

(e) Scale: 5 µm

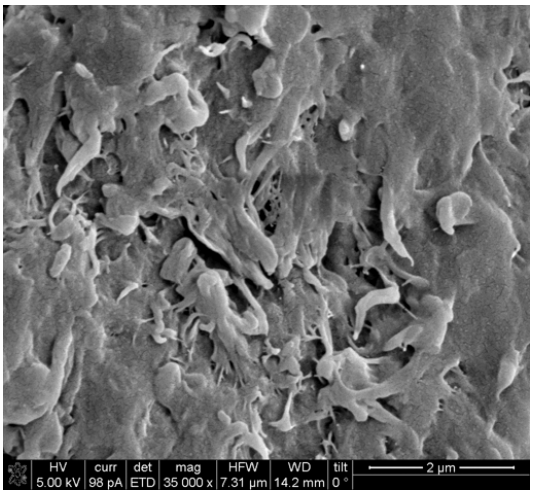

(f) Scale: 2 µm

Figure 4.3: SEM images of overflow PEK powder at increasing magnifications

and mid locations are very smooth compared to the other used grades and also the virgin and overflow powder.

At higher magnification however, the difference between the three locations becomes more apparent. The corner powder (Figure 4.4) shows a similar structure to overflow powder at 15000x magnification (Figure 4.4d), with bundles of short fibres present; in some regions these are much shorter than others. This is more clearly noticeable at 35000x magnification (Figure 4.4f), where some fibres are very short while others have almost disappeared completely. In the mid powder (Figure 4.5) there are no long fibres; all that remains are regions of unevenness covered in small round nodular structures. In the powder from the centre of the build (Figure 4.6) these have disappeared completely and the surface of the particle is almost entirely smooth.

The centre used image at 6500x magnification shown in Figure 4.6c appears to show a particle made up of smaller agglomerations of particles. This structure was observed by Wang et al [123] in virgin HP3 PEK powder, however was not seen in any of the virgin particles examined for the current study. Compared with the image taken by Wang et al the centre used particle is significantly rounder; this is in keeping with what has been observed from the other used powder particles.

The results of the location specific images show a trend; the closer to the centre of the build chamber the material is taken from, the smoother the internal structure of particles. Fibrous morphology is shown to recede until it disappears completely from the corner to the centre. The smallest reduction in the size of the fibrous bundles compared with virgin powder is seen in the corner powder, however that this occurs shows that all used powder is in some way affected by being held at temperature for the duration of the build. At the highest magnification the texture of the surface of the particles is visible; the structure of centre particles in Figure 4.6e appears almost lamellar, showing long oriented spherulites, while in the mid and corner images in Figures 4.5f and 4.4f this is less clear, potentially because of the fibrous structure. Wang et al [123] show a similar structure in the fracture surface of laser sintered PAEK samples, however without higher magnification

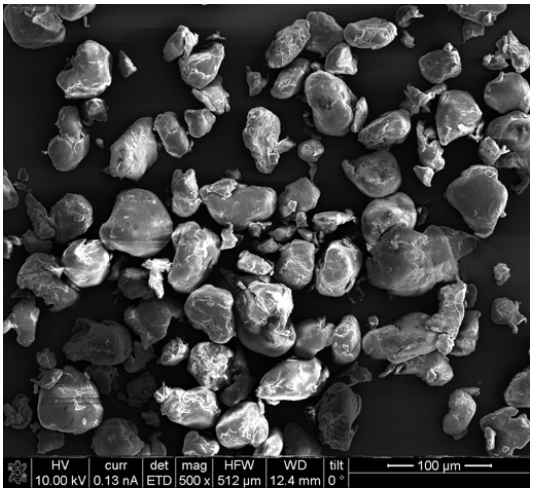

(a) Scale: 100 µm

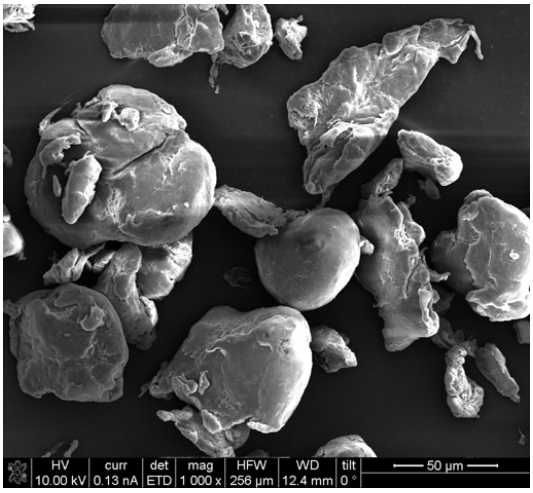

(b) Scale: 50 µm

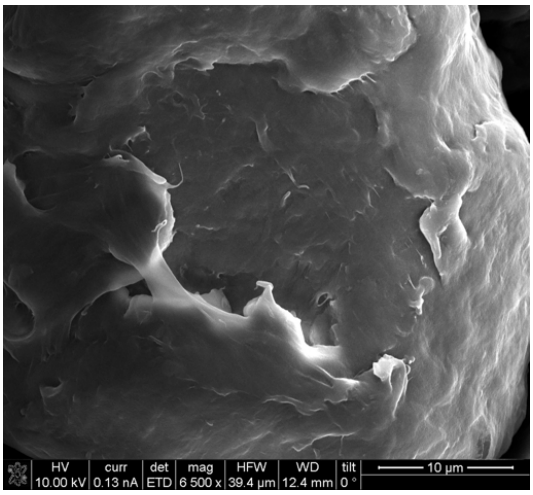

(c) Scale: 10 µm

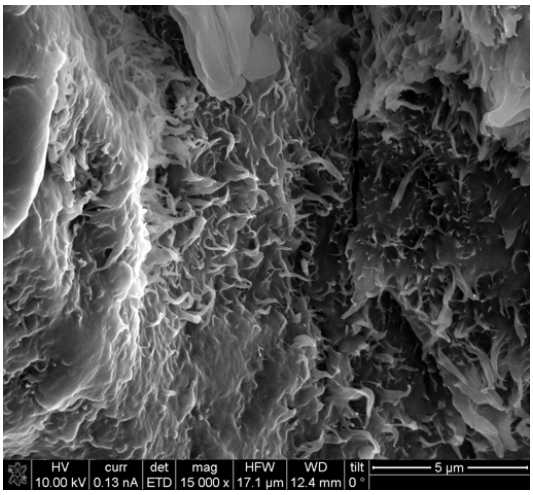

(d) Scale: 5 µm

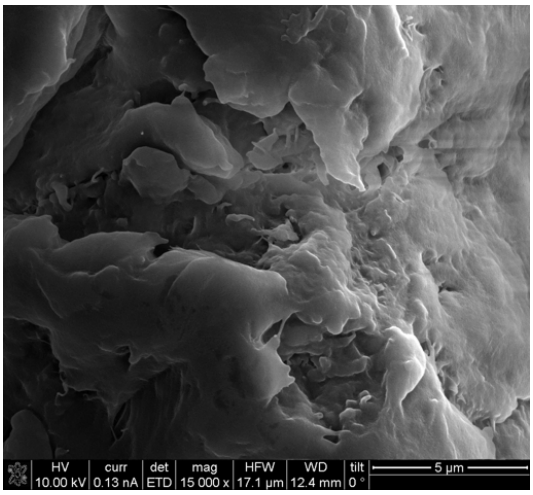

(e) Scale: 5 µm

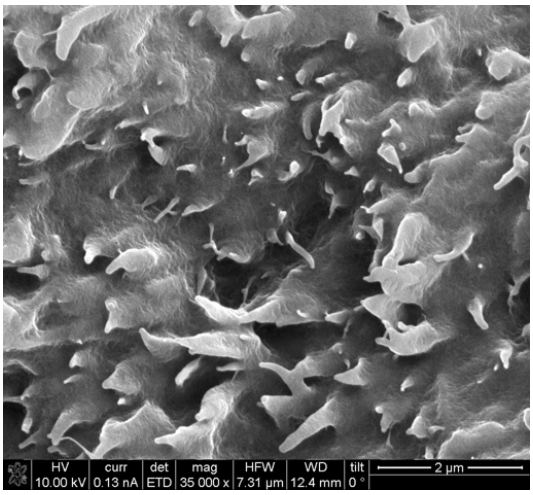

(f) Scale: 2 µm

Figure 4.4: SEM images of corner used PEK powder at increasing magnifications

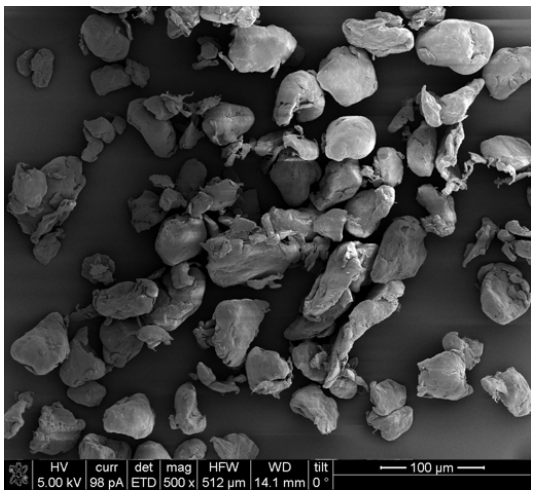

(a) Scale: 100 µm

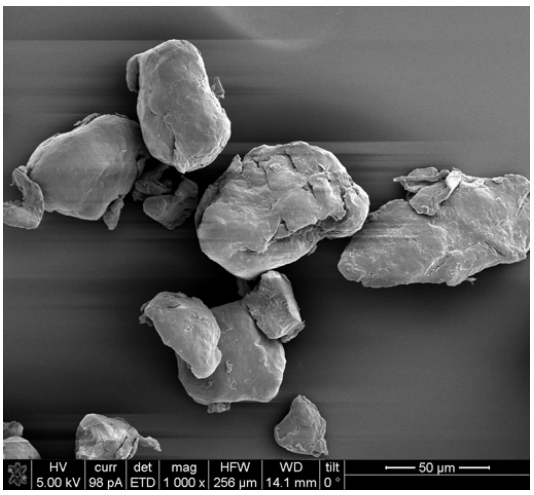

(b) Scale: 50 µm

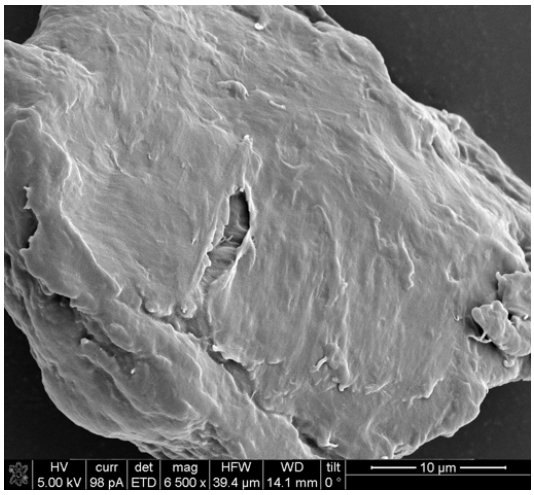

(c) Scale: 10 µm

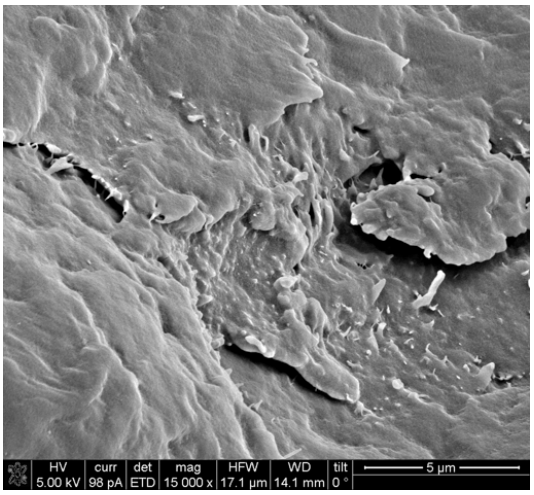

(d) Scale: 5 µm

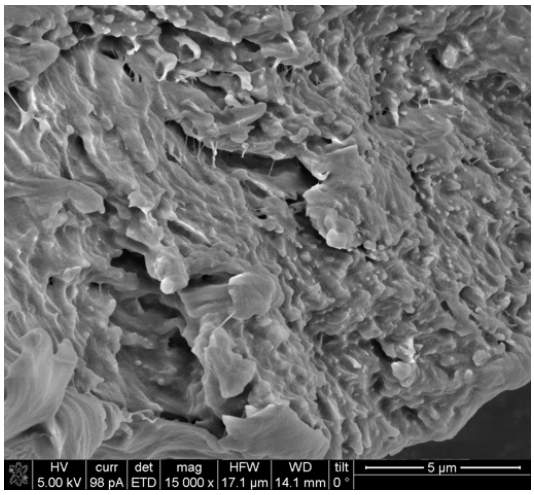

(e) Scale: 5 µm

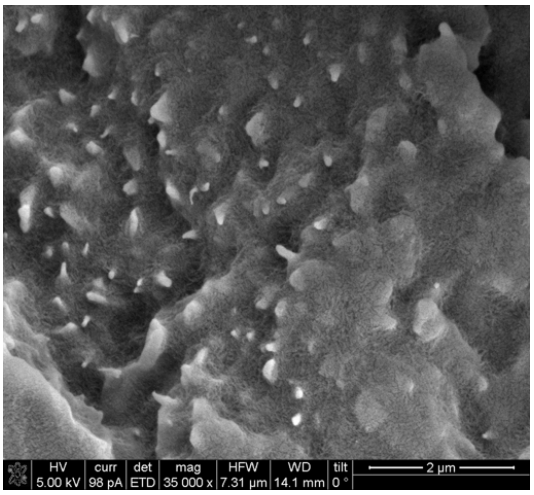

(f) Scale: 2 µm

Figure 4.5: SEM images of mid used PEK powder at increasing magnifications

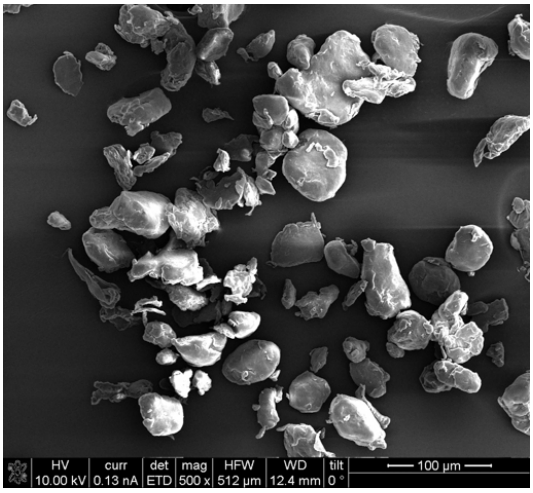

(a) Scale: 100 µm

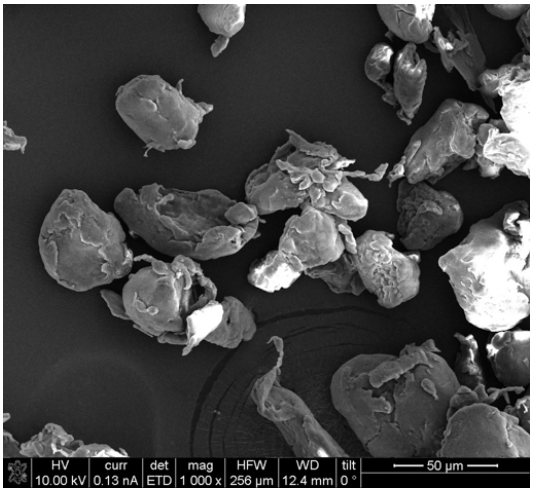

(b) Scale: 50 µm

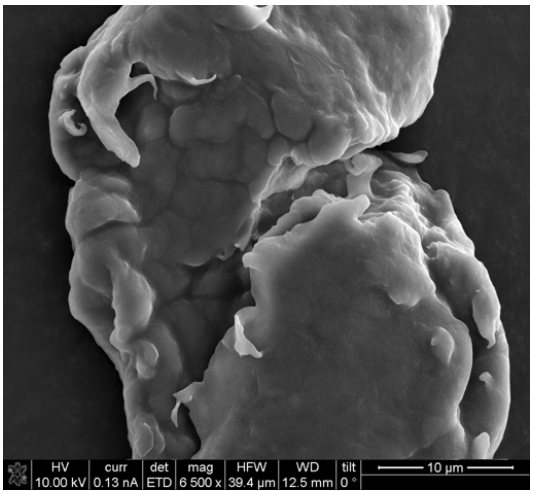

(c) Scale: 10 µm

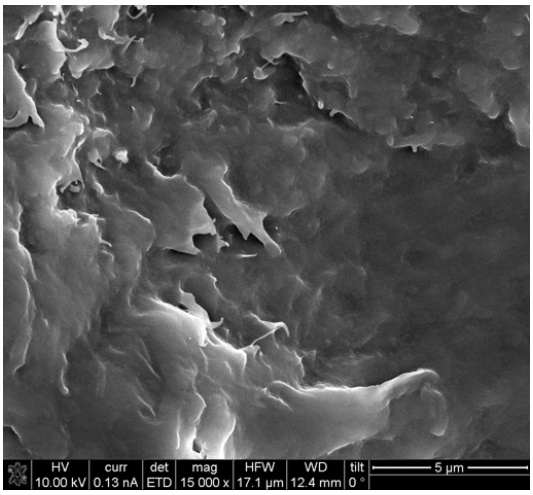

(d) Scale: 5 µm

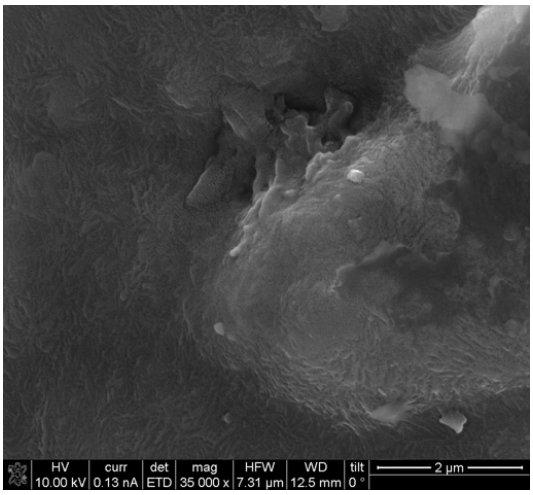

(e) Scale: 2 µm

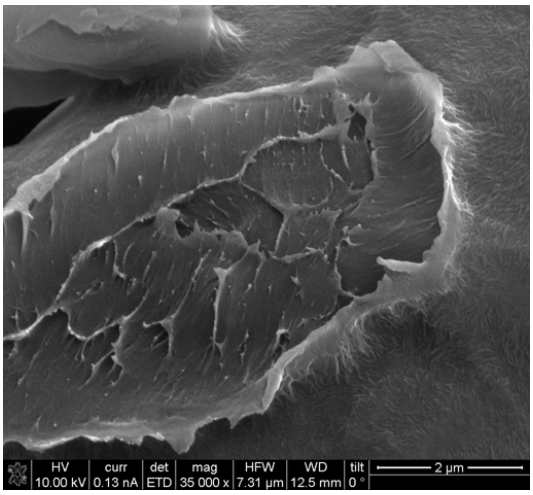

(f) Scale: 2 µm

Figure 4.6: SEM images of centre used PEK powder at increasing magnifications

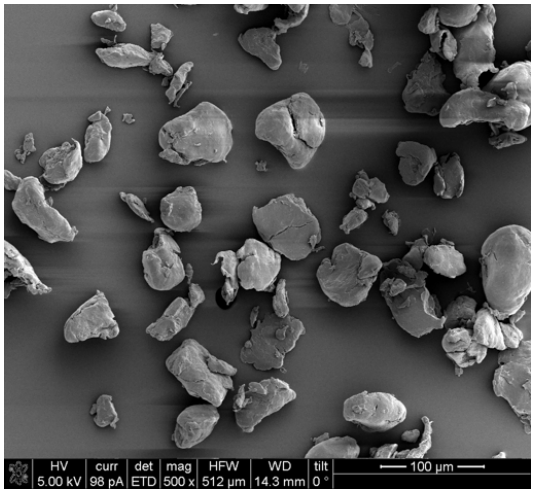

(a) Scale: 100 µm

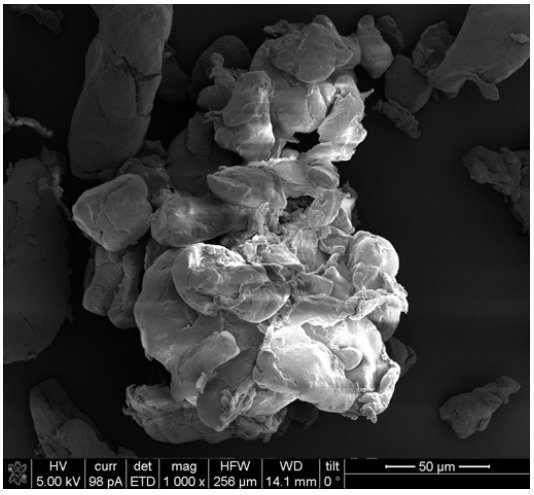

(b) Scale: 50 µm

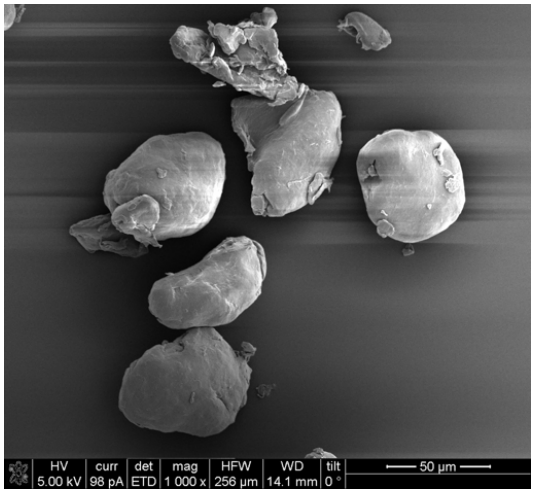

(c) Scale: 50 µm

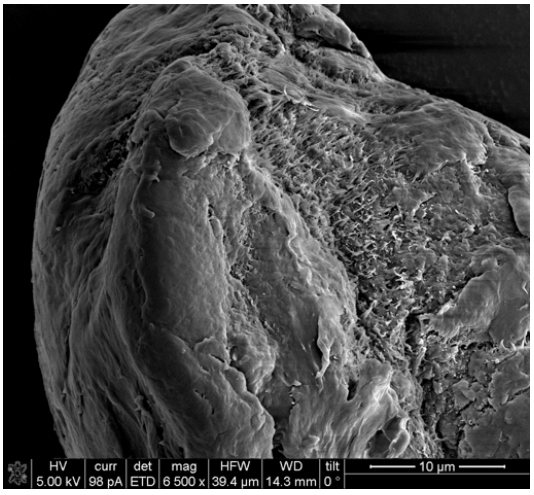

(d) Scale: 10 µm

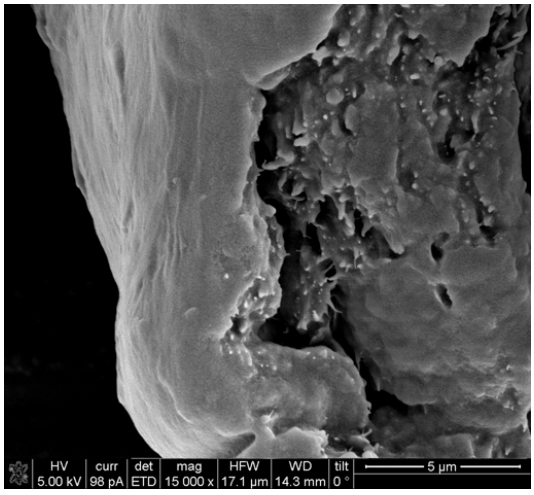

(e) Scale: 5 µm

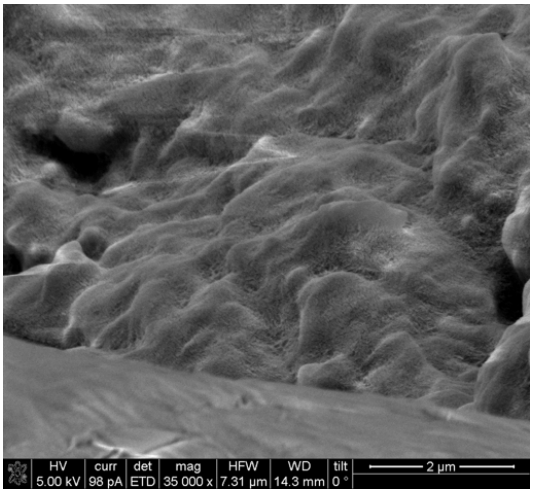

(f) Scale: 2 µm

Figure 4.7: SEM images of sieved mixed used PEK powder at increasing magnifications

images it cannot be confirmed whether the morphology seen on the powder is comparable.

The images of sieved mixed used powder are given in Figure 4.7 and show a combination of the structures seen from the three locations; all the images show different particles. This is to be expected given that the mixed powder is made up of powder from across the whole build. As the powder is sieved very large agglomerations of particles would have been removed, however any smaller than that 250 µm sieve mesh size would still pass through.

4.2.2 Particle Size Distribution

Particle Size Distribution (PSD) analysis was undertaken on virgin, overflow and sieved mixed used powder. The reason for not undertaking analysis on all grades of used powder is that unsieved powder would not be used in the actual build process, plus it was decided that the PSD at individual locations was less important than the overall PSD once the various grades have been mixed.

Figure 4.8 shows the average PSD for the three powder grades tested, and a simplified breakdown is given in Table 4.1. The results show that the PSD of overflow powder is quite similar to the PSD for sieved mixed used powder. As the overflow powder is stored separately away from the build chamber during the process, it was expected that the properties would be very similar to virgin powder. The SEM results show only small changes between the virgin and overflow particles so the significant difference in PSD is unexpected.

The simplified breakdown of PSD in Table 4.1 shows that the largest percentage of particles for all three thermal histories is between 37.5 and 63 µm, however this is over 5% higher for virgin than for overflow and used powder. Virgin has 10% more particles below 37.5 µm than the other two grades, while overflow and used powder have over 15% more particles above 63 µm than virgin.

SEM of sieved mixed used powder shows an agglomeration of small particles stuck together, however if these are agglomerations are below 250 µm then they will pass through the sieve. Agglomerations may register as one particle on the PSD

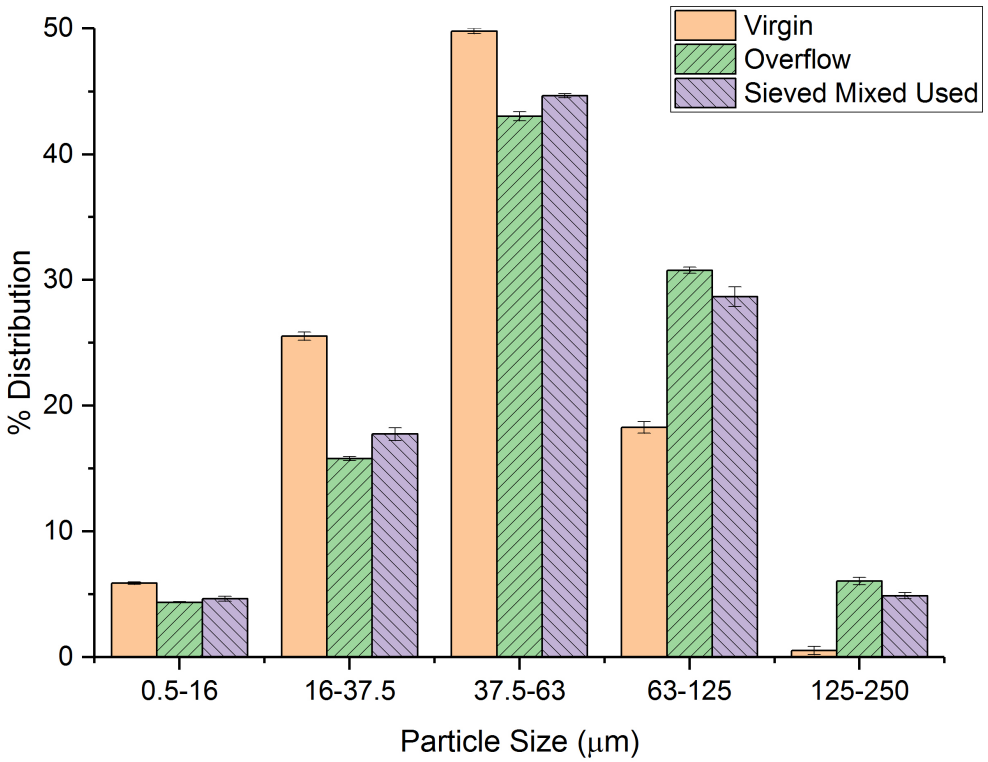

Figure 4.8: Particle size distribution of virgin, overflow and sieved mixed used HP3 PEK powder

	% Distribution		
Thermal History	Below 37.5 µm	37.5-63 µm	Above 63 µm
Virgin	31.4	49.8	18.8
Overflow	20.2	43.0	36.8
Sieved Mixed Used	21.8	44.6	33.6

Table 4.1: Simplified particle size distribution

equipment, giving the higher reading. SEM of overflow powder showed a number of irregular and elongated particles which may account for the higher percentage registered for this grade.

Particle size and shape are important because they strongly affect the packing and spreading of the powder, as well as the accuracy and mechanical properties of finished parts [74]. For polyamide, Goodridge et al [2] suggested that particles smaller than 45 µm can make powder spreading more difficult as static charge causes the small particles to stick together and to the recoater. However, they also suggest that a range of particle sizes can improve packing as the smaller particles fill in the gaps between the larger particles, without adversely affecting the flow of the powder. Therefore it would be interesting to investigate further how the difference in PSD between virgin and overflow and used powder affects flow and packing.

Pham et al [6] looked at virgin and used nylon powder using SEM and concluded that the size of the particles did not change during building, however they did not measure the PSD. The results here show that even though the particles may look the same, it is important to employ more than one characterisation method before drawing conclusions.

4.3 Crystallinity

Crystallinity is an important aspect of polymers as the crystal structure and degree of crystallinity are responsible for the mechanical properties of the material [21]; this is of particular interest for PAEKs as they were developed for demanding high performance applications.

Crystallinity was measured using differential scanning calorimetry (DSC) and x-ray diffraction (XRD) methods. Whilst both are capable of calculating percentage crystallinity, DSC can be used to identify the melting and recrystallisation temperatures of the material, while XRD traces can be used to identify whether the unit cell dimensions of the material change as a result of thermal history.

Percentage crystallinity was calculated using both the equipment proprietary

software and data analysis and graphing software OriginPro, thus producing two values for crystallinity for each of the techniques. The reason for this was that OriginPro allowed for greater control over the placement of baselines than the proprietary software, but introduced an element of subjectivity as the placement of the baseline is defined by the user; it was felt that it was not clear which of the software outputs presented the most accurate method of calculating crystallinity. Therefore the differences in output from the two pieces of software were also examined.

4.3.1 Differential Scanning Calorimetry

Differential scanning calorimetry is a thermal characterisation technique which allows thermal events such as melting and recrystallisation to be identified. The temperature at which these events occur can shed light on thermal history and degree and quality of crystallinity.

Crystallinity was calculated from the endotherms and exotherms of all results by integrating the area of the enthalpy underneath the baseline as explained in Section 3.3.2.1 on page 86. Crystallinity of each endotherm/exotherm were calculated for all tests results and then averaged.

4.3.1.1 Virgin

Seven DSC repeats were undertaken for virgin powder, and a representative trace is shown in 4.9. Baselines for the melting and recrystallisation peaks have been added for clarity. The melting endotherm is broad and has two peaks; one at 323°C and the second at 372°C. Two peaks are not uncommon for PAEKs and there has been much discussion about whether they are the result of thermal history or two different crystal structures [17, 27, 40, 42–44]. It is not possible to identify which from the DSC trace. However, it is thought that the thermal history is most likely the reason for the twin peaks; a patent filed by EOS for producing PAEK powder for LS details a tempering treatment to improve flow, which would explain a second endotherm with lower melting point [91]. XRD analysis will confirm whether or

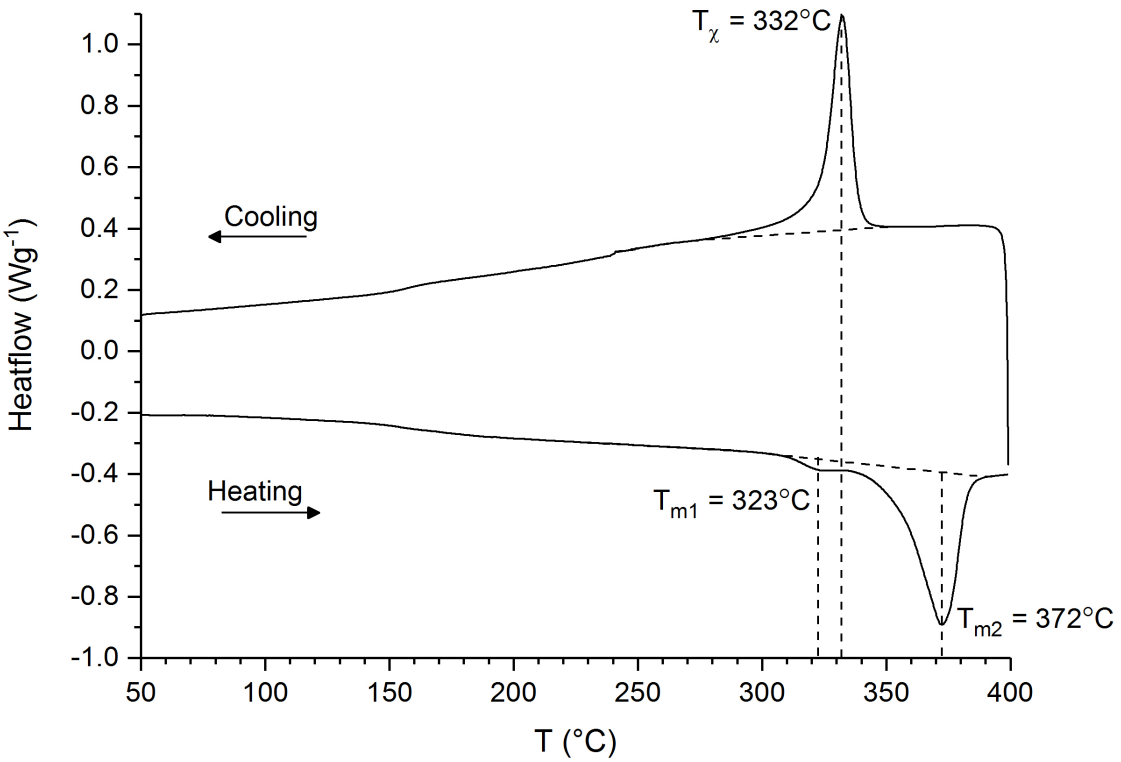

Figure 4.9: DSC curve for virgin HP3 PEK

not a secondary crystal structure is present as a different structure would affect the unit cells present in the trace.

The peak melting temperature is 372°C, which is consistent with results in the literature for PEK [177]. Of note is that the melting endotherm begins around 348°C; the standard hold temperature during LS is 368°C, which means that even powder which is not being sintered is melting during the building process. Melting in this range would be incomplete, which is why the material remains in powder form following building. However, this temperature would allow for reorganisation of crystal chains and potentially some fusing together of particles, which could account for the agglomerations of particles and the higher fraction of larger particles in overflow and used powder seen in Section 4.2.2. If the powder is annealed to improve flowability the elimination of the original thermal history during the building process is likely to affect the flowability (and therefore the effectiveness) of the material during re-use.

There is an overlap between the melting and recrystallisation peaks, that is,

melting and recrystallisation can occur concurrently between 305 and 348°C. This is at odds with several studies which explain that a clear gap between the melting and recrystallisation regions is necessary in order to produce good quality parts in LS; an overlap can lead to distortion caused by uneven shrinkage in parts [72,178]. A clear gap (or processing window) means the material stays in a liquid state for longer during processing before crystallising which reduces residual stresses which cause part warping. Concurrent melting/recrystallisation can also lead to localised shrinkage due to differing crystal properties from one region of the melt to another [75,97].

Lastly, Kruth et al [94] advise against materials which show a double melting peak, as the processing window which can be controlled in LS is very small and cannot cover melting peaks more than 5-10°C apart.

Percentage crystallinity was calculated using both proprietary software Mettler STARe and OriginPro; from the melting endotherm, crystallinity is 42.4% according to the Mettler STARe software, and 40.7% according to OriginPro software. The recrystallisation exotherm gives values of 38.5% according to Mettler software, and 43.1% according to Origin software. With a standard deviation of ≈ 3% from all calculations, these figures can be considered to be in good agreement.

4.3.1.2 Overflow

Six DSC repeats were undertaken for overflow powder and a representative trace is shown in Figure 4.10. It is very similar to the trace for virgin powder. The melting endotherm has twin peaks, similar to virgin, however the first peak is much smaller; these are at 324 and 372°C. Measurement of the first peak using Mettler STARe software gives an average value of 2.4% crystallinity for the first peak for virgin powder, but a value of just 1.5% for overflow powder. While this is a small change, it would suggest that overflow powder experiences enough heat during building for rearrangement of the crystal structure to occur. The melting temperature is the same as virgin at 372°C but the recrystallisation temperature is lower at 329°C.

The melt crystallinity average from the six repeats was 39.5% in both

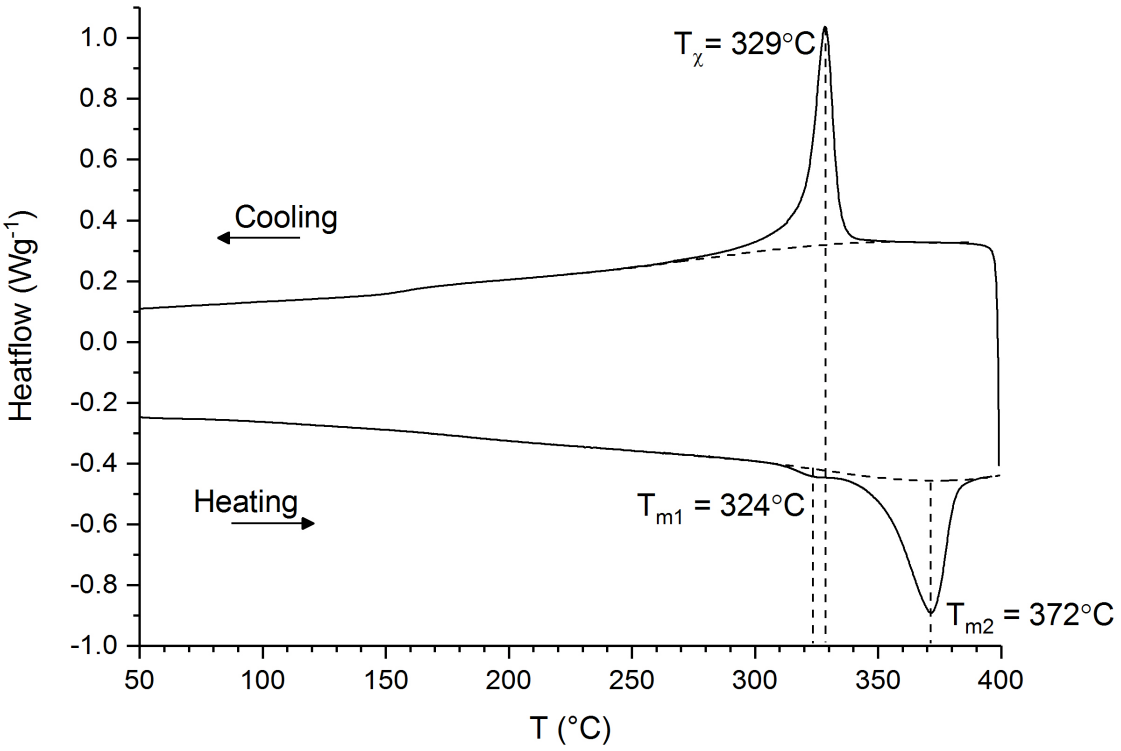

Figure 4.10: DSC curve for overflow HP3 PEK

Mettler and OriginPro software. This is slightly lower than the virgin powder. Recrystallisation crystallinity was measured by Mettler software to be 35.3% and by OriginPro to be 39.4%.

The different crystallinity values and temperatures combined with the results from the particle size distribution shows that some chemical change is clearly occurring in the overflow powder, even though it is not directly exposed to heat during building. However, as the temperature in the overflow chambers is not controlled or measured it is not clear exactly how much heated the powder is exposed to.

4.3.1.3 Used

DSC was undertaken on all grades of used powder, six repeats for each. Representative traces for the four grades are shown in Figure 4.11. The measured crystallinities for the melting and recrystallisation peaks are displayed in Figures 4.12 alongside the virgin results for comparison. The figures calculated by the Mettler and Origin software are in good agreement, particularly as the standard

	Melt (°C)			Recrystallisation (°C)		
	Onset	End	Width	Onset	End	Width
Virgin	303	394	91	356	248	108
Overflow	303	394	91	358	258	99
Corner	329	408	79	326	245	81
Mid	329	424	95	320	213	107
Centre	328	416	87	298	226	72
Sieved	299	413	114	323	233	91

Table 4.2: Comparison of onset and end temperatures for melt and recrystallisation of all powders

deviation is quite high on some grades, with results from sieved mixed powder in particular showing a highest crystallinity of 65% and a lowest of 55%. Overall, the results show that different heating regimes produce different characteristics.

The corner powder, Figure 4.11a has a melting temperature very similar to virgin powder, but only one melting peak and a much higher crystallinity. When melted and recrystallised, the crystallinity is similar to virgin; this suggests that the powder has essentially been annealed whilst in the build chamber but has retained its original properties. The very high crystallinity is not unusual; Bassett et al [38] were able to achieve 60% crystallinity in PEEK by holding at an elevated temperature for an extremely long time. Table 4.2 shows a breakdown of the onset and end temperatures for melt and recrystallisation, with virgin and overflow included for comparison. Corner, mid and used powder all shows a gap between between melting and recrystallisation, that is, a processing window; as virgin and overflow do not show this processing window, this theoretically means this powder could be more stable when used in LS than virgin [72].

Mid powder, Figure 4.11b also shows a high value of crystallinity but over a broader crystal size distribution than corner powder [179]. The melting temperature is 397°C, which is substantially higher than the T_m of virgin powder. The could be explained by the mid powder experiencing a higher temperature than the corner powder; Bassett et al [38] showed that T_m increases with annealing temperature and hold time and results by Cebe [51] agree. T_m also increases with crystal size; according to Gibbs and Thomson larger crystals are more stable

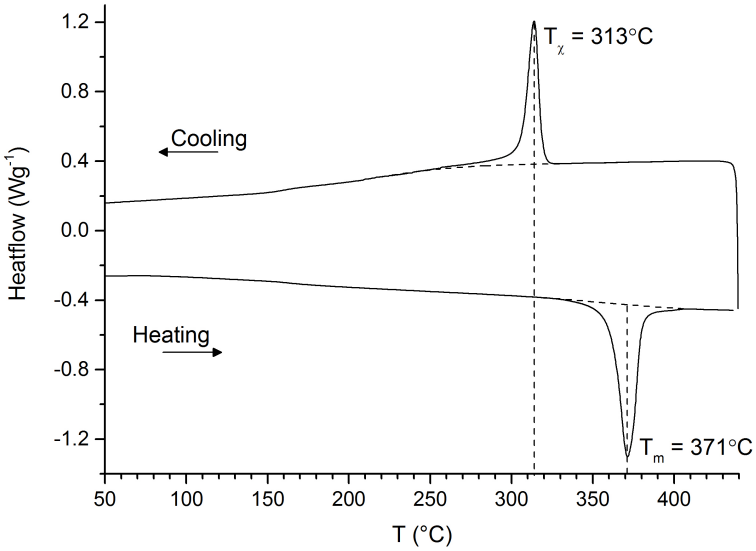

(a) Corner Used

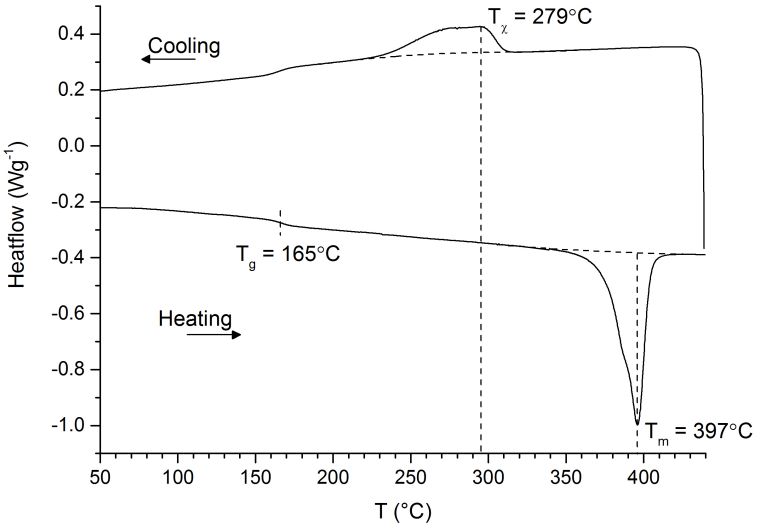

(b) Mid Used

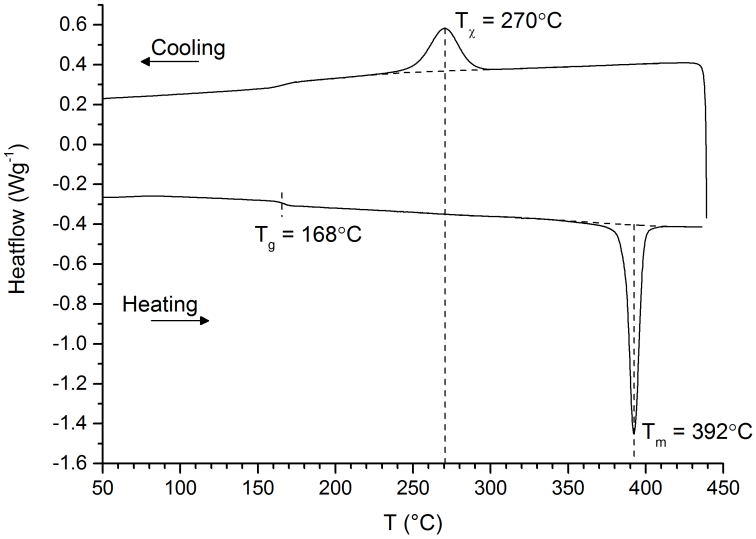

(c) Centre Used

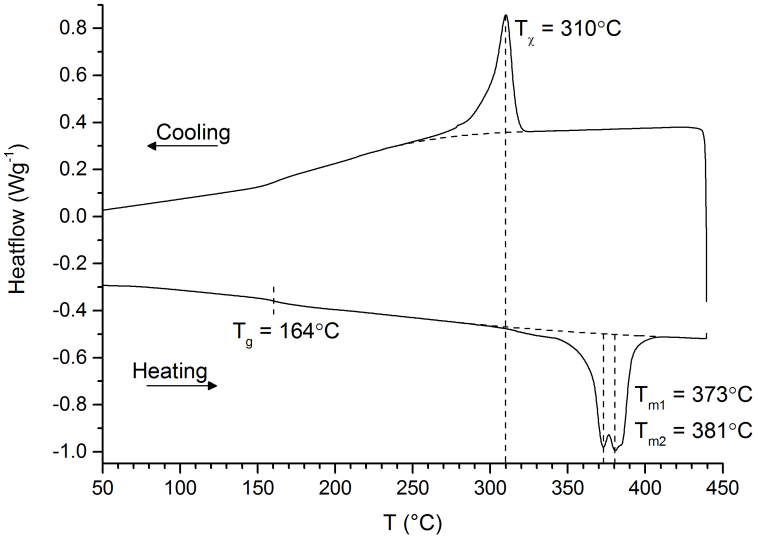

(d) Sieved Mixed Used

Figure 4.11: DSC Traces of unsieved used Powder from different locations vs sieved mixed used

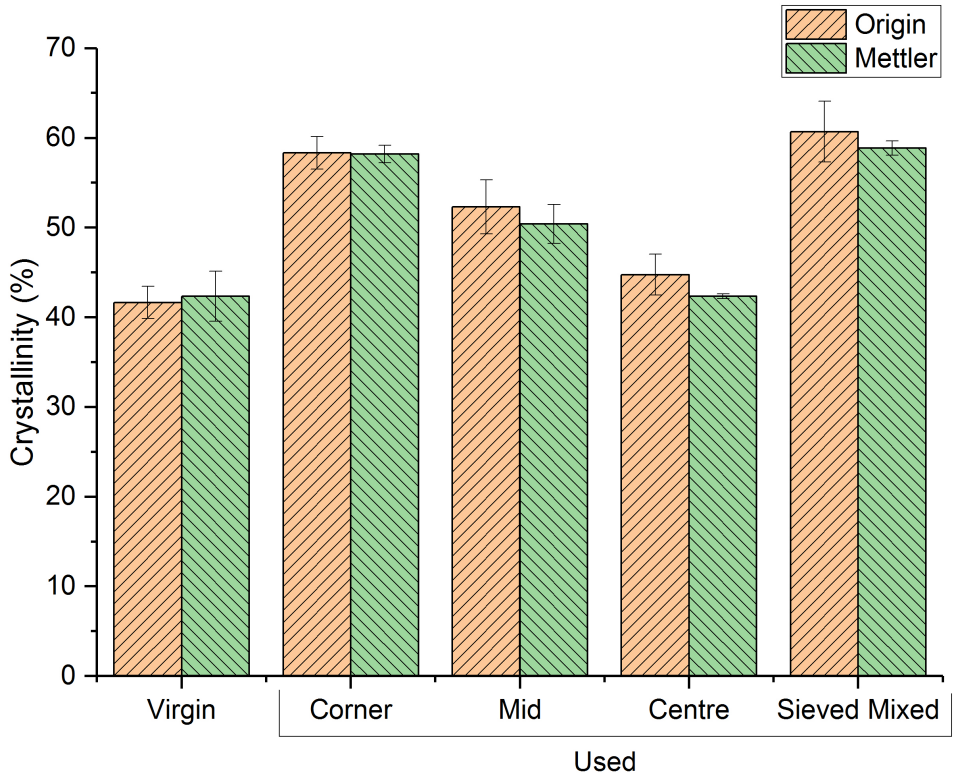

(a) Melting

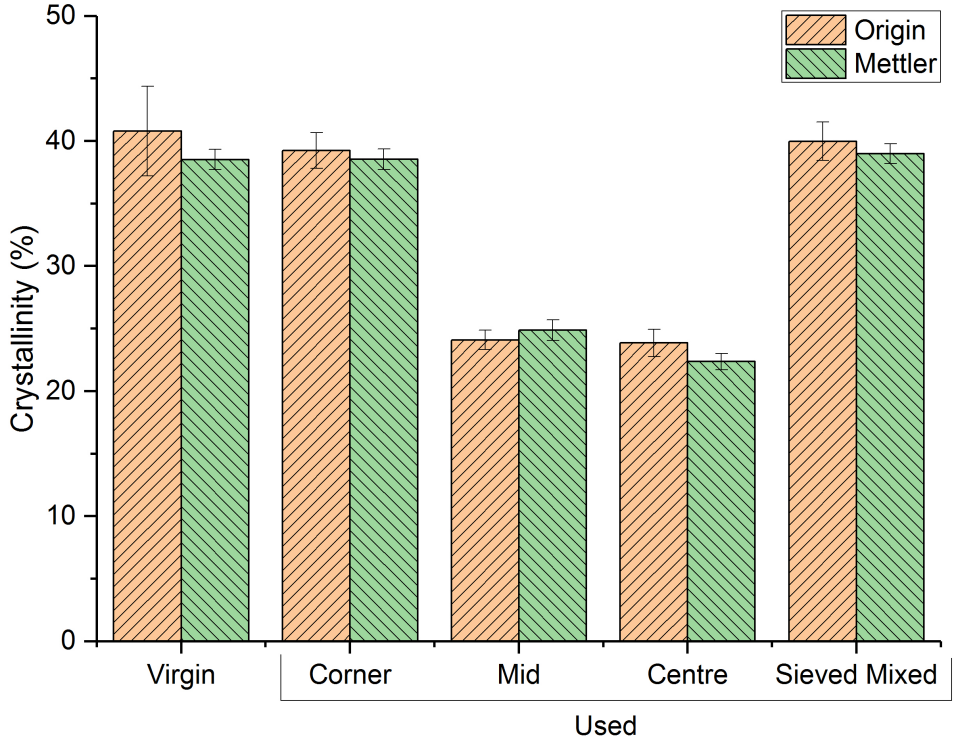

(b) Recrystallisation

Figure 4.12: Comparison of crystallinity from melt and recrystallisation for virgin and used powder using Mettler and OriginPro software

than smaller ones and require a higher temperature to break down the lattice structure [180]. However, the lower crystallinity compared with the lighter powder may be a sign that the powder has begun to degrade.

The biggest difference between the corner and mid traces is the recrystallisation exotherm. The peak recrystallisation temperature is much lower for the mid powder and rather than a sharp peak there is a small, broad peak instead. In some of the repeats more than one peak recrystallisation temperature was visible; overall the recrystallisation crystallinity is much lower, which is clear from Figure 4.12b. This supports the theory that degradation of the powder is occurring; Day et al [57] found that the amount of crystallizable material decreased as exposure time and temperature were increased. The multiple peaks indicate chain scission is occurring; as the long chains break down into chains of different lengths, crystals with different degrees of perfection will form during cooling. This results in a much broader temperature range over which recrystallisation will occur and smaller clusters of crystals with differing peak temperatures forming [12].

The trend of decreasing crystallinity during both heating and cooling continues with the centre powder. The melting peak in Figure 4.11c is extremely narrow which suggests that the majority of crystals are a similar structure and perfection. Whilst still higher than virgin, the melting crystallinity is lowest of all the locations tested. As the recrystallisation crystallinity is similar to the mid powder it is probable that the material is breaking down due to the higher temperature experienced by the very centre of the build chamber. The lower T_m than mid powder supports this theory; the conditions further from the centre enable high crystallinity and high quality crystals but at the very centre the temperature is too high to sustain them. Zhang and Zeng [59] found a similar result when annealing PEEK; initially the T_m increased with increased annealing time and temperature but beyond a certain point the T_m and measured crystallinity began to fall again.

The glass transition of the corner powder could only be measured from one trace, and was found to be 161°C. The glass transition for virgin and overflow powder was considered to be too faint on the trace to accurately identify, however literature

for PEK gives the glass transition of powder as manufactured to be 152°C [177]. Therefore from centre to mid to centre, the glass transition is increasing; T_g of centre powder is 16°C higher than virgin powder. Increasing T_g suggests that crosslinking is occurring [55, 181]; crosslinking would also explain the much lower value of recrystallisation crystallinity as a network of crosslinks inhibit crystallisation [182].

The increase in melt temperature, glass transition and reduction in crystallinity with location suggests two things; that the temperature is increasing from the corner to the centre, and that this increasing temperature is resulting in increasing degradation in the powder. Ghita et al [108] measured shrinkage of HP3 PEK tensile specimens and plotted them according to location in the build chamber; they found that shrinkage was highest at the centre and decreased towards the corners. They attributed this to thermal gradients present in the bed, with the highest thermal energy present in the centre. This would also explain the results seen here.

The mixed powder, Figure 4.11d displays a combination of the properties from the other three traces. The melting peak onset and end points cover the whole range measured for corner, mid and centre powder. There are two peaks with melting temperatures of 373°C - very similar to virgin powder and corner used - and 381°C - not as high as powder from the centre of the build but higher than powder from the corner. The overall melt crystallinity is 61%, which is the highest of all the grades of powder tested. The recrystallisation crystallinity is comparable to virgin and corner. All of these results are logical for a sample containing several different grades of used powder.

4.3.2 X-Ray Diffraction

X-Ray Diffraction (XRD) analysis was undertaken to compare crystallinity values with the DSC results and to identify whether thermal history affects crystal structure.

Percentage crystallinity is indicated by the area under each peak on an XRD trace once the amorphous fraction has been subtracted. Ideally, the

amorphous fraction would be identified experimentally by performing XRD on a fully amorphous sample, however it was not possible to obtain a fully amorphous sample of HP3 PEK. Therefore the amorphous fraction was estimated using software, in this case equipment proprietary software Bruker DIFFRAC.EVA and OriginPro. Crystallinity was then calculated using the method explained in Section 3.3.2.2 on page 87.

Due to time constraints, only virgin, overflow, mid used and sieved mixed used powder were tested; sieved mixed used in order to compare with virgin and overflow, and mid used in order to compare with sieved mixed used to confirm if the DSC results showing a location effect on crystallinity are correct. Three repeats were taken for each and the crystallinity calculated and averaged using both Bruker and OriginPro software. The traces are shown in Figure 4.13 and Figure 4.14.

Overall, it is apparent that the structure of all three grades are the same; all the major peaks occur in the same positions. This means that the higher crystallinity observed in the used powder is not the result of changes in the unit cell dimensions of the material. This also confirms that the thermal history is the reason for the double melting peak observed in virgin and overflow powder; mid used powder only shows one melting peak and yet the XRD traces for all three show the same peak positions. In the event of a secondary crystal structure it would be expected to see additional or shifted peaks using XRD [17]. The peaks for the overflow powder are sharper than the virgin, and the peaks for the used powder are sharper still; this is a sign of higher crystal perfection and confirms the DSC results [59].

The height of the peaks in mid used compared with sieved mixed used in Figure 4.14 confirm that the higher melting temperature observed in mid used powder is the result of increased crystal perfection. Of interest however is the values of crystallinity calculated for these samples; these are given in 4.3.

Two things in particular are significant; firstly the OriginPro software calculates both values to be the same, while the Bruker software shows only a small difference between them. Secondly, however, the values calculated are much lower than those observed in DSC; the OriginPro XRD values are 12% and 21% lower than OriginPro

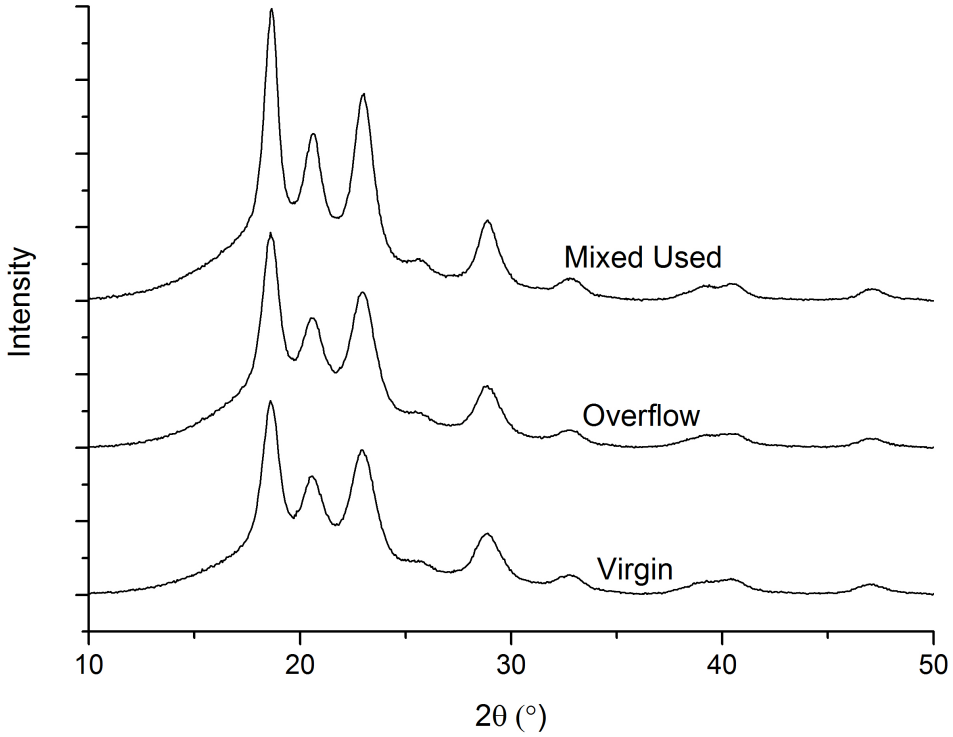

Figure 4.13: Comparison of XRD patterns for virgin, overflow and sieved mixed used Powder

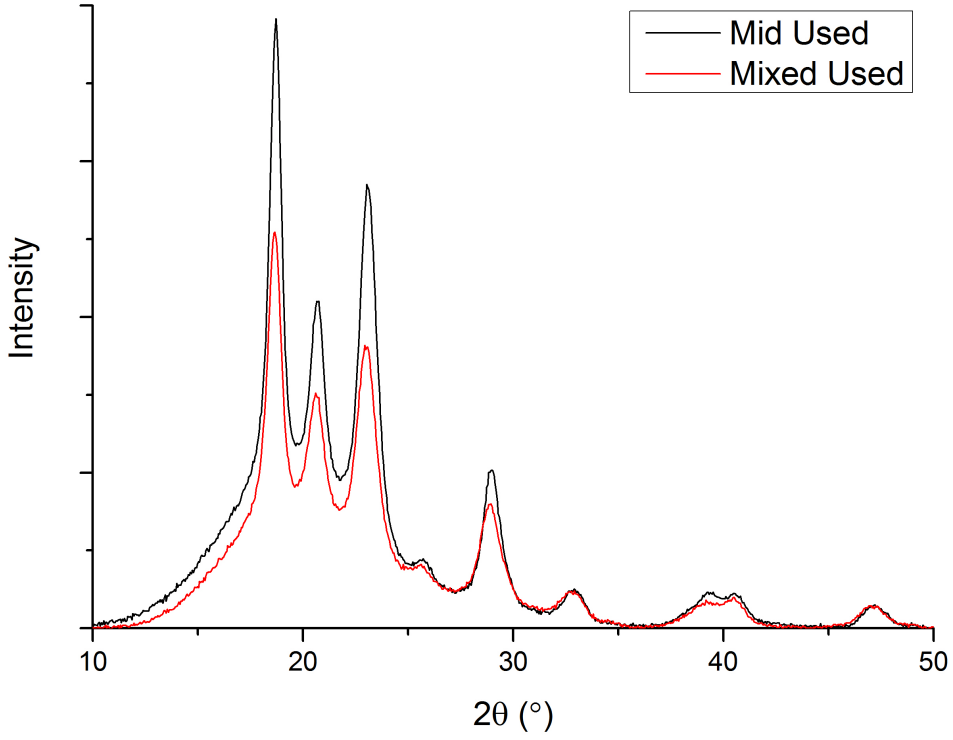

Figure 4.14: Comparison of XRD patterns for mid and sieved mixed used powder

	Origin	Bruker
Virgin	36.9±0.35	30.7±0.21
Overflow	36.6±0.63	29.6±0.26
Mid Used	39.6±0.21	34.9±0.3
Sieved Mixed Used	39.2±0.05	33.4±0.53

Table 4.3: Crystallinity as measured by XRD (all values are in %)

DSC for mid and sieved mixed used respectively, while the Bruker XRD values are 17% and 27% lower than OriginPro DSC values for mid and sieved mixed used respectively. There are two potential reasons for this discrepancy; differences in the way crystallinity is calculated using the different software packages, and differences in the way crystallinity is measured; these will be discussed in the next section.

4.3.3 Discrepancies in Measurement of Crystallinity

DSC and XRD were both used to examine crystallinity in order to see if the results compared. Calculation of crystallinity was undertaken using different software packages in order to investigate the effect of software bias and user skill on what should be objective, quantitative results; OriginPro was used to measure both DSC and XRD results as comparison to equipment specific analysis software. Average crystallinity values for all methods are shown in Table 4.4; in the case of DSC only the melt crystallinity is shown.

Whilst the DSC results are relatively similar, particularly given an average standard deviation of 3%, the Bruker software calculates much lower values for XRD than OriginPro, and standard deviation between repeats is between 0.4 and 1.1%, so this does not account for the difference. Furthermore, the XRD results are much lower than the DSC results, particularly for the used powder. So there is a need to understand how the crystallinity values are calculated from the various software packages, and how the equipment measures crystallinity.

4.3.3.1 Software Output

The mostly likely explanation for the discrepancies between software is the positioning of the baseline. The methods for positioning the baseline in the three

software packages are shown in Figures 4.15 and 4.16.

As explained, the difference between the Mettler STARe and OriginPro results are within the average error for all the repeats and is thus acceptable. This small difference may still be the results of placement of baselines, however. When analysing DSC data, positioning of the baseline in in Mettler software was made challenging by lack of control over where individual points were placed. Due to the slope of the trace, it was not possible for all repeats to place a straight line as a baseline. Therefore, a curved spline was defined as the baseline; this is shown in Figure 4.15a. As only a start and end point could be placed to govern plotting of the spline, there was limited control over the curve; it was felt that on some traces the spline curved too steeply and as a result the area which was integrated to find enthalpy of melting did not include the whole endotherm, thus erroneously returning a lower value of crystallinity than was present.

A number of points could be used in OriginPro to plot the baseline (Figure 4.15b) and the points moved until the spline followed the curve of the trace more closely, which it was felt was more accurate than the Mettler software. On average, the crystallinity measured using OriginPro was higher than using the Mettler software, which was as suspected. However, given that the difference between the Mettler and Origin values is within the limits of acceptable error, this not a significant problem.

Analysing XRD results has always been the subject of some discussion. There are several different methods for determining the amorphous fraction [14, 183, 184].

	DSC (%)		XRD (%)	
	OriginPro	Mettler	OriginPro	Bruker
Virgin	41.7	42.3	36.9	30.7
Overflow	38.8	39.5	36.6	29.6
Corner Used	58.3	58.2	N/A	N/A
Mid Used	52.3	50.4	39.6	34.9
Centre Used	44.8	42.3	N/A	N/A
Sieved Mixed Used	60.7	58.9	39.2	33.4

Table 4.4: Comparison of all crystallinity values for XRD and DSC from different software

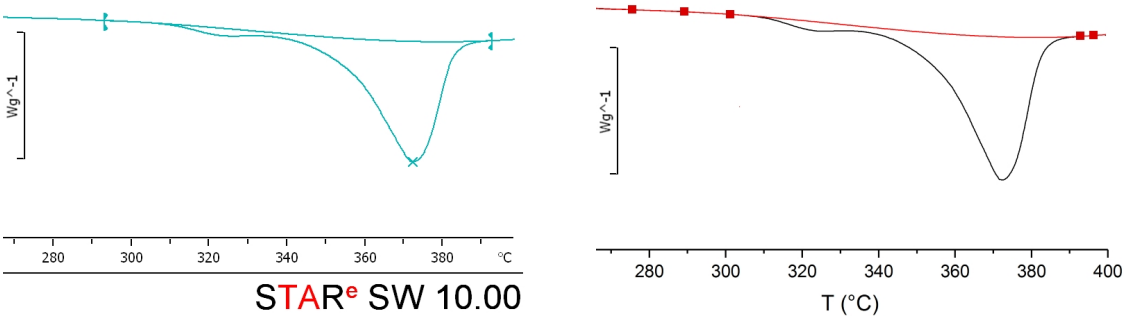

(a) Mettler DSC (b) Origin DSC

Figure 4.15: Baseline placement for DSC in Mettler STARe and OriginPro

The favoured method of calculating the amorphous fraction is to use XRD results for a fully amorphous sample of the material being analysed. However, it is not always possible to obtain an amorphous specimen of the sample. In this instance, it is common to use an algorithm to estimate the amorphous fraction by connecting the bottom points of each peak [14].

Using the Bruker software, there is limited control over the algorithm which sets the amorphous baseline. As shown in 4.16a, the baseline curves upwards into the crystalline areas on the smaller peaks. This could explain the lower values of crystallinity output by the software. By contrast, OriginPro allowed placement of the points used to construct the baseline so the spline fitted more closely to the experimental trace; this is likely why the OriginPro results are much higher than the Bruker.

4.3.3.2 DSC vs XRD

It is not unusual that the DSC and XRD results do not agree; other studies on PAEKs have also found the values to be different [185–187]. The difference is likely due to the way that crystallinity is measured using the methods. During DSC the sample is heated beyond its glass transition temperature and there is the possibility that thermal changes are taking place during the experiment. As XRD is a room temperature measurement these changes would not be present and discrepancies between the XRD and DSC results could arise [20, 185].

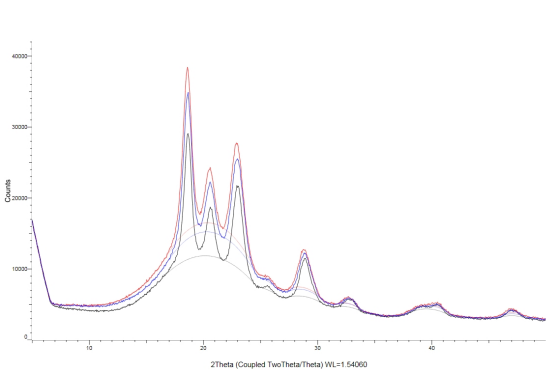

(a) Bruker XRD

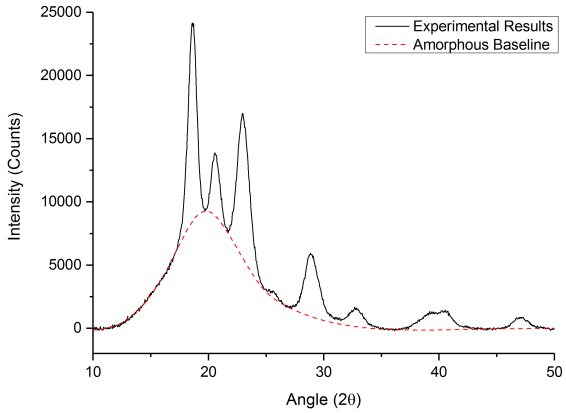

(b) Origin XRD

Figure 4.16: Amorphous fraction determination for XRD for Bruker DIFFRAC.EVA and OriginPro

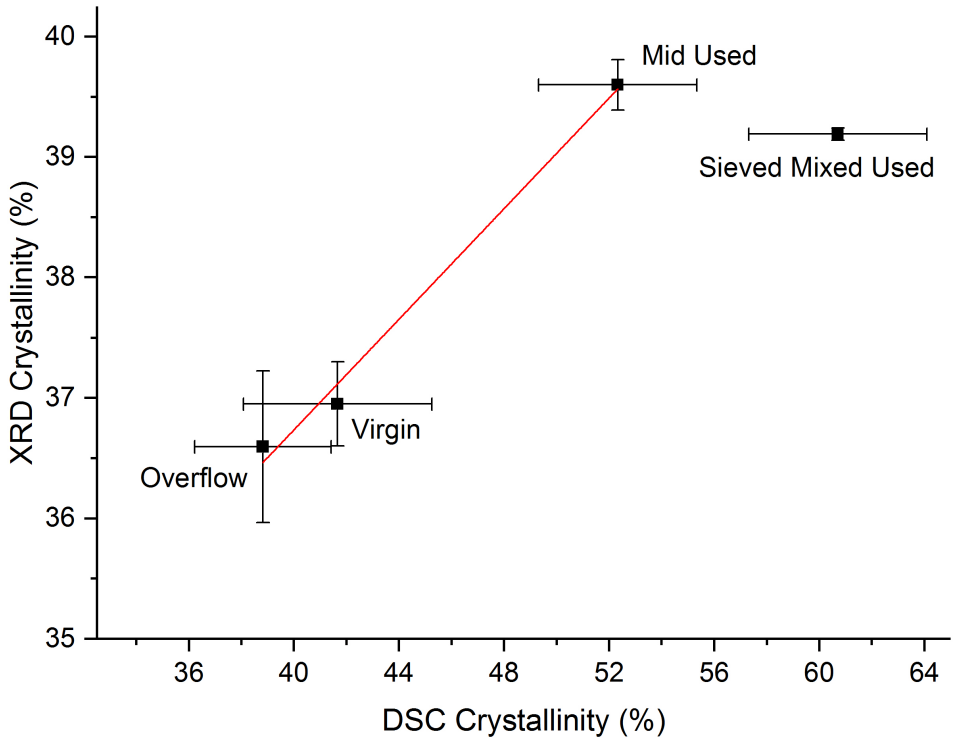

Figure 4.17: Correlation of OriginPro values of crystallinity for XRD and DSC

Where the XRD and DSC results differ significantly, they can still be considered comparable if the results correlate with each other; that is, the difference between the results is even for each grade tested [187–189]. Plotting the XRD and DSC calculated using OriginPro results show that for virgin, overflow and mid used powder, there is a correlation, although the standard deviation in the DSC results is high; this is shown in Figure 4.17. The value for sieved mixed used is an outlier; it is not clear why the difference between XRD and DSC for this sample is so large. Studies disagree over whether XRD or DSC is more accurate [184, 189] for calculating crystallinity so it is not clear which of the two sets of results is more likely to reflect the true crystallinity of the samples.

4.4 Degradation

As laser sintering takes place above the melting temperature of the material, it is important to understand at what temperature the material degrades and how degradation is manifested. There are two types of degradation which need to be understood; the first is degradation occurring in virgin powder during the building process as it is heated in the build chamber, and the second is the impact of very long periods held at high temperature on the used powder. As it is not known what temperature the overflow powder is subjected to, understanding the state of the powder may lead to assumptions about what the temperature is in the overflow chambers.

Thermogravimetric Analysis (TGA) was undertaken to find out how HP3 PEK decomposes, the physical appearance of the powder was considered and UV-Visible Spectroscopy was undertaken to try to quantify the physical changes observed.

4.4.1 Thermogravimetric Analysis

Thermogravimetric analysis (TGA) is a thermal characterisation method which can be used to examine the stability of a material as temperature is increased. As a material is heated it undergoes chemical changes such as absorption or loss of

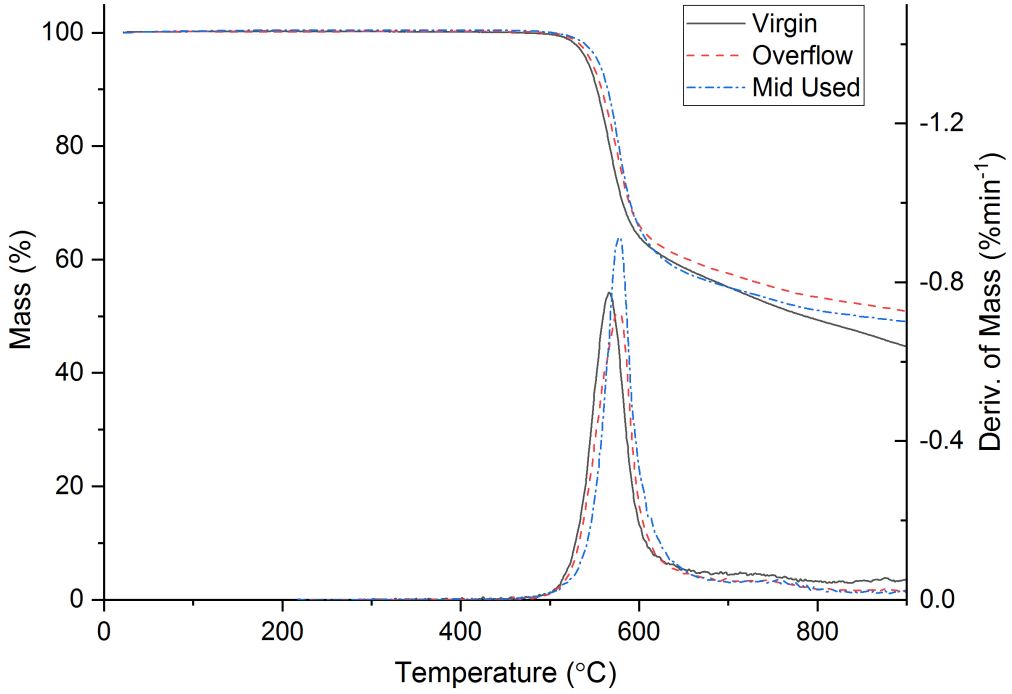

Figure 4.18: Comparison of TGA curves for virgin, overflow and mid used Powder

water, oxidation and decomposition. These chemical reactions result in a change of mass. By measuring change in mass as temperature is increased, a graph can be plotted which shows the temperature at which chemical changes occur.

TGA is also a useful tool for determining the maximum temperature to which an LS material should be subjected during building in order to avoid degradation. More recently TGA data has been used to establish a stable sintering region; this will be covered in more detail in Section 4.5.

TGA was undertaken using a heating rate of 10°C min^{-1} on virgin, overflow and mid used powder, three repeats for each. A comparison of representative traces is shown in Figure 4.18. All three grades show very similar decomposition trends, with mass loss occurs linearly in one stage. The three grades show small differences in the temperature at which mass loss begins.

Virgin powder is stable up until 466°C, at which point it loses mass very quickly up until 590°C. Mass loss between 590°C and 900°C is much slower. In total, 37% of the total mass is lost between 466°C and 590°C, and 18.4% is lost between 590 and 900°C, a further 18.5% is lost. Overall, 44.2% of the material remains following the test.

In overflow powder, mass loss begins at 495°C, and at 500°C in used powder. The majority of mass loss occurs between 500 and 600°C; both overflow and used show a mass loss of 34% in this period. From 600°C to 900°C, overflow powder loses an additional 15%, while used powder loses an additional 17%. At the end of the test, 50.8% of overflow power remains, whilst 48.9% of used powder remain.

Thus, overflow powder and used powder are more stable than virgin up until 495°C and experience lower mass loss overall. Decomposition of virgin powder begins 93°C above the melting temperature. This is quite low compared with results seen for PEEK; PEEK has a melting temperature of 343°C and Day et al [62] found that decomposition did not begin until 500°C, some 157°C higher than the melting temperature. Other authors have found onset of decomposition of PEEK to be 555°C or higher [65,190]. However, Hay and Kemmish [49] found that decomposition in PEK was very similar to PEEK, with decomposition beginning at around 427°C, so the results seen here can be assumed to be accurate.

The first derivative was calculated in order to identify the temperature at which peak mass loss occurs. This was done for all repeats and the results averaged. Peak mass loss was found to occur on average at 563°C for virgin powder, and 579°C for both overflow and used. The higher temperature for overflow and used is an indication that more energy is required to break down the structure of the material. This may be as a result of crosslinking which has occurred during building; crosslinking in known to increase thermal stability [54].

The value required from the TGA data to determine a stable sintering region is the temperature at which 1% mass loss occurs; it is assumed that if the material is heated above this temperature during LS then degradation will result in poor properties in the finished parts [10]. 1% mass loss was calculated for virgin powder to occur 475°C, at 525°C in overflow powder and 529°C for used powder. In practice, 100% overflow or used powder would be unlikely to be used in the build process as degradation of the powder would negatively impact on parts, however it is still useful to understand decomposition of these grades so that they are used appropriately when refreshing virgin powder.

During LS the powder is held very close to its melt point but only the material being sintered is melted. Given the high temperatures required to trigger decomposition it can be assumed that the degradation seen in used powder is unlikely to be as a result of mass loss caused by excessive temperature.

4.4.2 Change in Colour

It was observed that the colour of the various grades of powder was different, and in particular changes with use. Overall, used powder is much darker than virgin powder and powder from the centre of the build is darker than powder from the corner. Images of the powder are shown in Figure 4.19. Powder from the centre of the build shows the most change, while powder from the corner is not dissimilar to virgin and overflow.

Change in colour has been observed by other studies and is attributed to the length of time the material is held at high temperature; the longer the time held at temperature, the greater the discolouration [52, 108]. This effect is usually most pronounced in air and less visible in material held in a nitrogen atmosphere [52].

Discolouration was observed by Hay and Kemmish [49] in PEK heated in nitrogen above 400°C for 16 hours, accompanied by an increase in molecular weight and regions of crosslinked formations. The powder in the build chamber is held at close to its melting point for the duration of an entire build, which can be 24 hours or more, so it is not unreasonable to assume this may explain discolouration seen here. Also, although the P800 builds under a nitrogen atmosphere it has been noted that the oxygen sensor cannot withstand very high temperature and is by necessity some distance away from the powder delivery point [108]. There may be more oxygen in the build chamber than is recognised by the sensor.

As the time held at temperature is the same for all used powder, it is suggested that the temperature itself is also significant; the higher the temperature, the greater the discolouration. Thermal analysis undertaken so far as well as work by Ghita et al [12] support the theory that the temperature is hotter at the centre than in the corners.

(a) Virgin

(b) Overflow

(c) Corner Used

(d) Mid Used

(e) Centre Used

(f) Sieved Mixed Used

Figure 4.19: Colour of powder according to thermal history

4.4.3 UV-Visible Spectroscopy

UV-Visible Spectroscopy can be used to identify and express which wavelengths of light and how much of each are absorbed by a material. It has potential as a complementary tool for estimating the degradation seen in HT-LS components. Thermal analysis so far has identified some of the changes occurring in PEK powder as a result of high temperature and time spent in the build chamber and degradation which occurs as a result. If degradation results in a change in colour dependent on thermal history, then measuring the colour of the samples before thermal analysis and building up a set of correlations could subsequently provide a method of estimating thermal history based on appearance.

As an initial investigation into UV-Visible spectroscopy as a tool for distinguishing the difference between different coloured LS parts, tests were undertaken on laser sintered samples which showed a clear colour gradient from light to dark. The samples are shown in Figure 4.20. The samples were built at the same z-height and located between the centre and the outside edge of the build chamber as shown in Figure 3.4 in Section 3.3.3.2. It was noted that the discolouration was not uniform on the six samples; therefore readings were taken from both ends of each sample. Readings were taken from the end of the sample as it could be set up in such a way that the same location was tested each time in order to repeat the readings. Each location was tested three times.

A comparison of the results is shown in Figure 4.21. The darkest sample absorbs most frequencies resulting in a shallow, broad spectra across the whole range of wavelengths while the lightest absorbs low frequency wavelengths between 380-420nm and less across the rest of the range. This is to be expected as the samples are varying shades of brown, a composite of many colours; and a similar spectra was seen for discoloured PEEK by Day et al [52].

The spectra express the colour of the samples, but there may be a simpler method of quantifying how light or dark a sample is. In order to quantify colour it must be expressed as a function of the quantities of blue, red and green it contains and is complicated by how the surface of the material reflects light. The CIE

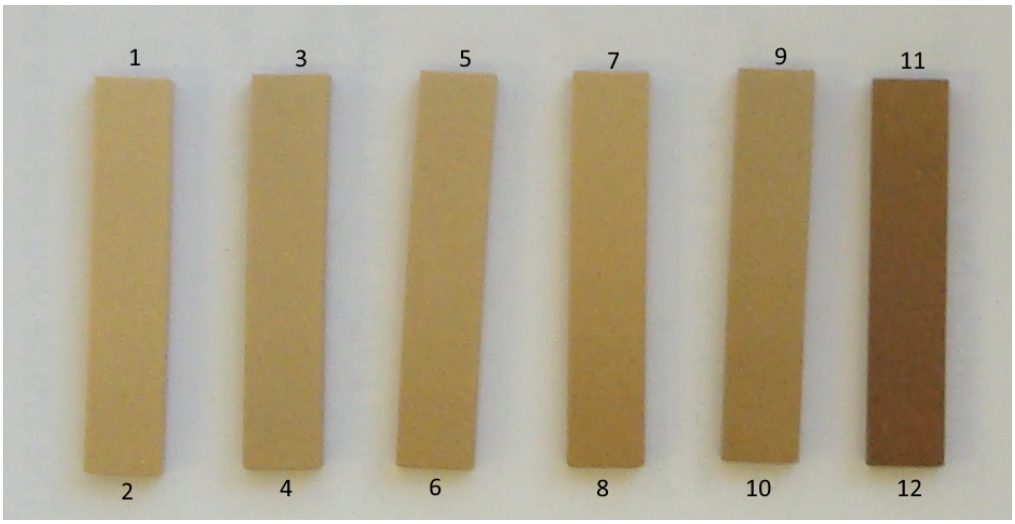

Figure 4.20: Laser sintered samples used for UV-Visible spectroscopy

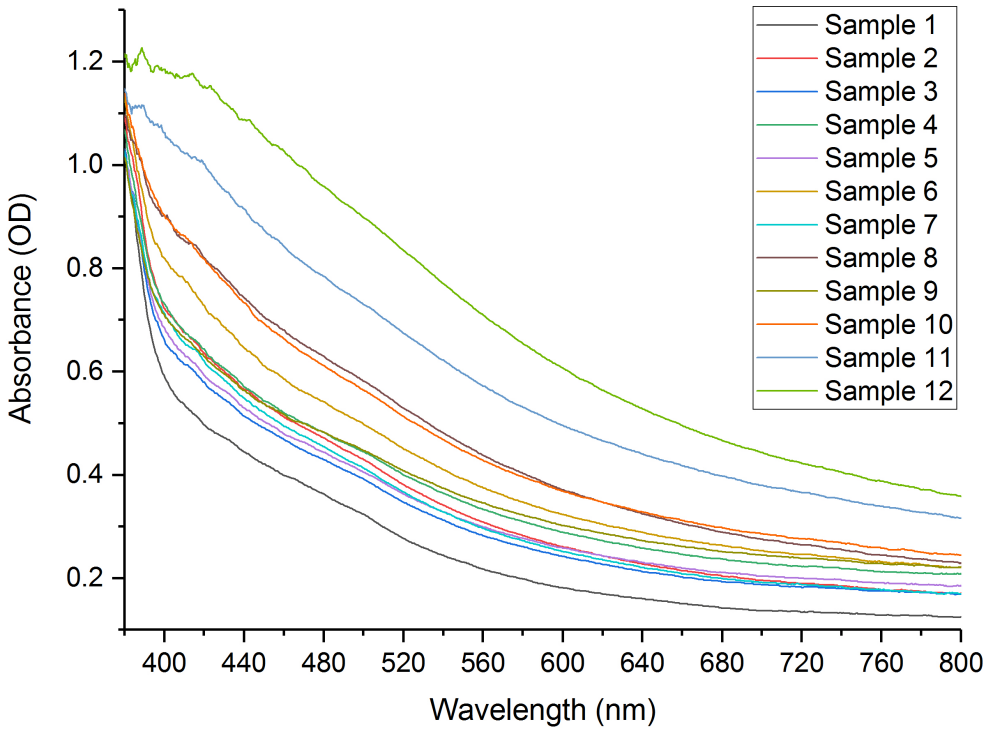

Figure 4.21: UV-Visible spectra for laser sintered samples: 1 = lightest sample, 12 = darkest

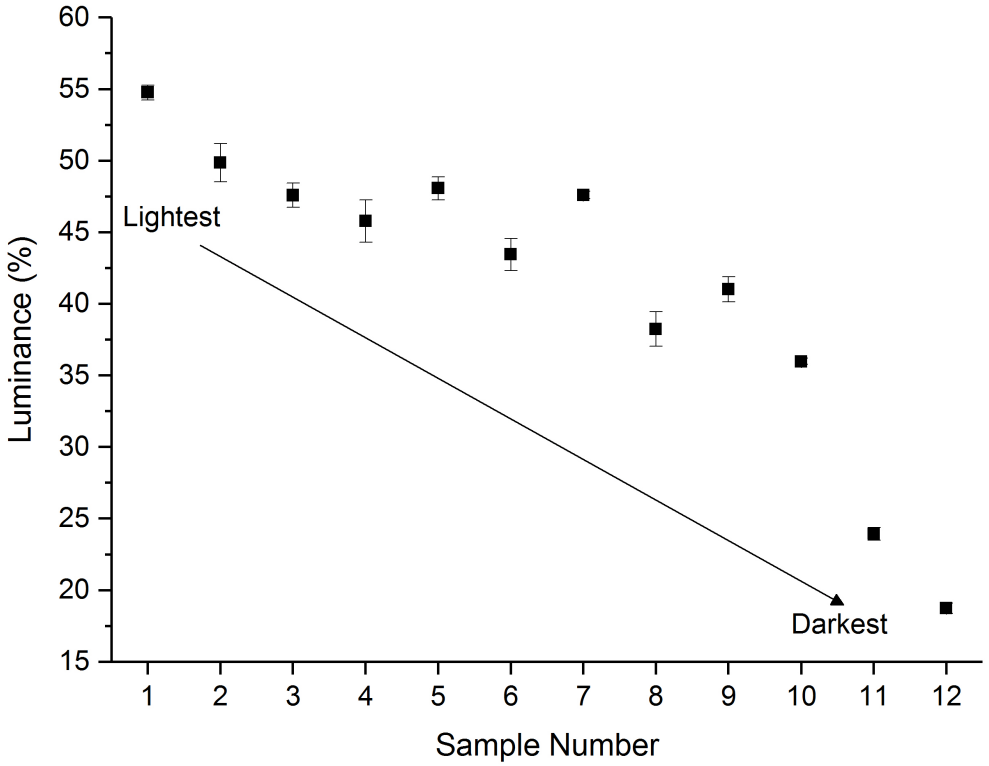

Figure 4.22: Average luminance of laser sintered samples

Tristimulus values X, Y and Z express light intensity as a function of red, green and blue and present an objective way to express light which is internationally recognised [191]. The SpectraSuite software used to control the spectrometer outputs all three CIE Tristimulus values alongside the spectra; the values are obtained from spectral data by matching them with CIE colour-matching functions from a database which represent the amount of red, green and blue required to produce a particular wavelength.

The CIE Y value presents an approximate correlation of lightness called luminance; luminance describes perceived brightness and expresses it as a percentage between 0 and 100, where 100 represents white/perfect reflectance and 0 means that all light is absorbed [191]. As it is of interest to quantify the lightness/darkness of LS samples, luminance is a simple method of expressing how light or dark a sample is. The luminance values output for each spectra were averaged for each sample and the graph is shown in Figure 4.22.

The graph shows clearly how the samples progress from light to dark. Values

were plotted by sample number, even though the samples do not range from light to dark linearly due to the labelling convention; this is expressed well by the graph. The luminance values clearly demonstrate the difference between samples which by eye alone look very similar.

Measuring and quantifying colour is a complex science as perception of colour is affected by multiples factors [191]. Precision of UV-visible spectrometers can be affected by calibration, the angle from which a sample is viewed, the morphology of the surface of the sample and light emitted from sources around the equipment. However, in this small study UV-visible spectroscopy has been shown to be a useful tool for measuring samples relative to each other and it has potential as a non-destructive method of looking at material properties.

4.5 Stable Sintering Region

The so-called processing window of LS material has been mentioned during analysis of DSC results and until recently has been a commonly used method of establishing the suitability of materials for use in LS [72, 178]. The stable sintering region is a concept introduced by Vasquez et al [10, 11] which takes into account more of the intrinsic properties of a material in order to identify how to process it using LS. The stable sintering region is defined as the temperature range in which optimised machine parameters will ensure complete material melting but without triggering decomposition of the material.

The stable sintering region is calculated using differential scanning calorimetry, hot stage and thermogravimetric analysis data; the end of the DSC melting curve validated by visual confirmation using hot stage analysis defines the lower limit of the region, while the 1% mass loss calculated by TGA defines the upper limit of the region. At this point, there were no hot stage results available to validate the temperature at which melting has completed, however Berretta [126] compensated for this by choosing a temperature known to be well above the end of the melting range in order to find the stable sintering region for PEEK 450PF. Therefore, 400°C was chosen for virgin HP3 PEK, as the DSC data suggests that all melting

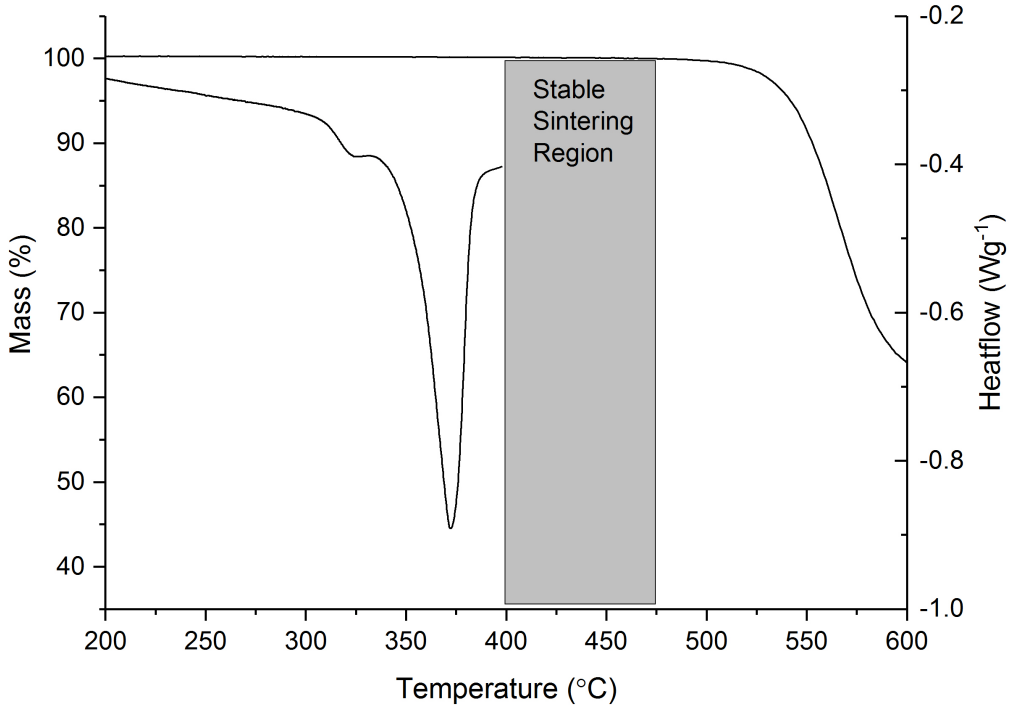

Figure 4.23: Stable sintering region for virgin HP3 PEK

is complete by 390°C. The 1% mass loss temperature was 475°C. The stable sintering region for virgin HP3 PEK is shown in Figure 4.23, and is calculated to be 75°C wide. Compared to PEEK 450PF, which has a stable sintering region of 250°C, this is quite narrow [126]. PA12 has a stable sintering region of 120°C [102], also much higher than HP3 PEK.

The stable sintering region represents the temperature range in which a material can be heated in LS to ensure complete melting without incurring degradation. The small region found for HP3 PEK would suggest that the build parameters need to be chosen carefully in order to ensure degradation does not occur.

It is common practice for other LS materials to build with a combination of virgin and overflow/used powder, a process known as refreshing [2]; this is seen as a significant advantage of the LS process as it reduces material waste and therefore the overall cost of producing parts.

Currently it is not recommended that HP3 PEK be refreshed [12]. DSC of overflow powder shows that is has a similar melting temperature to virgin powder, and TGA data shows that the 1% mass loss temperature is higher than virgin; thus

it could theoretically be mixed with virgin without affecting the stable sintering region calculated for virgin. DSC of sieved mixed used powder shows that melting is not complete until 413°C. In the event of refreshing virgin power with sieved mixed used material, the upper limit of the stable sintering region would remain the same in order to ensure degradation of the virgin material does not occur. However, the lower limit would need to be raised in order to ensure full melting of the sieved mixed used ratio. Thus, the stable sintering region of virgin powder refreshed with sieved mixed powder would be a maximum of approximately 60°C, resulting in a smaller range of potential build parameters than for virgin powder alone.

4.6 Conclusions

Experiments were undertaken to characterise HP3 PEK powder with differing thermal histories, and to assess the suitability of HP3 PEK for LS by comparing it with characteristics of other LS materials found in literature.

Scanning electron microscopy shows that virgin powder is a mixture of round, oval and irregular shaped particles. Particles display regions of fibrous morphology made up of short bundles; this has also been identified by other authors [123]. Other grades show differing quantities of the fibrous morphology; overflow powder is similar to virgin, while used powder shows that the structure recedes with proximity to the centre of the chamber. The particle size distribution of overflow powder is similar to sieved mixed used powder; both grades show fewer smaller particles than virgin and a greater portion of larger particles.

The melting temperature and crystallinity values of virgin HP3 PEK are in agreement with the literature for similar materials; a double melting peak is likely a result of the thermal history. The melting and recrystallisation peaks overlap due to the lower temperature endotherm. Overflow powder is very similar to virgin. Used powder shows differing melting temperatures and crystallinity according to location; the DSC traces suggest that the quality of crystals is higher at the centre than at the corner, which could be explained by a higher temperature at the centre.

The glass transition temperature increases with proximity to the centre of the build, which is an indication of the presence of crosslinking.

DSC and XRD analysis give very different values of crystallinity but appear to correlate well when analysed using the same software. Discrepancies between the two techniques are likely a result of thermal changes occurring in the sample during DSC which would not be present in XRD measurements.

Thermogravimetric analysis shows that overflow and used powder are more thermally stable than virgin, however decomposition is not activated until significantly beyond the end of the melting range identified by DSC. Differences in material colour were observed; used powder gets progressively darker with proximity to the centre of the build. This is most likely due to the long time spent at high temperature during building, and supports the theory that the build chamber is hotter at the centre than in the corners. UV-Visible spectroscopy was introduced as a new method of quantifying colour in order to correlate it with intrinsic material properties.

Overall, virgin HP3 PEK powder shows many characteristics which literature states are undesirable in a LS material; the particles are oval and irregular, it shows a double melting peak when heated and there is no clear gap between the temperature ranges of melting and recrystallisation [72, 75, 76, 97, 178]. The fibrous morphology could lead to locking together of the particles during spreading, resulting in potentially poor flow and packing [126]. PSD shows a number of small particles which are inadvisable as they generate static forces which can make powder spreading difficult [2]. The stable sintering region is approximately 75°C, which compared to PA12 and PEEK 450PF is very narrow [102, 126]. Thus the processing conditions need to be carefully controlled in order to minimise degradation.

Conversely, overflow and used powder particles are smoother than virgin, with fewer small particles and a larger processing window between melting and recrystallisation, which in theory should lead to better flow and packing and more stable sintering than virgin powder. However, due to the higher melting

temperature of used powder, refreshing virgin with used would lead to a smaller stable sintering region than for virgin alone.

Research shows that HP3 PEK can be successfully sintered, producing 100% dense parts with stable mechanical properties, albeit lower than those seen in injection moulded parts [108, 122]. Therefore comparing HP3 PEK with assumptions in the literature about what characteristics are required to ensure effective sintering shows that the assumptions do not apply to all materials. This is confirmed by Berretta [126] for other PAEK materials and by Vasquez [11] for some elastomers. Some different characterisation approaches may lead to qualification of a more diverse range of materials for LS. The stable sintering region is one such method which can identify a processing range for materials which by previous assumptions are not considered suitable for LS.

Material characterisation has shown some insights into the properties of used powder which do not explain why it is not recommended for re-use in the P800. It is particularly important for HT-LS to understand the impact of heat on the material, and to understand how heat is controlled during the build process. Thus the following chapters will focus on the temperatures involved in sintering of P800, which may explain some of the material properties seen here.

Chapter 5

Coalescence Characterisation

5.1 Introduction

Thermal characterisation methods alone do not fully describe how the application of heat affects laser sintering materials. As the purpose of applying heat is to cause a specific area of the powder bed to coalesce to form a dense structure, it is helpful to understand how and why coalescence occurs and what governs coalescence behaviour. The mechanical and physical properties of the final laser sintered part can be influenced by what occurs during coalescence [131].

An investigation was undertaken to observe the coalescence of HP3 PEK and to quantify the impact of temperature, time, heating rate and thermal history on the merging of pairs of particles. Experimental results were compared with theoretical models which have been shown to accurately predict coalescence behaviour of other materials in order to better understand the unique properties of HP3 PEK.

An overview of the work in this chapter in the context of the wider study is given in Figure 5.1.

5.2 Best Practice for Quantifying Coalescence

Whilst the method for observing coalescence is described in Section 3.4.1 on page 90, the best practice for measuring coalescence was experimentally determined, and

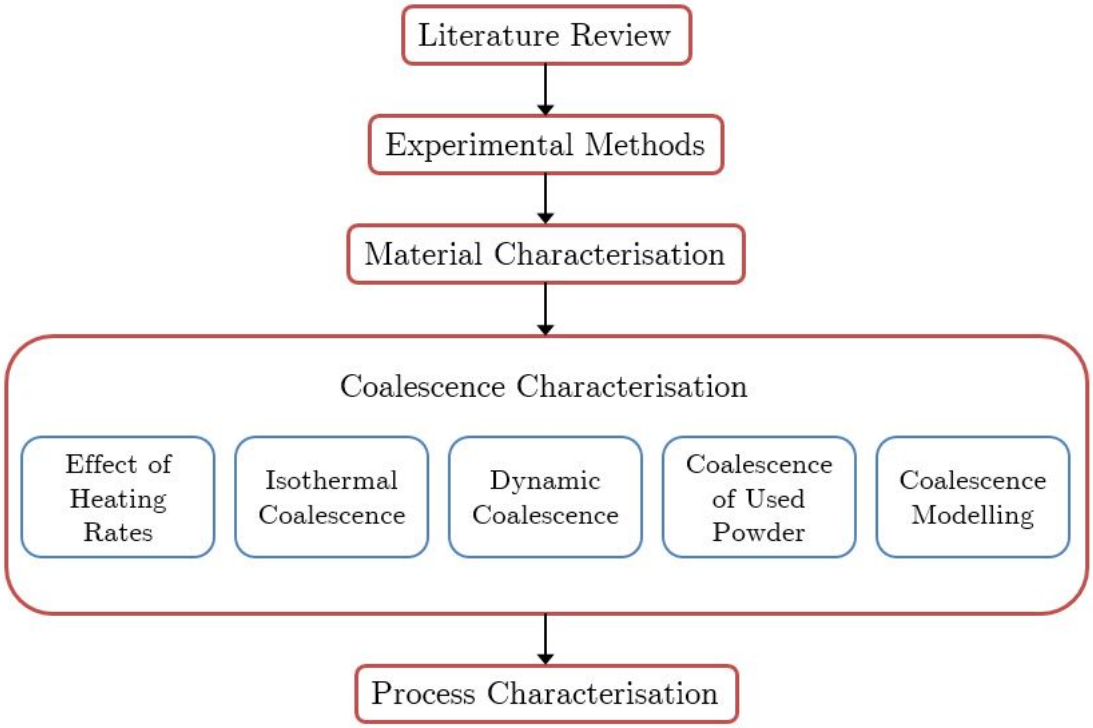

Figure 5.1: Overview of coalescence characterisation chapter in context

the observations from this investigation are detailed here.

The general method for observing coalescence was to scatter a thin layer of powder on a glass slide, then place it in the hot stage under the microscope and search at ambient temperature for suitable pairs of particles. Due to the small size of the particles it was impractical to place the particles together but particle pairs displaying the correct attributes were found using the scattering approach. Suitable particle pairs displayed three attributes: approximately round, approximately the same size and approximately touching; these attributes were desired in order to be as close as possible to the theoretical description of coalescence, which has been covered in Section 2.4 of the Literature Review and is shown again in the top line of Figure 5.2. Once a pair had been located, the test was carried out. Images were taken during the tests which were then measured to take the values required for characterisation and comparison with theoretical models.

Frenkel's model for viscous sintering is as follows:

$$\frac{x}{a} = \left(\frac{3}{2}\frac{\Gamma t}{\mu a_0}\right)^{1/2} \tag{2.1}$$

where x is the radius of the neck between the particles, a_0 is the initial particle radius, t is time and Γ and μ are surface tension and viscosity respectively. Frenkel's equation assumes the particle radius is constant throughout coalescence and only the time and neck radius change. In practice, the particle radius does not remain constant at the initial value, therefore throughout this chapter the particle radius is referred to as a, to demonstrate that it changes with time. The ratio of x/a describes how the neck growth develops as a function of the particle radius over the coalescence, where $x/a = 0$ refers to two whole particles with a point contact between them, and $x/a = 1$ is the end result when both particles have fully merged and total coalescence has occurred. This dimensionless value is referred to as the coalescence or contact ratio. It was considered useful to measure the neck radius x and the particle radius a from the images in order to plot the coalescence ratio so that the progress of the coalescence could be quantified against temperature or time and results from different pairs of particles could be compared.

The progression of coalescence in theory and as applied to images from experiment is shown in Figure 5.2; this method applies to both dynamic (increasing temperature) and isothermal (stable temperature held for a period of time) experiments. In this figure, the values i and ii are not significant, they are used simply to represent that time has elapsed. At (a) the test has not started so time = 0 and temperature is ambient, and two particles are present. At (b) either temperature (T) or time (t) equating to "i" has elapsed and the particle and neck dimensions have changed. Figure 5.2c shows a further progression of temperature/time to "ii". Figure 5.2d shows the final state of the particles at the end of the test, temperature/time = f.

In theory, the two particles would be perfectly round and exactly the same size with only a point contact between them, shown in the upper image of Figure 5.2a. Most particles were not the same size so it was necessary to measure both particles, denoted as 1 and 2 in the lower image of Figure 5.2a. The average of the two radii

was used when calculating x/a. As has been shown, HP3 PEK particles are more oval in shape, so it was necessary to approximate each particle as a circle. Two different size particles did not prove significant to the outcome of the coalescence; this will be explained in Section 5.5.2.

A point contact was in practice very difficult to achieve and it was found that if there was not sufficient contact between the particles before the start of the test they drifted apart rather than coalescing together when heated. Through trial and error it was found that $x/a = 0.3$ was the lowest contact ratio which would result in coalescence.

Frenkel's theory assumes a constant particle radius during coalescence which holds true for the early stages, but it was observed that the particle radius changed over the test so it was necessary to measure this from each image. In theory, the two particles remain distinct with a clear neck between them during the coalescence. In practice it was found the neck was often quite indistinct and the edges of the particle difficult to see as a result of the magnification. Therefore in order to find x, the diameter of the neck $2x$ was taken and divided to get the neck radius. The particle radius a was found by measuring z from the approximate centre of each particle to the centre of the neck, and using Pythagorean Theorem to find a. Values were taken from each image and the x/a ratio plotted against temperature for dynamic tests and time for isothermal tests.

Finally, in theory the final neck radius would equal the final particle radius resulting in a coalescence ratio of 1. Whilst this was observed for some particle pairs, it was more likely that the final particle shape was not perfectly circular, resulting in two particles still being measurable. However, in images where it was clear that full coalescence had occurred, the neck radius was in many cases found to either be equal to or in excess of the average of the radii for the two particles, resulting in a coalescence ratio of 1 or higher, in spite of the fact that the end result was not perfectly circular. Thus, the measurement of x/a is a useful tool for quantifying coalescence, even though experimentally the images do not necessarily match up with theory. As $x = 1$ refers to complete coalescence, results exceeding

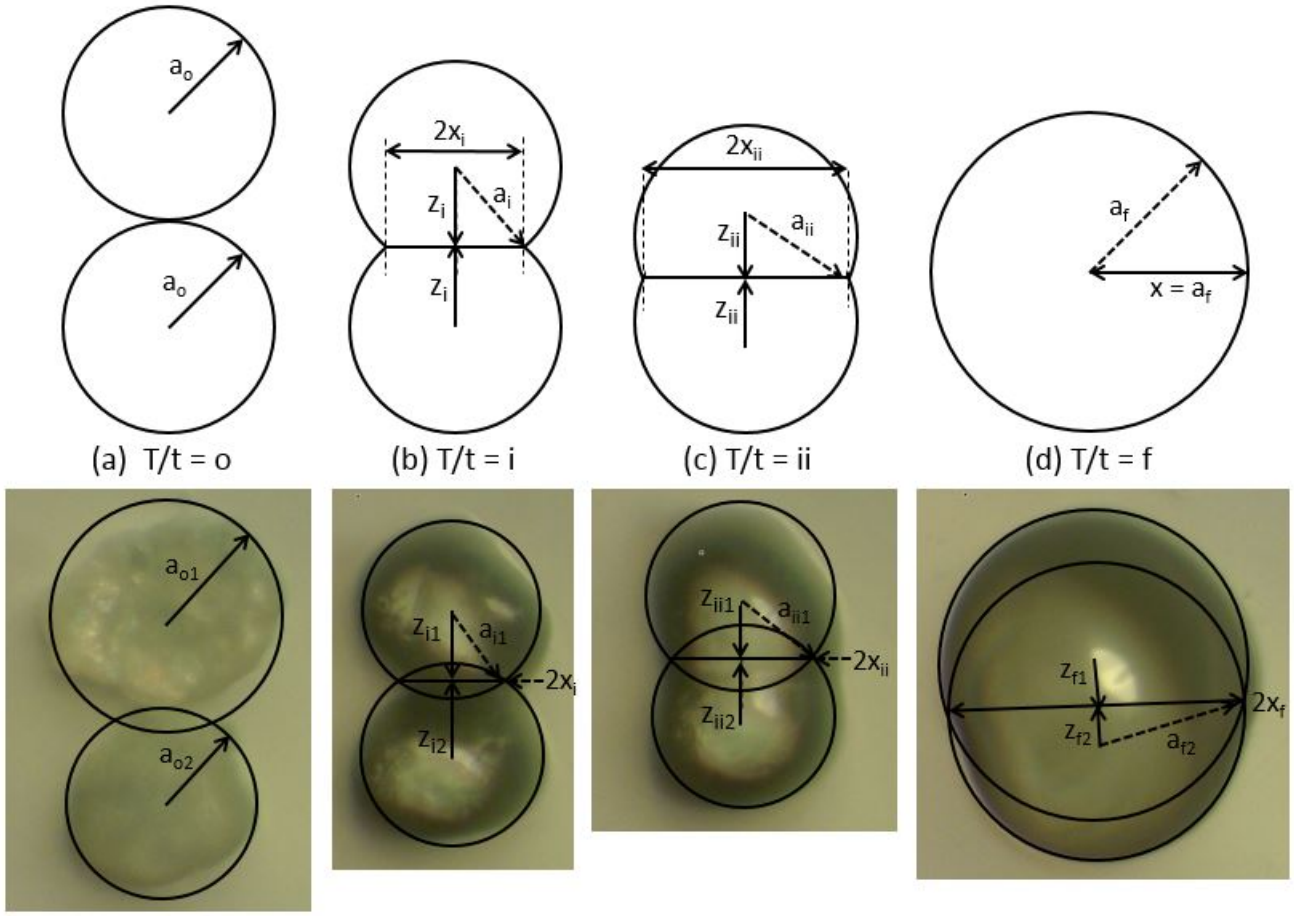

Figure 5.2: Method for measuring coalescence. T/t refers to temperature or time (a) o is ambient temperature or time = 0, (b) and (c) show progression of coalescence during experiment where i is a period after o and ii is a period after i, and (d) f is final result

this value were plotted as $x = 1$ for ease of comparison with other curves.

5.3 Investigation into Heating Rates

The initial aim of the work was to capture the coalescence process in images. An initial heating rate of 1°C min^{-1} was chosen to make the coalescence easier to observe but was found to be so slow that even several degrees higher than the melting temperature, coalescence was incomplete. This is shown in Figure 5.3. A darkening of the particles is observed at the melting temperature (T_m) 373°C and a certain degree of particle shrinkage was noticeable compared with the particles at ambient temperature. However, at 400°C, which is well beyond T_m, very little coalescence is apparent. Rather there is more discolouring and the particles have shrunk in size with apparently minimal merging.

The heating rate was increased in each experiment until significant coalescence was observed. This first occurred at 8°C min^{-1}. However, as can be seen in Figure 5.4 the particles do not fully merge. Even at 440°C, equilibration - described by Mazur [130] as the point at which there is no longer a neck between the two particles - has not been achieved.

The heating rate was gradually increased until the physical limit of the hot stage had been reached. Initially this made it difficult to capture images given the short time frame in which to do so but a new microscope and software with an automatic time-lapse image capture function meant this was possible for later tests. At 20°Cmin^{-1} and 60°Cmin^{-1} much more coalescence was observed than at slower heating rates and at 80°Cmin^{-1} and 100°Cmin^{-1} the two particles merged completely to form one drop, as shown in 5.5.

Figure 5.6 shows the progression of x/a over time for increasing heating rates. It is clear that as the heating rate is increased, the final x/a value which can be achieved also increases. Full coalescence ($x/a = 1$) is possible at heating rates over 80°C min^{-1}. The speed at which the particles coalesce also increases with the heating rate. Full coalescence is achieved at increasingly lower temperatures as the heating rate is increased; at 10°C min^{-1} the maximum x/a value of 0.8 is reached

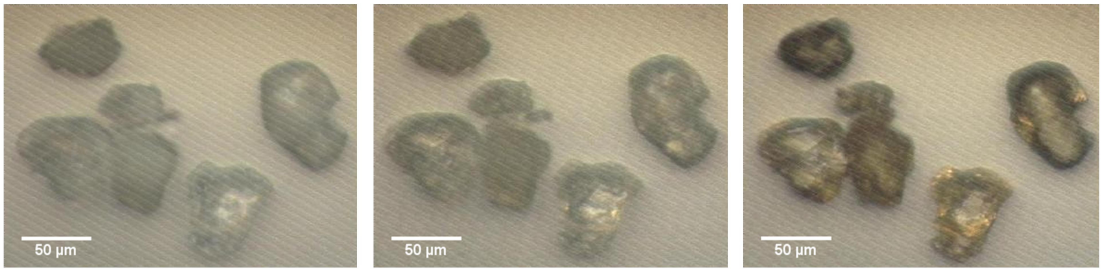

Figure 5.3: Virgin particles, heating rate 1°C min^{-1} as temperature is increased

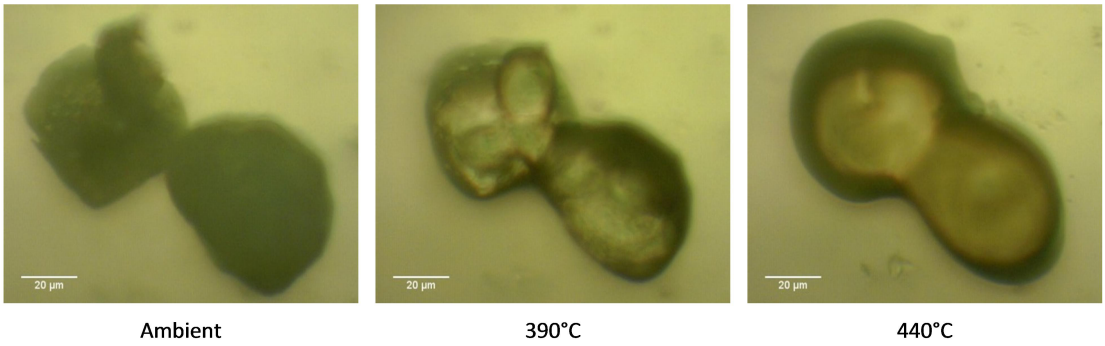

Figure 5.4: Virgin particles, heating rate 8°C min^{-1} as temperature is increased

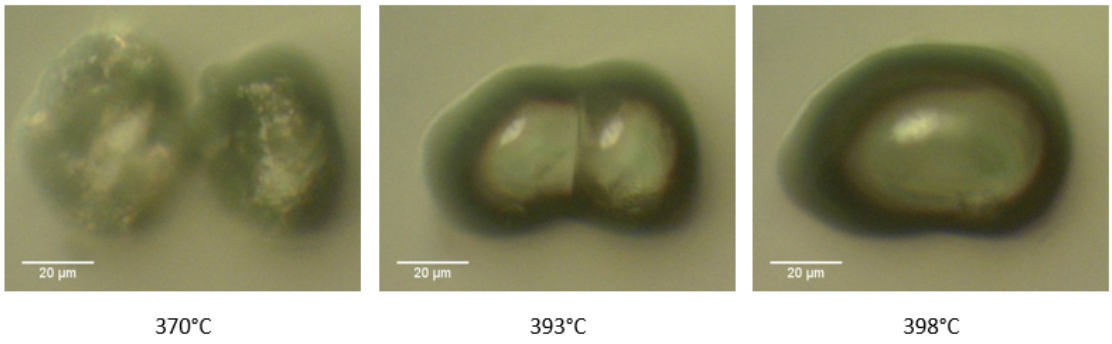

Figure 5.5: Virgin particles, heating rate 100°C min^{-1} as temperature is increased

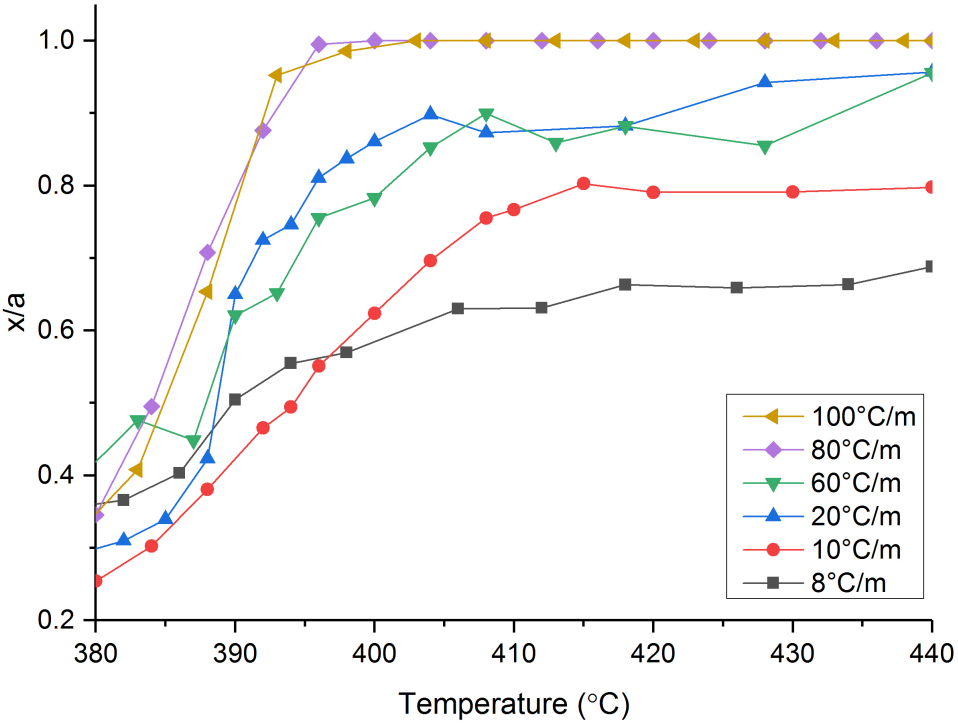

Figure 5.6: Comparison of coalescence ratio x/a against temperature for increasing heating rates

at 415°C but increasing the heating rate to 20°C min^{-1} results in $x/a = 0.89$ being reached at 404°C. By further increasing the heating rate to 80°C min^{-1} the particles reach $x/a = 1$ at 396°C. However, this appears to be the maximum speed of coalescence reached as the results are almost exactly the same at 100°C min^{-1}.

The most probable reason why the heating rate impacts the coalescence is due to degradation occurring in the air atmosphere.

PEK is typically processed in a nitrogen atmosphere as it has been shown that degradation is accelerated in an air atmosphere. Day et al [52] found that PEEK heated in air at 400°C showed a reduced intrinsic viscosity and high insoluble fraction, which they attributed to oxidative chain scission reactions and cross-linking of the polymer chains. Whilst their experiments were conducted over a matter of hours, they found the majority of the chemical changes occurred very early in the test. They also posited that oxygen is transported through the melt resulting in oxidative degradation [62]. Yao et al [61] found that the decomposition rate of PEEK decreased as heating rate was increased and suggested that this

occurred as the time available for the sample to react to oxygen was reduced when heating rate was faster. It is possible therefore, that the higher heating rates allow more coalescence to occur before chemical changes in the material can hinder further progress.

Vasquez [11] was able to successfully capture full coalescence of several LS materials including different grades of polyamide and various elastomers at a heating rate of 10°C min^{-1} in an air atmosphere. Likewise Bellehumeur [134] was able to observe full coalescence of polyethylene and polycarbonate powders at heating rates of 20°C min^{-1} or lower in an air atmosphere. It seems reasonable, therefore, to suggest that the properties of HP3 PEK are the reason why it does not coalesce at similar heating rates.

5.4 Isothermal Heating

Frenkel's model predicts sintering at a constant temperature. Although LS takes place using dynamic heating, isothermal tests were undertaken for better comparison with theory. Initially, five hold temperatures were tested; 375, 380, 385, 390 and 395°C. It has been shown using DSC in Section 4.3.1 that the melting range of virgin HP3 PEK is between 348 and 392°C; 375°C was chosen as the lower limit of the range as the peak melting temperature has been observed to be 373°C, and 395°C chosen as the upper limit as this is verified by the DSC as above the endpoint of melting and also in the earlier hot stage tests as a point at which significant coalescence has occurred when heated at the higher heating rates. It was anticipated that following these initial tests a narrower range of temperatures would then be tested to identify one in which full coalescence could be observed isothermally. Isothermal sintering of polymers has been recorded by other authors [134, 137, 139] so it was expected that the correct temperature for isothermal coalescence of HP3 PEK could be identified experimentally.

The method in the current study was to input the pre-determined hold temperature into the hot stage controller, then heat to the hold temperature at 100°C min^{-1}, the maximum heating rate of the hot stage. It was observed that

Hold Temp (°C)	Ambient	Hold Temperature	After 20 minutes
375	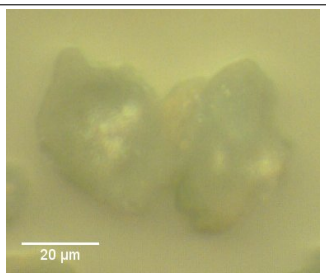	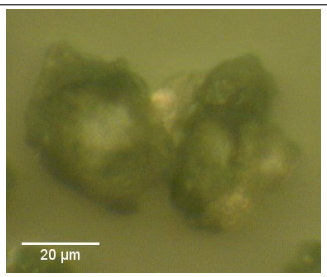	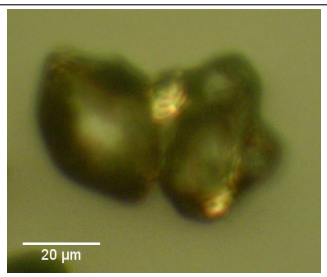
380	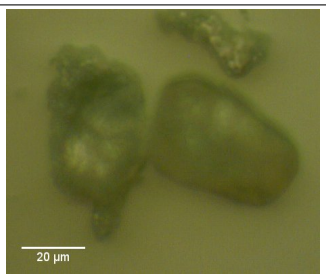	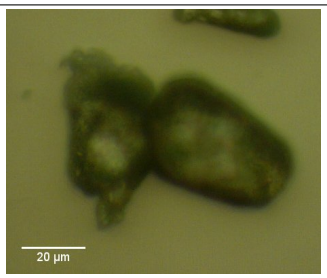	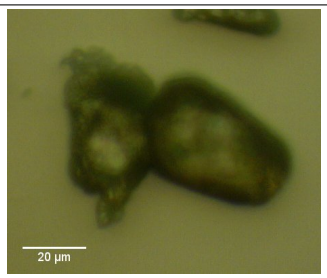
390	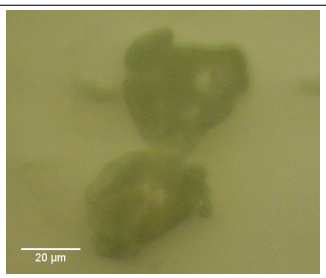	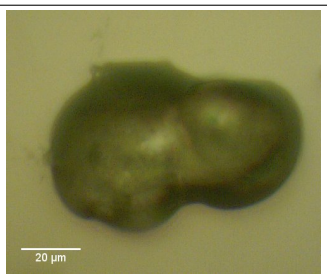	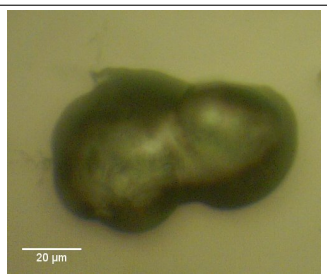
395	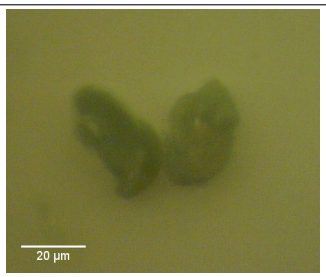	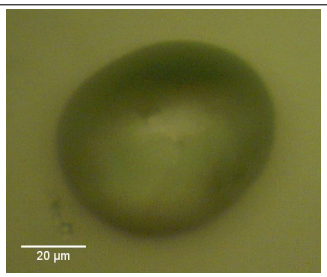	

Table 5.1: Images from isothermal heating tests at ambient, hold temperature and after 20 minutes has elapsed

the hot stage slowed the heating rate once the temperature was 2-3°C below the hold temperature so no overshoot above the hold temperature was observed on the controller screen. Images were taken as soon as the hold temperature was reached and at regular intervals thereafter while the particles were held at the same temperature for 20 minutes.

Images of the results are shown in Figure 5.1. These correspond to ambient

	Coalescence Ratio (x/a)					
Hold Temp (°C)	Ambient	Hold Temp	+5 mins	+10 mins	+20 mins	Isothermal Change
375	0.52	0.54	0.56	0.59	0.6	0.06
380	0.24	0.66	0.66	0.66	0.67	0.01
390	0.36	0.82	0.84	0.84	0.84	0.02
395	0.3	1.14	N/A			

Table 5.2: x/a values for isothermal tests; final column shows change in x/a between hold temperature and end of test

temperature before the test began, the first image taken once the hold temperature had been reached and the final image after 20 minutes had elapsed. The particle radius and neck radius of the particle pairs were measured as described in Section 5.2 and x/a values calculated for each. These numbers are given in Table 5.2 for the ambient temperature, as soon as the hold temperature is reached, and then every five minutes for the 20 minute hold time. The final column shows the overall coalescence occurring isothermally; that is, between the hold temperature being reached and 20 minutes later. The results at 385°C could not be measured due to uneven spread in the melt, and have therefore been excluded.

At 375°C it can be seen that some change has occurred before the hold temperature as the particles are darker and a noticeable degree of shrinkage and neck growth appear to have occurred. After 20 minutes at 375°C the particle edges have rounded showing that some melting has occurred, however the neck does not appear to have grown significantly. This is confirmed by the x/a calculation which shows a change of 0.02 before the hold temperature is reached and a further change of only 0.06 after 20 minutes. The total x/a increase for the 375°C from ambient temperature to the end of test is 0.08, which is the lowest increase of all the temperatures tested.

At 380°C, the neck growth observed between ambient temperature and the hold temperature equates to $x/a = 0.42$. Visually this change is not as noticeable as the changes observed in the later tests, which reinforces the usefulness of the coalescence ratio calculations as a measure of coalescence. The particles are significantly

discoloured by the time the hold temperature is reached and no more coalescence appears to take place during the 20 minute hold time.

At 390°C there is significantly less neck visible at the hold temperature than at 380°C. As with the earlier tests, the coalescence observed during the hold period once 390°C has been reached is insignificant compared with the coalescence which occurs during the initial heating period. By the time the 395°C hold temperature has been reached, complete coalescence has occurred; there are no longer two particles visible and the coalescence ratio is 1.14.

The initial shapes of the particles were not consistent across all tests but this does not appear to have affected the final results. Likewise, the initial x/a value does not appear to affect the results. The initial coalescence ratio for 375°C is 0.52, which is significantly higher than the other tests, and it would be expected that this initial contact would result in more neck growth across the test due to the greater surface area in contact between the particles. However, whilst the neck growth observed during the test is highest at this temperature at $x/a = 0.06$, it is still very small, particularly compared with the amount of neck growth required for full coalescence, and as has been pointed out the total change in x/a across the whole test is lowest at this temperature. Likewise, whilst the x/a value at the 390°C hold temperature is higher than at 380°C, the actual increase is 0.46, which is quite similar to the $x/a = 0.42$ increase observed at 380°C.

Discolouration of the particles was observed during holding at all temperatures. This is generally associated with oxidative degradation, which would explain why coalescence does not occur even when held for long periods [52]. Degradation as a result of the air atmosphere has already been covered in Section 5.3.

From these results it would appear that no hold temperature results in isothermal coalescence; almost all coalescence observed occurs before the hold temperature is reached.

However, to check whether a longer hold time would result in fuller coalescence, it was proposed to run trials between 380°C and 385°C with a hold time of two hours. This range was chosen based on visual inspection of the first set of tests; at

380°C the neck is still clearly visible between the two particles while at 385°C the particles have equilibrated and the neck is no longer visible. It was expected that the temperature which results in equilibration and by extension full coalescence lay between the two.

Images undertaken at a hold temperature of 381°C are shown in Figure 5.7. Some coalescence has occurred before the hold temperature is reached; calculation of the coalescence ratio shows a change of $x/a = 0.28$ between ambient temperature the first image at the hold temperature. By contrast to the earlier tests, a further increase of 0.18 occurs in the first minute of the hold period. However, by ten minutes into the hold period, this has only increased by a further 0.02, and at the end of the two hour period, the final x/a value is 0.79, somewhat short of full coalescence. There is still a distinct neck between the two particles; this is not clear at 381°C + 10 minutes but this is almost certainly due to drift in the focus of the microscope as it is visible at the later times in the test. The focus appeared to drift as a result of the high temperature of the test and was manually adjusted often but adjustments would inevitably result in some differences being observed between images.

It is interesting that more coalescence has occurred at 381°C than was seen during the test at 380°C. Calibration of the hot stage shows a slight drift of less than 1°C per 100°C but this would be sufficient for the two test temperatures to be very similar. It may also be down to surface morphology which is not visible at the magnification used; it has been shown in Section 4.2.1 that some virgin particles show a fibrilar structure which will increase the surface area of the particle and potentially result in faster coalescence. If the coalescence is in competition with oxidative degradation as seems likely, then the quicker coalescence rate would result in higher overall coalescence.

It does not seem appropriate however, to call the coalescence which occurred during the first minute of the hold period isothermal as it could be accounted for by thermal lag, as discussed in Section 5.3. If isothermal coalescence were occurring it would be observed well beyond the first minute as has been seen for other polymers

such as polyethylene and PMMA [134, 137].

During traditional sintering, which is a solid state process, the merging of particles occurs below the melting point and often involves diffusion across grain boundaries, resulting in the process being very slow [192]. However, coalescence of semi-crystalline polymers occurs in the liquid phase, above the melting point, and semi-crystalline polymer chains do not diffuse in the same way as metals [72]. Therefore it is does not seem necessarily appropriate to approach the coalescence of PEK powder assuming that it will occur isothermally.

Instead, it was decided to pursue dynamic heating of the powder. The initial heating rate tests showed that full coalescence can be achieved using dynamic heating throughout the test whereas the only coalescence observed during the isothermal tests occurred either before the hold temperature was reached or very shortly thereafter. This can be explained by what is occurring during heating. The two dominant forces are surface tension and viscosity; surface tension acts on the surface of the polymer, while viscosity drives motion of the internal molecular structure. As the temperature is increased, surface tension effects result in the particles changing shape, whilst the internal viscosity decreases, allowing the two particles to merge. The hypothesis is presented here that the increase in temperature is required in order for the viscosity to decrease sufficiently for full coalescence to occur. There is no single temperature at which coalescence takes place, as the decreasing viscosity results in coalescence occurring as soon as the material is in a molten state. However if held at too low a temperature, the internal viscosity will remain too great for full merging to take place. Therefore, the temperature must be increased until it is high enough for full coalescence to take place, which due to the limitation of the hot stage requires a dynamic heating rate as it is not possible to simply attain the temperature required without this gradual heating.

Furthermore, dynamic heating is a better representation of what is occurring during LS. During building, the material is held very close the melting point and the temperature raised very quickly through the melting point in order to selectively

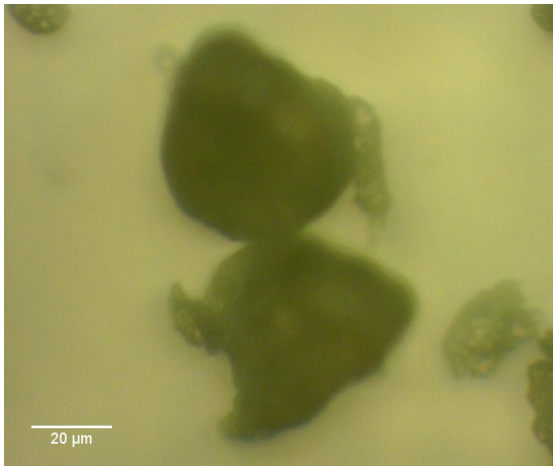

Ambient, $x/a = 0.3$

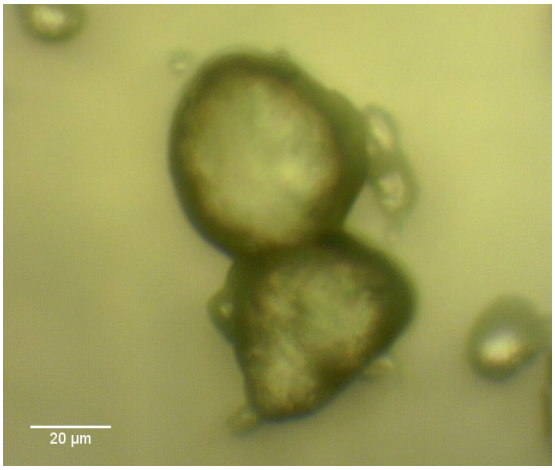

Hold Temp = 381°C, $x/a = 0.58$

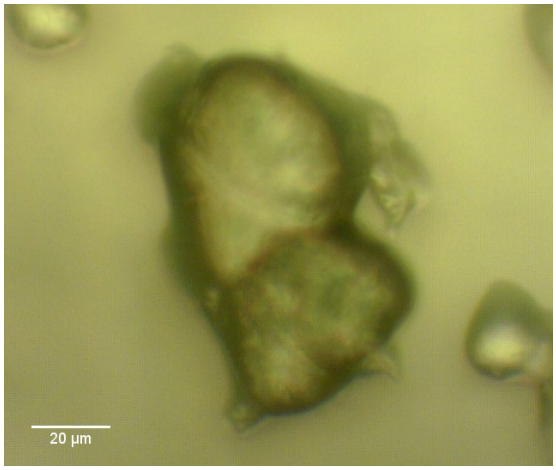

381°C + 1 minute, $x/a = 0.76$

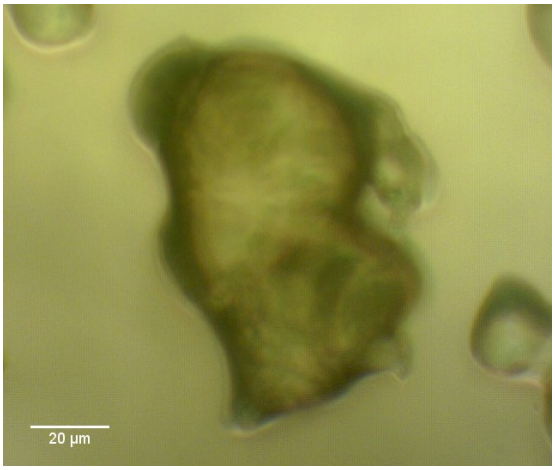

381°C + 10 minutes, $x/a = 0.78$

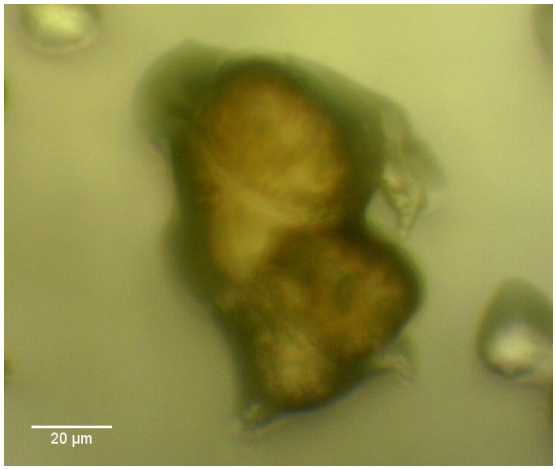

381°C + 30 minutes, $x/a = 0.79$

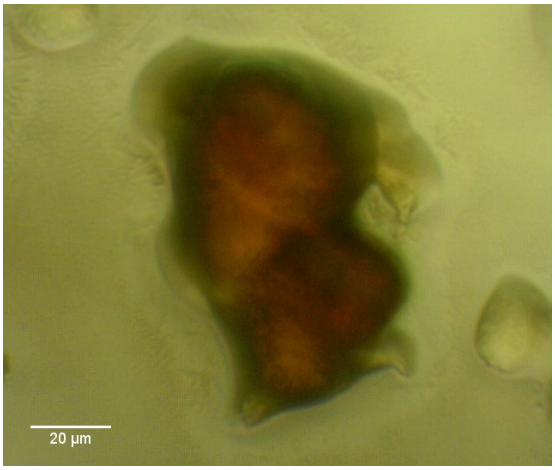

381°C + 120 minutes, $x/a = 0.79$

Figure 5.7: Images from isothermal heating test held for two hours at 381°C

fuse sections of particles. Vasquez [11] that the heating rate of the LS process when applied to polyamide is approximately 22,000°C min^{-1}. Whilst this heating rate is not within the capability of the hot stage, it seems more useful for understanding an LS material to heat it dynamically rather than isothermally.

In order to ensure full coalescence and minimise oxidation effects, it was decided to undertake all further dynamic tests at 100°C min^{-1}.

5.5 Dynamic Tests at 100°C min^{-1}

In order to compare with theory, there were three attributes desired of the initial particle pair:

- Similar size
- Near-spherical shape
- Small initial contact area (approximately $x/a = 0.4$ or less)

Even when these initial requirements were met, lots of variation in the coalescence behaviour was observed. The results here will be covered in two sections; those which showed uniform coalescence, that is, coalescence which very closely matched the behaviour described by the theory, and those which demonstrated characteristics not described by theory which were consequently considered non-uniform. The purpose of categorising uniform and non-uniform results was two-fold; firstly to quantify the impact of uniform or non-uniform behaviour on the overall coalescence, and secondly to match theoretical models later on with results which most closely match the behaviour they are predicting.

5.5.1 Uniform Results

Images of an approximately uniform coalescence are shown in Figure 5.8. At ambient temperature, the particles have a small contact between them. At 383°C, some neck development has occurred and the particles have begun to change shape. Surface tension effects result in the molten particles seeking to minimise surface

energy by reducing the surface area; the most efficient shape for this is a sphere, thus the particles attempt to become rounder [193].

At 391°C, the particles have shrunk considerably compared with ambient temperature and the neck between them is much larger. According to Jagota et al [194], the particles are drawn together by molecular van der Waals interactions, which have the effect of "zipping" the particles together to increase contact area between them. The particles have lost much of their individual shapes but the interface between the particles is still in tact. According to Mazur [130], what is occurring during this neck growth stage is deformation of the particles but molecularly they remain two separate entities. At 398°C, the neck between the particles has disappeared; Mazur [130] refers to this phase as equilibration and it occurs when the molecular structure relaxes, allowing the polymer chains from both particles to mix and combine to form one body. A schematic of these phases in shown in Figure 2.16.

At 413°C, the coalesced particle is much rounder, and also much larger; the force of gravity on the droplet exceeds the force exerted by surface tension, causing the melt to spread on the slide [193]. Finally, at 440°C the melt is approximately circular and coalescence is complete.

Of all the tests undertaken, six were considered to show uniform coalescence. The particle and neck radii were measured and the x/a values calculated for each temperature and the results were averaged to produce the curves shown in Figure 5.10. The variation is also plotted.

Figure 5.10a shows the progression of the neck radius and the particle radius dimensions as the temperature increases. The particle radius initially decreases as the particles change shape towards spherical, whilst the neck radius increases steadily as the particles seek to increase contact area between them. The curves are a similar shape through the second half of coalescence and converge to a similar dimension at 440°C, which is required for an x/a value of 1. The variation in the neck radius is quite low throughout the whole coalescence, while there is greater variation in the particle radius during the initial stage. This is expected as the

Ambient, $x/a = 0.32$

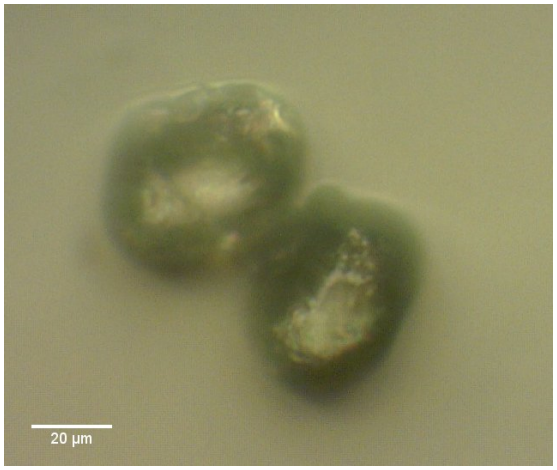

383°C, $x/a = 0.46$

391°C, $x/a = 0.75$

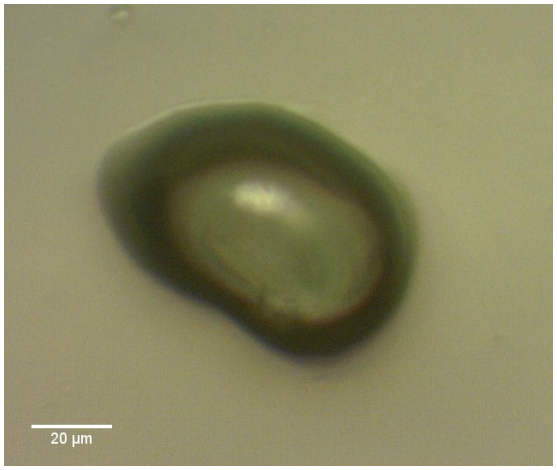

398°C, $x/a = 0.89$

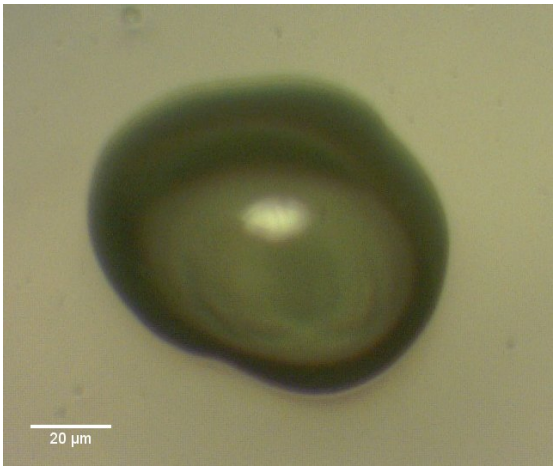

413°Cs, $x/a = 0.97$

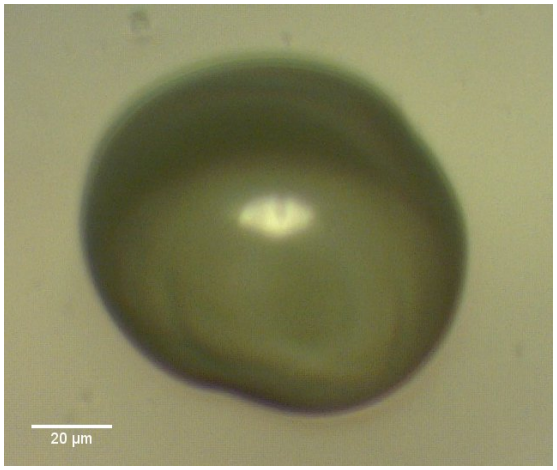

440°C, $x/a = 1$

Figure 5.8: Uniform coalescence at 100°C min^{-1}

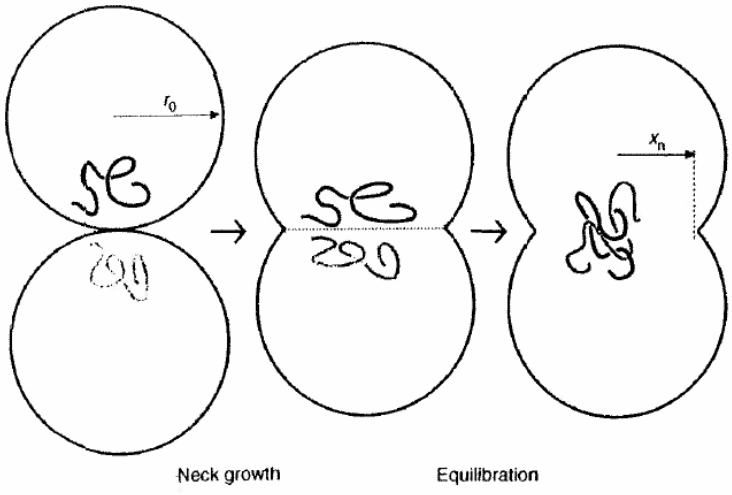

Figure 2.16: Stages of coalescence according to Mazur [130] (repeated from page 66)

particle pairs tested come from a range of different sizes, however the shape of the curves show that the melting behaviour is approximately the same regardless of initial size.

The dimensions for the particle and neck radii help to explain the x/a curve given in Figure 5.10b. Between 380°C and 385°C the neck grows rapidly even though the radius of the particles remains relatively constant. The effect of the initial shape change of the particles translates to a slow overall change in the coalescence ratio during this early stage.

Following this, the coalescence ratio increases quickly until it reaches 0.9, at which point it slows down dramatically. This is evident in the images of the coalescence in 5.8; the change in x/a between 383°C and 398°C is 0.43, but from 398°C to 413°C only increases by 0.08, and the final 0.03 takes a further 27°C to occur. The speed of sintering slows as coalescence nears completion because as the particle approaches the lowest surface energy state the surface tension effects are lower [139].

Looking at the coalescence ratio as a percentage of the total coalescence, it can be shown that 30% occurs between 370°C and 384°C, 60% of the total coalescence occurs between 385°C and 411°C, while the remaining 10% occurs between 411°C and 440°C. It was observed that equilibration occurs on average around 400°C and

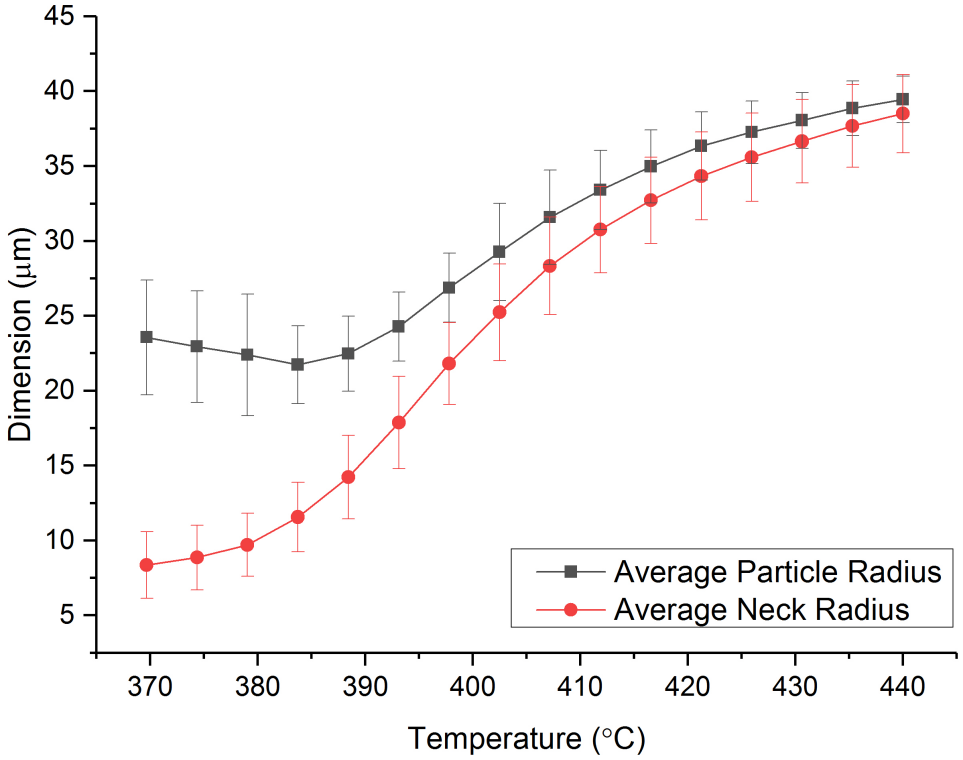

(a) Average particle radius and average neck radius

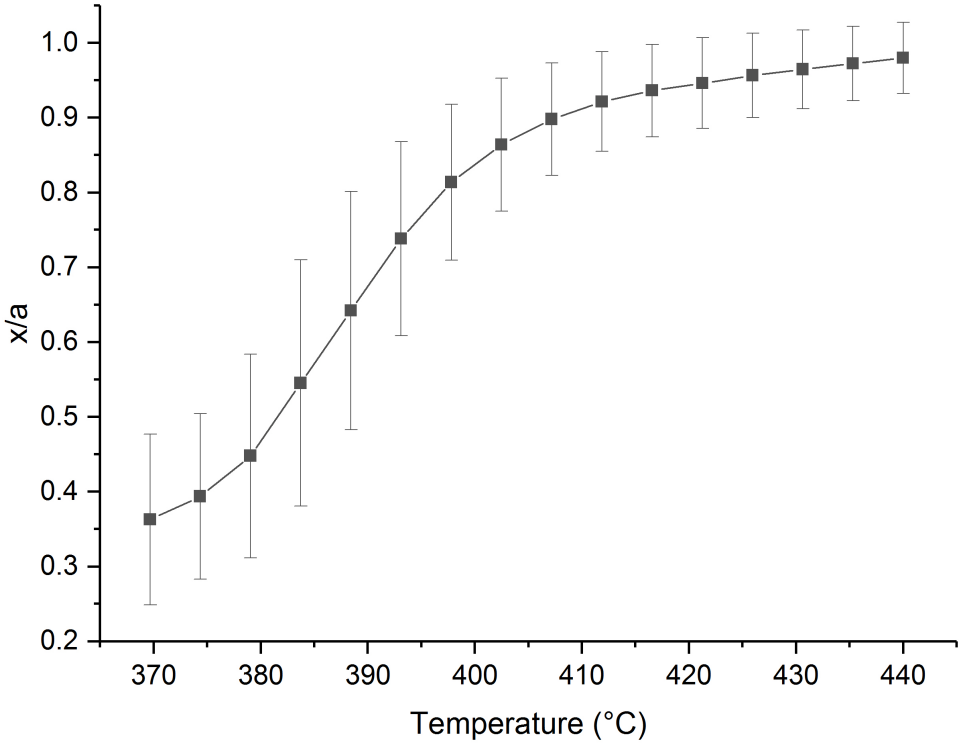

(b) Average coalescence ratio

Figure 5.10: Average values for dimensions and coalescence ratio for uniform results at 100°C min^{-1}

the coalescence after this temperature is dominated by the particle spreading into the final circular droplet. The thermal conductivity of PEEK has been shown to increase as the temperature is increased due to the mobility of the polymer chains, and the structure of PEEK results in efficient energy transfer along the polymer chains, particularly compared to polymers such as polypropylene and polystyrene [195]. Thus it makes sense that the rate of coalescence increases as the temperature is increased.

The variation in the average coalescence ratio results is very large during the early stages but much smaller at the higher temperatures. Despite the large variation, the curve is very smooth; the results themselves may be very different but the shape of each curve is more or less the same. This is of particular interest as the non-uniform results explained in the next section show significant deviation from the uniform curve.

5.5.2 Non-Uniform Results

Whilst every attempt was made to find suitable particles which were very similar, this was not always possible and would not be representative of the material being investigated. SEM of virgin powder in Section 4.2.1 showed that the powder is a mixture of round, oval and irregular shapes. Obviously it is not possible to filter all odd-shaped particles out of the powder when preparing a laser sintering build, therefore understanding how these particles coalesce is also important.

Very high magnification SEM of virgin powder (see Figure 4.2e in section 4.2.1) shows that some particles include small nodules connected by fibrous strands, and these findings have also been published by Wang et al [123]. Studies by Siegmann et al [145] and Truss et al [146] found that complex morphology on the surface of the powder was an important factor in the coalescence of crystalline polyethylene and UHMWPE, resulting in either faster coalescence than was anticipated or no coalescence at all; this was discussed earlier in Section 2.4.3.

Not all HP3 PEK particles show this surface morphology; nodules and fibrils were particularly evident in particles which were cracked or broken, and particles

which were whole had much smoother surfaces. The evidence presented in the literature would suggest that the particles with the morphology shown in Figure 4.2e melt quicker than the particles which are smooth. The slower melting of the smooth particles may be slowing down the overall process. The presence of nodules and fibrils can only be seen with high magnification SEM imaging therefore it will not be possible to identify how particular morphologies affect coalescence. However, it is be expected that different types of melting behaviour of particles will be observed and these are covered here. Of the 16 tests which were undertaken, six did not produce results which could be measured because the particles either drifted apart or coalesced with surrounding particles. Of those which could be measured, six were considered uniform and the remaining four were considered non-uniform.

In the four tests considered non-uniform the following phenomena were observed:

- Non-round powder particles
- Different size powder particles in the pair
- Particles drifting apart before necking later
- Particles showing unusual melting behaviour

These phenomena can be grouped according to whether the observed outcomes are a result of the effect of particle shape or effect of melting behaviour.

Effect of Particle Shape

Figure 5.11 shows the x/a curve for tests in which the initial particle pair were either different sizes or not completely round. The curves are compared with the average curve of x/a for uniform results calculated earlier; see Figure 5.10b. The graph shows that coalescence of non-uniform particle pairs is initially slower than for uniform particles.

Figure 5.12 shows the images of the coalescence process of powder particles which are not completely round at ambient temperature. As the temperature is

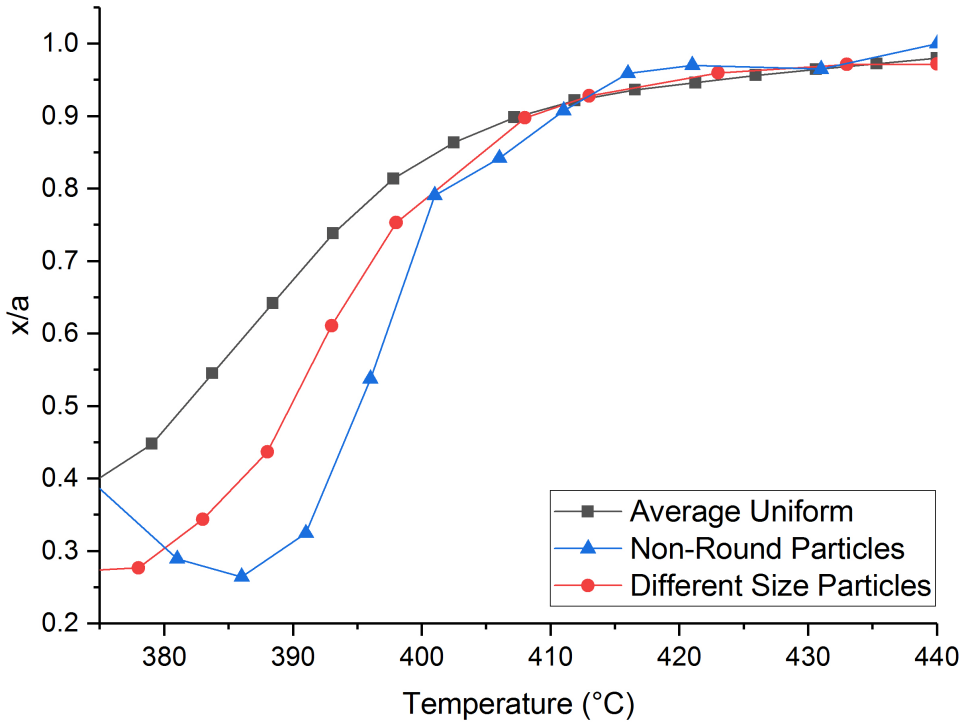

Figure 5.11: Comparison of average curve for uniform coalescence with non-uniform initial particle shapes, heated at 100°C min^{-1}

increased, the upper particle melts but does not become a spherical drop. As seen in the uniform results, initially the x/a curve shows slow coalescence as the particle radius decreases but the neck radius increases. In the case of this test however, the neck radius is not increasing as a result of the non-uniform melt of the upper particle; a more drastic shape change is required in order for the particle to become rounder than would be seen for a particle which was initially close to spherical. This translates to a drop in the coalescence ratio between the melting temperature and 386°C. Once the initial change in particle shape has occurred however, neck growth proceeds rapidly and the temperature at which full coalescence is achieved is much the same as that observed for uniform particles. The final particle mass has not retained any of the initial shape of the particles.

Similarly, the x/a curve for two different size particles shows that the early stage of coalescence is slower than for uniform particles. At ambient temperature one particle is much larger than the other. As the radii of the two particles are averaged before calculating the coalescence ratio this is not shown by the curve, however the

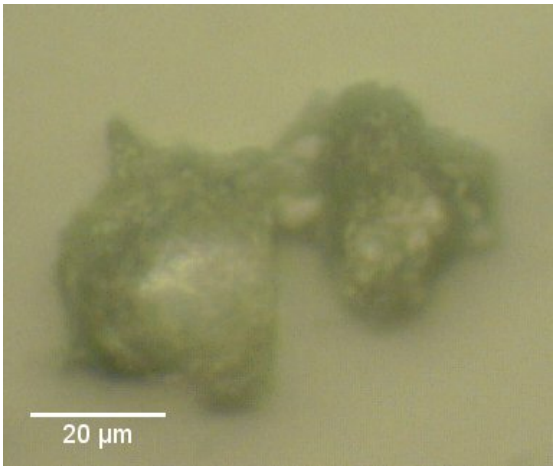

373°C, $x/a = 0.27$

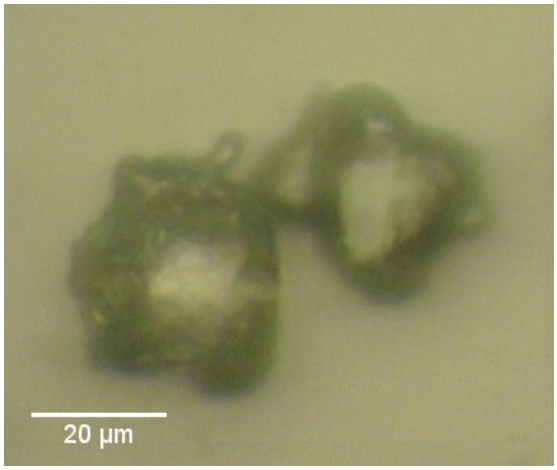

384°C, $x/a = 0.34$

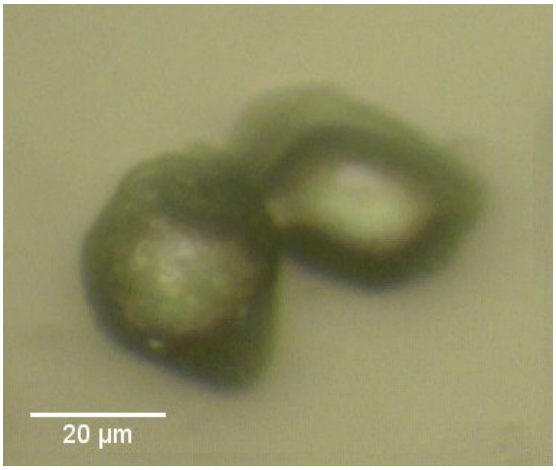

396°C, $x/a = 0.65$

401°C, $x/a = 0.79$

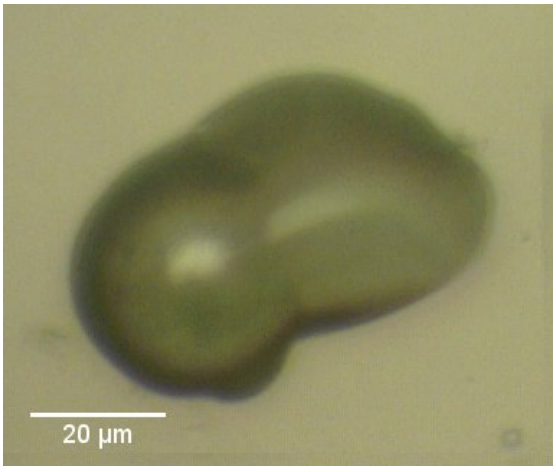

409°Cs, $x/a = 0.90$

440°C, $x/a = 0.97$

Figure 5.12: Coalescence of non-round particles at 100°C min^{-1}

neck radius remains small in the early stages because the possible contact area between the two particles is restricted by the size of the smaller particle. The larger particle spreads quicker than the smaller as a result of the greater effect of gravity and encapsulates the smaller, leading to neck growth. Once equilibration has occurred only one particle remains and surface tension effects are the same as for uniform coalescence, thus complete coalescence still occurs.

In both cases, the condition of the particle pair affects the onset of coalescence but not the final shape of the merged particles or the amount of neck growth which occurs.

Effect of Particle Melting Behaviour

The x/a curves for tests which were considered non-uniform as result of the effect of particle melting behaviour are shown in Figure 5.13. These include particles which exhibited unusual melting behaviour compared with other tests and particles which drifted apart but formed a neck and coalesced later in the test. Images of the tests are shown in Figures 5.14 and 5.15. The particles which showed different melting behaviour produce an x/a curve very similar to the uniform powder, whilst the particles which drift apart and neck later also achieve full coalescence, albeit much later than for other particle pairs.

Figure 5.14 shows two particles which appear to show different melting behaviour compared with other tests. At 388°C the there does not appear to be a neck forming between the particles; rather they are both melting separately without apparently being in contact with each other. This was difficult to capture in the x/a curve; the measuring method meant that a neck radius could still be measured, even though the images do not appear to show the particles forming a true neck. However, at 403°C a neck has formed between the two particles and the curve shows that overall, the coalescence is not affected by the apparently unusual melting behaviour early on. The position of the neck at 403°C shows that the bottom particle has melted and spread faster than the upper particle, however as the particle radii are averaged before calculation of the x/a value this does not

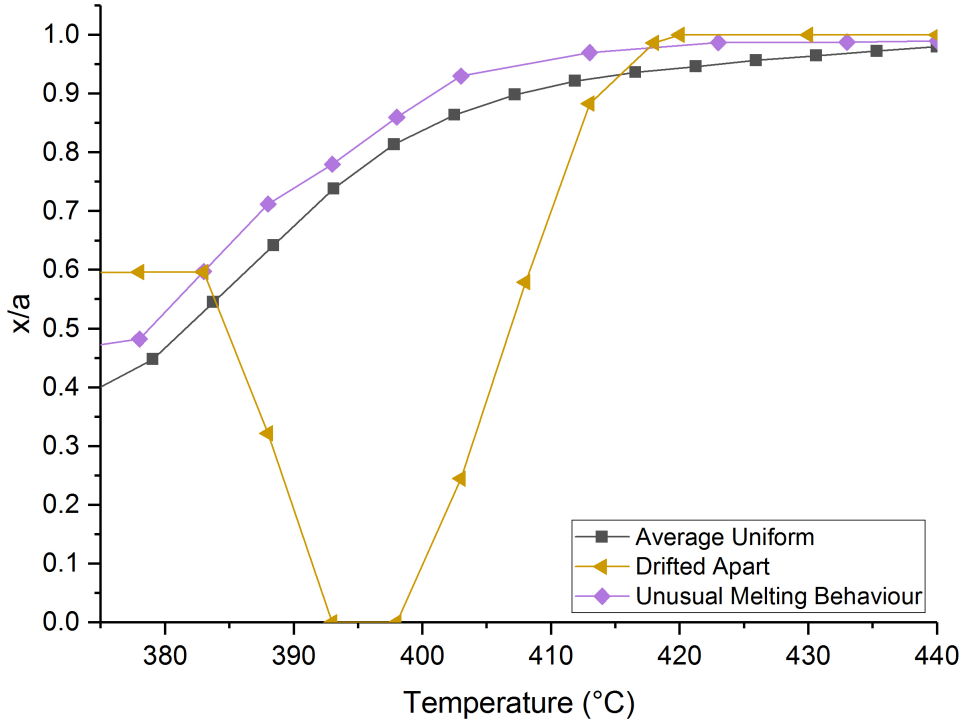

Figure 5.13: Comparison of average curve for uniform coalescence with non-uniform melt behaviour, heated at 100°C min^{-1}

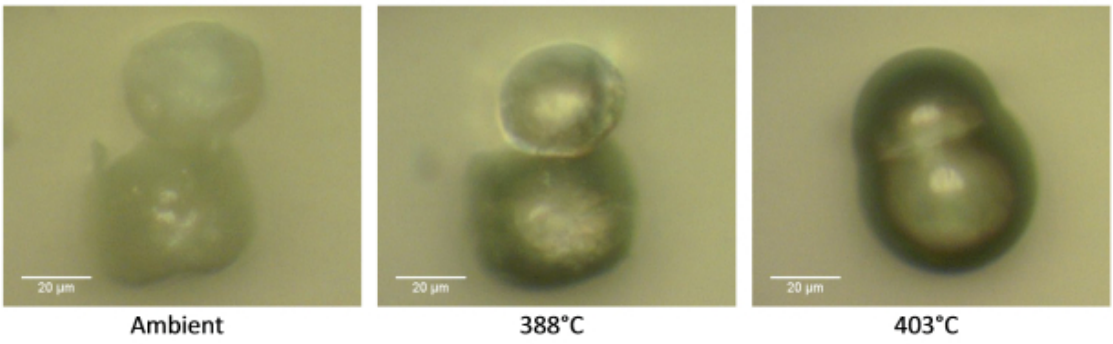

Figure 5.14: Particles show different melting behaviour as temperature is increased

impact on the shape of the curve. The x/a curve is almost identical to the uniform curve; in this respect it can be said that the unusual melting behaviour seen here does not result in non-uniform coalescence. This behaviour was observed in three of the experiments.

In Figure 5.15, the melting behaviour results in the particles drifting apart. At ambient temperature, the particles are very similar, although the bottom is a little darker in colour than the top particle. At 383°C, both particles are showing signs of melting but are no longer in contact. As the particle become rounder, the gap between them increases. However, as the particles melt and spread, a neck forms around 403°C and coalescence occurs quickly, resulting in $x/a = 1$ being achieved by 420°C.

In spite of the merging of the two particles beginning very late, the temperature at which $x/a = 1$ is achieved is very similar to those particles showing unusual melting behaviour, at 420°C and 423°C respectively. This is slightly quicker than the average curve for uniform particles, where $x/a = 0.98$ is reached at 433°C. In Figure 5.11, the non-round and different size particle pairs show very similar x/a values to the average uniform curve from approximately 410°C. So the overall pattern for the tests considered non-uniform is that the particle shape and size and the melting behaviour do not impact on the final coalescence attained; in all these results the temperature appears to be a far more significant factor in when complete coalescence occurs. Therefore, while the non-uniform coalescence behaviour observed produces x/a curves which will not compare well with theoretical sintering model curves, during the LS process the behaviour is unlikely to adversely affect the parts produced.

5.5.3 Effect of Adhesion

Bellehumeur reported for polyethylene powders that whilst adhesion effects were not significant for large particles, adhesion could affect the coalescence of smaller (diameter <174µm) particles [134]. As over 75% of HP3 PEK powder particles are within the range of diameter 16-63µm [12], tests were performed on slides

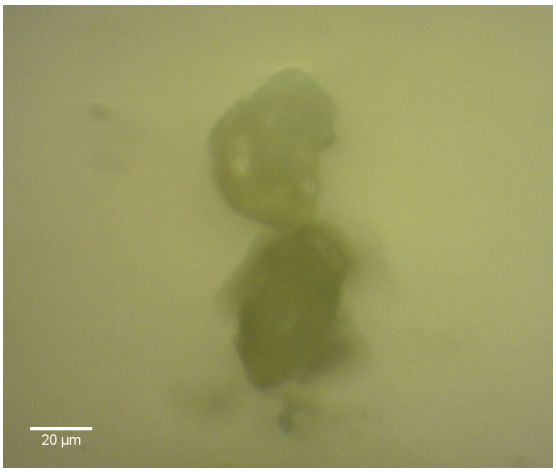

Ambient, $x/a = 0.38$

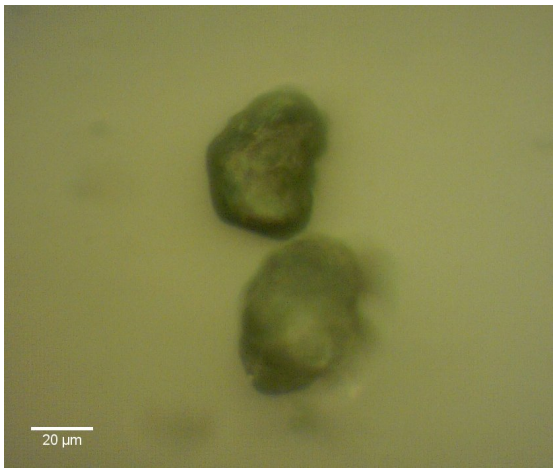

383°C, $x/a = 0$

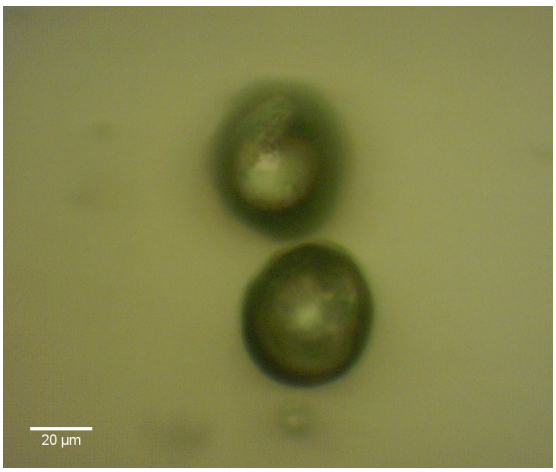

393°C, $x/a = 0$

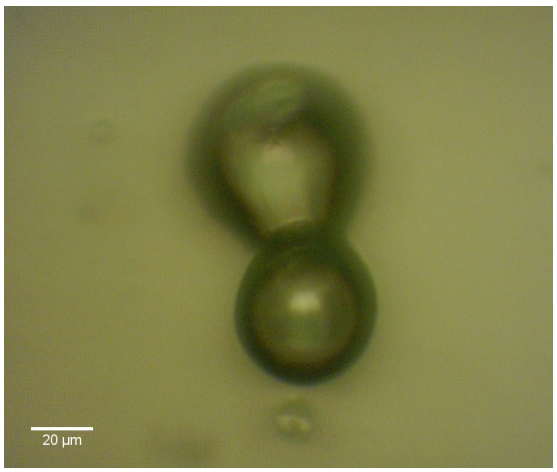

403°C, $x/a = 0.58$

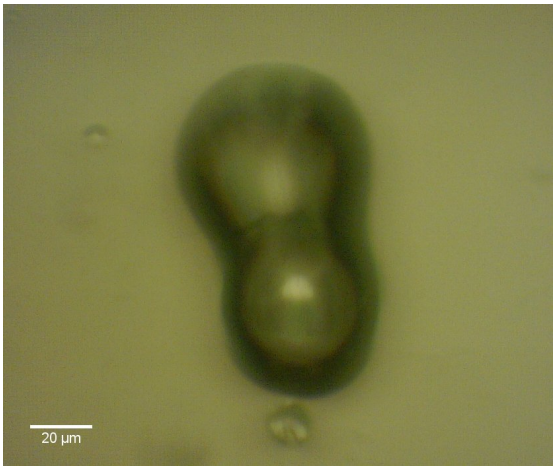

408°Cs, $x/a = 0.88$

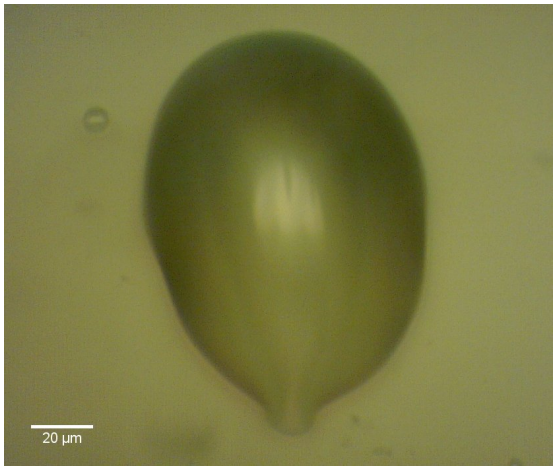

420°C, $x/a = 1$

Figure 5.15: Particles drift apart before coalescing, heated at 100°C min^{-1}

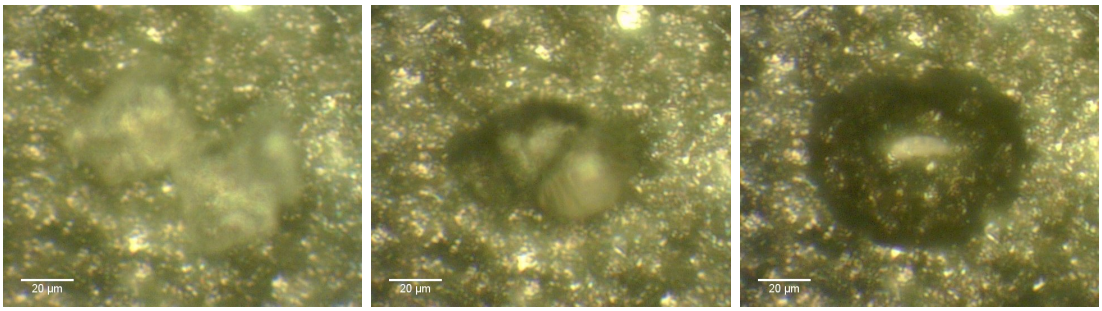

Test 5: 375°C, $x/a = 0.46$ Test 5: 390°C, $x/a = 0.93$ Test 5: 440°C, $x/a = 0.99$

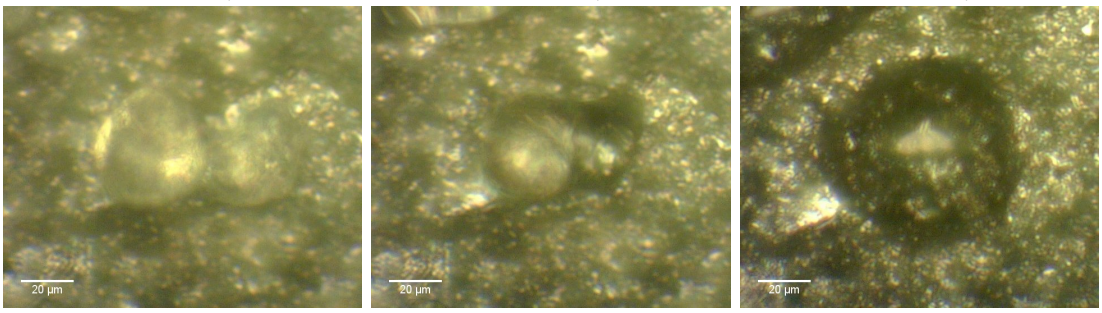

Test 8: 375°C, $x/a = 0.52$ Test 8: 390°C, $x/a = 0.76$ Test 8: 440°C, $x/a = 1$

Figure 5.16: Coalescence of tests 5 and 8 on non-stick coated slides, heated at 100°C min^{-1}

coated with a lubricant in order to investigate whether adhesion was a factor in coalescence. Whilst the use of a lubricant coating on the glass slides was not found to cause a significant difference in the overall speed of coalescence, some changes in the shape of the coalescence curve were observed.

The slides were coated with a carbon-based dry lubricant, which was the only one which could be sourced suitable for the high temperatures required to melt the powder. The coating made the particles quite difficult to see, particularly during the early stages of melting when the slide and the particles were a very similar colour; a selection of images are shown in Figure 5.16. This may affect the accuracy of the results as the measurements were taken from the images manually, and ensuring accurate measurements when the visibility of the particles was poor was challenging. However, many of the results were considered comparable with those from tests without the non-stick coating so are considered usable.

Ten tests were undertaken. Two could not be measured due to particles drifting apart or coalescing with surrounding particles. Of the eight results which could be measured, three showed uniform coalescence as described in Section 5.5, and

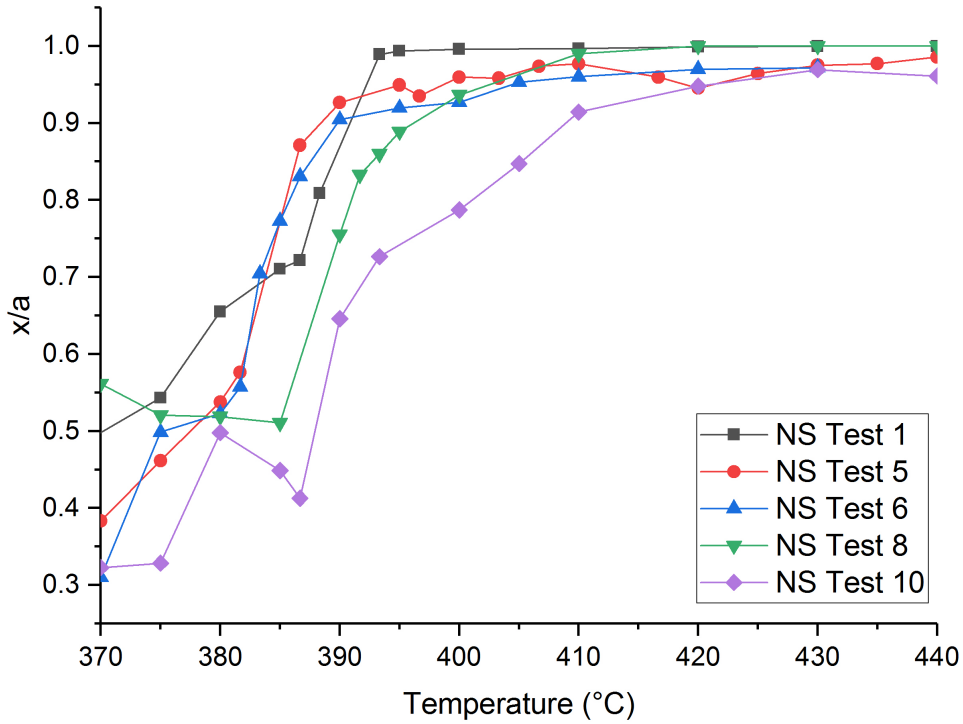

Figure 5.17: Coalescence curves for tests achieving $x/a > 0.95$ on non-stick (NS) coated slides, heated at 100°C min^{-1}

the other five tests showed non-uniform melting behaviour. The final x/a values varied between 0.84 and 1. Five of the tests reached $x/a > 0.95$; these included both uniform and non-uniform coalescence behaviour.

The five results which reached $x/a > 0.95$ are shown in Figure 5.17; both uniform and non-uniform melting behaviour are plotted together to show the variation in results. In the two non-uniform tests displayed, the x/a value drops in the early stages before going on to complete coalescence. This is reminiscent of the curve for non-round particles shown in Section 5.5.2. However, the drop in the coalescence ratio seen here is not related to the particle shape, which is very close to spherical for all tests. Rather, the particles move on the slide once they begin melting. The non-stick coating provides the particles with significant freedom of movement compared with the tests undertaken on the uncoated glass slide. A small neck is sufficient to stop the particles from drifting apart and the connected particles travel together as the initial shape change occurs. As the particle neck increases, less movement is observed. All of the non-uniform results displayed this

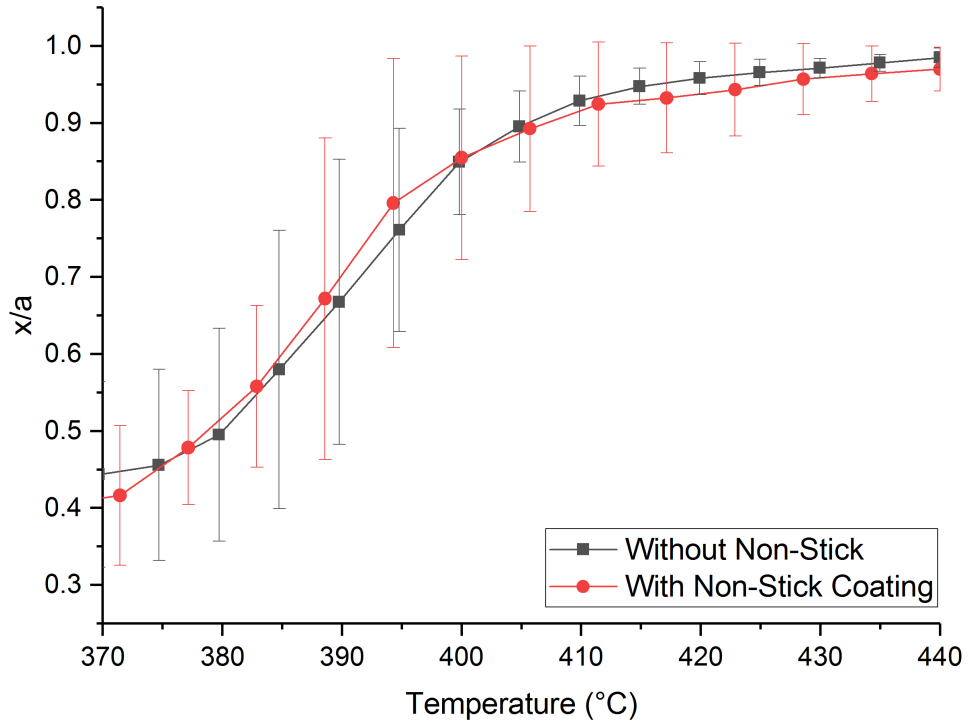

Figure 5.18: Average coalescence curves for tests achieving $x/a > 0.9$ both with and without non-stick coating on slides, heated at 100°C min^{-1}

behaviour.

To see how the non-stick results compare with those without non-stick coating, average curves were plotted. Instead of separating the results of uniform and non-uniform coalescence, an average was taken for all tests which achieved $x/a > 0.9$; the one exception to this was the result shown in Figure 5.15 as x/a drops to zero and this was the only test in which this occurred. Thus, eight tests were averaged from those without non-stick coating, and seven tests from those with non-stick coating. The results are shown in Figure 5.18. The standard deviation is plotted to show the variation across all the tests included.

The results are surprising; the average curves both with and without non-stick coating are very similar. It was anticipated that the inclusion of non-uniform coalescence curves would significantly change the shape of the curve compared with the average uniform curve seen in Figure 5.10 in Section 5.5.1, however this is not the case.

In the tests without non-stick coating, there is greater variation in the starting

x/a values than for those with non-stick; i.e. there are tests included where the contact area between the two particles before the test begins is higher than in the non-stick tests. It is therefore interesting to note that even though the starting conditions for the particles on non-stick coating are very similar for all tests, the coalescence behaviour observed differs significantly between tests compared to those without non-stick coating, where starting conditions vary more.

Around 390°C, the variation both with and without non-stick is quite similar. As the temperature increases, the variation seen in the results without non-stick coating gets smaller, while it remains very high for the results with non-stick; that is, the temperature at which full coalescence is achieved varies far more for the non-stick tests than those without non-stick. However, whilst the variation in the results from the non-stick tests shows that adhesion does affect coalescence behaviour, the similarity between the average curves both with and without non-stick coating show that the rate of coalescence and the temperature at which full coalescence is achieved are on balance, not affected by adhesion effects.

5.6 Used Powder

A small investigation was undertaken into coalescence of used powder. The DSC curves shown in Section 4.3.1.3 show that melting is occurring in used powder, as evidenced by the presence of a melting endotherm, however observation of the surface of the samples in the pan following heating/cooling show distinct particles are still present. Figure 5.19 shows DSC pans for virgin and sieved mixed used powder following 10 cycles of heating to 400°C and cooling to 30°C under a nitrogen atmosphere; the virgin powder shows a smooth surface consistent with total coalescence, but in the used sample the individual particles are still visible.

Used powder is not recommended for reuse in the EOS P800 but at the time of writing, only a small amount of research has been undertaken into the properties of used powder which make it unsuitable for reuse; a study by Ghita et al [12] showed that used powder does not coalesce fully even when heated to 440°C at 100°C min^{-1}, which they attributed to crosslinking due to the amount of time spent at

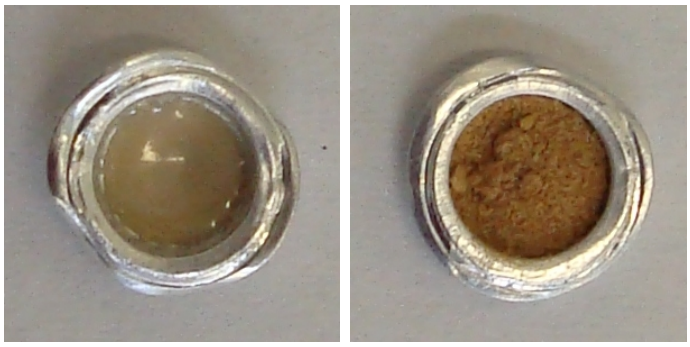

(a) Virgin powder (b) Mixed used powder

Figure 5.19: Images of DSC pans following 10x heating/cooling cycles

high temperature in the build chamber during the HT-LS process.

In Section 5.3 it was suggested that degradation is the primary cause of the lack of coalescence seen in virgin powder at low heating rates. It was observed in Section 4.3.1.3 that the location the powder has been taken from affects its thermal properties, with powder from the corner showing very different properties to powder taken from the centre and it has been suggested that differing amounts of degradation is occurring in these locations. Therefore, it would be interesting to see if the coalescence behaviour of the material from different locations within the build chamber is also different; it is expected that the results will show how differing amounts of degradation affect melting and coalescence behaviour.

The coalescence tests on used powder from various locations were undertaken using the Bruker microscope which was not equipped with a time-lapse image feature, making it difficult to capture the results at high heating rates. Therefore two test regimes were used on the powder. The first used a heating rate of 10°C min^{-1} so that images could be taken through the duration of the test. The second used a heating rate of 100°C min^{-1} but the powder was only photographed at ambient temperature and at 440°C the end of the test, so the overall change could be seen.

5.6.1 10°C min^{-1} Heating Rate

Images of the results for the corner, mid and centre locations are shown in Figure 5.20. The x/a value was calculated for each location as described in Section 5.2 and the results are plotted against temperature in Figure 5.21. The plot for virgin powder heated at 10°C min^{-1} is given for comparison.

The powder from the corner location shows some melting at 390°C and further melting with some neck growth at 440°C. The final x/a value for this location is 0.57, an increase of 0.17 from the initial value at ambient temperature. The curve shows early in the test the coalescence ratio decreases; this is consistent with results from virgin powder for non spherical particles which show a tendency to change shape when they initially melt in order to minimise surface energy, before coalescing later. The final coalescence ratio is significantly lower than virgin particles at the same heating rate, in spite of having a much larger contact ratio initially. As the DSC curve for the corner used powder shows it has a similar melting and recrystallisation temperature to virgin, it would be expected that the coalescence results would be similar.

In comparison with the results for mid and centre used powder however, the coalescence observed in the corner particles is significant. Both mid and centre used powder show an overall decrease in coalescence ratio from ambient temperature to 440°C; this was not seen in any of the tests on virgin powder.

The two particles in the mid powder test are a similar shape and size, but appear to be slightly different colours at ambient temperature. This becomes more apparent at 390°C, where the top particle is darker and shows some melting while the lower particle has not changed at all; the measured dimensions of the particle show an insignificant change between the two temperatures. At 440°C, the top particle is rounder compared to ambient temperature and shows some shrinkage, while the lower particle shows a smaller change by comparison but still some difference from ambient temperature. The final x/a value is 0.47, an overall decrease of 0.03 from the initial value. The curve shows that this is not a steady decline, but that the coalescence ratio drops as low as 0.42 before increasing later

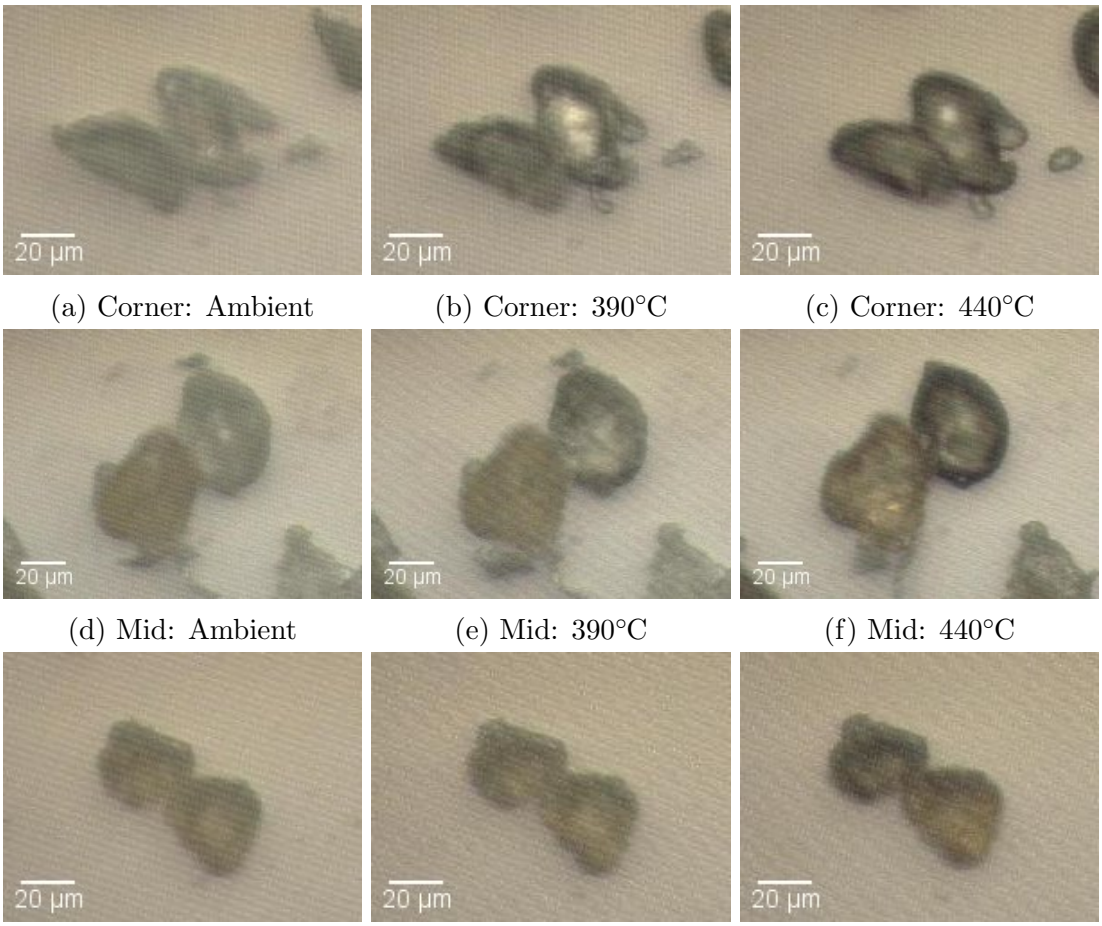

(a) Corner: Ambient (b) Corner: 390°C (c) Corner: 440°C

(d) Mid: Ambient (e) Mid: 390°C (f) Mid: 440°C

(g) Centre: Ambient (h) Centre: 390°C (i) Centre: 440°C

Figure 5.20: Images of used powder by location heated at 10°C min^{-1}

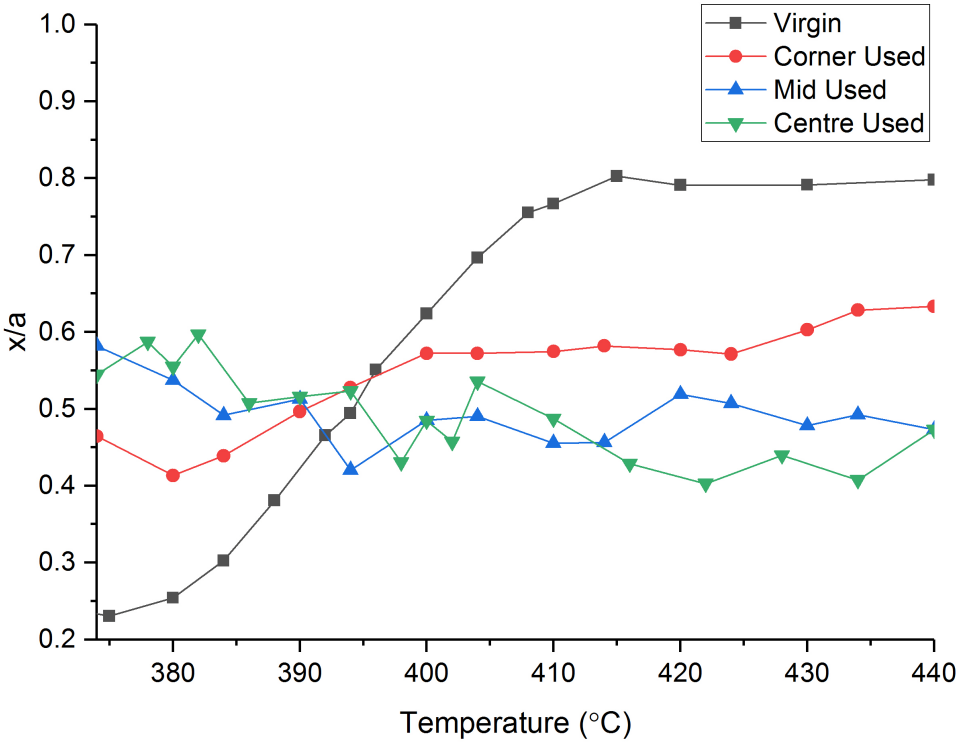

Figure 5.21: Coalescence ratio against temperature for used powder from different locations compared with virgin, heated at 10°C min^{-1}

on. It can be concluded that particle shrinkage has occurred but neck growth has not.

A similar result is observed in the centre used particles; these particles also show some visible shrinkage, however little coalescence. The curve of the coalescence ratio is quite erratic; this can be explained by slight movement of the particles during the test. As the particles shrink between 390 and 430°C they both drift across the slide whilst retaining a small contact between them; the top particle also shrinks towards an oval rather than round shape which is not quantified by the measuring technique which assumes the particles remain circular. The final x/a value is 0.08 lower than at ambient temperature and it is evident from the images that the only change which has occurred is in the shape of the particles.

The progression of coalescence of sieved mixed powder is shown in 5.22. Whereas the results from single locations around the chamber have shown the particles to behave similarly, the behaviour of the two particles of mixed used powder show differences. At ambient temperature one particle is lighter in colour

than the other but otherwise the particles look similar. Both show some change at 380°C, however at 388°C the lower of the two particles appears to have changed shape more than the top particle. Over the next several degrees, the bottom particle melts, spreads and appears to coalesce around the top particle, although the other particle does also appear to be changing shape. At 400°C there is very little of the top particle still visible, and by 430°C only one shape remains.

It is unclear from these images if the top particle has coalesced with the lower, or if the upper has only partially melted and been totally encapsulated by the lower. However, this is the most significant overall coalescence observed from all of the used powder tests and the only instance from all tests undertaken on both virgin and used powder where total coalescence has been observed at 10°C min^{-1}. This may be in part because the initial coalescence ratio is measured to be 0.76, which is far higher than all other tests undertaken. The unusual shape of the coalescence made measuring the dimensions of the particles challenging, however total coalescence appears to occur at approximately 410°C.

It was expected from the sieved mixed powder that there would be a variety of particles which coalesced in different ways as the sample is made up of powder from all locations. A second sample of sieved mixed powder is shown in Figure 5.23. The melting behaviour of the two particles is once again different and far less coalescence occurs in this sample than in the first. The shrinkage in the bottom particle is particularly high - 23% from ambient temperature to 440°C - during coalescence of both particles this might otherwise have been missed as equilibration evens out the radii of the two particles. Here there is still a distinct neck between the two particles which makes the shrinkage more evident.

It clear from the 10°C min^{-1} tests that there is significant variance in the properties of used powder particles and potentially also melting behaviour which has not been observed in virgin powder. However, it was outside the scope of this small investigation to study this behaviour in more detail.

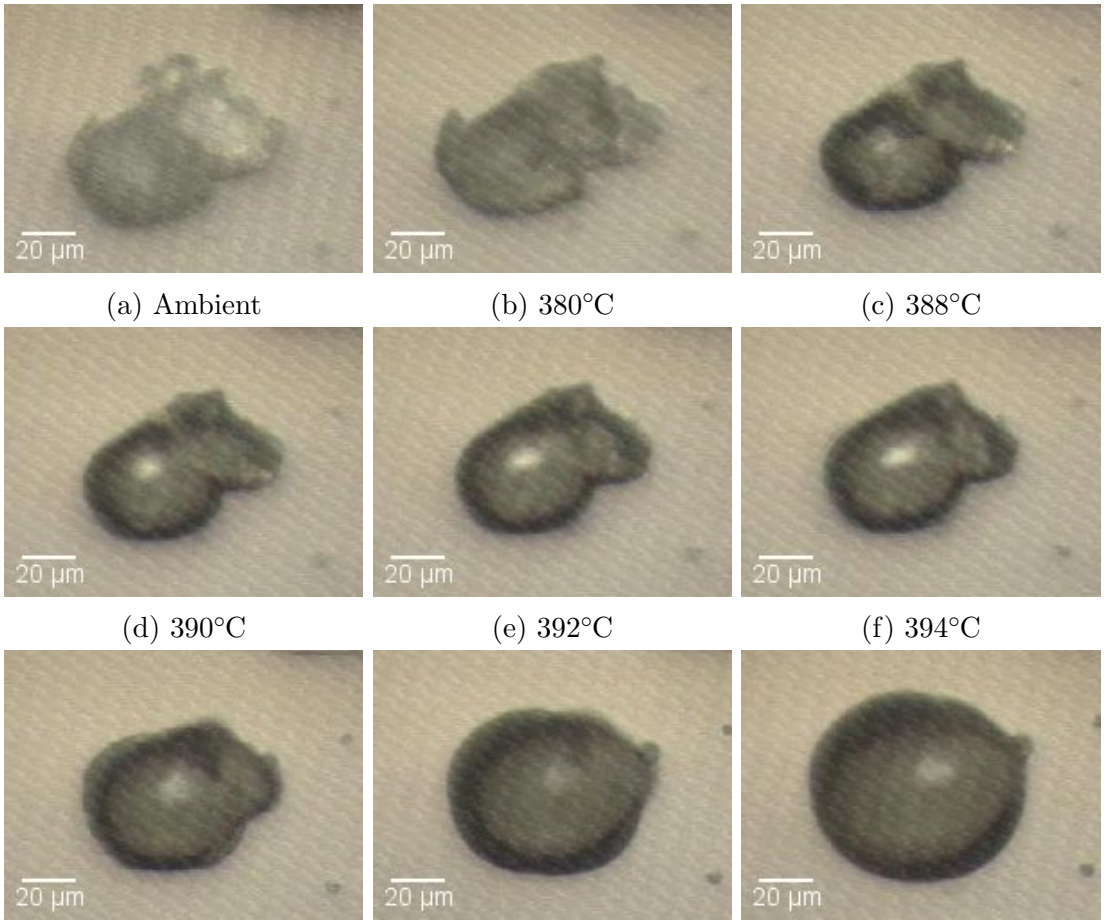

(a) Ambient (b) 380°C (c) 388°C

(d) 390°C (e) 392°C (f) 394°C

(g) 400°C (h) 410°C (i) 430°C

Figure 5.22: Progression of coalescence of sieved mixed used powder heated at 10°C min^{-1}

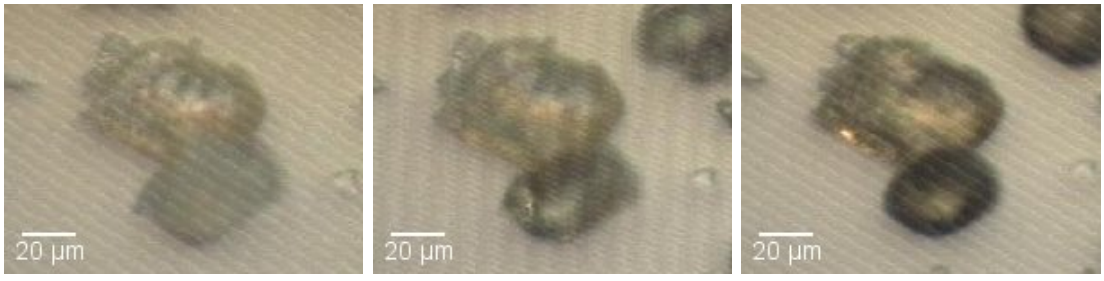

(a) Ambient (b) 398°C (c) 440°C

Figure 5.23: Another sieved mixed powder sample heated at 10°C min^{-1}

5.6.2 100°C min^{-1} Heating Rate

The results from the tests at a heating rate of 100°C min^{-1}, shown in Figure 5.24, show a similar trend to those from the 10°C min^{-1} tests, however more coalescence is observed in the corner and mid used tests. The results for the corner powder show total coalescence has occurred by 440°C, going from an initial x/a value of 0.43 to a final value of 0.98, a change of 0.54. It was suggested that the powder from the corner location should behave similarly to virgin as the DSC trace shows similar thermal properties; when heated at 100°C min^{-1} this behaviour is observed.

The mid test shows some coalescence occurring; the change in x/a is 0.16, with a final value of $x/a = 0.76$. More melting of the particles can be seen than in the 10°C min^{-1} tests; the other particles in the image show similar levels of shrinkage from ambient temperature to the end of the test. By contrast the particles from the centre test again show no coalescence, with the final coalescence ratio down on the value from ambient temperature by 0.05. Some spreading of the lower particle can be seen but very little shape change has occurred. Therefore it seems that the chemical changes which have occurred in the centre used powder result in it being unable to coalesce regardless of the heating rate.

Rather than observing two particles of sieved mixed used powder, a small line of four particles were found which all appear different at ambient temperature; it was thought that these would produce an interesting results. The images are shown in Figure 5.25. An image taken at approximately 400°C shows some of the particles have melted and are coalescing around other particles which are more distinct; these particles remain distinct at 440°C but one has been almost entirely swallowed by the rest of the melt. Whereas at 10°C min^{-1} it was not clear whether one of the particles had melted or been encapsulated in the melt, it is clear from the images from the 100°C min^{-1} test that some particles have not melted.

A similar phenomenon was noted by Ghita et al [12] during the coalescence of virgin and used particles; the virgin particles melt and encapsulate the used particles which remain solid even at high temperature. They proposed a coalescence mechanism whereby crosslinked chains in the used powder have the potential to

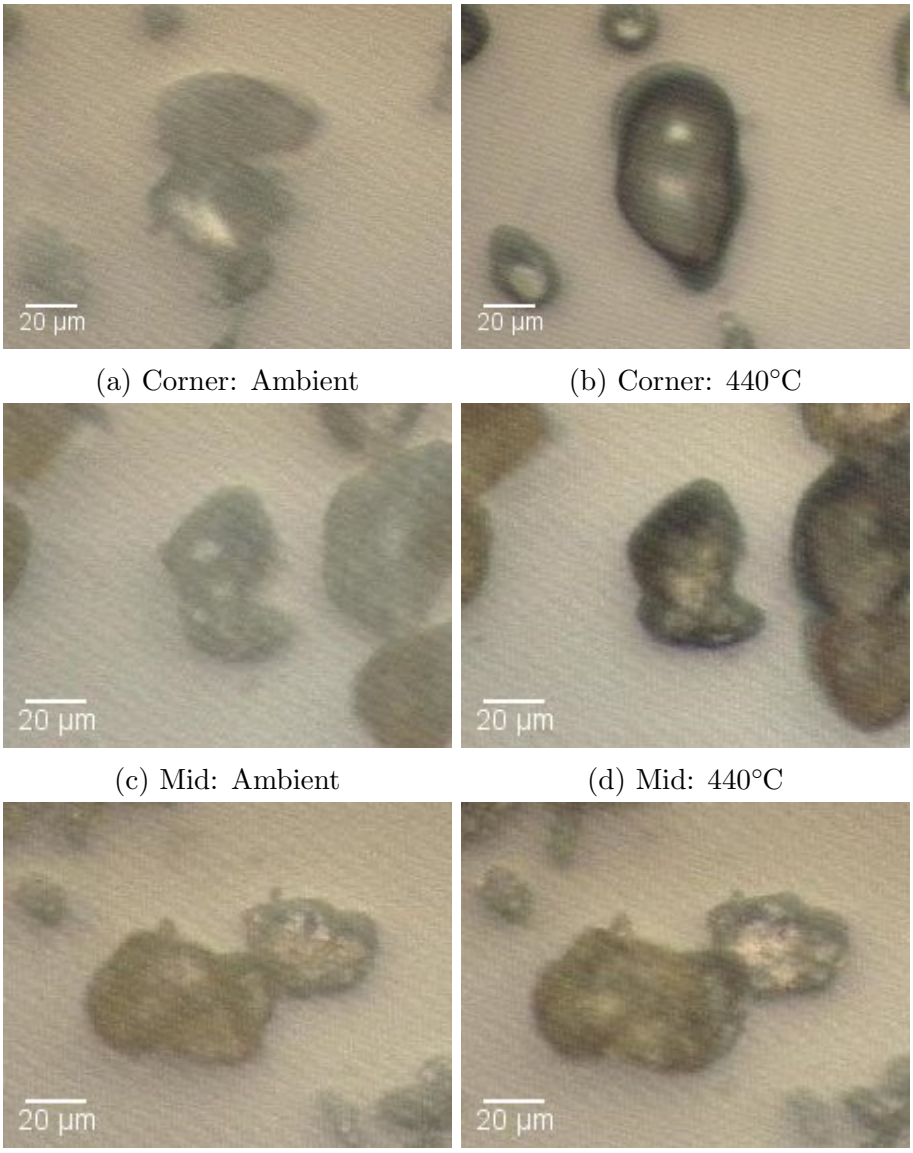

(a) Corner: Ambient (b) Corner: 440°C

(c) Mid: Ambient (d) Mid: 440°C

(e) Centre: Ambient (f) Centre: 440°C

Figure 5.24: Images of used powder by location heated at 100°C min^{-1}

(a) Ambient (b) ≈ 400°C (c) 440°C

Figure 5.25: Sieved used powder heated at 100°C min^{-1}

obstruct neck growth resulting in low overall coalescence, however depending on the location of the chains in the particle coalescence is still possible. In this way, particles which look the same at ambient temperature may behave differently when heated. Considering the properties of the corner used powder and very similar to virgin at 100°C min^{-1}, the sieved mixed powder behaves in a similar way to the virgin and used particles. Therefore this theory could explain why some sieved used particles show coalescence but others do not.

5.6.3 Remarks on Coalescence of Used Powder

Overall, the results from the tests on used powder at both 10°C min^{-1} and 100°C min^{-1} show the same trend; whilst the properties of some particles are not significantly affected during the build process and show coalescence behaviour, others have undergone irreversible chemical change and show little reaction when heated. Sieved powder is a combination of particles from all around the build chamber, therefore some particles melt while some are heavily degraded and remain intact during heating. As HT-LS involves very high heating rates, the results from 100°C min^{-1} are likely to be more indicative of what is occurring during the build process than 10°C min^{-1}. It should be pointed out that the process of measuring the particles contains several sources for inaccuracy; as the particles are measured by eye the values are subjective, the images from the Bruker camera are low resolution and the focus of the microscope had a tendency to drift at high temperature requiring regular readjustment. As a result the x/a values are by no

means absolute and the small change observed in the mid and centre results could be attributed to user error. In this regard the quantitative analysis of the particles is as valuable as the qualitative.

The results which have been collected during this small investigation are too few to conclusively prove that the location the powder is taken from is the primary factor in whether or not it will subsequently melt and coalesce when heated again. However, as a preliminary study the results appear to show this, and further investigation into the properties of particles from specific locations could be useful for identifying how more of the powder can be reused without impacting on the properties of the final parts. Furthermore, it has been proposed that chemical changes in the particles can result in particles with a similar thermal history behaving differently under application of heat; further investigation could identify the different mechanisms which are occurring which would inform decisions about how to reuse powder.

One question which is raised by the properties of powder from different locations is what is occurring in these locations which results in such different outcomes. The final chapter of this thesis concerns the temperatures at the centre and corner locations of the build chamber and it is expected the results will explain some of the behaviour seen here.

5.7 Coalescence Modelling

The idea of modelling coalescence has been introduced in Section 2.4 in the Literature Review. Modelling of coalescence is useful for understanding material behaviour. Its purpose is to predict how a material will behave under application of heat. Applied to LS sintering, theoretical models could provide an initial idea of what coalescence behaviour will look like and a tool for explaining behaviour in terms of the physico-chemical mechanisms which are occurring.

The models which were selected for prediction of coalescence behaviour were Frenkel, Frenkel/Eshelby, Hopper. Frenkel and Frenkel/Eshelby were chosen because they remain the starting point for almost all coalescence modelling,

and experimental coalescence was quantified using Frenkel's equation as a guide. Hopper's model was used because it predicts the whole coalescence, taking into account the changing shape of the two particles as they merge together and has been shown to be a better fit experimentally than Frenkel and Frenkel/Eshelby [131]. Whilst other models also fit this description, Hopper was chosen because the maths is relatively straightforward.

5.7.1 Measurements Required for Models

All of the models listed above express coalescence as a function of the dimensional changes occurring in the particles and the neck, and the surface tension and viscosity of the material. The models were developed for isothermal coalescence and are therefore related to the time required for sintering to take place.

Values for the particle radius and neck radius have been measured from images as described in Section 5.2. The average particle dimensions and average curve for uniform coalescence as shown in Figure 5.10 were used to compare with the models.

Incorporating Dynamic Coalescence into Models

Traditionally coalescence models have been applied to isothermal coalescence, that is, holding the material at the same temperature and measuring the time elapsed for coalescence to occur. However, tests undertaken on HP3 PEK showed that coalescence does not occur isothermally; see Section 5.4. Whilst some coalescence does occur when held at the same temperature for a given period, this is only the case where some coalescence has already occurred before this temperature is reached, and full coalescence was not observed during isothermal tests. Tests which were undertaken with a dynamic heating rate showed that full coalescence occurs within a temperature range as long as it is heated quick enough. Thus the coalescence rate was experimentally determined from tests with a heating rate of 100°C min^{-1}.

Furthermore, it has been discussed that heating during laser sintering is dynamic, with a heating rate estimated to be 22,000°C min^{-1} applied to powder

which is already quite close to melting temperature. Therefore it seemed sensible to apply the models to dynamic heating rather than isothermal. 373°C was chosen as time t = 0 as this is the peak melting temperature of the material. The results were displayed as a function of time by calculating the elapsed time between each temperature measurement; as the heating rate was 100°C min^{-1}, this equated to approximately 1.67°C sec^{-1}. For clarity, both time and temperature are plotted on the graphs later in this section.

Viscosity and surface tension are temperature dependant properties; the viscosity and surface tension of polymers decrease as the temperature is increased [11, 193]. Therefore a range of values for viscosity and surface tension at the temperatures during the test are desirable. As these values for HP3 PEK are not yet available due to the material being relatively new, it was necessary to determine them experimentally.

5.7.1.1 Viscosity

Viscosity was measured using a capillary rheometer. Tests were undertaken at 390, 395 and 400°C. Below 390°C the material would not melt sufficiently to be forced through the die, and 400°C was the physical limit of the equipment. The average values for 390, 395 and 400°C were 218, 202 and 194 Pa.s respectively. The datasheet for Victrex PEK powder HT P22 gives a melt viscosity of 200 Pa.s at 400°C so the experimental values were assumed to be accurate [177]. The relationship between viscosity and temperature is described by the Arrhenius equation and this was used to find the rest of the values required:

$$\mu = \mu_0 e^{E_a/RT} \tag{3.3}$$

Where μ is viscosity, μ_0 is viscosity at a reference temperature, E_a is activation energy, R is the Universal Gas Constant and T is temperature.

Equation 3.3 can be rearranged to give the following expression:

$$\ln(\mu) = \frac{E_a}{R}\left(\frac{1}{T}\right) + \ln(\mu_0) \tag{3.4}$$

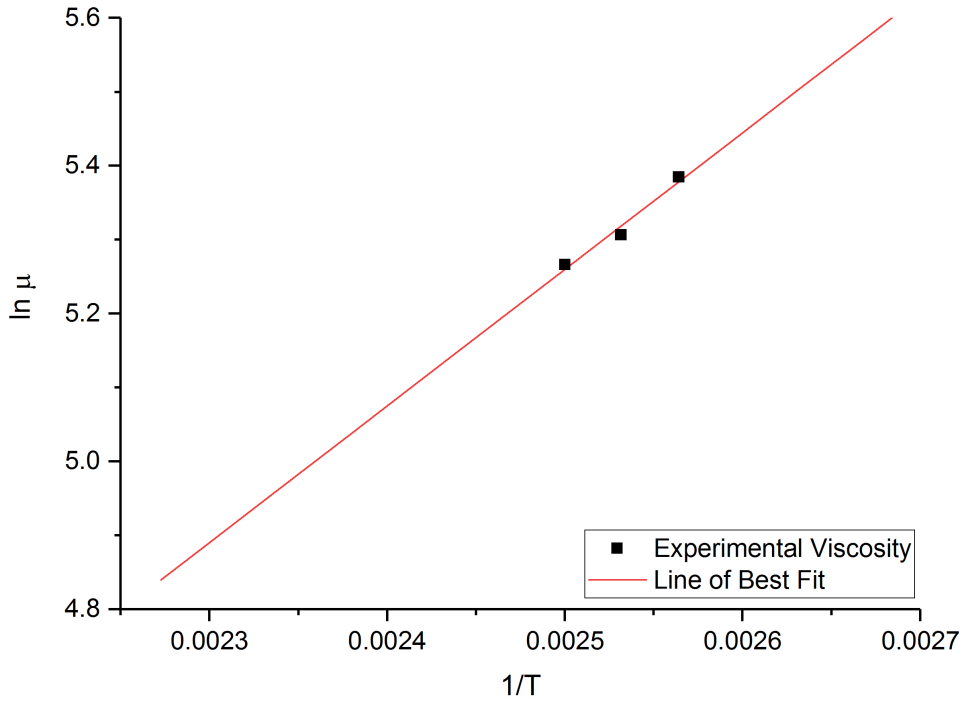

Figure 5.26: Arrhenius plot calculated from experimentally determined viscosity values

In this form, the Arrhenius expression describes the equation of a straight line in the form $y = ax + b$ where, $\ln(\mu)$ and $1/T$ are known values, calculated from experimental data, E_a/R is the slope of the line, and $\ln(\mu_0)$ is the intercept.

The calculated values of $\ln(\mu)$ were plotted against their respective $1/T$ values. A line of best fit was drawn between the three points, and the equation of the line of best fit used to plot the Arrhenius graph shown in Figure 5.26; the three experimental points are shown. From the curve it was calculated that $\ln(\mu_0) = 0.638$ and $\frac{E_a}{R} = 1848.726$, thus the equation looks like:

$$\ln(\mu) = 1848.726\left(\frac{1}{T}\right) + 0.638 \tag{5.1}$$

The equation of the line was used to extrapolate the viscosity values for a range of temperatures between 370 and 440°C. The resulting curve of viscosity against temperature is shown in Figure 5.27.

From here, the viscosity for a given time could be calculated based on the heating rate; 100°C min^{-1} results in an increase of 1.67°C each second. From this,

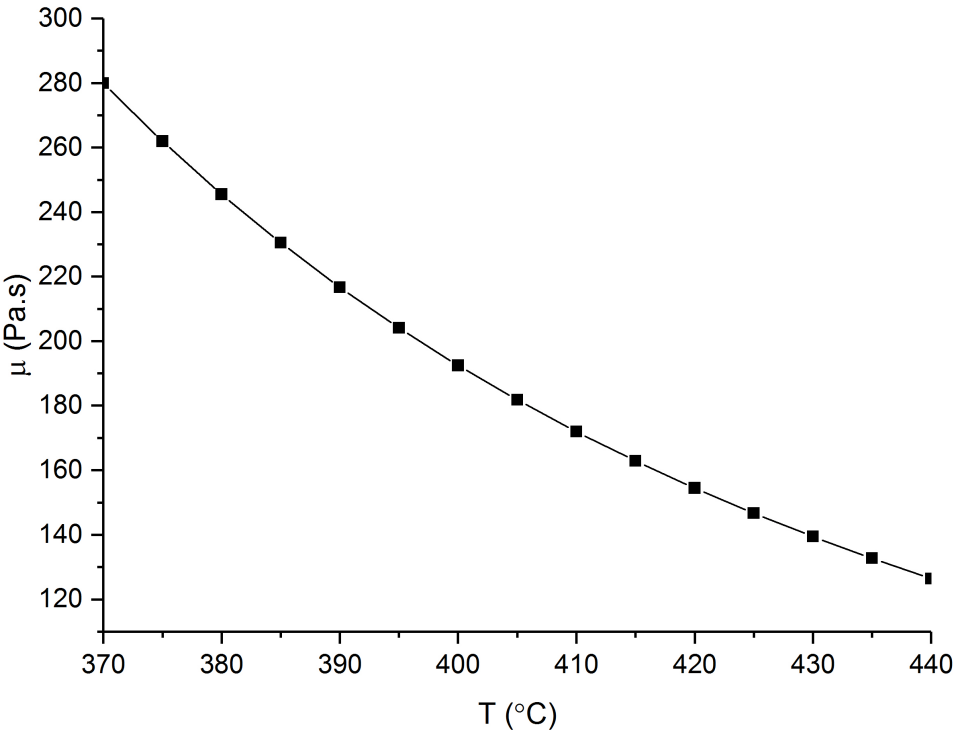

Figure 5.27: Extrapolated viscosity against temperature, calculated from Arrhenius equation

time was equated to a temperature, e.g. 374.7°C = 1 second, 376.3°C = 2 seconds, 378°C = 3 seconds. Viscosity values were calculated for each temperature using Equation 5.1 and assumed to be true for the corresponding time, thus at t = 1 second, μ = 263 Pa.s, for example. These corresponding time/viscosity values were then used in the equations, so that as time - and by association temperature increases - the viscosity decreases as would be expected experimentally.

5.7.1.2 Surface Tension

Measuring the surface tension of PEK is a challenge because it has a high melting temperature and surface tension measurements require the sample to be molten. No equipment was available which was capable of reaching the melting temperature of HP3 PEEK. An extensive search of literature found no values of surface tension for PEK. However, PEEK is morphologically similar to PEK [25], with a slightly lower melting temperature of 343°C. Jankova et al [196] attempted to identify the surface tension of PEEK using the Pendant Drop method. They found that at

400°C, molten PEEK did not form a droplet suitable for measuring surface tension and were thus unable to obtain a value.

Whilst surface tension measurements could not be found, some surface energy measurements were available. Values of surface tension and surface energy of a liquid are the same, however whilst surface tension is measured from a liquid, surface energy can be measured from a material whilst it is solid and at room temperature, thus eliminating the difficulty of measuring the value whilst the material is molten. Surface energy is identified from the interaction of the solid with a liquid and a gas of known surface tension values, typically water and air [193, 197]. It is desirable for the accuracy of the models to have values taken over the temperature range of the test, as surface tension is known to decrease as temperature is increased. However, in light of the difficulty obtaining surface tension values at 380°C and above it was decided to use a surface energy value measured using contact angles at 20°C from literature. A value of 42.1mNm^{-1} was used [198].

5.7.2 Frenkel & Frenkel/Eshelby

The Frenkel and Frenkel/Eshelby equations are given in Equations 2.1 and 2.2 respectively.

$$\frac{x}{a} = \left(\frac{3}{2}\frac{\Gamma t}{\mu a}\right)^{1/2} \tag{2.1}$$

$$\frac{x}{a} = \left(\frac{\Gamma t}{\mu a}\right)^{1/2} \tag{2.2}$$

In both, x is the radius of the neck between the particles, a is the initial particle radius, t is time and Γ and μ are surface tension and viscosity respectively.

Model curves were calculated by inserting known values into the right hand side of the equation in order to obtain a value for the left hand side of the equations. Surface tension Γ was set at 42.1mNm^{-1} as explained in 5.7.1.2. Initial particle radius a was 23μm, the average particle radius at 373°C from the uniform

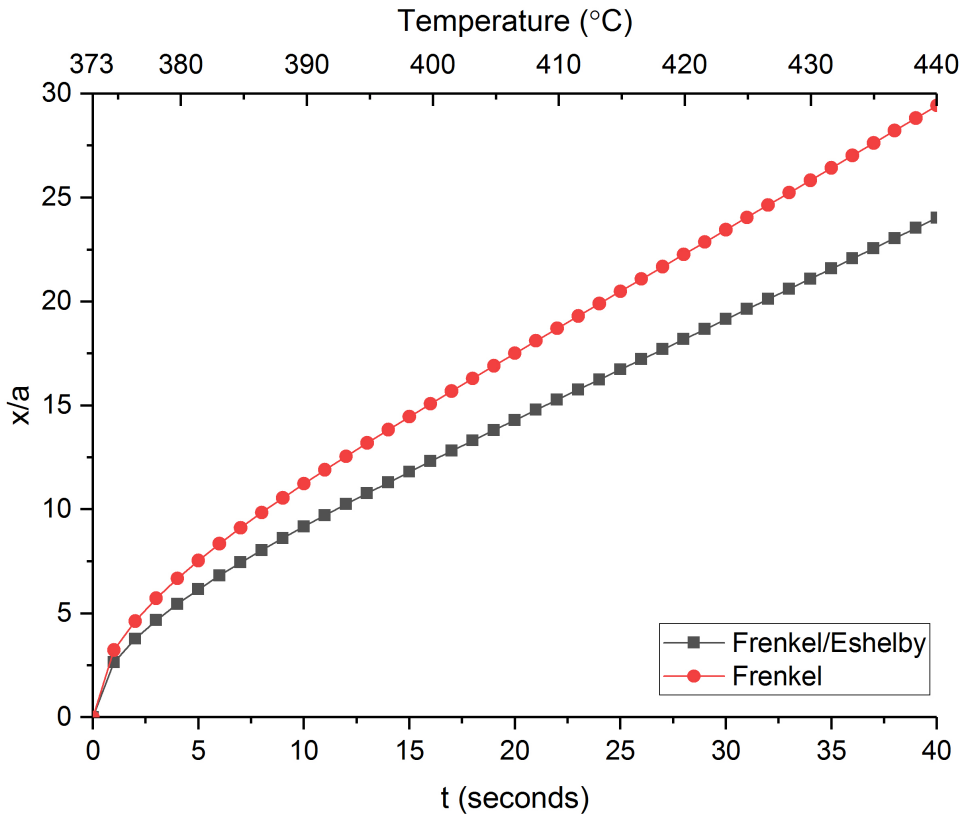

Figure 5.28: Predicted coalescence curves for Frenkel and Frenkel/Eshelby equations

coalescence results. x/a was calculated for time from 0-40 seconds, as this is the time taken to reach 440°C, and the viscosity was varied for each time step as explained in Section 5.7.1.1. The calculated Frenkel and Frenkel/Eshelby curves are shown in Figure 5.28.

Frenkel's model predicts that by the time one second has elapsed, the x/a value will be 3.23. Frenkel/Eshelby is slightly lower at 2.64. By the time 40 seconds has elapsed and the temperature has reached 440°C, the final x/a values are 29.42 and 24.02 for Frenkel and Frenkel/Eshelby respectively. Herein lies a flaw with both equations; full coalescence occurs at $x/a = 1$ and it is possible dimensionally to reach up to $x/a = 1.4$. Any value above this would essentially mean that the neck radius is larger than particle radius, that is, the particles have coalesced into a circle but continued changing shape thereafter. In other papers, the Frenkel predicted curve has not been plotted beyond $x/a = 1.5$; it has been plotted here to show comparison with the time which elapses experimentally. It is somewhat

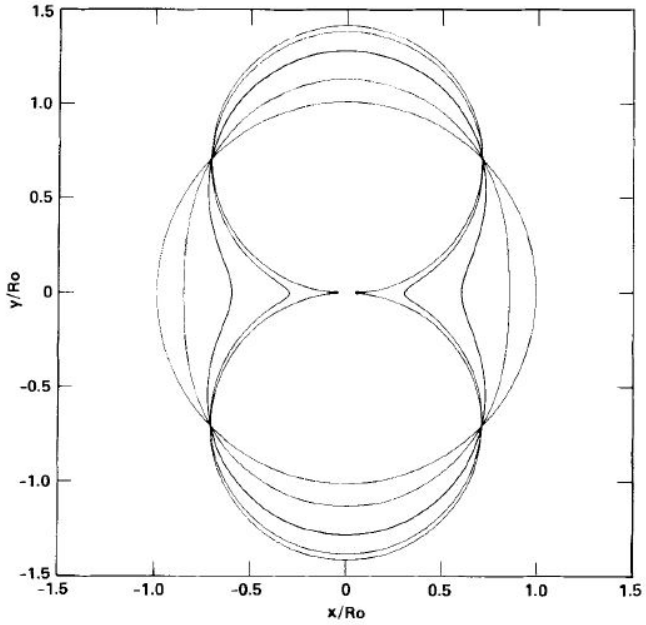

Figure 2.20: Shape evolution according to Hopper [162] (repeated from page 74)

surprising that complete coalescence is predicted so quickly; comparison with the experimental x/a curve will be drawn later in the section. It is worth noting however, that the time predicted is not dissimilar to the predicted curve for virgin PA-12 calculated by [140] et al.

5.7.3 Hopper

Hopper's model is expected to predict a curve which more closely approximates the shape of the experimental coalescence curve as it shows the behaviour of the coalescing particles as x/a tends towards 1. The equations map the changing shape of the particles as they coalesce, assuming that the shape of the neck between the particles is an inverse ellipse. Figure 2.20 shows the changing shape of the particles and is a reasonable approximation of what has been observed experimentally for uniform coalescence. Hopper's equations are given in Equations 2.6 and 2.7.

$$\frac{x}{a_f} = \frac{(1-\alpha)}{\sqrt{1+\alpha^2}} \tag{2.6}$$

$$\frac{\Gamma t}{\mu a_f} = \frac{\pi}{4} \int_{\alpha^2}^{1} \frac{1}{(\beta\sqrt{(1+\beta)}\mathrm{K}(\beta)} \mathrm{d}\beta \tag{2.7}$$

where a_f is the final particle radius and α is a number between 0 and 1; when $\alpha = 0$ the curve is a circle and as $\alpha \to 1$ the curve approaches the shape of two circles. Γ and μ are surface tension and viscosity respectively, as before. The function $K(\beta)$ is the complete elliptic integral of the first kind, as defined by Gradshetyn and Ryzhik [165].

$$K(\beta) = \int_{0}^{1} [(1-\chi^2)(1-\beta\chi^2)]^{-1/2} \mathrm{d}\chi \tag{2.8}$$

where χ is a parameter of the elliptic integral ranging from 0 to 1.

Equations 2.6 and 2.7 were solved for a range of values of α between 0 and 1, increasing in 0.025 increments. The integral calculator on computational website Wolfram Alpha was used to find the solution to Equation 2.8 and to perform the integration in Equation 2.7 [199].

In order to plot x/a against t for comparison with the other results, it was necessary to convert the results from a_f to a, and rearrange the left hand side of Equation 2.7 to find t. The method for this as described by Bellehumeur et al [131] is as follows:

Where $\alpha \geq 0.1714$:

$$\frac{a}{a_f} = \frac{1}{4} \frac{(1+\alpha^2}{\sqrt{\alpha}\sqrt{1+\alpha^2}} \tag{5.2}$$

And where $\alpha \leq 0.1714$:

$$\frac{a}{a_f} = \frac{(1-\alpha)}{\sqrt{(1+\alpha^2)}} \tag{5.3}$$

Finally, x/a could be calculated thus for each value of α:

$$\frac{x}{a} = \frac{a_f}{a} \times \frac{x}{a_f} \tag{5.4}$$

Rearranging the left hand side of Equation 2.7 for t gives:

$$t = \frac{\mu a_f A}{\Gamma} \tag{5.5}$$

where $a_f = a_0\sqrt{2}$, a_0 being the initial particle radius of 23μm, and A is the result for the right hand side of the equation as calculated earlier. As t was calculated independently of the viscosity, it was not possible to use the range of temperature dependent values as in the Frenkel and Frenkel/Eshelby models. Instead, the value of viscosity at 373°C was used for the whole model; this was 269 Pa.s. Surface tension Γ was 42.1mNm^{-1} as before.

The calculated Hopper curve is shown in Figure 5.30b, along with the Frenkel and Frenkel/Eshelby curves. It will be discussed in comparison with the experimental results in the next section.

5.7.4 Comparison of Models with Experimental Data

The results for the three theoretical models are shown alongside the experimentally determined results for average uniform particles in Figure 5.30. For the purposes of comparison, the increase in temperature which would occur during the time predicted by the theoretical models is shown on the model curves, while the time which elapses as the temperature is heated from 373°C to 440 °C is plotted on the experimental curve. Both have been calculated from the heating rate used during the tests, which was 100°C min^{-1}, equating to 1.67°C per second. Time = 0 was set at 373°C, the peak melting temperature of the material. On the Frenkel and Frenkel/Eshelby plots shown in Figure 5.28, time was measured in whole seconds and plotted for the experimental duration. In Figure 5.30a the curve has only been plotted up to $x/a = 1$; in order to see the true shape of the curve data points have been calculated at time increments of 0.01 seconds.

It is difficult to draw comparisons between the theoretical and experimental curves for the very early stage of coalescence as the models begin at $x/a = 0$ whilst the average x/a for the experimental work is 0.39; beginning with a particle contact much smaller this invariably resulted in the particles drifting apart rather

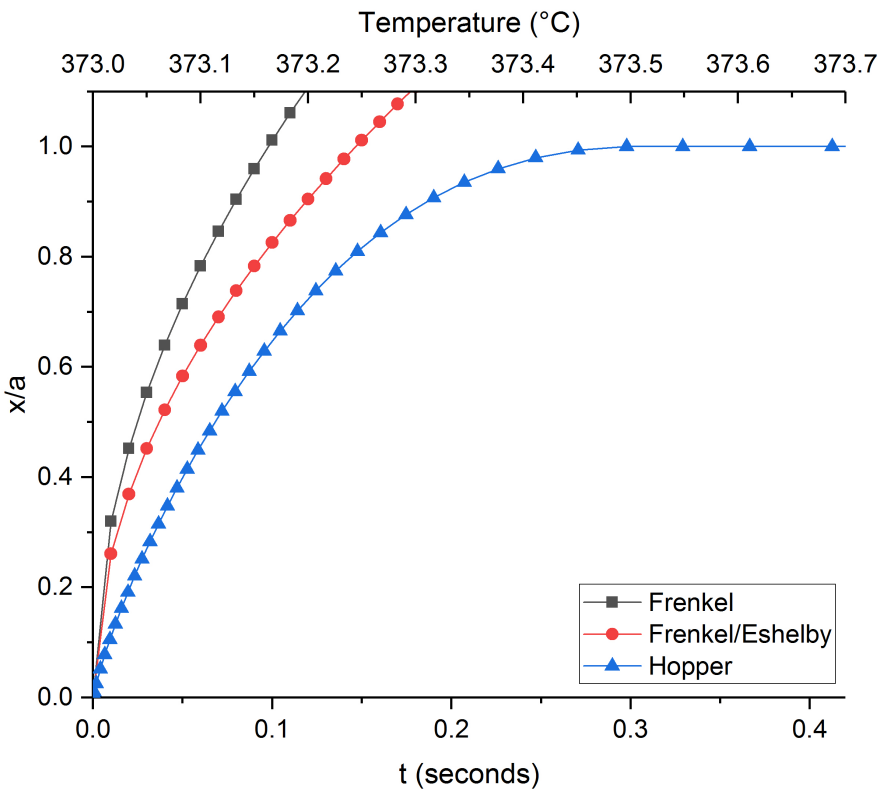

(a) Predicted coalescence curves from Frenkel, Frenkel/Eshelby and Hopper models

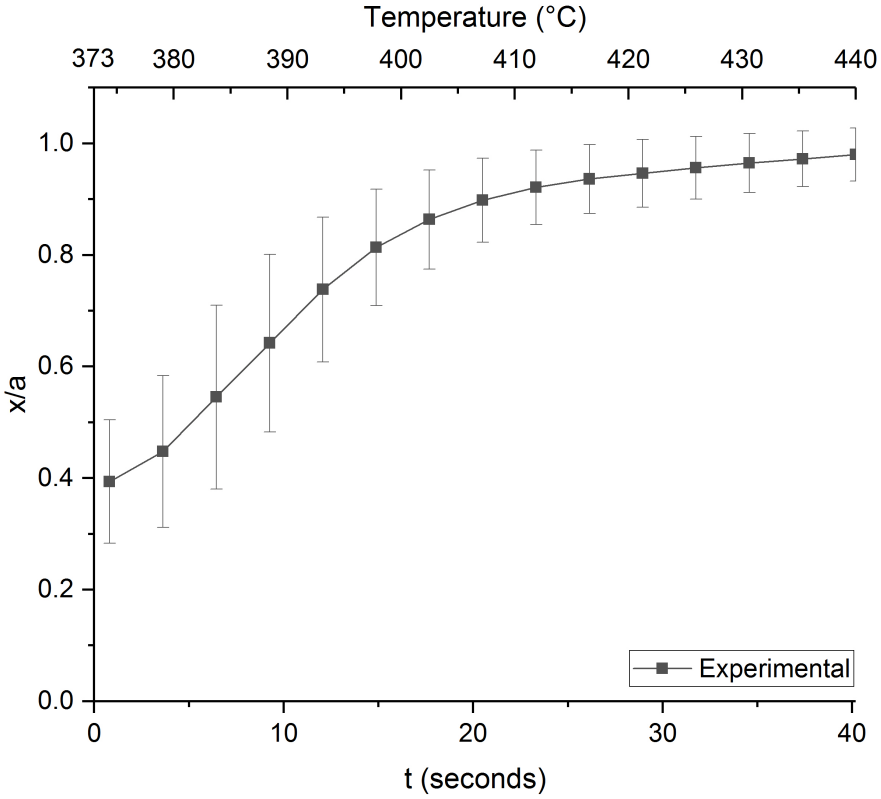

(b) Average uniform coalescence curve, plotted against time as well as temperature

Figure 5.30: Comparison of model coalescence curves with experimentally determined average uniform curve

than coalescing. However, between $x/a = 0.4$ and 0.6, the models show different behaviour from the experimental curve. During this period, the three models predict that the coalescence is extremely fast, slowing down later on, whilst experimentally coalescence is quite slow initially, before speeding up later.

From $x/a = 0.6$ to 0.8, the shape of all the curves is relatively similar, albeit the Frenkel and Frenkel/Eshelby curves show much steeper coalescence rates than Hopper. Beyond $x/a = 0.8$ however, only Hopper shows a similar trend to the experimental results. This is to be expected, as Frenkel and Frenkel/Eshelby are only true for the early stages of coalescence when the particle radius is almost constant whilst Hopper's model is applicable for the whole coalescence, taking into account the change in curvature at the particle neck throughout the process. In this regard, Hopper's model is a good approximation of how the particles coalesce.

Regarding the estimation of time required to achieve full coalescence, all three models overestimate rate of coalescence significantly. Frenkel predicts the fastest sintering rate, taking 0.1 seconds to reach a $x/a = 1$. Frenkel/Eshelby is not far behind, predicting 0.15 seconds to reach full coalescence. Hopper predicts the slowest coalescence rate, taking 0.3 seconds to reach a $x/a = 1$. In terms of temperature, full coalescence is predicted to occur between 373.1 and 373.5°C.

Experimentally, the average uniform coalescence curve does not reach $x/a = 1$; the final average coalescence ratio is 0.98 at 440°C. However, comparing the results with the Hopper model, $x/a = 0.9$ is reached at 407°C experimentally where t = 20.5, whilst the Hopper model predicts $x/a = 1$ at 0.19 seconds. The model predicts that coalescence will occur approximately 100 times faster than is seen in practice.

The simplest explanation for why the models might not accurately reflect the shape of the experimental curves and the time required to reach coalescence is that the traditional model for viscous sintering does not fully describe the melting behaviour of HP3 PEK. It was necessary to adapt the models to incorporate coalescence with increasing temperature rather than time as the material does not coalesce fully when heated isothermally. This behaviour has not been seen elsewhere in the literature for other materials; even for materials where Frenkel and

other models have been shown to be inaccurate, isothermal heating conditions have been sufficient for coalescence to take place [145, 151]. It would appear therefore, that further investigation is required to determine why the melting behaviour of PEK is different to other thermoplastics; overall very little research is available on the sintering of high performance thermoplastics, particularly those used for HT-LS.

In other cases where polymers have deviated experimentally from theoretical curves, factors such as surface morphology or the size and shape of the particles have been shown to be important. Truss et al [146] found that the fibrous morphology of UHMWPE was key to coalescence occurring, although they were investigating cold compaction moulding which is very different to the melt coalescence being considered here. Much of the work undertaken to compare experimental coalescence with theory used polymer beads rather than powder particles, which tend to be larger and more uniform in shape [133, 139]. Work with powder particles has been successful, however they have been larger ($> 300\mu$m) than those used here ($\approx 20\mu$m) [131]. Particle shape was shown in Section 5.5.2 to impact on the coalescence curve, resulting in a decrease in x/a early on; Cutler and Henrichsen [147] found that shrinkage observed in irregular shaped glass particles resulted in a different coalescence curve from that predicted by theory, and suggested that in crystalline materials this would be more significant as shrinkage of crystalline materials is not linear. Shrinkage of the particles early in the coalescence process was shown even for powder which was considered uniform; this explains why the rate of coalescence is slow during the early stages; see Figure 5.10 in Section 5.5.1. Haworth et al [140] hint that the high level of elasticity in polymers can slow the observed coalescence rate during sintering, however the authors do not elaborate further.

Lastly, it has been pointed out that incorporating only surface tension and viscous flow is a very simplistic view; other factors such as molecular inter-diffusion between the particles, viscoelastic adhesive contact or curvature based forces at the neck of the two particles, and viscoelastic relaxation forces in the melt may impact on coalescence [149–151].

Besides the models themselves, the measurements used to calculate the values seen here are likely to have introduced some inaccuracy compared with the experimental results. It has been explained that a value of surface energy calculated at room temperature was used rather than the surface tension at the melt; from contact angle analysis of polyamide 12, Haworth et al [140] determined surface energy at room temperature to be 46.1mN/m, whilst literature showed the surface tension at melt to be 25mN/m, decreasing further as temperature is increased. However, assuming that PEK shows a similar difference in surface tension between room temperature and melt to polyamide, the inaccuracy introduced would still be too small to account for the many orders of magnitude by which the models in Figure 5.30 overestimate the coalescence.

The shear viscosity for HP3 PEK was measured and used in the models here as a capillary rheometer was the only equipment available capable of measuring viscosity of HP3 PEK at up to 400°C; Frenkel [135] does not specify which measurement of viscosity his model is based on, whilst Hopper [162] determines only "dynamic" viscosity. Bellehumeur et al [131] and Haworth et al [140] used zero shear viscosity measurements in their models; Bellehumeur et al found good agreement with experimental work while Haworth et al did not compare their model with experimental results. Hornsby and Maxwell [139] found good agreement with their results using Trouton viscosity (three times larger than shear viscosity.) There does not appear to be firm agreement in the literature about which determination of viscosity is the "correct" one to use for sintering models; it is therefore unclear if the use of shear viscosity here explains the difference between theory and experimental work seen.

Given the significant overestimation of sintering time seen in the three models compared with the experimental results, the usefulness of the models for predicting coalescence of HP3 PEK seems questionable. In the work undertaken it has been shown that the coalescence of powder particles is often far from uniform so a model which predicts uniform behaviour cannot describe all coalescence behaviour which will occur. However, quantifying melting behaviour in terms of the neck

radius and particle radius allows for comparison between many different shapes and sizes of particle pairs and has been used here to look at the difference between virgin and used powder, as well as to examine the speed of coalescence and the temperature at which it occurs. In this regard, Frenkel's equation is still useful as it provides the basis for these measurements. Comparison of the models with the experimental work has raised several questions about what is occurring during the melt and shown that HP3 PEK may behave differently to other polymers during coalescence, which is important for determining how to best use the material during laser sintering.

While the models presented here may not necessarily be helpful in accurately predicting the coalescence behaviour of LS polymers, they still have the potential to be a useful tool in identifying what is occurring during melting. Many authors have not directly compared models with experimental results, considering that if the overall shape of the theoretical and experimental curves are similar this is sufficient to ascribe certain behaviour to that material. If the surface tension and viscosity data are available, the models are simple to undertake, which makes them attractive as a complementary method of material analysis alongside other techniques such as differential scanning calorimetry.

5.8 Conclusions

Hot stage microscopy was undertaken on HP3 PEK powder in order to understand the kinetics of coalescence. Using Frenkel's model of viscous sintering as a basis, pairs of particles were heated and the coalescence quantified by measuring the particle radii and the radius of the neck connecting the particles in order to obtain a coalescence ratio. This was then plotted against temperature or time in order to view the progression of coalescence. With the exception of a specific investigation into coalescence of used powder, all tests were undertaken on virgin.

The rate at which the particle pairs were heated was found to have an impact on the amount of coalescence observed. At low heating rates very little coalescence was observed in virgin particle pairs, even at very high temperatures. As the heating

rate was increased, the amount of coalescence increased and at heating rates above 80°C min^{-1} full coalescence, that is $x/a = 1$ was observed. It was suggested that degradation of the material in the air atmosphere of the hot stage was the reason for the low coalescence seen at slow heating rates; at low heating rates degradation of the material is occurring more quickly than coalescence while at higher heating rates coalescence occurs more quickly than degradation and is thus less inhibited.

Tests into isothermal heating showed that holding the material at a set temperature did not result in coalescence; in the tests where coalescence was observed it occurred before the hold temperature was reached, with very little seen thereafter. The exception to this was one test at 381°C, where some coalescence occurred in the first minute after the hold temperature was reached. Overall, however, isothermal heating was not considered the reason for the coalescence which was observed and it was decided to undertake all further tests using a dynamic heating rate of 100°C min^{-1}.

Results from tests at 100°C min^{-1} were categorised as either uniform or non-uniform according to whether their behaviour matched theoretical description of the coalescence process. Coalescence of uniform particles was shown to be slow at first due to initial shrinkage of the particles, speeding up once the temperature exceeds 385°C. Initially neck growth is governed by deformation of the two particles as they are drawn together by adhesive forces, followed by equilibration - the point at which the neck between the two particles breaks down and they merge to become one; this occurs around 400°C.

Non-uniform coalescence occurred as a result of non-uniform particle shapes or non-uniform particle melting behaviour. This was not found to impact coalescence overall, only the rate at which full coalescence was achieved. Thus non-uniform coalescence behaviour is unlikely to adversely affect parts built during laser sintering.

A non-stick coating was applied to some glass slides in order to investigate the impact of adhesion effects. The non-stick coating was found to impact the shape of the coalescence curve obtained but not the final x/a value or the speed at which

this was achieved; even though more non-uniform coalescence was observed with the non-stick coating than without it, the average coalescence curves both with and without non-stick coating were almost identical. Thus adhesion effects, whilst present, do not adversely impact on coalescence.

Used powder showed varying amount of coalescence depending on where in the powder bed it was removed from and what heating rate was used. Corner powder showed more coalescence than mid powder at both 10°C min^{-1} and 100°C min^{-1}, whilst centre powder showed no coalescence regardless of heating rate. Assuming that location is linked to degradation, with level of degradation increasing with proximity to the centre, degradation has a significant impact on whether the powder will melt and coalesce. It was suggested that investigation into the temperatures occurring at these locations would shed more light on levels of degradation.

Comparison of experimental results with theoretical models by Frenkel, Frenkel/Eshelby and Hopper showed that all three models predict coalescence will occur approximately 100 times faster than is seen experimentally. As expected, the shape of Frenkel and Frenkel/Eshelby curves are similar to experimental results up to $x/a = 0.8$, whilst beyond this only Hopper is a good approximation of the experimental coalescence curve. The main reason for the mismatch between the model prediction and experimental results is likely to be the melting behaviour of HP3 PEK, which as observed during isothermal tests is quite different to other polymers, coalescing only under dynamic heating. Inaccuracy in the material measurements may have been a factor. Overall, the models may not be an accurate predictive tool for the rate of coalescence, but provide a method to quantify coalescence which allows comparison between virgin and used melting behaviour, and can be useful alongside other material characterisation methods such as differential scanning calorimetry.

Chapter 6

Process Characterisation

6.1 Introduction

Results from material and coalescence characterisation show that there are significant differences between the properties of virgin and used powder, and also between used powder samples taken from different locations in the build chamber.

In order to understand what is causing this, it is desirable to understand what temperatures are occurring inside the powder bed during building. The P800 system has built-in heaters which control the temperature of various parts of the chamber, and sensors which monitor the temperatures, and measuring the temperatures in the system experimentally and comparing with the system readings could provide insight into what is occurring in the powder. Thus the purpose of this chapter is two-fold:

- Understand and document how heat is controlled by the P800 system and see if the output of the sensors is an accurate reflection of the temperatures occurring during building.
- Build a thermal map of the powder bed showing the temperature distribution across the platform so that the effect on powder and parts can be understood.

An overview of the work in this chapter is given in Figure 6.1.

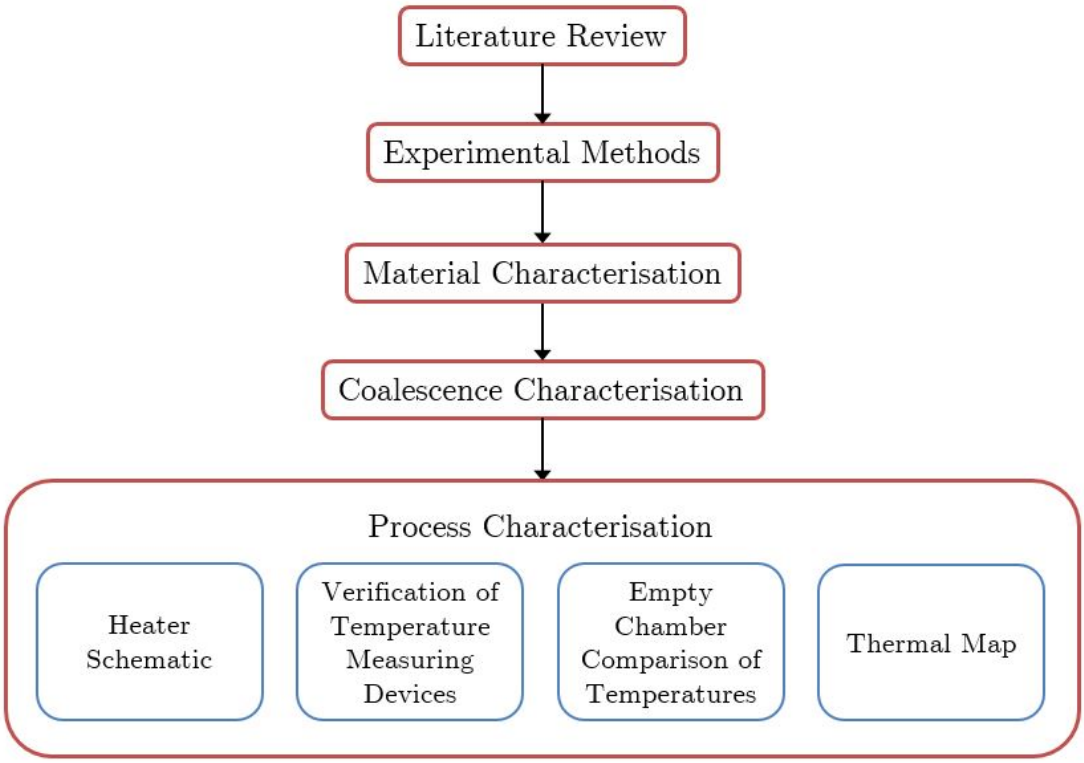

Figure 6.1: Overview of process characterisation chapter in context

6.2 EOSINT P800 Heater Schematic

The EOSINT P800 is very similar to the EOSINT P700 series but is modified to handle the working temperatures required to sinter high melting temperature polymers. The layout of the system is shown in Figure 6.2. As explained in Chapter 3, Section 3.1 on page 81, the build chamber dimensions are 700 x 380 x 560 mm, and the material is sintered by two lasers, one for each half of the build chamber. The system settings can be viewed and controlled using EOS proprietary software PSW. A screenshot is given in Figure 6.3; the main image shows a topdown view of the build chamber and the division between the two halves is clearly marked. Parts are virtually arranged in the build chamber using this software and the system is monitored from here during building.

The appropriate temperatures for the system during building are measured by the operator during a lengthy procedure which requires testing temperatures within a certain range of the material melting temperature and visually checking

for discolouration of the powder bed and then building test parts and checking for smoke during sintering [173]. The "set temperatures" for the process chamber, exchangeable frame and build platform are determined using this method.

The PSW software determines the input to the heaters based on the set temperatures. The actual temperatures are measured by sensors in the process chamber, exchangeable frame and build platform and the input to the heaters is adjusted accordingly during the building process to maintain the system at the set temperatures. The location of the heaters and sensors that govern the process chamber, exchangeable frame and build platform are described briefly below.

The surface of the powder bed is heated by four infrared heating lamps which are located in the process chamber above the exchangeable frame; see Figure 6.2A. The powder bed temperature is constantly measured by an optical temperature sensor which looks down onto the no build zone of the machine; this is located at the intersection of the two halves of the build chamber and is shown in Figure 6.3, marked a. The software labels this the "process chamber" temperature.

There are two separate bands of heaters fitted around the sides of the exchangeable frame, Figure 6.2B and Figure 6.4; an upper band fitted around the top of the frame and a lower band fitted around the bottom. The temperature is measured using thermocouples or PT100 sensors fitted into the top front, top rear, top left and bottom front of the frame, in between the glass frame wall and an insulation layer. There are more sensors in the upper band as this is more critical to the building temperature, while the lower band is primarily used to control the cooldown [personal communication, Nov 2017]. The software labels this the "exchangeable frame" temperature; it is possible to view the separate temperatures of the front, back and left/right sensors but as a default the software displays whichever temperature in these sensors is the highest.

The sensor which measures the temperature of the building platform is mounted centrally below the metal platform.

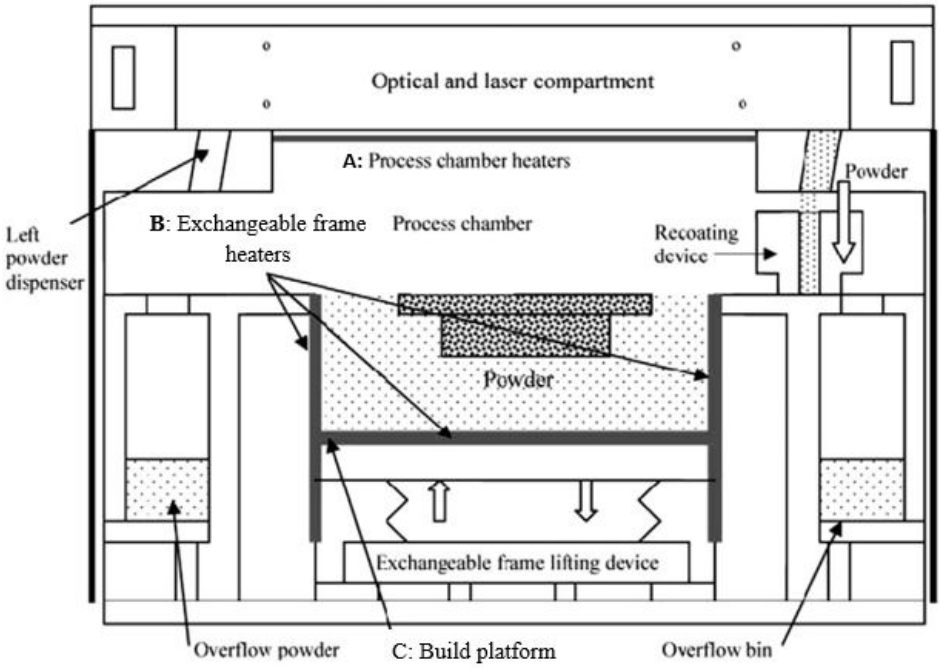

Figure 6.2: EOSINT P700 [6] with position of P800 heaters marked

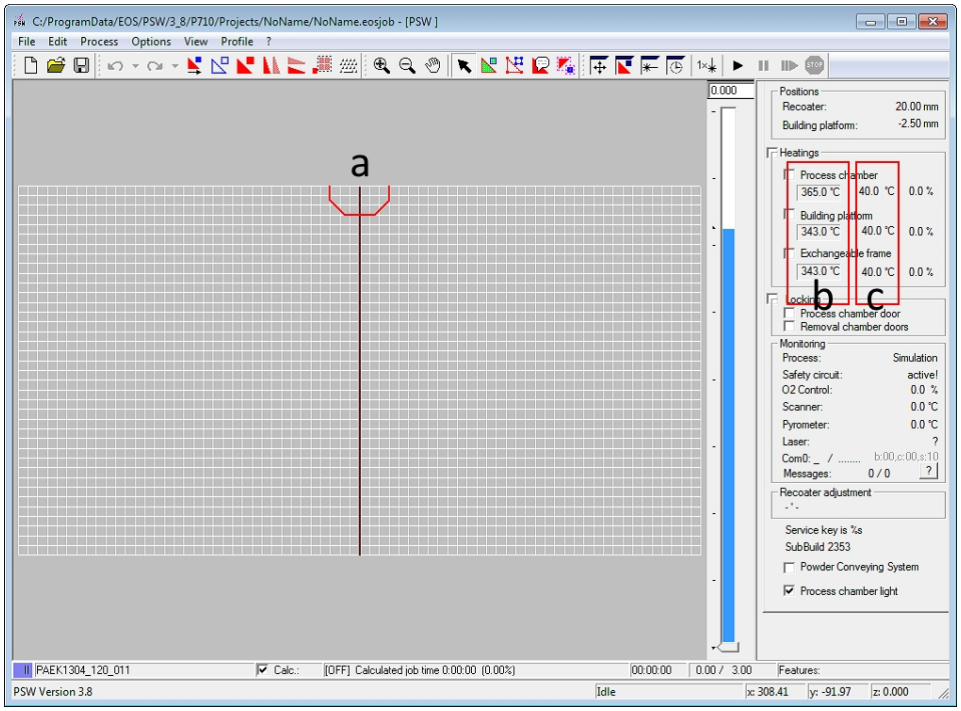

Figure 6.3: EOS PSW software for controlling and monitoring P800 building. a) no-build zone, b) set temperature, c) current temperature [200]

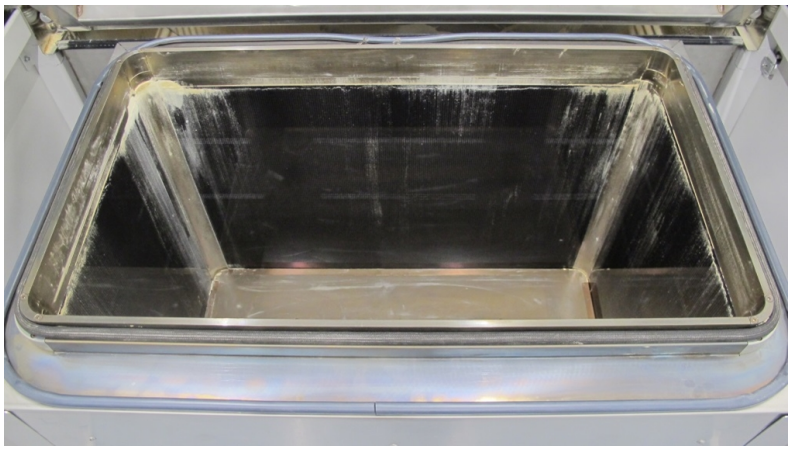

Figure 6.4: Inside of exchangeable frame [201]

6.3 Background to Experimental Method

Full details of the experimental methods used in this chapter are given in Section 3.5 of the Experimental Methods chapter. This section explains how the experimental method was determined.

The set temperatures for the P800 at the time of the study were 368°C for the process chamber, 347°C for the build platform, and 345°C for the exchangeable frame. The aim of the characterisation exercise was to measure the temperatures inside the powder bed at various locations during building and compare them with the temperatures measured by the sensors.

Two types of temperature measuring equipment were available for measuring temperature in the chamber for comparison with the temperatures output by the system sensors; thermocouples and button data loggers. Thermocouple wires were capable of withstanding the high temperature of the building process, but the controllers connected to the thermocouple wires were not, which necessitated keeping them outside the P800 system, requiring the system to be closed with the wires trailing out, risking damage to the wires. Furthermore, placing wires in the system would interfere with the action of the recoater and were unlikely to remain in position as the build platform was lowered and powder spread across. Button data loggers required no wires; data was read from them by connecting them to a reader following the build, thus they could be placed in the powder bed during a

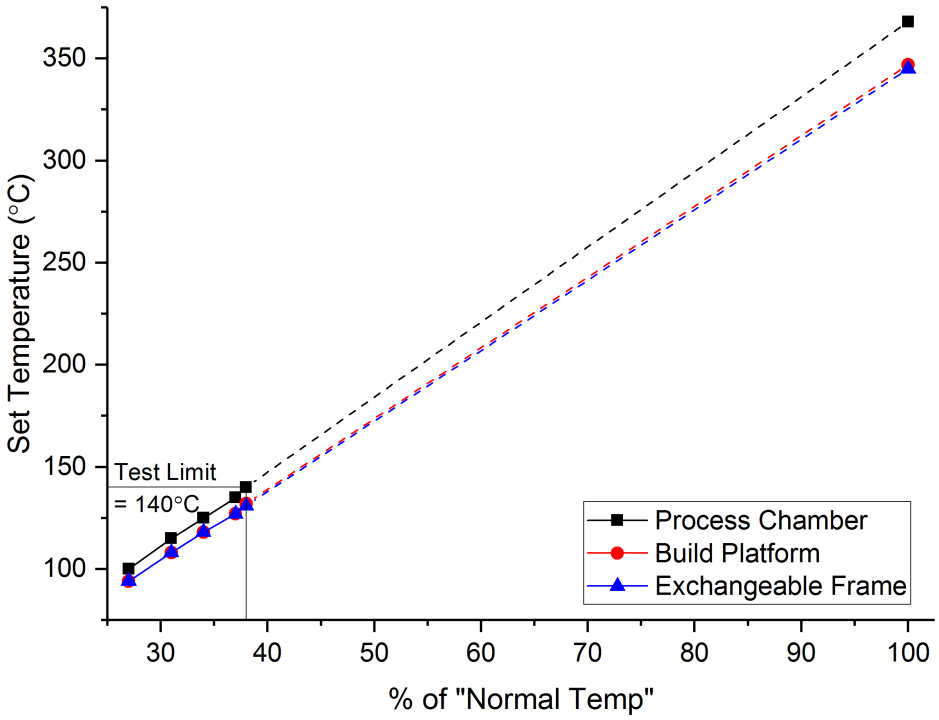

Figure 6.5: Extrapolated set temperatures from test to "normal" build temperatures

	Ref	Test 1	Test 2	Test 3	Test 4	Test 5
% of "normal" temp	100%	27%	31%	34%	37%	38%
Process (°C)	368	100.0	115.0	125.0	135.0	140.0
Build (°C)	347	94	108	118	127	132
Frame (°C)	345	94	108	118	127	131

Table 3.1: Temperature profiles tested in P800 (repeated from page 96)

build as the build platform was lowered and without interfering with the recoater. However, they were only capable of withstanding temperatures up to 140°C, which is substantially lower than the set temperatures required for building with HP3 PEK.

It was decided to test a range of set temperature profiles which represented a percentage of the actual temperatures used during building and then extrapolate the test data up to the actual set temperatures in order to estimate the temperatures during building with HP3 PEK. It was assumed that the extrapolation would be linear. Five process chamber set temperatures were chosen which were within the range of the data loggers. The percentage these

Thermocouple	1	2	3	4	5
Data Loggers	Top Right	Bottom Left	Top Left	Bottom Right	Centre

Table 6.2: Thermocouples paired with data loggers

temperatures represented of the "normal" building temperature were calculated, and the percentages used to calculate the set temperatures for the exchangeable frame and the build platform. A graph showing the intended extrapolation is shown in Figure 6.5 and the set temperature profiles are repeated from the experimental methods in Table 3.1.

6.4 Thermocouple/Data Logger Comparison

In order to check the data loggers, which had not been used before, and to compare the data logger data with thermocouple data, a thermocouple wire was taped to each data logger and placed in an oven. The temperature was raised to 140°C and then cooled back to room temperature. The graphs for each logger/thermocouple pair are shown in Figure 6.6. The solid black lines show the thermocouples and the dashed red lines show each of the data loggers. Which thermocouples were attached to which loggers is given in Table 6.2. The names given to data loggers correspond to the positions in which they were used on the P800 build platform during the later experiments with powder; in the context of this test the names are arbitrary but were useful for telling the loggers apart.

Due to limitations in being able to collect thermocouple temperatures, readings for one thermocouple were taken every 30 seconds for five minutes, then readings for the next thermocouple were taken, and so on. This was undertaken twice, producing two sets of data for each thermocouple/logger pair covering the whole heating/cooling profile of the test. For simplicity, only the readings from the data loggers corresponding to the same time period for the thermocouples are shown on the graph, even though the loggers were recording continually.

Overall, the thermocouples and the data loggers are within 5°C of each other for all profiles. When the temperature is increasing, the thermocouples log a higher

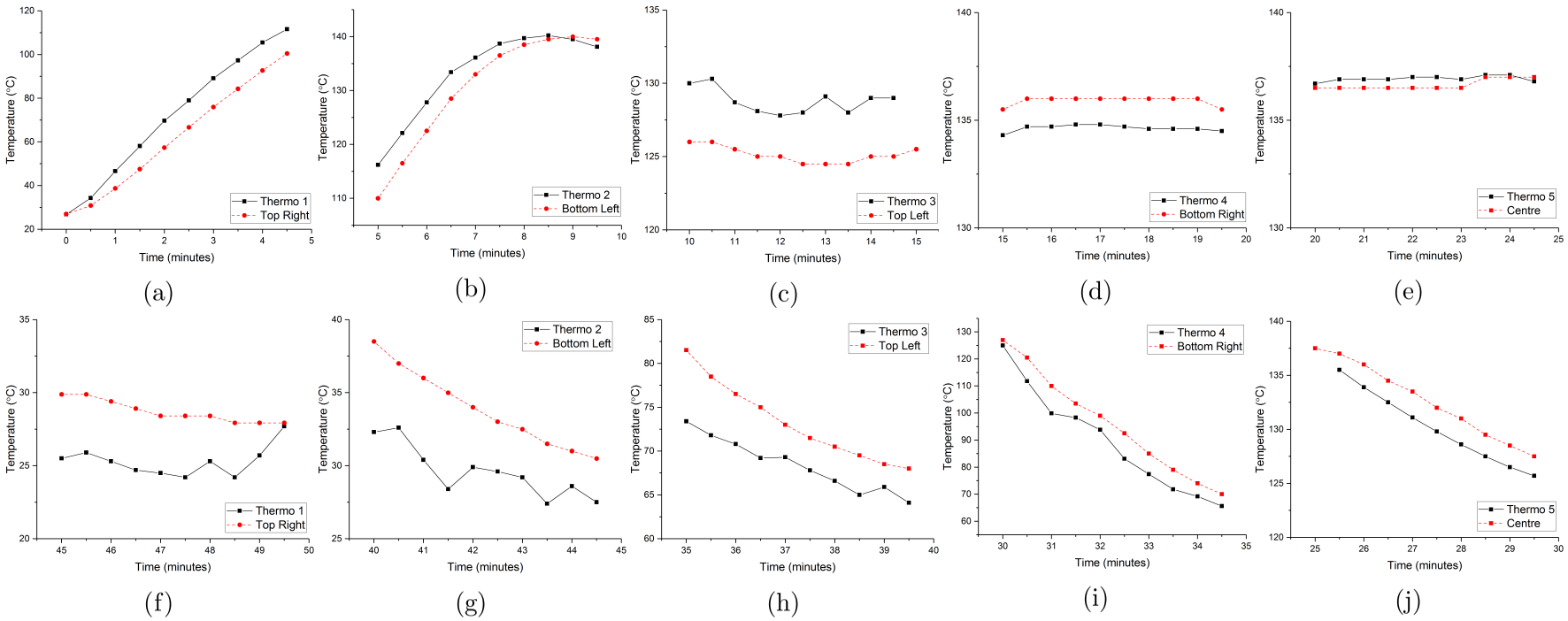

Figure 6.6: Temperature comparison of thermocouples taped to data loggers; solid black line = thermocouple, red dash line = data logger

temperature than the data loggers, and when the temperature is decreasing the data loggers register a higher temperature than the thermocouples. This appears to indicate that the thin thermocouple wire registers changes in temperature more quickly than the data loggers. This is confirmed by the profiles of the curves; the data loggers show a smoother temperature profile than the thermocouple wires which is consistent with a more gradual heating and cooling, while the erratic profile of the thermocouple results shows they are sensitive to very sudden changes in temperature.

It is worth bearing in mind that the data loggers may not accurately register very fast changes in temperature when interpreting the results of later tests.

6.5 Stability of P800 at "Low" Temperatures

As the P800 is designed to operate at temperatures in excess of 300°C, it was decided to assess whether the system was stable at the "low" temperatures required to use the data loggers. Tests were undertaken in an empty chamber without powder present so that thermocouples could be used together with data loggers in order to collect more data.

Thermocouples and loggers were placed in strategic locations in the empty build chamber and the system heated to each of the pre-determined set temperature profiles given in Table 3.1; a repeat of the locations of the thermocouples and loggers from the experimental methods is given in Figure 3.5. Once the temperatures had stabilised, the profile was held for 30 minutes and then the temperature set points were raised to the next profile, left to stabilise and held for 30 minutes and so on until all five profiles had been tested. Temperatures were then compared with output from the P800's onboard temperature sensors.

A description of the nomenclature used to describe each temperature measurement and where the measurement was taken from is given in Tables 6.3, 6.4 and 6.5 for the P800 built-in sensors, thermocouples and data loggers respectively.

Results were plotted for all readings against the process chamber and build platform/exchangeable frame set temperatures separately. The set temperatures

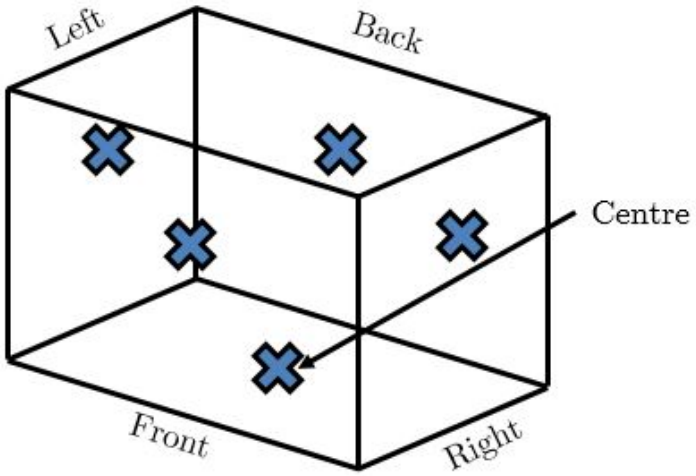

(a) Location of thermocouples during chamber low temperature validation tests

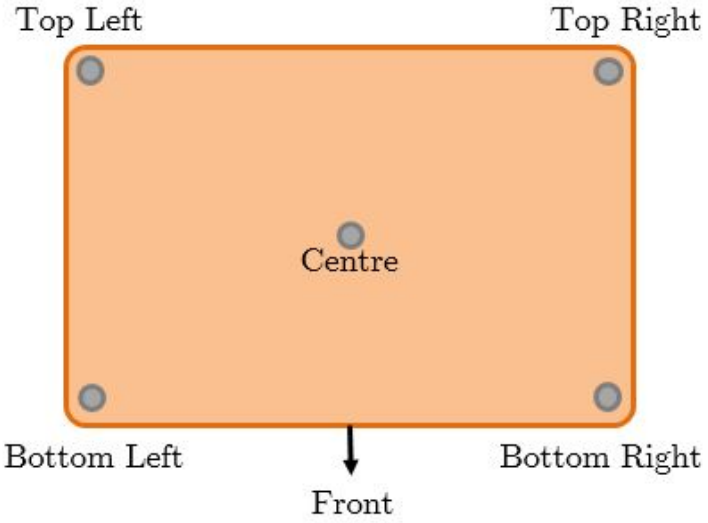

(b) Location of button data loggers during low temperature validation test and experimental builds with powders

Figure 3.5: Placement of thermocouples and loggers (repeated from page 98)

	Short Name	Description/Location
P800 Built In Sensors	P8 Process	Process chamber optical sensor over no-build zone
	P8 Build	Sensor mounted centrally below build platform
	P8 Frame Front	Sensor mounted in upper band of exchangeable frame front, closest to machine door
	P8 Frame Back	Sensor mounted in upper band of exchangeable frame back, furthest from machine door
	P8 Frame Left/Right	Sensor mounted in upper band of exchangeable frame on left hand side of chamber

Table 6.3: Nomenclature of temperature measurements output by P800 sensors, recorded from PSW software

	Short Name	Description/Location
Thermocouples	TC Centre	Thermocouple taped to centre of build platform
	TC Front	Thermocouple taped to middle of upper heating band, closest to machine door
	TC Left	Thermocouple taped to middle of upper heating band on left hand side of chamber
	TC Back	Thermocouple taped to middle of upper heating band, furthest from
	TC Right	Thermocouple taped to middle of upper heating band on right hand side of chamber

Table 6.4: Nomenclature of thermocouple temperature measurements, read manually from thermometer

	Short Name	Description/Location
Data Loggers	DL Centre	Data logger placed on build platform in the centre
	DL Top Left	Data logger placed on build platform in left corner furthest from machine door
	DL Top Right	Data logger placed on build platform in right corner furthest from machine door
	DL Bottom Left	Data logger placed on build platform in left corner closest to machine door
	DL Bottom Right	Data logger placed on build platform in right corner closest to machine door

Table 6.5: Nomenclature of temperature measurements from data loggers, recorded automatically by the loggers and downloaded to computer following build

for the building platform and the exchangeable frame were the same for four of the five tests; the exchangeable frame set temperature is 1°C lower than the build platform set temperature in test 5. However, for the purposes of comparison, they have been assumed the same for all tests.

6.5.1 Comparison of Measurements with Set Temperatures

6.5.1.1 P800 Sensors

The data from the in-built sensors in the P800 is shown in Figure 6.8. Measurements from the sensors in the build platform, process chamber and front, back and left/right sensors in the exchangeable frame were recorded.

The data from the build platform sensors compares well with the build platform set temperature for each profile. Compared with the process chamber and exchangeable frame the build platform heats relatively slowly. A small overshoot is observed when the set temperature is reached; this is consistently 0.5°C for all profiles. When the set temperature has been reached it consistently maintains for each profile, fluctuating by no more than 0.2 of a degree.

The exchangeable frame temperatures are exaggerated compared to the build platform and process chamber. The temperature increases very quickly and overshoots to between 3 and 6°C below the set temperature for each profile, before taking an average of 15 minutes to cool to a stable temperature. The stable temperature reached is below the exchangeable frame set temperature by 11-12°C for all profiles. The frame front is slightly hotter than the frame back and frame left/right for the higher temperature profiles but only by 1°C. Once the temperature has stabilised for each profile, it fluctuates by no more than 0.5°C.

The set temperature for the process chamber is higher for each profile than the set temperature for the exchangeable frame and the build platform. The process temperature output is the highest of all the sensor measurements but is consistently 5-6°C lower than the set temperature for all profiles once a stable temperature has been reached. Like the other sensors, there is initially an overshoot before a stable temperature is reached; this is approximately 1°C for all profiles. The temperature

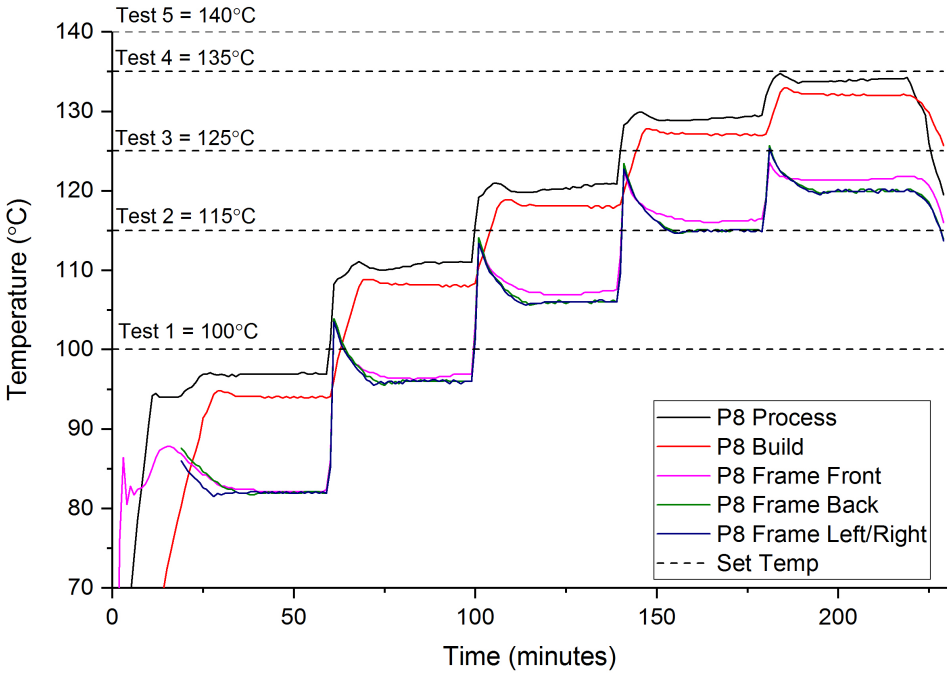

(a) Process chamber set temperature

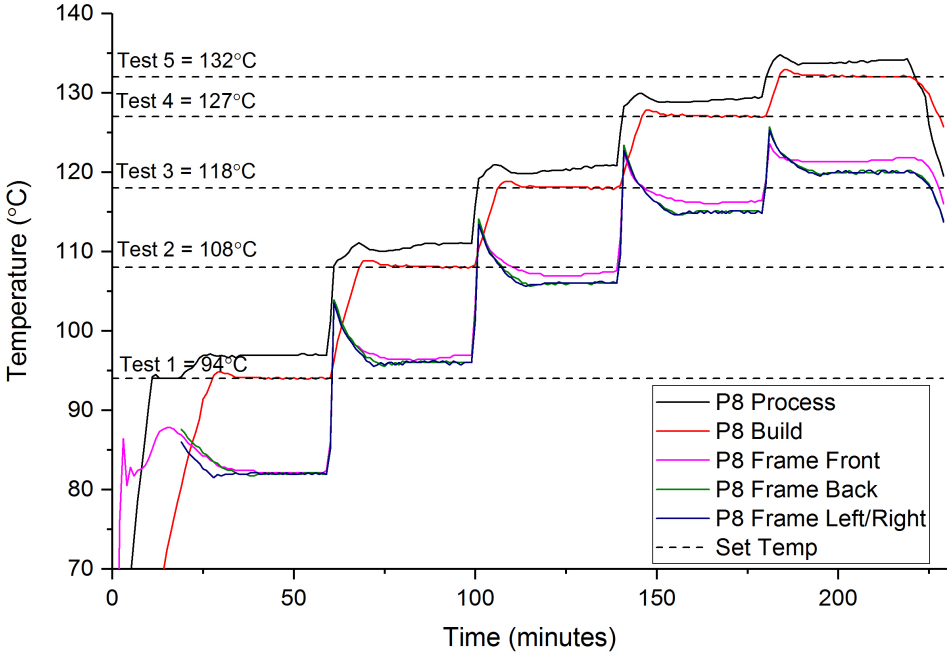

(b) Build platform/exchangeable frame set temperature

Figure 6.8: Comparison of temperatures output by P800 sensors for all heating profiles

slowly creeps up by 1-2°C during the 25 minute period period in which the set temperatures are maintained.

6.5.1.2 Thermocouples

The data from the thermocouples is shown in Figure 6.9. It is expected that the data from the thermocouples taped to the exchangeable frame should be similar to the data from the P800 sensors in the frame, and the data from the thermocouple in the centre of the build platform should be similar to the sensor data from the build platform, given the proximity of the measuring equipment to the sensors. This comparison will be discussed in detail later. The shape of the curves for all but the centre thermocouple are quite similar to the sensor data, with an initial overshoot followed by a stable region. However, the temperatures are not the same for all locations.

The back and front of the frame show quite similar temperatures and are higher than the left and right of the frame; on average there is an 8°C difference between the highest and lowest temperatures from the four thermocouples taped to the sides of the frame. The back and front thermocouples are within 3°C of the set temperature for the exchangeable frame, but the left is on average 7°C below the set temperature and the right thermocouple is nearly 10°C lower.

The profile of the data from the centre thermocouple taped to the build platform looks very different from the frame bands. The beginning of the profiles do not show a sharp overshoot, but increase gradually to the stable temperature. The stable temperature for the centre thermocouple is on average 7°C higher than the exchangeable frame/build platform set temperature in all tests and in several profiles matches the set temperature for the process chamber; this is potentially to be expected as due to the chamber being empty the process heaters are radiating heat directly onto the build platform.

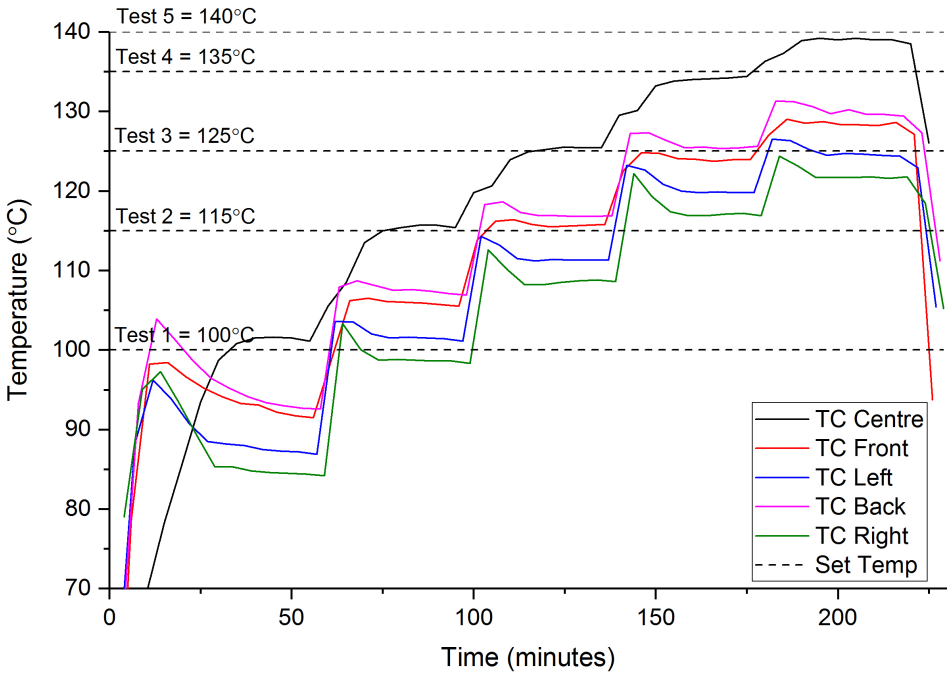

(a) Process chamber set temperature

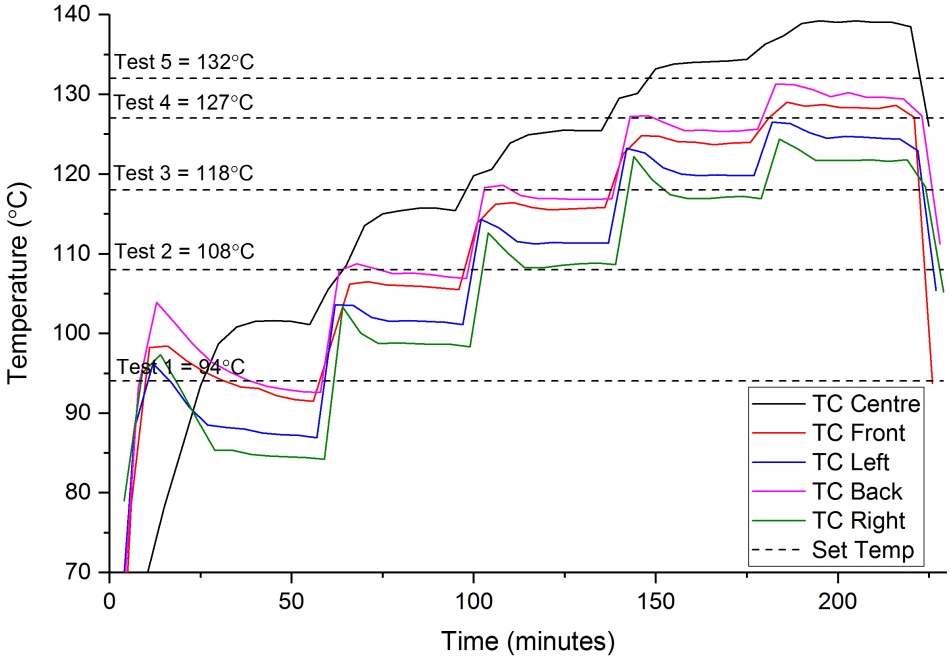

(b) Build platform/exchangeable frame set temperature

Figure 6.9: Comparison of temperatures output by thermocouples for all heating profiles

6.5.1.3 Data Loggers

The results from the data loggers are shown in Figure 6.10. The loggers were all placed on the build platform, in each of the four corners and one in the centre. The results suggest that the four corners all show similar profiles but with small differences in temperature depending on location. All corners show a small overshoot.

The bottom right and bottom left loggers show the highest temperatures and there is an average difference of 5.5°C between the highest and lowest temperatures across all profiles. The bottom right is on average 4°C below the set temperature while the top right is 9°C lower than the set temperature.

The curve for the centre logger is not dissimilar to the curves for the corners, but shows no overshoot. The centre logger is on average 7°C higher than the exchangeable frame set temperature for all five of the heating profiles and is quite close to the process chamber set temperature.

6.5.2 Comparison of All Readings

To compare the location specific data from the various measurement methods, the relevant curves have been plotted together for the build platform and the exchangeable frame.

6.5.2.1 Build Platform Readings

Figure 6.11a considers how the loggers on the build platform compare to the sensor in the build platform. The curve of the P800 sensor data is similar in shape to the readings from the data loggers in the four corners but the temperature is higher; the closest logger readings are from the bottom right corner, which are on average 3.8°C cooler than the build platform sensor at the stable temperature across the five profiles.

By contrast, the centre logger is on average 6.8°C hotter than the sensor across the stable region of each profile. As the sensor is placed underneath the build platform, it appears the temperature is not evenly distributed right the way through

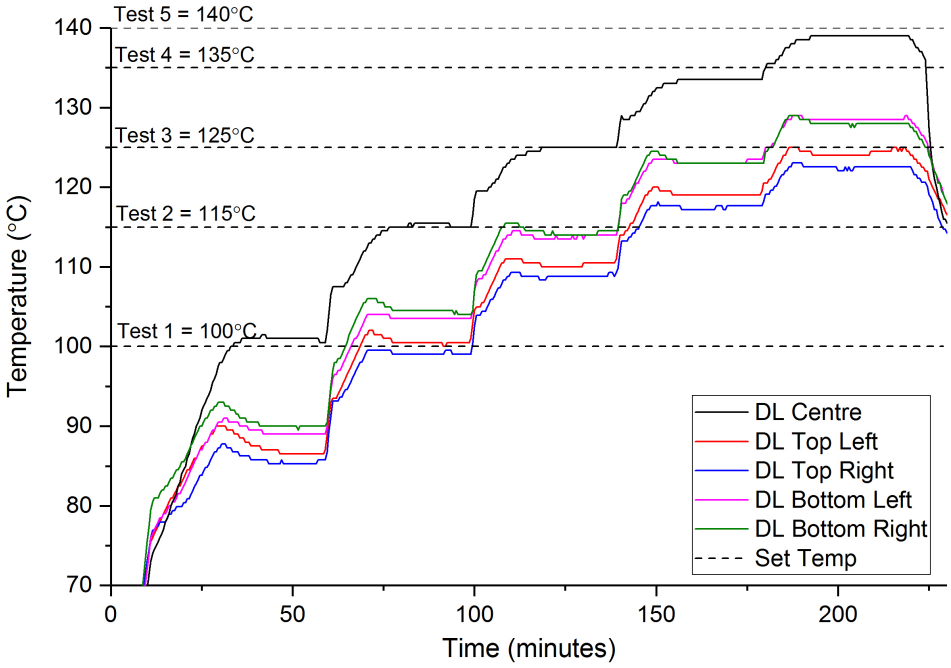

(a) Process chamber set temperature

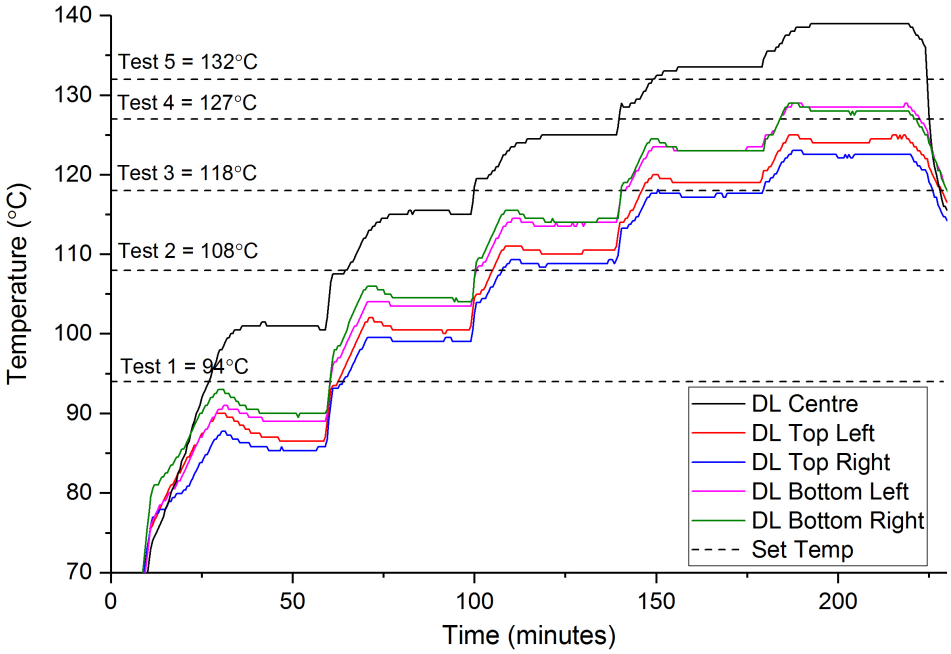

(b) Build platform/exchangeable frame set temperature

Figure 6.10: Comparison of temperatures output by data loggers for all heating profiles

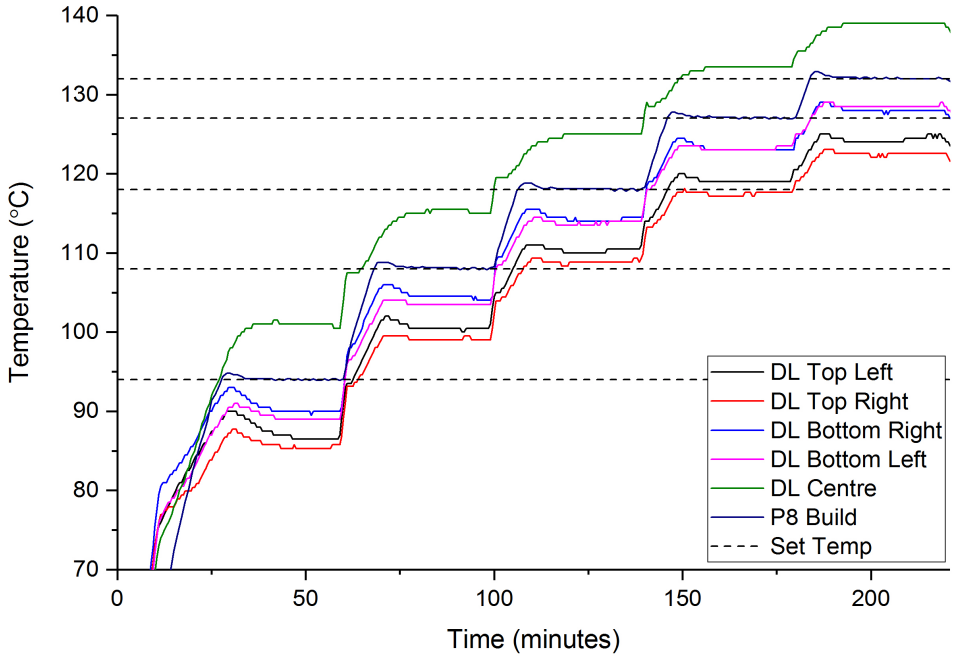

(a) Data loggers and build platform sensor

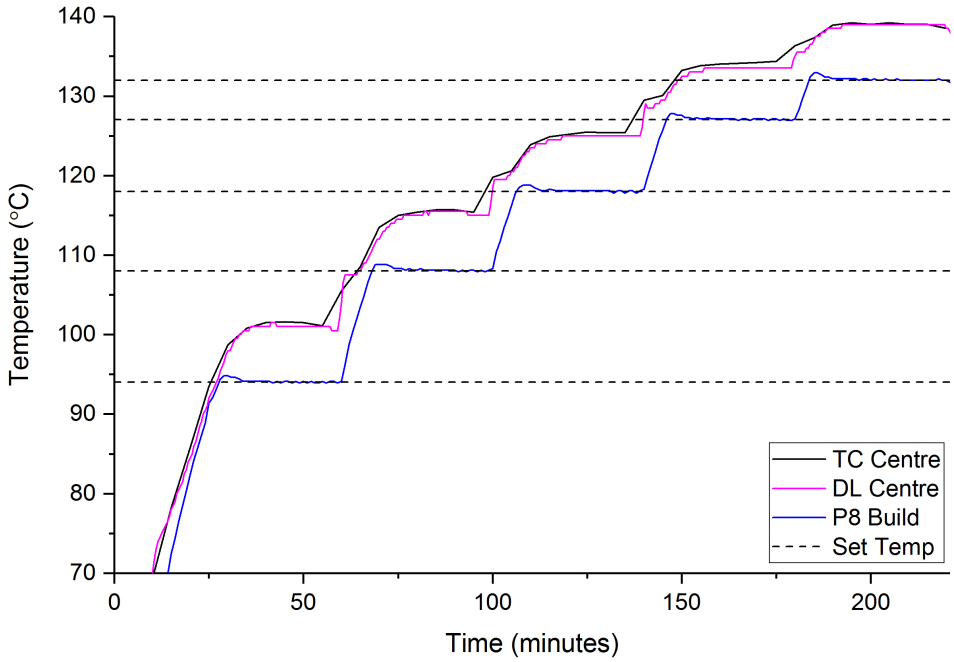

(b) Centre of build platform and build platform sensor

Figure 6.11: Comparison of data for build platform; set temperatures are for exchangeable frame/build platform

the platform; it is hotter on the surface. The average of the stable temperatures of all five loggers is still 3.6°C lower than the sensor readings so it is clear that the sensor reading does not take into account the temperature across the whole platform.

Figure 6.11b shows how the readings for the centre logger and thermocouple compare with the data from the build platform sensor. The thermocouple and logger readings are in very good agreement with each other; the beginning of each profile shows that the thermocouple heats quicker than the logger, which verifies the observation made during the oven test (in Section 6.4) that the loggers do not register temperature change as quickly as the thermocouples. The temperatures measured by the thermocouple and the logger are closer to the process chamber set temperature than the build platform set temperature; this is potentially due to the process chamber heaters, which are radiating onto the platform where usually there would be powder.

6.5.2.2 Exchangeable Frame and Process Chamber Readings

A comparison of the data from the thermocouples and the sensors in the exchangeable frame is shown in Figure 6.12. Like the data from the centre of the build platform, the thermocouples register a higher temperature than the built in sensors. The correlation between the shape of the thermocouple and sensor curves is not perfect, but this is likely to be due to the infrequency with which the readings were taken from the thermocouples - one data point is plotted for each curve every 5 minutes rather than every minute as with the sensors. In general, the thermocouples and sensors are in agreement that a large temperature overshoot occurs at the beginning of each profile and the shape and duration of the stable period for each profile is similar.

The thermocouple data sits in between the sensor data for the frame and for the process chamber - this makes sense as the thermocouples were attached to the surface of the frame and were likely affected by the temperature change of both the frame and the process chamber, but were situated far enough away from the

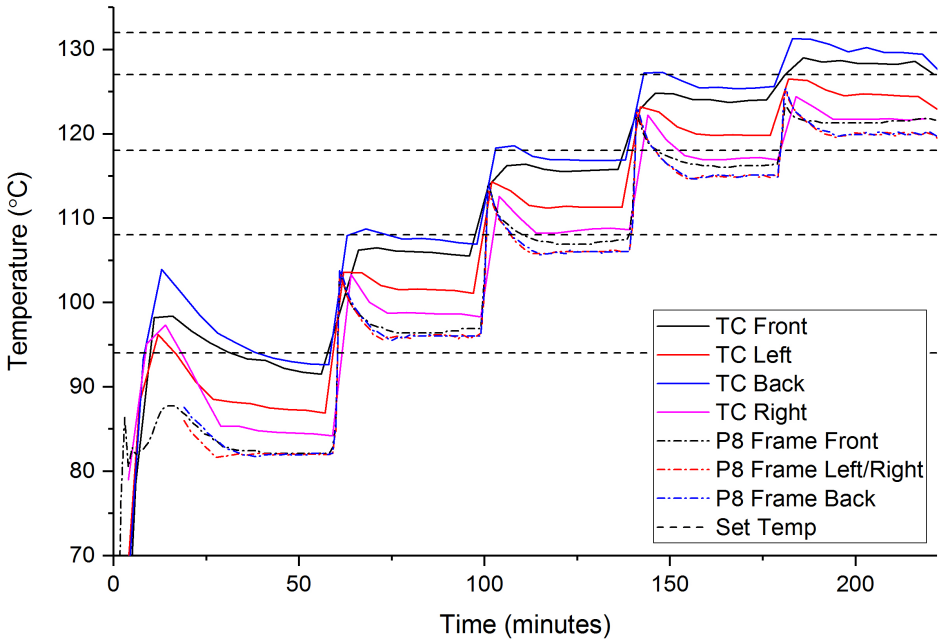

Figure 6.12: Thermocouples on frame bands and frame sensors; set temperatures are for exchangeable frame/build platform

process chamber heaters not to experience the highest temperatures.

Overall it can be concluded that the P800 is capable of maintaining the "low" temperatures set for each of the five heating profiles. However, the sensors do not appear to take into account the variation in temperature experienced across different locations in the chamber, particularly the build platform. It is worth noting that the P800 is designed to maintain temperature in a full build chamber, not an empty one. This means that some of the temperatures can be expected to be different during later tests were powder is used and this may account for some of the temperatures being lower than expected.

6.6 Thermal Map During Building

Having established that the system was stable during each of the five profiles described in Section 6.3, tests were undertaken during a simulated build with powder. The build platform was lowered by 20mm and filled with powder. The loggers were placed just below the surface of the powder in the four corners and the centre as described in Figure 3.5. The system was heated to the set temperature

for the profile and left to stabilise for two hours. The test involved building 90mm of layers with laser exposure set to none; i.e. no sintering took place. The readings from the data loggers were plotted against z-height for each location, and compared with sensor data recorded by the P800 which was retrieved from the build logs. Sensors and data logger results are labelled as per the nomenclature described earlier in Tables 6.3 and 6.5.

Set temperature names have been abbreviated to reduce the amount of text on plots; process refers to process chamber, frame refers to exchangeable frame and build refers to build platform. Where frame/build set temperature is referred to, it is because the set temperature for both the exchangeable frame and the build platform were the same.

6.6.1 Data Presentation

6.6.1.1 Smoothing

Much of the raw data recorded by the EOS sensors was very noisy so average adjacent smoothing was applied to present the data more clearly; Figure 6.13 shows the comparison between the raw and smoothed data; smoothing settings were chosen to minimise noise whilst retaining the shape of the curve.

6.6.1.2 Differences Between Repeats

Each test was undertaken at least twice; more if there were irregularities during the test (such as build interruptions) which would make comparing the data difficult. Given the sheer quantity of data collected it would be very difficult to represent repeats with error bars. Instead only one repeat for each test is shown in the following graphs. As can be seen in Figure 6.14 there are subtle differences between the results but the overall shape is very similar. Therefore it was decided that only presenting one repeat for each test was a fair representation of the results.

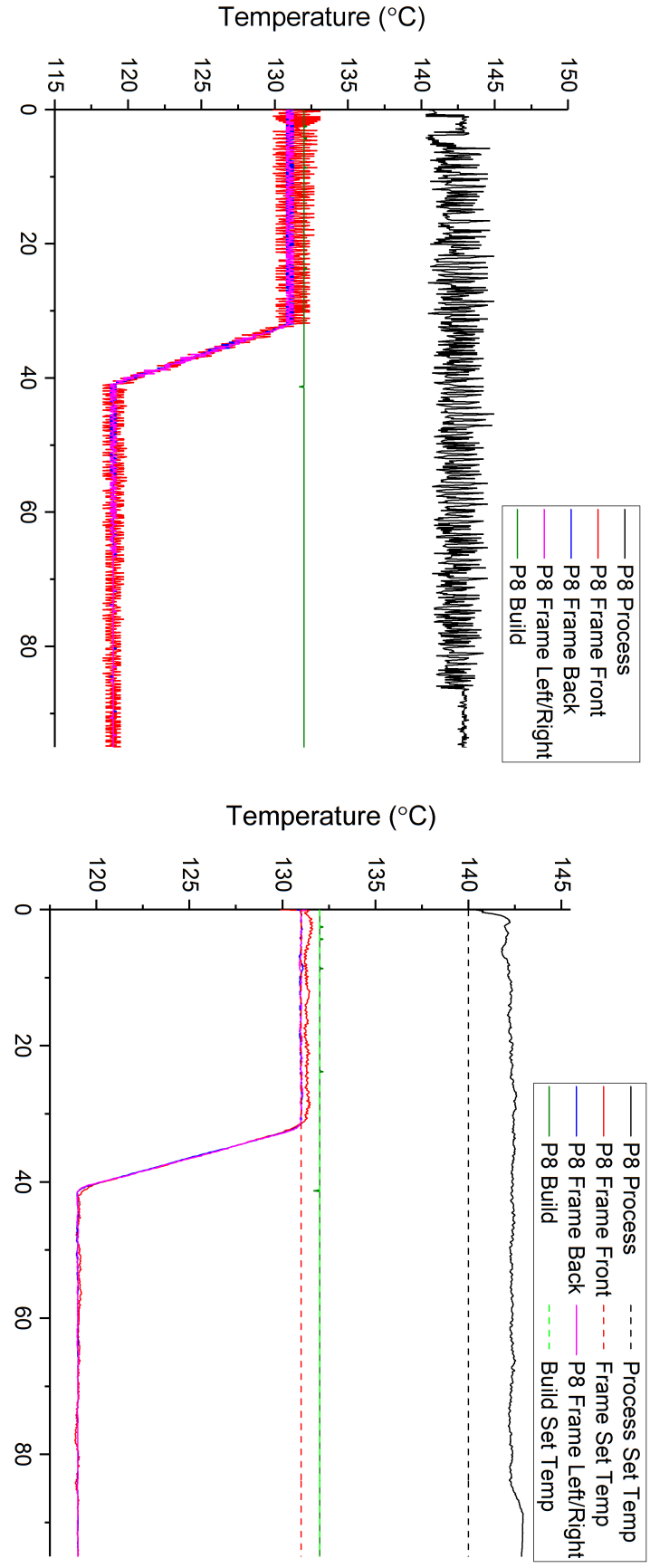

(a) Raw data output by P800 sensors

(b) Data from P800 sensors with smoothing applied

Figure 6.13: Comparison of noisy raw P800 data with smoothed P800 data

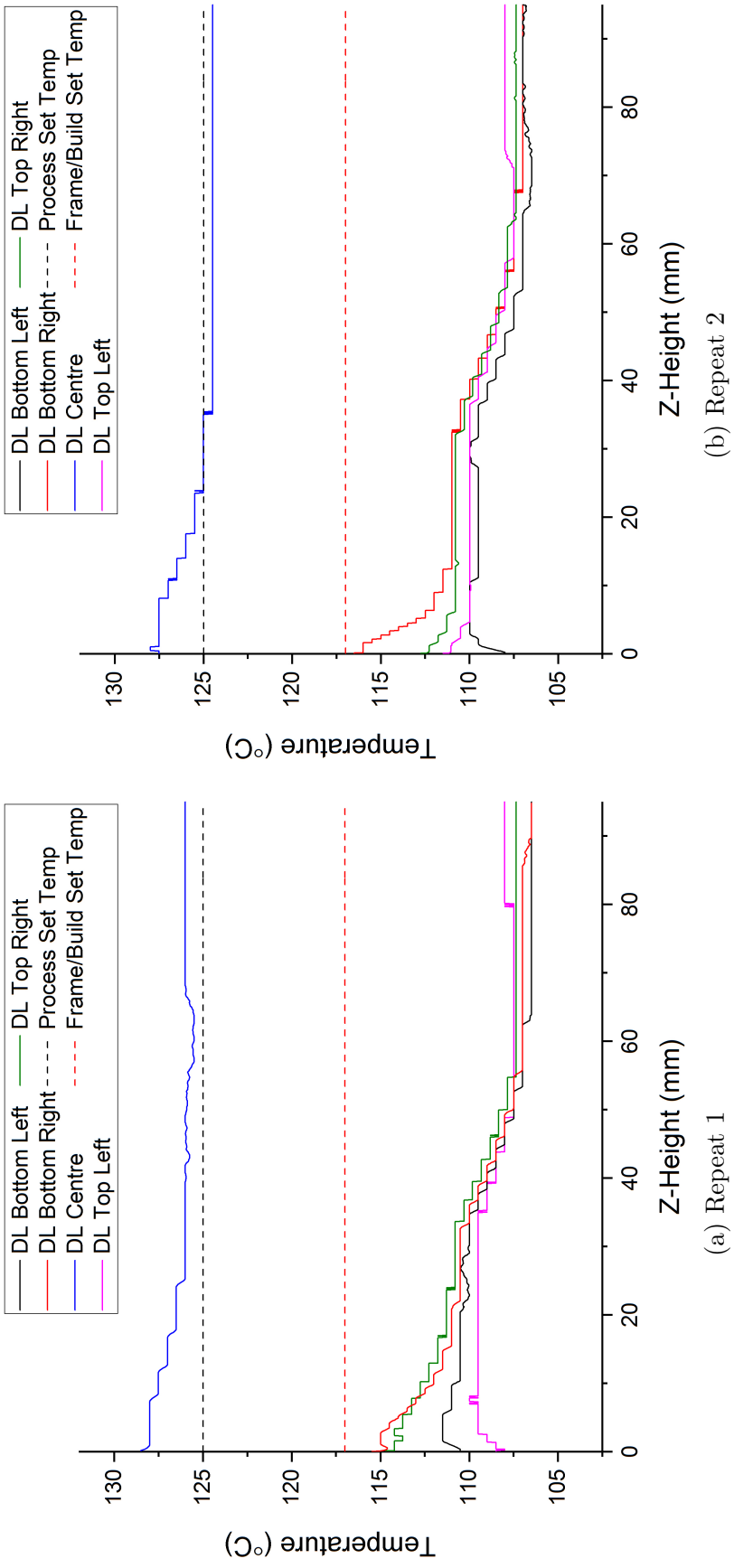

(a) Repeat 1

(b) Repeat 2

Figure 6.14: Comparison of repeat data from loggers for Test 3

6.6.2 P800 Sensors vs Logger Data

The results for each the five heating profiles are shown in Figures 6.15 to 6.19. They are ordered from lowest set temperatures (Test 1) to highest (Test 5).

6.6.2.1 P800 Sensor Data

The results output by the P800 sensors are very consistent for each test.

The build platform temperature achieves the set temperature during heating, is already at the set temperature when the test begins and doesn't deviate on any of the results.

The temperatures from the different locations in the frame are in good agreement with each other and for each test they follow the same profile. The frame temperatures closely match the set temperature until approximately 28mm and then drop to 12-13°C below the set temperature over the next 8-10mm at a rate of 1.3°C mm^{-1}, before maintaining this lower temperature for the remainder of the test. It is not clear why the frame temperatures follow this profile; it is possible that at the set height where the temperature changes the powder bed is retaining a lot of heat and the temperature is reduced in order to prevent the powder bed getting too hot and causing degradation of the remaining powder and the sintered parts.

It is potentially worth noting that whilst the height at which the temperature drop starts and ends is very similar in Tests 1-4, varying by no more than 0.5mm and around 12°C, the results from Test 5 (the highest temperature profile, shown in Figure 6.19) are slightly different. The z-height at which the temperature drop begins is 4mm higher than the other average of the other four tests, and the temperature drop is 13.7°C, compared to an average of 12.3°C for the other four tests. This is a small difference but given the consistency of the results for Test 1-4 it may be indicative that the profile change is dependent on the set temperature and the results recorded during these "low" temperature tests are not exactly the same as the profile during building.

The process temperature by contrast is higher than the set process temperature

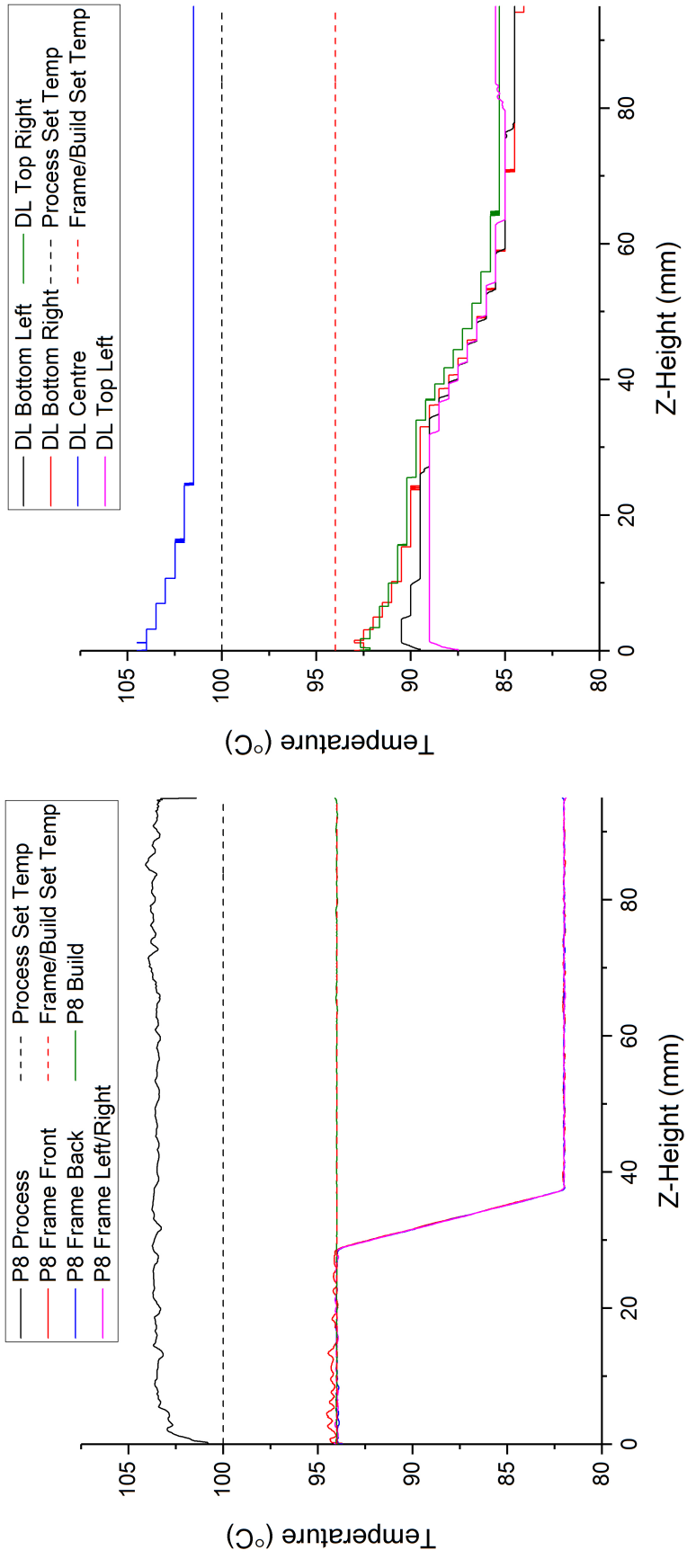

(a) Smoothed data output by P800 sensors

(b) Data from loggers

Figure 6.15: Comparison of data from P800 sensors and data loggers for Test 1

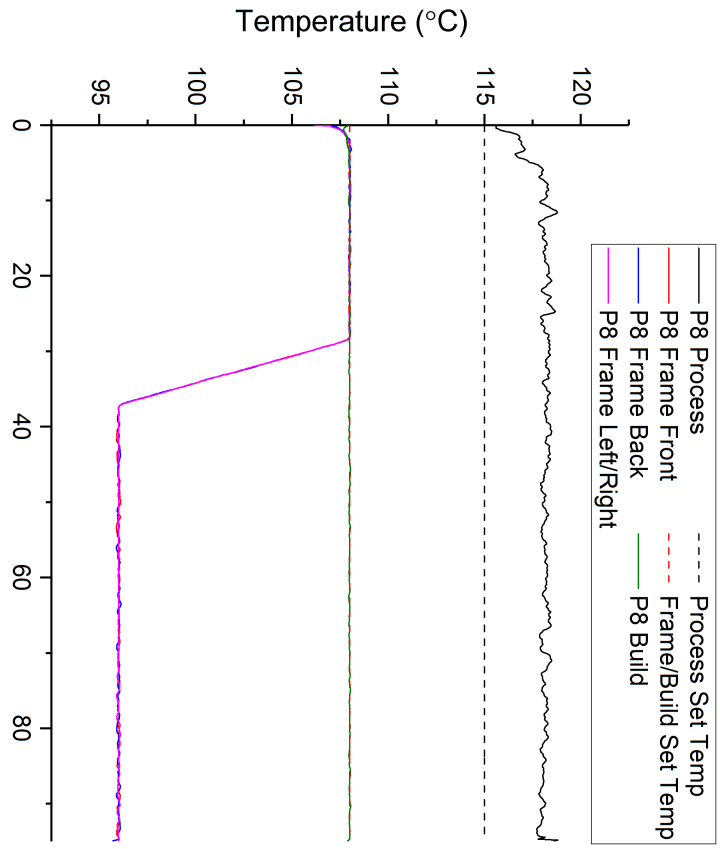

(a) Smoothed data output by P800 sensors

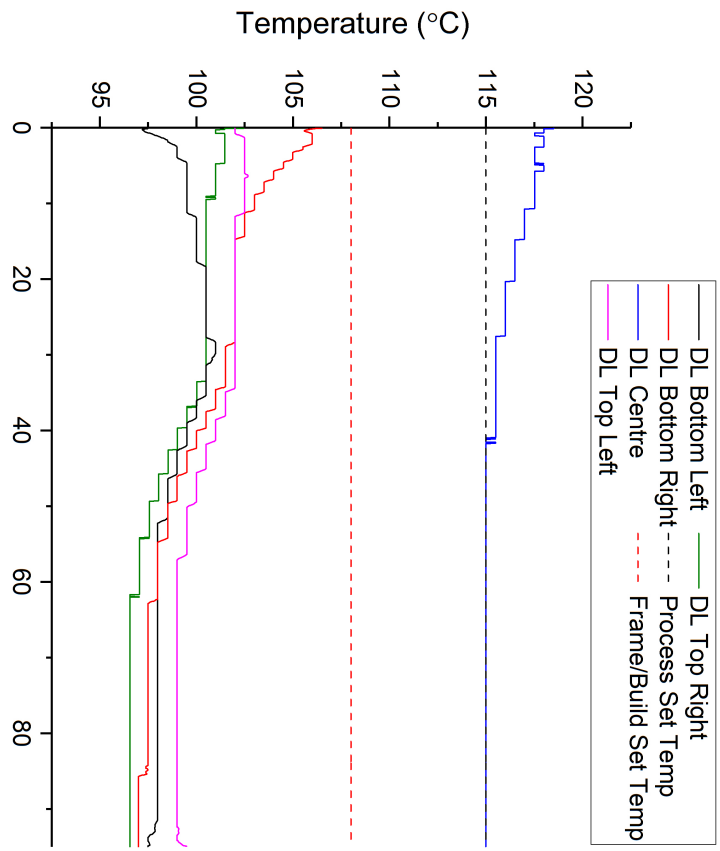

(b) Data from loggers

Figure 6.16: Comparison of data from P800 sensors and data loggers for Test 2

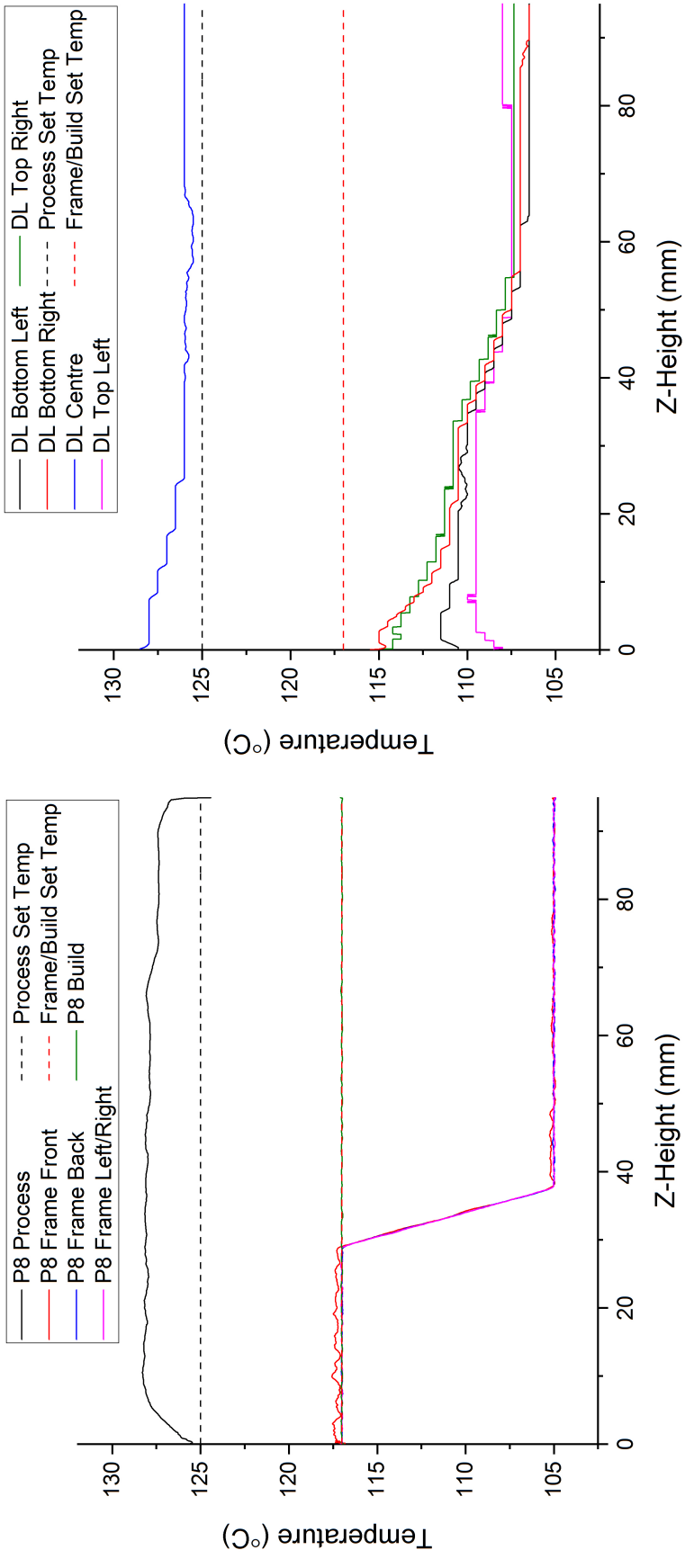

(a) Smoothed data output by P800 sensors

(b) Data from loggers

Figure 6.17: Comparison of data from P800 sensors and data loggers for Test 3

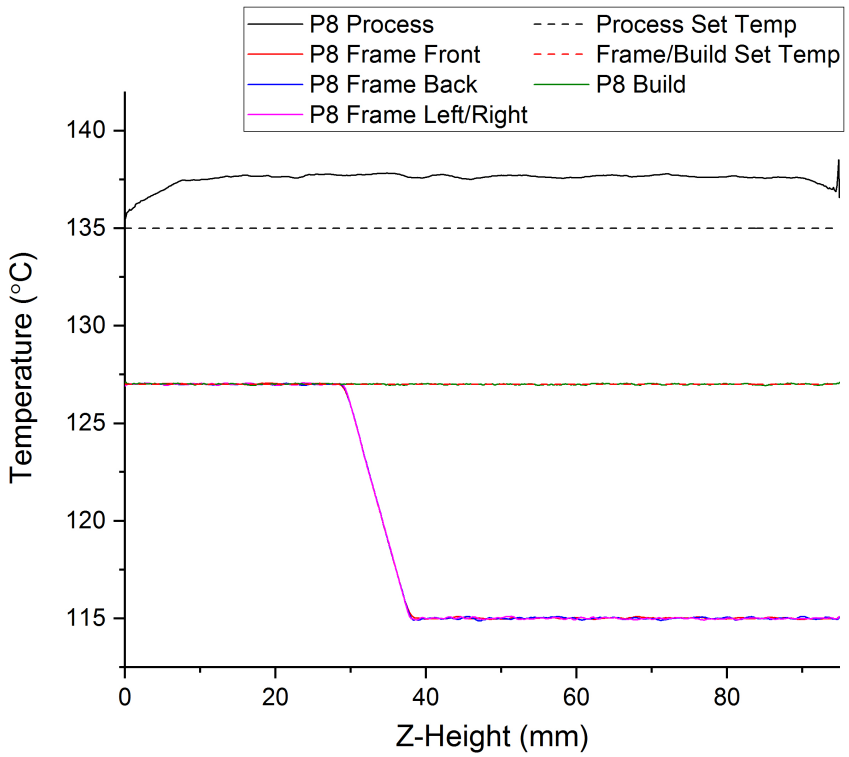

(a) Smoothed data output by P800 sensors

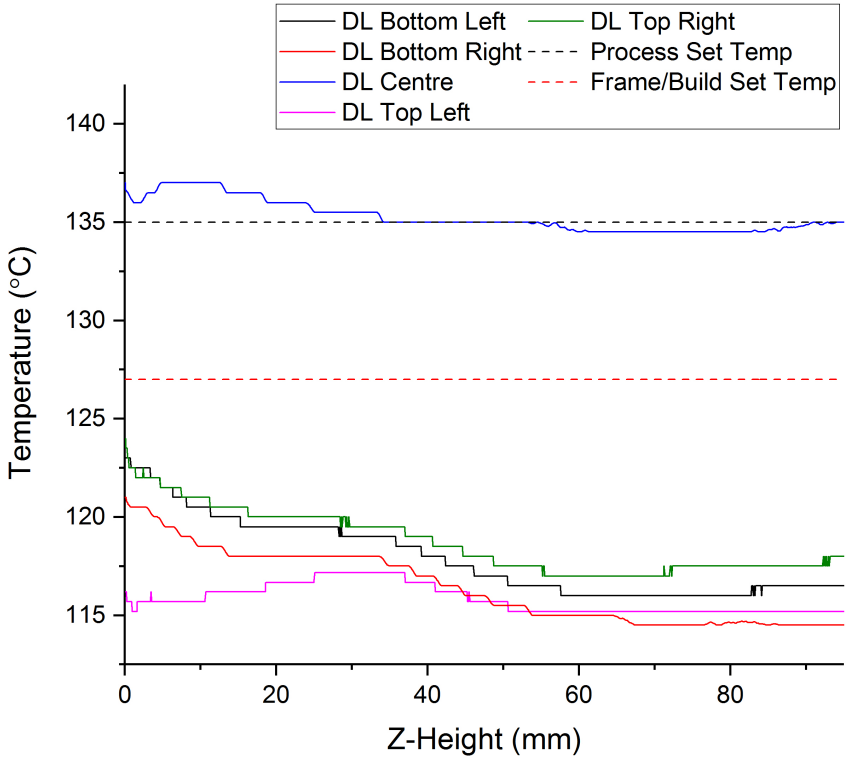

(b) Data from loggers

Figure 6.18: Comparison of data from P800 sensors and data loggers for Test 4

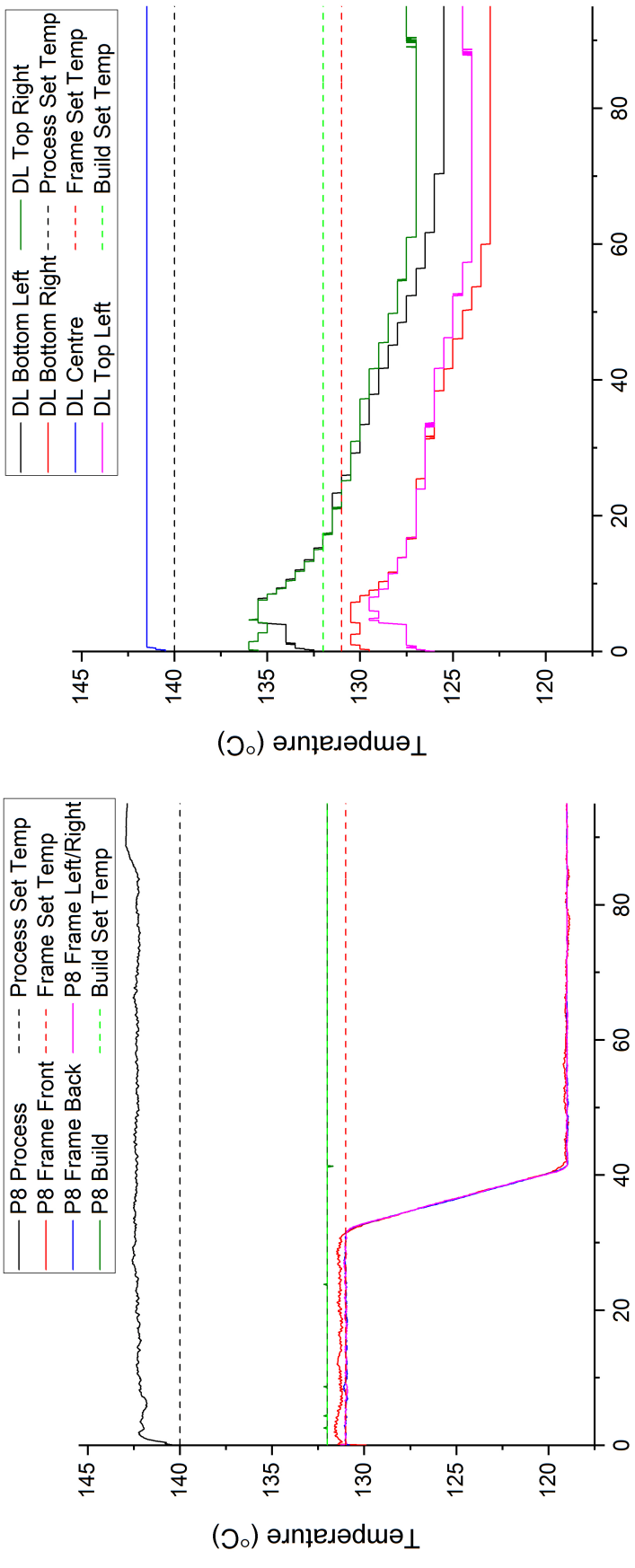

(a) Smoothed data output by P800 sensors

(b) Data from loggers

Figure 6.19: Comparison of data from P800 sensors and data loggers for Test 5

for all the tests. The amount by which the temperature is above the set point reduces as the set temperature is increased; in Test 1 (Figure 6.15) where the set temperature is 100°C the data shows the temperature is 103.5°C, a difference of 3.5°C. In Test 5 (Figure 6.19) the set temperature is 140°C and the recorded temperature is 142°C, only 2°C higher. The difference reduces incrementally in each test as the process chamber set temperature is increased. This could mean that at the actual build temperature the temperature in the process chamber is closer to the set temperature. During the empty build chamber tests the process temperature was lower than the set temperature; the results from the tests with powder confirm that the temperature in the process chamber is affected by the presence of the powder bed.

6.6.2.2 Logger Data

There is some similarity between the shape of the profiles of the logger data and the P800 sensor data in that they show a reduction in temperature from a higher to a lower temperature at some point during the test and then remain at a stable lower temperature for the remainder of the test. However, the heights and rates of the change differ for each test and in most tests there is a clear difference in the temperatures according to the location.

At the start of the profile the temperatures are all very different; the powder bed was left to pre-heat for a set period of time before the test began so it would be expected that the temperature for all locations would be similar. However, some trends can be observed; the top right and bottom right loggers begin at a higher temperature for most of the tests and slowly reduce, while the the top left and the bottom left loggers start from a lower temperature and increase or remain stable in most of the tests. It may be the temperature close to the surface of the powder is affected by the process chamber heaters inconsistently according to location.

As with the P800 sensor data, in all of the tests there is a clear region where the temperature drops steadily before reaching a stable temperature at which it stays throughout the rest of the test. This drop begins at an average height of

34.5±1.5mm whilst the end point is between 55.7 and 64.8mm. The temperature drop begins around the height that the temperature drop stabilises in the sensor data, likely due to the time it takes for the powder to absorb the heat from the heaters. The drop in temperature varies according to location as well as test - the largest temperature drop is the Top Right logger in Test 1, which drops 3.9°C, whilst the smallest drop is 1.5°C is registered by the Top Left logger in Test 3. Overall, the average drop across all corners for all tests is 2.9°C; with the exception of Test 1, most of the loggers drop by between 2.5 and 3°C between their highest temperature and the stable temperature at which they remain for the rest of the test.

There does not appear to be a correlation between the highest temperature observed and the set temperature for any of the tests. The Bottom Right logger in Test 1 begins at 1°C below the 94°C set temperature of the build platform/exchangeable frame. The largest recorded gap between the logger data and the set temperatures is the Top Left Logger in Test 4, which is 10°C lower than the 127°C set temperature. Overall, the Bottom Right comes closest to the set temperature across all tests, while the Top Left is the furthest away, however the individual values vary significantly from one test to another. Only in Test 5 do any of the loggers exceed the set temperature; in this case the Bottom Left and Top Right loggers record 3.5 and 4°C above the 132°C set temperature respectively.

There is however a correlation between the set temperature and the final stable temperature across Tests 1-4; on average for all all locations in these tests the stable temperature is 10.5°C lower than the set temperature, within a range of 1°C. The gap between the stable temperature and the set temperature is much smaller than this in Test 5 for the Bottom Left and Top Right loggers, while it's still slightly lower than the average for the Bottom Right and Top Left loggers. Across all the tests the Bottom Right is consistently the furthest below the set temperature but the other three locations show similar results with none clearly closer to the set temperature than the others.

The difference between the highest temperature and the stable temperature

show location specific results. The Top Left logger shows the smallest difference between the highest and stable temperature; an average of 3.5°C for all tests. The Bottom Left logger shows the second smallest average drop from highest to stable temperature at 6.4°C, however this is misleading as these range between 3.8°C in Test 2 to a 10°C drop in Test 5. This represents the largest range across all the corner locations; Top Right and Bottom Right show an average drop of 7.3 and 8.4°C respectively with a range of 3°C for both. Overall this makes the Bottom Left logger the most unstable in terms of temperature drop as each test is very different. The results for Test 5 do differ from the Tests 1-4 for some of the locations however; in the Top Left and Top Right the Test 5 drop is 2°C greater than the average of the other four tests, whilst for the Bottom Left the drop is 4.5°C greater than the average for the other four tests. Only in the Bottom Right is the temperature drop relatively consistent across all five tests.

In the lower temperature tests, the location data from all four corners is in relatively good agreement. In Tests 1 and 3 (Figures 6.15 and 6.17 respectively) the gap between the highest and lowest temperature is 0.8°C whilst in Test 2 (Figure 6.16) the gap is 1.9°C. The gap broadens in Test 4 (Figure 6.18) to 2.3°C between highest and lowest, although there is quite good agreement between the Top Left and Bottom Right curves. In Test 5 (Figure 6.19) however, there is a clear difference between the Bottom Left/Top Right and the Bottom Right/Top Left data; the gap between Bottom Left and Top Left is 3°C while the overall gap between the highest (Top Right) and the lowest (Bottom Right) is 4°C. The trend of this increasing gap as the set temperature is increased suggests that at the build temperature the difference between the locations could be amplified, that is, the temperatures at the four corner locations will differ significantly from each other.

The data from the centre for each test is a stark contrast to the four corners. In Tests 1-4 the profile for the centre logger is similar, beginning at a peak temperature and then slowly dropping to a lower temperature. In Tests 1 and 2 a stable temperature is reached and maintained for the rest of the test, while in Tests 3 and 4 this varies more. The difference between the highest and lowest temperatures for

the centre loggers varies between 2 and 3.5°C for Tests 1-4. The temperature in the centre is between 7 and 8°C higher than the build platform and exchangeable set temperature for these four tests and is far closer to the process chamber set temperature. Overall, the temperature at the centre of the test is on average 17.9°C higher than the lowest corner temperature measured. If this trend is true of the data at the actual build temperature then the centre of the powder bed is much, much higher than the corners and this will undoubtedly contribute to the degradation of the surrounding powder and to the very dark colour of the parts.

In Test 5, the data from the centre logger shows that the temperature remains stable at 141.5°C. However, the high temperature alarm was flagged when reading the results from the loggers and the lack of variation in the line would suggest that this temperature is the highest temperature the logger could read, not the actual temperature in the centre of the chamber. It is not possible to determine how much higher than the 141.5°C the temperature was but given the trend in the rest of the tests the actual temperature is probably around 143-4°C.

6.6.3 Comparison of Location Data

There are many factors which could influence the thermal map. Examining all of these simultaneously would be very difficult given the amount of data generated across all the tests. However, trying to analyse the factors in isolation is also ill-advised as many of the variables are likely to be co-dependent. Nonetheless, as a starting point graphs were plotted to look at how the test temperatures were affected by variation in location and build height.

There are two main factors to take into account; effect of location in XY, and the effect of variation in the build height.

6.6.3.1 Effect of Location in XY

The curves from each location are plotted against each other in Figure 6.20. They show that in general, the shape of the curve for each location is very similar. The initial peak varies somewhat but the overall rate at which the temperature decreases

for each location is the same regardless of the temperature of the actual test. The biggest difference in the shape of the peak is from Test 5 data for all locations; the curve from Test 5 for the centre can be discounted for reasons explained in the previous section. As previously discussed, it is not clear whether the difference between the Test 5 data and the data from the other four tests is indicative of a different temperature profile which may be closer in shape to the build temperature profile than these "lower" temperature tests. However, as it is only the initial peak which differs and the rest of the shape of the curve is similar for all tests it looks likely that the different profiles for each location are indicative of location specific temperature phenomena.

6.6.3.2 Effect of Variation in Build Height

To see how the temperature changes with build height, values were plotted for each location over a range of heights; in order to build an accurate thermal map it is important to understand how the temperature changes during the build. The resulting graphs are shown in Figure 6.21; the "test temperature" measured by the loggers is plotted against the set temperature for the process chamber, as this is the highest and as the closest to melting temperature of 373°C is the most significant.

Overall, they show that the temperature drops slightly as the build height increases. How much the temperature drops by varies between locations - at the centre the temperature drop between 10mm and 90mm is a maximum of 2.5°C, while at the bottom right the temperature drop is up to 6°C. However, the shape of each curve for a given location is the same regardless of height, therefore it can be assumed that the build height does not result in a significant change in temperature distribution and a curve extrapolated from data taken at 10mm would also be representative of the temperature at 90mm.

The data does show however that the relationship between test temperature and set temperature is not completely linear. The set temperatures were chosen as a percentage of the full temperatures required for sintering of PEK in the assumption that the temperature change would be linear; this was shown earlier in Figure 6.5.

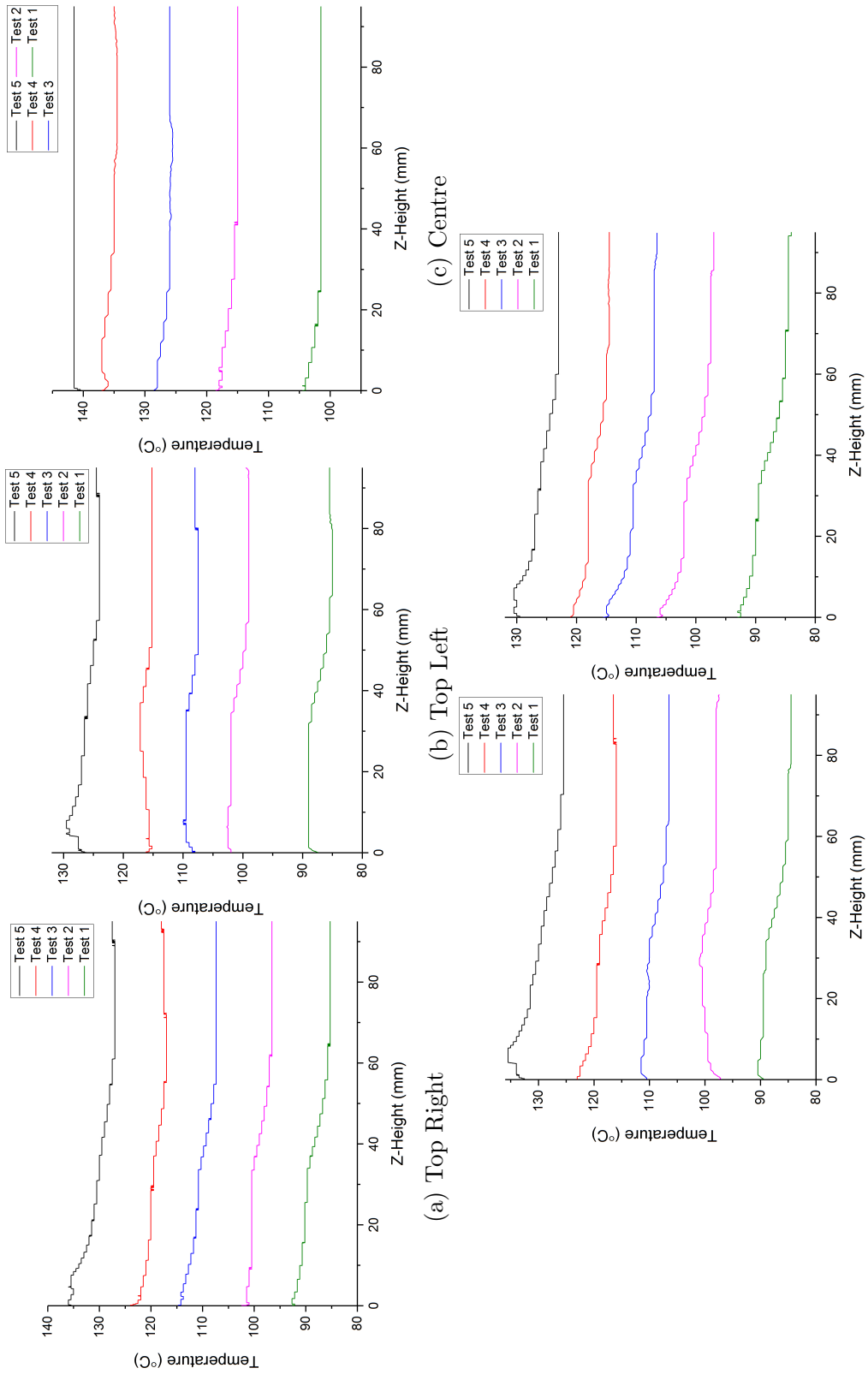

Figure 6.20: Comparison of logger data recorded a different locations

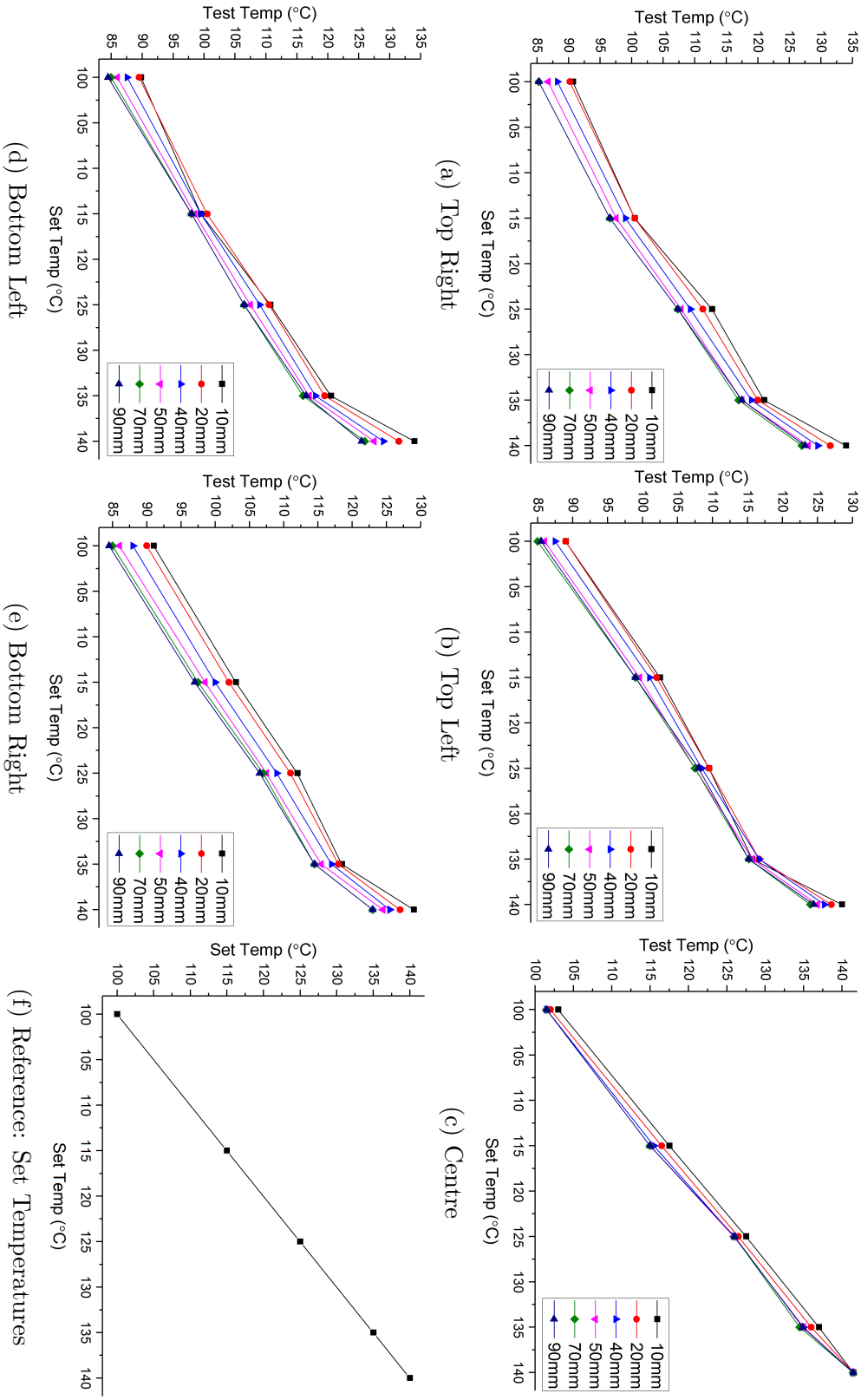

(a) Top Right (b) Top Left (c) Centre

(d) Bottom Left (e) Bottom Right (f) Reference: Set Temperatures

Figure 6.21: Comparison of location data recorded at different heights

The set temperature for the process chamber are plotted against themselves in Figure 6.21f to show how this compares to the test data. The test results show that the relationship between test temperature and set temperature is linear for the lowest four set temperatures (Tests 1-4). The test temperatures for the four corner locations are lower than the set temperature, particularly the top left and bottom right. Only the centre is quite close to the set temperatures for all tests; this has already been shown to be slightly higher than the process chamber set temperature.

The final point (Test 5) for the four corner locations does not follow the same straight line but is much higher, resulting in an overall curve. Differences in the temperature profile between Tests 1-4 and 5 have been seen throughout the data and it has been theorised that Test 5 may be indicative of a different temperature profile for a higher set temperature. It is unclear therefore, whether the results from Test 5 are erroneous compared with Tests 1-4 or associated with a different temperature profile compared to Tests 1-4.

As before, the results from the centre logger for Test 5 are the same regardless of height as a result of the actual temperature being above the limit of the logger capability. It can be safely assumed that the data recorded is not accurate which makes extrapolating this data particularly difficult.

6.6.4 Extrapolation of Test Data

The data does not show one clear trend from which a fitting method could be determined in order to extrapolate the temperatures up to the actual set temperatures for building. Thus it was decided to try three different fitting methods which seemed appropriate based on the discussion so far. Plotting the extrapolated curves from all three methods together should provide a range which may approximate the temperatures which take place during high temperature laser sintering:

1. Linear Method 1 (L1): assume that the data from Test 5 is erroneous, which is why it does not fit the linear relationship between Tests 1-4. Draw a line

of best fit through points from Tests 1-4 and extrapolate linearly to the build temperature.

2. Linear Method 2 (L2): Assume a linear relationship between all test data, even though Test 5 does not neatly fit with results from Tests 1-4. Create a line of best fit which passes through all five test points and linearly extrapolate to the build temperature.

3. Polynomial Method (Poly): Find a polynomial curve of best fit which runs through all five data points.

In the case of the centre logger only option 1 is possible, as the temperatures in Test 5 are considered inaccurate and therefore should not be included.

In order to find the extrapolated temperature, first the test values were plotted for each location and a line of best fit determined for each using the in-built Fitting function in OriginPro. The equation of the line was then used to find values for 345 and 368°C; these temperatures represent the set temperature for the exchangeable frame and the process chamber respectively. In the case of the polynomial method the equation was used to find a range of points in between the test data and the build set temperatures in order to produce a smoother curve. For simplicity only the values for one height were used for each extrapolation; graphs for 10mm and 90mm were plotted in order to compare how the height affects the temperature change.

The generic equations used to find the extrapolated temperatures are shown in Equations 6.1 and 6.2 for the linear methods and the polynomial method respectively:

$$y = a + bx \tag{6.1}$$

$$y = a + cx + dx^2 \tag{6.2}$$

where a is the intercept and b, c and d are constants specific to each set of data, calculated using OriginPro.

6.6.4.1 Linear Extrapolation Method 1

A line of best fit was plotted for each location for Linear Method 1 (L1) using data from Tests 1-4 and overall there was very good agreement between the data and the fitted line, with an average R^2 of 0.99. Some examples are given in Figure 6.22 to show the agreement and the data produced by OriginPro is given in the top left corner.

The extrapolated results are shown in Figure 6.23. At a Z-height of 10mm (Figure 6.23a), the range between all the extrapolated values at 368°C is 69°C between the highest and the lowest temperatures, and 33°C between the highest and lowest corner temperatures. The centre value is the closest to the set temperature, predicting 364°C, only 4°C lower. The lowest corner temperature is predicted to be 295°C in the top left, 73°C lower than the set temperature.

At a Z-height of 90mm (Figure 6.23b), the range at 368°C is much smaller, at 44°C between the highest and the lowest temperatures, and just 17°C between the highest and lowest corner temperatures. The centre value is 8°C lower than the set temperature, predicting a value of 360°C. The lowest corner temperature is predicted to be 315°C, still in the top left but only 53°C lower than the set temperature.

Overall, the extrapolated data shows that at 90mm the temperatures are more homogeneous across the build chamber; the temperature in the centre has decreased compared to 10mm but the corner temperatures have increased, with a much smaller range between the four corner locations. Whilst it was previously assumed that as the shape of the curve was roughly equivalent across the range of heights there would be little difference between the extrapolated values at each height, the amplifying effect of extrapolating to a much higher temperature shows the differences more clearly.

In practice what this would mean is that as the height of the build increases, the temperature becomes more stable across the XY plane which is likely to result in more even shrinkage and a lower likelihood of deformation due to temperature gradients at this level. By contrast the sintering will be less even at lower build

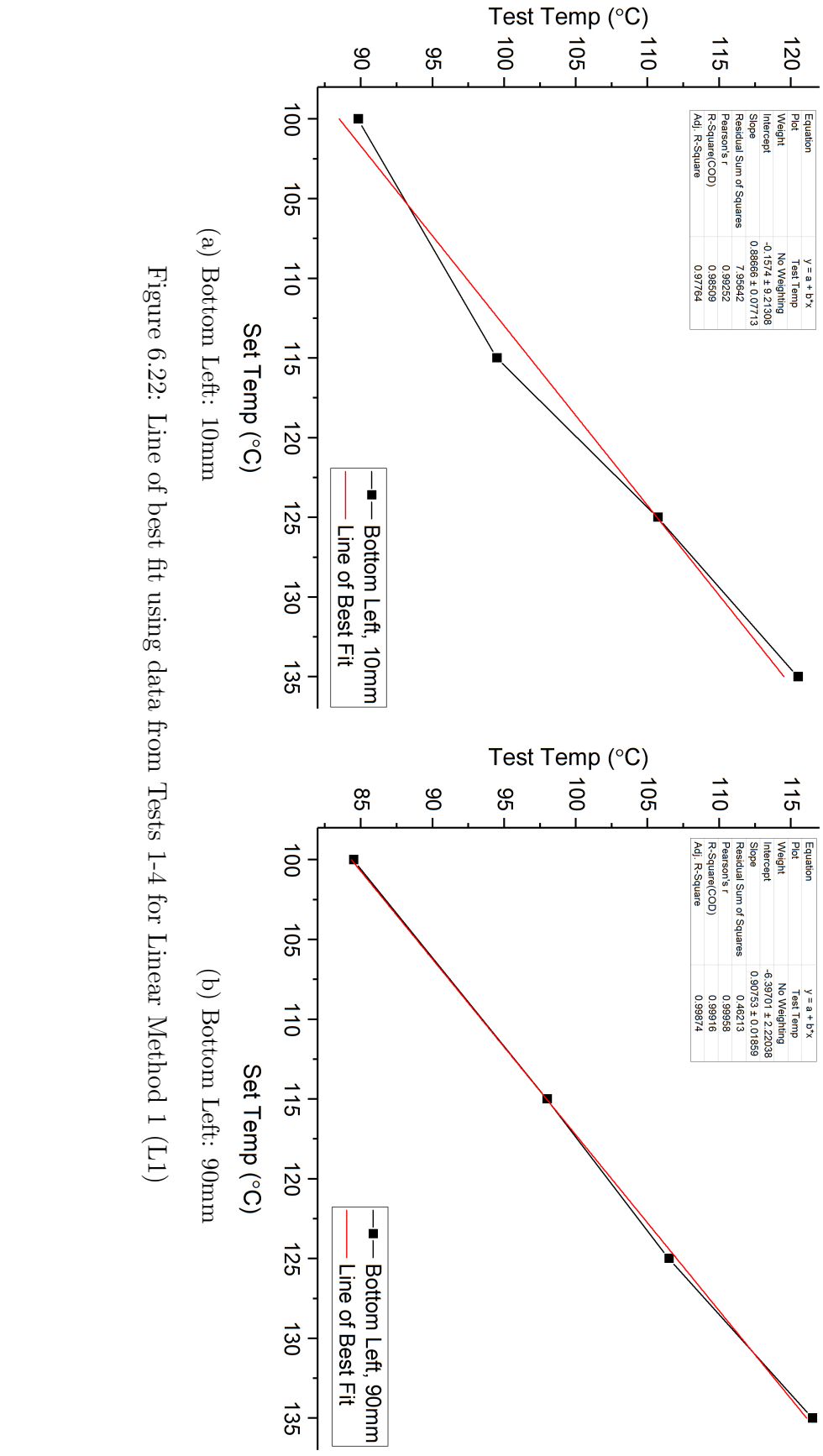

(a) Bottom Left: 10mm

(b) Bottom Left: 90mm

Figure 6.22: Line of best fit using data from Tests 1-4 for Linear Method 1 (L1)

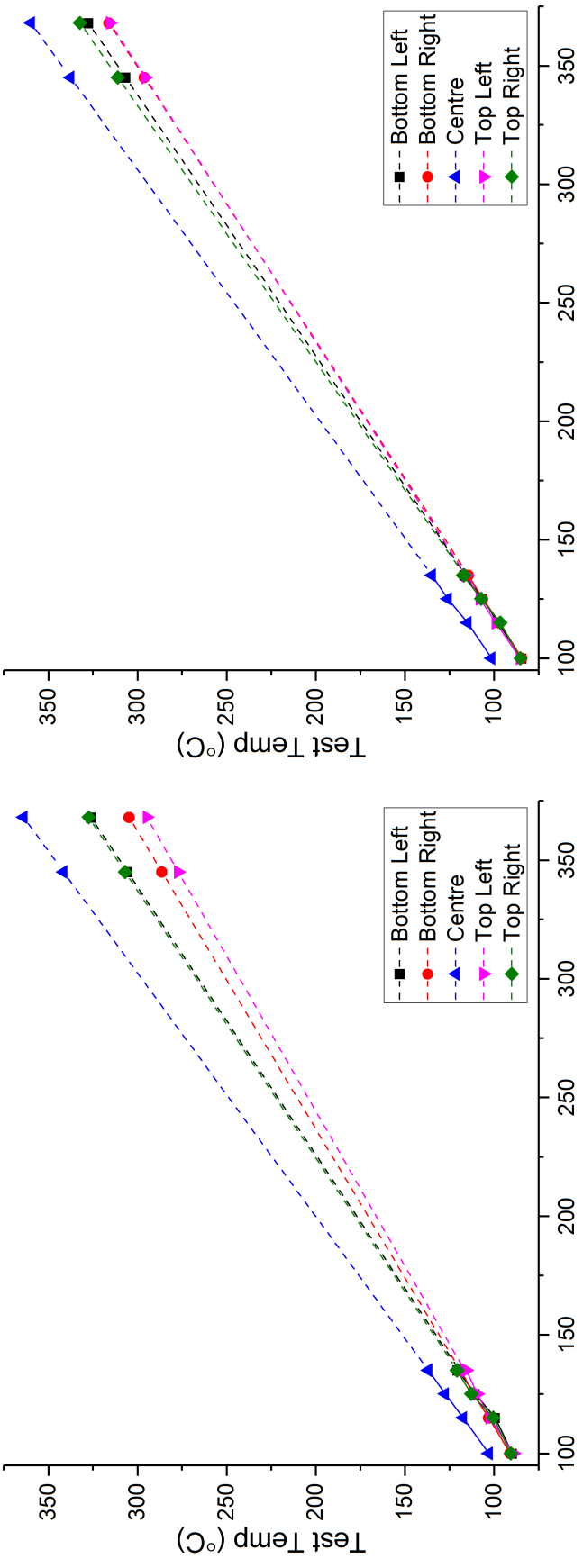

(a) Z-Height = 10mm

(b) Z-Height = 90mm

Figure 6.23: Linear Method 1 extrapolated temperature data: Solid line = test data, dotted line = extrapolated data

heights as the temperature range is larger. However, the tests were undertaken without the presence of parts in the chamber and this will change the thermal profile so these results are still only an indication of what could be occurring.

6.6.4.2 Linear Extrapolation Method 2

A line of best fit was plotted for each location for Linear Method 2 (L1) using data from Tests 1-5. At 10mm, the agreement between the data and the fitted line is good, with an average R^2 of 0.96; this lower than for Method L1. At 90mm the R^2 value is 0.99, demonstrating a more linear relationship between all five tests at higher z-height than had previously been assumed. Some examples of the fitting for Method L2 are given in Figure 6.24 to show the agreement and the data produced by OriginPro is given in the top left corner.

The extrapolated results are shown in Figure 6.25. At a Z-height of 10mm (Figure 6.25a), the range between all the extrapolated values at 368°C is 40°C between the highest and the lowest temperatures. The bottom left value is in agreement with the process chamber set temperature of 368°C, while the top right is not far behind, predicting 365°C. There is a distinct difference between the bottom left/top right values and the bottom right/top left values; the temperatures for the latter two are 330°C and 329°C respectively, a difference of 38°C between both the set temperature and the bottom left corner. This predicts a slightly higher discrepancy between corner locations than Method L1.

At a Z-height of 90mm (Figure 6.25b), the range at 368°C is 25°C between the highest and the lowest temperatures. All temperatures are lower than the process chamber set temperature; the top right is closest, predicting 359°C. The bottom right and top left are still the lowest temperatures, predicting 333°C and 334°C respectively.

The extrapolated data predicted by Linear Method 2 show similar trends to Linear Method 1; there are large differences between the temperatures at the four corners, and the temperature is more homogeneous at 90mm across all locations. However, rather than showing a range of temperatures between highest and lowest,

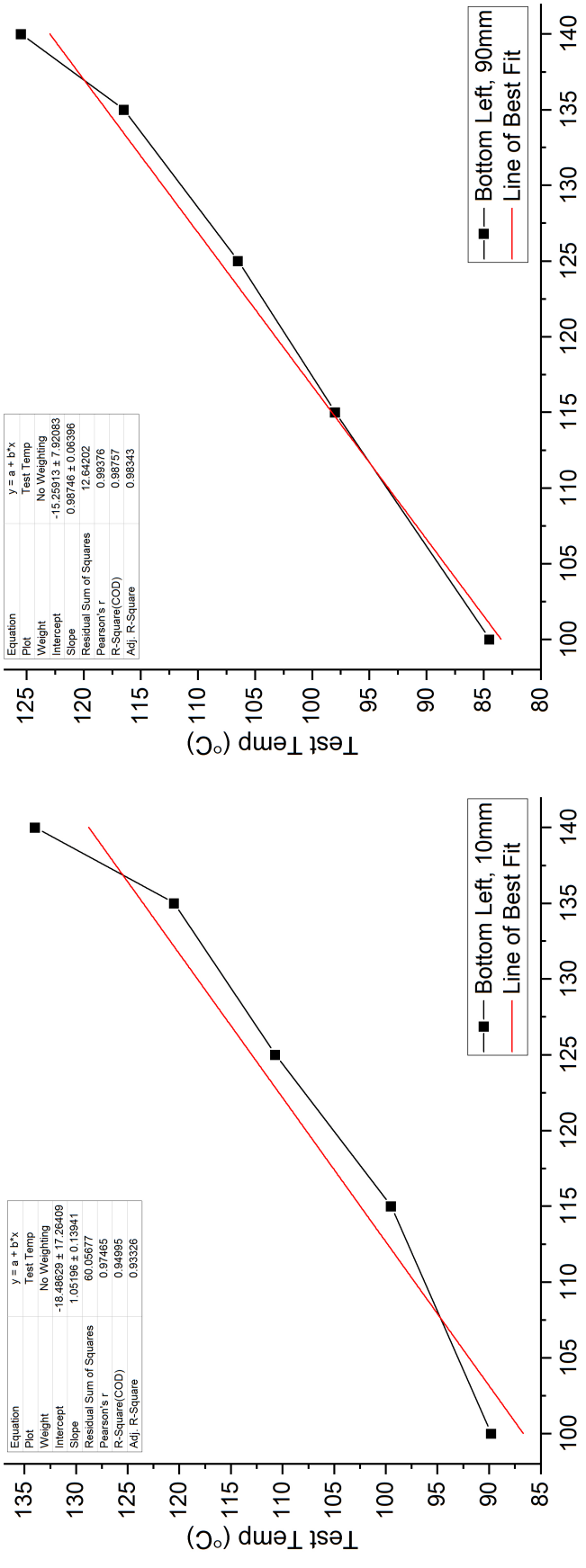

(a) Bottom Left: 10mm

(b) Bottom Left: 90mm

Figure 6.24: Line of best fit using data from Tests 1-5 for Linear Method 2 (L2)

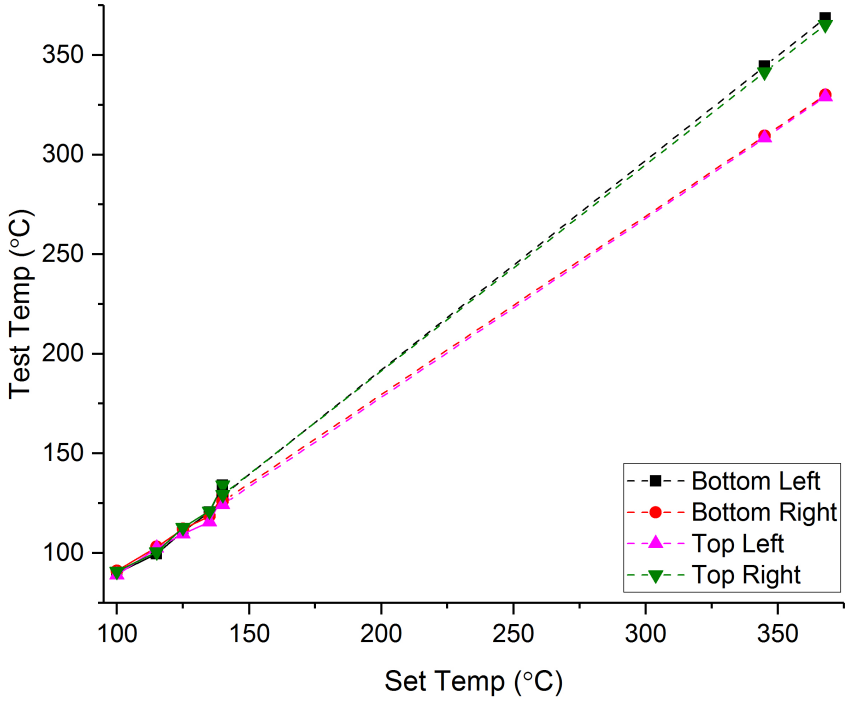

(a) Z-Height = 10mm

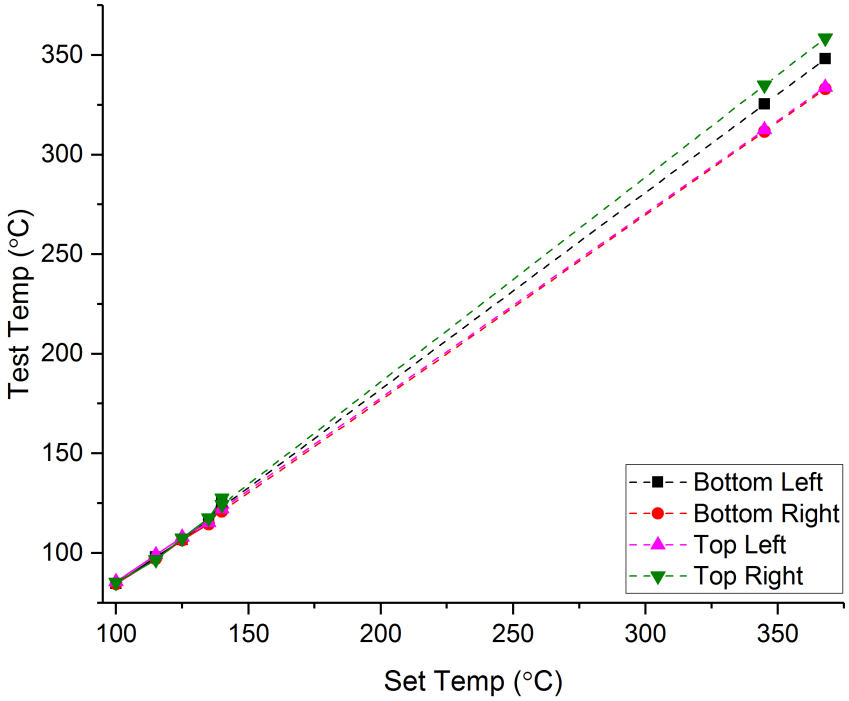

(b) Z-Height = 90mm

Figure 6.25: Linear Method 2 extrapolated temperature data: Solid line = test data, dotted line = extrapolated data

this method suggests that there are two distinct temperature ranges at 10mm for the bottom left/top right and bottom right/top left locations.

Overall, the temperatures predicted by Method 2 are higher than those for Method 1, but are still lower than the set temperature.

6.6.4.3 Polynomial Extrapolation

Using OriginPro, a polynomial order 2 fitting curve was applied to all five data points for each of the four corner locations; some best fit curves are given in Figure 6.26. The curves are in relatively good agreement with the data, showing an average R^2 of 0.98 for 10mm, and 0.99 for 90mm. Extrapolated values for the build set temperature were calculated from the equation of the curve of best fit as explained earlier, and the results are shown in Figure 6.27.

Overall, the results from the polynomial method seem unrealistic. The highest temperatures predicted are 1460°C in the bottom left at 10mm, and 1073°C in the top right at 90mm, which are substantially higher than the 368°C set temperature and even the 373°C melting temperature. The lowest temperatures predicted are 722°C in the bottom right at 10mm, and 564°C in the top left at 90mm. Such high temperatures would result in total melting of the powder bed as well as significant decomposition, which occurs in virgin powder above 590°C as determined in Section 4.4. Thus of the three extrapolation methods, the polynomial extrapolation method appears to be the least likely to reflect actual build temperatures, even though the curves of best fit were in good agreement with the data.

6.6.4.4 Comparison of Results

In order to compare the methods, the three extrapolated curves for each location were plotted together and the results are shown in Figure 6.28 for 10mm and in Figure 6.29 for 90mm. Only Linear Method 1 (L1) could be used on the data for the Centre logger, so only one line is shown for this location. As it was not considered realistic that the temperature in the chamber is exceeding 500°C, the plots were limited to this temperature and the process chamber set temperature is

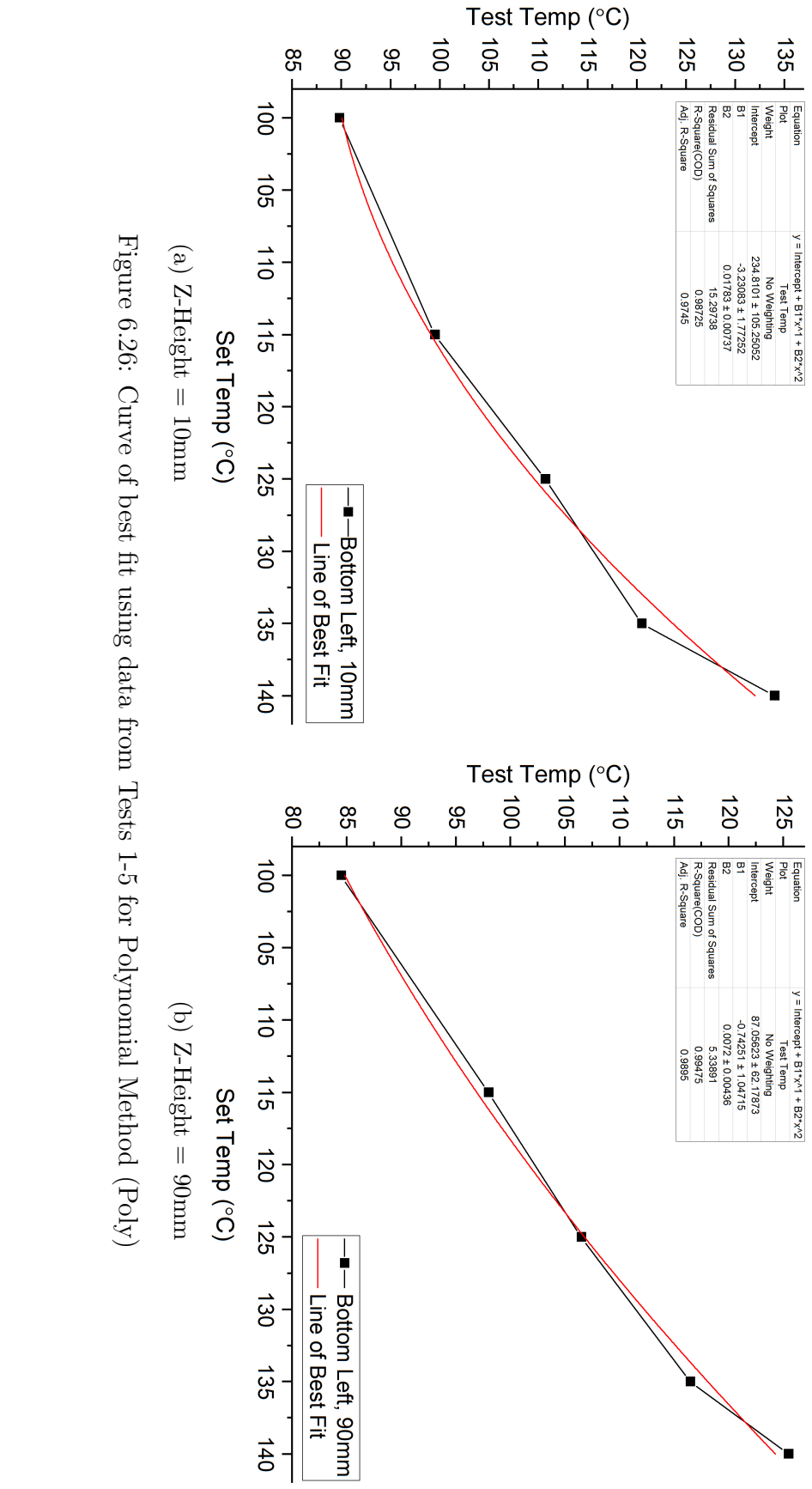

(a) Z-Height = 10mm

(b) Z-Height = 90mm

Figure 6.26: Curve of best fit using data from Tests 1-5 for Polynomial Method (Poly)

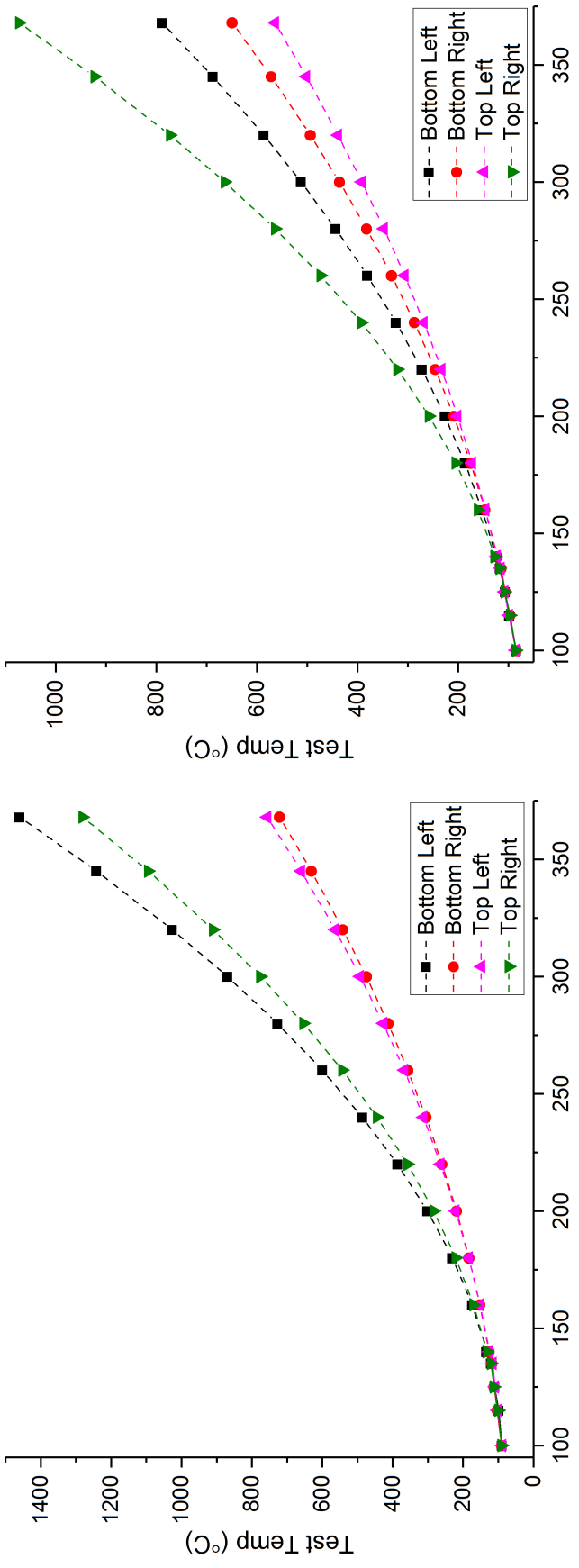

(a) Z-Height = 10mm

(b) Z-Height = 90mm

Figure 6.27: Polynomial Method extrapolated temperature data: Solid line = test data, dotted line = extrapolated data

shown for comparison.

The results are consistent across all tests; L1 predicts the lowest temperatures, L2 shows slightly higher temperatures, and the polynomial method predicts the highest temperatures. Of all three methods, L2 is consistently the closest to the process chamber set temperature. There is significant variation in the predicted temperatures for each of the corners; the bottom right and the top left in particular are higher than the top right and the bottom left, although the difference between the four corners is lower at 90mm than at 10mm.

L1 predicts that the centre of the chamber reaches the set temperature while the corners do not. Earlier results about the material properties show greater degradation in the centre than in the corners; the results here show a higher temperature in the centre than in the corners which conclusively confirms this finding. However, the low temperatures predicted by the linear methods may not be enough to cause the degradation seen in the powder, as the TGA results showed that mass loss associated with decomposition of the material does not begin until 466°C. This suggests that the temperatures at the build height are higher than the linear methods predict.

The polynomial method suggests that the set temperature is exceeded for all four corners. Given the maximum temperatures which the polynomial method predicts, it is not suggested that the correlation between the set temperature and the predicted test temperatures is accurate. However, the curve of best fit showed good agreement with the experimental data, so even though the temperatures predicted by the polynomial curve are unrealistic, it cannot be concluded that they are completely wrong. Furthermore, if the temperatures must be higher than the linear methods predict in order for degradation to occur, it follows that the actual temperatures must fall in the range predicted between the linear methods and the polynomial method.

As all three lines of best fit show good agreement with the experimental data, it can be assumed that all three offer valid insights into what is occurring at actual build temperatures. Whilst the range of temperatures predicted is extremely broad

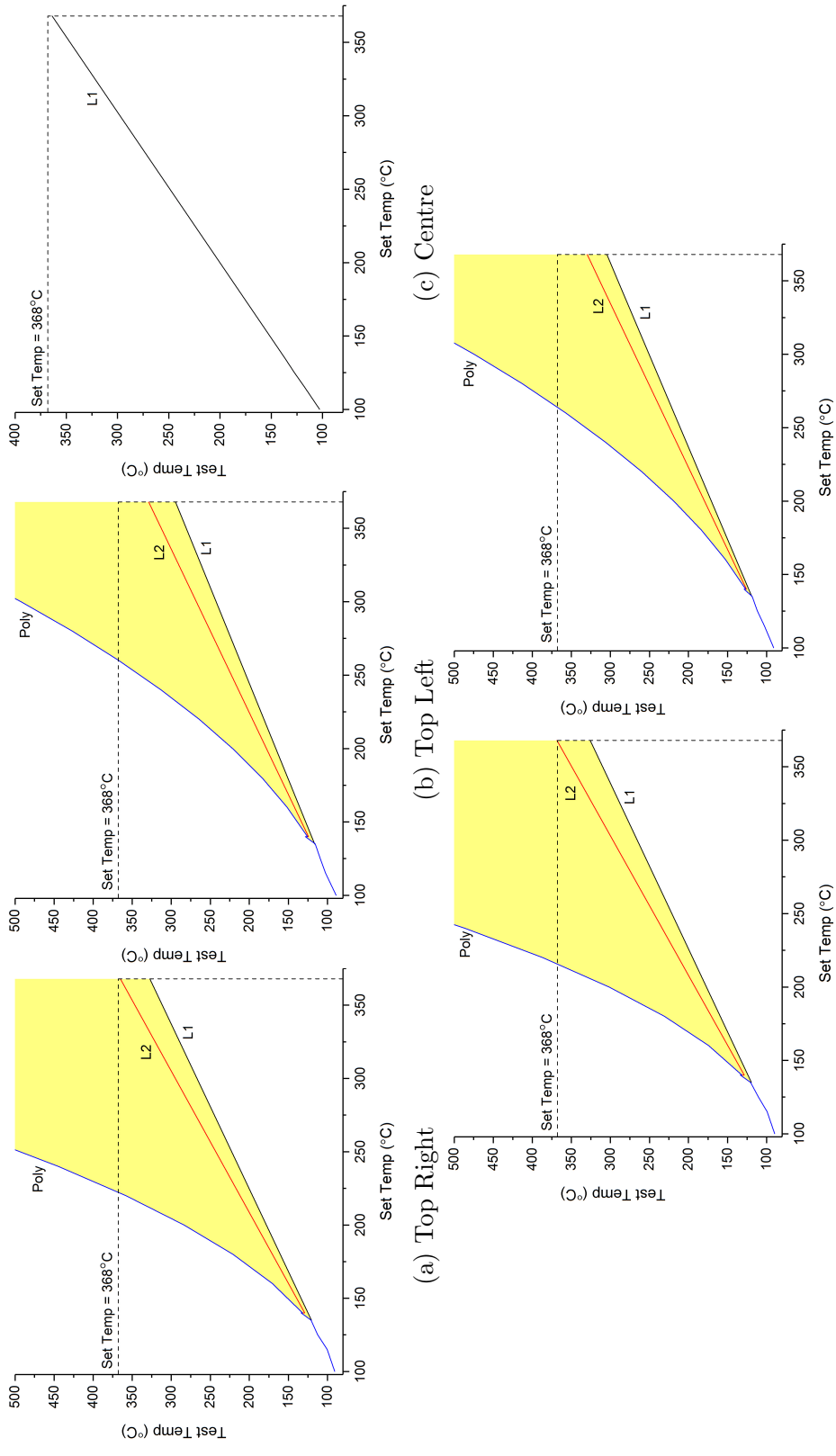

(a) Top Right (b) Top Left (c) Centre

(d) Bottom Left (e) Bottom Right

Figure 6.28: Comparison of extrapolation methods for indivdual locations at 10mm. Black Line = Linear 1 (L1), Red Line = Linear 2 (L2), Blue Line = Polynomial (Poly). Process chamber set temp = dashed line

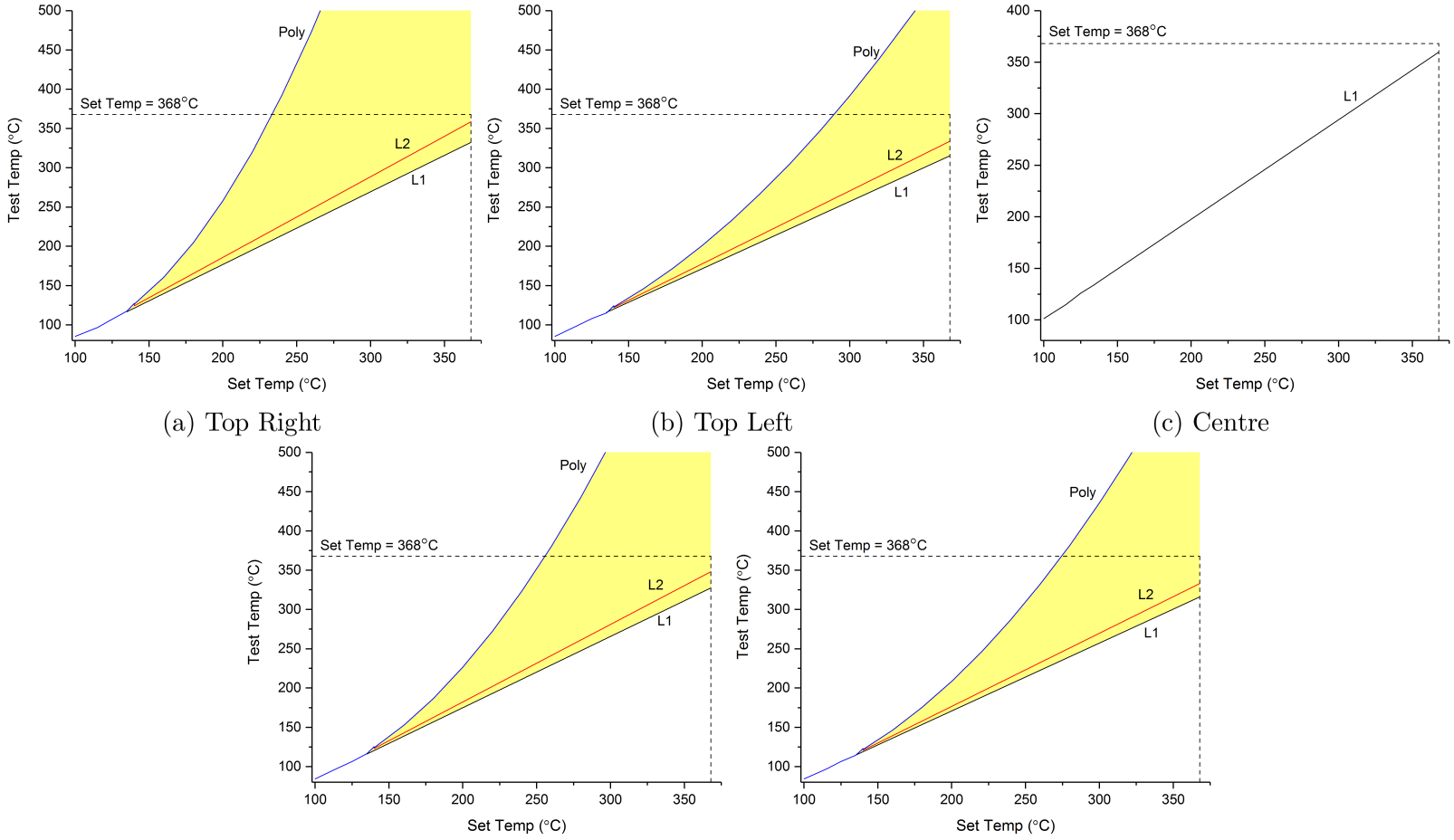

(a) Top Right (b) Top Left (c) Centre

(d) Bottom Left (e) Bottom Right

Figure 6.29: Comparison of extrapolation methods for indivdual locations at 90mm. Black Line = Linear 1 (L1), Red Line = Linear 2 (L2), Blue Line = Polynomial (Poly). Process chamber set temp = dashed line

and therefore is not necessarily helpful for specifying the temperatures which are occurring and how they may result in the properties seen in used powder, there is a clear difference between the four corner locations and the centre which does confirm earlier findings. Only powder from one corner was considered for material characterisation; the results here suggest if powder were tested from all four corners they may show different characteristics from each other.

Research undertaken to examine temperature distribution has generally consisted of either building parts and testing them in order to infer what is occurring in the powder bed [108], or taking measurements at the surface of the powder to create a 2D map in the XY direction [67, 110]. All of the research either demonstrates or infers an uneven temperature distribution with a higher temperature in the centre than at the edges, and the current study shows that this is also occurring in the P800.

More invasive methods of temperature measurement involving modifications to the system to accommodate sensors have been able to produce 3D maps of temperature variation [112]. The method presented in the current study does not require modification to the system, thus making it potentially useful for systems which are in use in a production environment rather than simply academic. A potential improvement to the method presented here could be to use thermal imaging at the surface of the powder as well as the loggers, as was undertaken by Wegner and Witt [113]. They were able to compare the results to show that the powder bed temperature reduces with distance from the surface, which is important for understanding how the properties of parts built at the bottom of the build differ from parts built towards the top.

6.7 Conclusions

The purpose of the work in this chapter was to understand how the P800 system controls heat, and to map the temperatures which are occurring by location in X, Y and Z directions.

Experiments undertaken to verify the accuracy of readings from the data

loggers showed that they were comparable to thermocouple readings for constant temperature but experienced a lag during quicker changes in temperature.

By undertaking tests in the chamber whilst empty it was established that the P800 is capable of heating to and maintaining a lower temperature range than is required during building; the temperature limit of the wireless data loggers intended for measuring the temperature inside the powder bed was far lower than the temperature required to sinter PEK, necessitating using a lower temperature to compare measured data with the sensor output. Variation in temperature across the build platform was not displayed by the sensor output. The four heater bands display different temperatures from each other, with some much closer to the set temperature than others.

The P800 sensors showed a very consistent heating profile during the reduced temperature builds. The build platform matched the set temperature whilst the exchangeable frame initially matched the set temperature before reducing partway through the test, presumably as the powder retains a significant amount of heat and the heating required of the system is lower. The process temperature read higher than the set temperature but the difference between the two reduced as the set temperature increased, which may be indicative that the temperatures are more closely aligned at full build temperature.

Data from the loggers showed a similar profile to the P800 sensor data but at a different z-height in the build to the sensors. There was also far more inconsistency in temperature according to location. Overall, all four corner locations were below the set temperatures whilst the centre was higher. However, the shape of the profile for each location was similar for each set temperature, showing that the profile observed was consistent and specific to that location.

Values plotted for each location across a range of build heights showed a linear relationship between set temperature and test temperature across Tests 1-4 but with a significant increase in temperature in the test temperature in Test 5, regardless of height. The temperature was shown to decrease slightly as the z-height increased, likely as a result of the distance of the powder away from the process

chamber heaters which are set higher than the other heaters.

Three different methods were used to extrapolate the test data upwards to predict the build temperatures and showed a range of temperatures beginning lower than the set temperature but also far exceeding it. The temperatures predicted linearly by plotting a line of best fit through all five data points was closest to the process chamber set temperature for all locations. Predicting actual temperatures using a polynomial curve suggested temperatures in excess of 500°C which would result in significant decomposition of the material if they were occurring. However, the linear methods do not predict temperatures considered high enough to result in the degradation seen in the earlier results, thus the polynomial predicted temperatures may have some merit.

The extrapolated data shows difference in the temperatures in the four corners, with all potentially below the set temperature. However, the centre of the build was very close to the process chamber set temperature, suggesting that if the temperatures are higher than the linear methods predict, the temperature at the centre exceeds the set temperature which could cause the degradation seen in the Chapter 4.

The preliminary work taken to verify the accuracy of the data measuring equipment and the consistency of the heaters to maintain the set temperatures shows that the method used to measure the temperatures in the chamber was sound and therefore the results are reliable. As all three lines of best fit show good agreement with the experimental data, it can be assumed that all three offer valid insights into what is occurring at actual build temperatures. The key points taken from the thermal map are that the temperature distribution is uneven across the powder bed in the X, Y and Z directions, and the temperatures which are occurring in the system may be higher than the P800 sensors read.

Comparison with other research into temperature distribution shows that uneven temperature distribution within the powder bed is common in all laser sintering systems. Furthermore, whilst the current study reinforces results from other studies regarding temperature distribution in laser sintering systems, this may

be the first to compare measured temperatures with data output by the system's built-in sensors in order to demonstrate that there is a discrepancy between what is occurring and what the system is able to measure. This is important as the ability of the system to measure and control the temperatures in the powder bed determine the properties which can be achieved in built parts and the reusability of used powder.

Chapter 7

Conclusions & Further Work

7.1 General Conclusions

The scope of the thesis, entitled "Material and Process Characterisation of PolyEtherKetone for EOSINT P800 High Temperature Laser Sintering" has been to investigate the commercially available EOSINT P800 high temperature laser sintering system and associated material HP3 PEK, with a specific view to understanding the properties of as-received and used powder and how they behave when exposed to heat, and how temperature is controlled and distributed in the EOSINT P800.

Material characterisation was undertaken on samples of HP3 PEK powder with different thermal histories in order to understand the physical and thermal properties of virgin material and the difference between the as-supplied powder and used powder.

Following this, an extensive investigation into the coalescence of virgin and used powder was undertaken in order to understand the kinetics of coalescence in these materials and the temperatures involved to achieve complete coalescence of powder with differing thermal histories. Theoretical sintering models were suggested as a potential method of predicting coalescence behaviour based on material data and were compared with experimental data.

Lastly, tests were undertaken to examine the temperatures inside the EOSINT

P800 during building; low temperature data loggers were embedded in the powder during a simulated build and compared with temperature output from the heat sensors built into the P800. From this a thermal map was constructed showing how temperatures in different locations for a given X-Y layer compare and the data extrapolated to predict what temperatures may be occurring during a regular build.

Whilst some studies into the P800 and HP3 PEK have been undertaken previously, this is the first to systematically investigate both the material and the machine in order to build up a complete picture of how the material behaves under application of heat and what temperatures the material is subjected to which results in the unique properties of the used powder. Used powder was considered in terms of its location and significant variation was seen from the centre to the corner. This has implications for use of the P800 if consistency of parts across all building locations is to be achieved.

In general terms, coalescence and process characterisation have been shown to be useful for understanding the behaviour of material when heat is applied and how the machine may be contributing to certain material characteristics as a result of the temperature in specific locations. Furthermore, while previous studies have undertaken to consider the temperature at the surface of the powder [110, 111], or the effect of temperature on shrinkage or mechanical properties on built parts [2, 108], this may be the first study to embed sensors in the powder in order to measure the temperature inside the powder bed during a simulated build, thus showing the impact of an uneven temperature distribution over height in the Z-direction as well as in the X-Y plane. The comparison of experimentally determined temperatures with those measured by sensors built into the machine show that machine hardware needs to be significantly improved if greater consistency is to be achieved in LS components.

7.2 Specific Conclusions

7.2.1 Material Properties (Chapter 4)

The majority of previous research undertaken into LS materials has been on polyamide and variants thereof; its properties and behaviour are well established and guidelines for new materials are generally based on the properties of PA which make it effective for LS. HP3 PEK was considered in terms of these guidelines and the following observations were made:

- Virgin HP3 PEK powder is a combination of round, oval and irregular shaped particles with a fibrous morphology, which according to literature could inhibit flow and result in poor packing. The particle size distribution shows a number of particles below 37.5 µm which are inadvisable due to the potential for static forces making powder spreading difficult.

- Thermal analysis shows that virgin HP3 PEK has a double melting peak, and a distinct overlap between the melting and recrystallisation temperature ranges, that is, it has no clear processing window. This in theory could result in uneven shrinkage and localised differences in crystallinity when used in LS.

- By contrast, overflow and used powder particles are smoother than virgin, with fewer small particles and a larger processing window between melting and recrystallisation, which in theory should lead to better flow and packing and more stable sintering than virgin powder.

- The stable sintering region for virgin HP3 PEK calculated from DSC and TGA results is 75°C, which is much smaller than PA12 and PEEK 450PF. Refreshing with overflow powder would not affect the stable sintering region but refreshing with sieved mixed used powder would reduce the stable sintering region to 60°C.

In this regard it was shown that some guidelines in literature which are predominantly based on PA are potentially too restrictive as HP3 PEK shows

many so-called undesirable properties and yet works for HT-LS according to other studies [12, 122]. The stable sintering region is a recent method of identifying the temperature at which LS materials can be processed which take into account more of the material properties and shows that materials which do not have a processing window can be successfully sintered.

In addition,

- The location in the build chamber that used powder is taken from significantly affects its thermal properties; DSC shows that while used powder in general has higher crystallinity than virgin, the overall crystallinity reduces with proximity to the centre of the build chamber. Recrystallisation is similarly reduced in centre powder, and the glass transition temperature increases with proximity to the centre of the build chamber. This points to degradation of the powder by crosslinking, with the amount of crosslinking increasing with proximity to the centre of the chamber.

- Discolouration was observed in overflow and used powder compared with virgin, with the temperature getting darker with proximity to the centre of the build chamber. Long periods of time held at high temperature are known to produce discolouration in PAEKs, but the difference in colour by location supports the theory that there is significant temperature variation across the powder bed.

- UV-visible spectroscopy was introduced as a method of measuring discolouration which could potentially be used to link physical properties of powder with intrinsic properties such as crystallinity and melting temperature.

7.2.2 Coalescence Behaviour (Chapter 5)

Observation of the coalescence of pairs of particles has been undertaken for many materials in order to identify the working temperatures required for different processing methods and to understand melting behaviour. Some work has been

undertaken previously on coalescence of LS materials in order to verify the stable sintering region. However, this is the first to look at how particle properties and melting behaviour affect coalescence, and to study the coalescence behaviour of used powder in order to understand both how it differs from virgin and how it is affected by the location in the build chamber.

- Heating rate was shown to affect coalescence, with low heating rates resulting in little to no coalescence, and greater coalescence occurring as heating rate was increased. Full coalescence in virgin powder occurs at heating rates of 80°C min^{-1} or higher. In used powder, full coalescence of corner powder was observed at 100°C min^{-1}, but less in mid powder and none in centre powder, regardless of heating rate.

- Virgin powder does not coalesce when heated isothermally; in isothermal tests almost all coalescence was shown to occur before the isothermal holding temperature was reached or within a couple of minutes of the temperature being reached, which could be attributed to thermal lag.

Comparison of experimental data with theoretical models calculated using material data for PEK predicted coalescence occurring approximately 100 times faster than was seen in practice. The melting behaviour of HP3 PEK appears to differ from other polymers which coalesce isothermally, although application of the theoretical models to dynamic hot stage tests rather than isothermal may also account for the discrepancy between theory and experimental results.

7.2.3 Temperatures in the P800 (Chapter 6)

Used HP3 PEK powder is not recommended for re-use in HT-LS and shows very different properties compared with virgin; thus it is desirable to understand what temperatures are occurring in the build chamber during a typical build and how they result in the properties seen in used powder;

- Data from the EOS sensors shows that the temperature of the build platform closely matches the set temperature, but that the exchangeable frame follows

a profile whereby the temperature is reduced partway through the build. The logger data shows a similar profile, albeit it with significant variation by location, with some corners showing lower temperatures than others and the highest temperature recorded in the centre.

- Extrapolation of logger data up to the standard build temperature for HP3 PEK suggests that the temperatures are in excess of those recorded by the built in sensors, and are high enough to cause the degradation observed during earlier material and coalescence characterisation of used powders.

- The extrapolated data shows an uneven temperature distribution across the build chamber; the temperature at the four corner locations differ from each other, with the top left lowest and the top right highest, while the centre is significantly hotter than all four corners.

7.3 Limits

The EOSINT P800 and HP3 PEK are relatively new to market and very little published research is currently available. As such, this study presents a preliminary investigation covering a broad range of topics.

Investigation into the properties of used powder would be considerably strengthened by analysing powder from that location in multiple builds, or from more locations such as all four corners rather than just one.

Particle shape was considered qualitatively from SEM images; thorough analysis of the particles using the method for roundness and circularity as described by Berretta [126] would quantitatively demonstrate the difference between virgin, overflow and used grades of powder.

XRD analysis was very general and crystallinity calculated in order to compare with DSC findings; XRD is a powerful tool capable of identifying specific crystal structures and unit cell dimensions which may explain more thoroughly the differences between different grades of powder.

Some of the limitations of the results presented in this thesis are as a result

of the difficulty performing tests at high temperature. Surface tension of the melt could not be measured due to lack of availability of equipment capable of achieving up to 400°C. Likewise 400°C was the physical limit of the capillary rheometer requiring calculation of viscosity at higher temperatures, thus potentially introducing inaccuracy into coalescence models.

The data loggers were only suitable up to 140°C; thus it was necessary to undertake tests at lower temperatures and extrapolate upwards to the standard build temperature for HP3 PEK. Three methods were devised to interpret the data in order to extrapolate to higher temperature and all gave different results. The temperature range predicted represents an estimate of what is occurring.

Lastly, the thermal map is presented for a build in which no sintering is undertaken. In practice the presence of parts in the build will increase the temperature in those areas; thus the temperature predicted for the corners will inevitably be higher if parts are being built there. Similarly, the temperature in the centre may exceed even the values calculated here depending on the size and distribution of parts being built.

The amount of data collected from the five locations as well as the data from the built in sensors presented a challenge in terms of analysis; whilst data from specific locations or a specific height could be compared for each of the temperature profiles tested, plotting changes occurring in the X, Y and Z directions simultaneously for each profile in a manner which allowed for clear presentation of results was considered infeasible. However, breaking the data down into specific subsets made identifying the connections between different events which were occurring a challenge. If data could be collected for only the temperature at which building takes place, this may simplify analysis.

7.4 Suggestions for Further Work

As a body of work undertaken in a finite period of time, it was not possible to pursue thoroughly everything which was of interest;

This section will cover two elements; projects arising from this work which may

merit further investigation, and projects which could be undertaken in order to build on and develop the work undertaken here.

7.4.1 General Recommendations

Several trends have been identified in used powder according to the location it was taken from, specifically varying degradation from the corner to the centre as a result of uneven thermal distribution within the powder bed. A more systematic investigation into the properties of used powder by location is recommended in order to prove conclusively some of the results found during this study, particularly regarding crosslinking as this permanently alters the material properties and thus whether it can be successfully re-used, and whether the uneven temperature distribution results in different properties in powder from all four corners of the chamber.

UV-visible spectroscopy presents an interesting new method of non-destructively identifying the properties of built components by measuring their colour. A suggested study would be to measure the spectra of tensile samples and subsequently test them both for tensile properties and using DSC in order to build up a database which correlates mechanical properties and crystallinity with specific spectra.

Other models such as Kuczynski's [153] could provide insight into what flow mechanisms are occurring in the melt which would further understanding of coalescence. Furthermore, numerical simulation of the coalescence process of HP3 PEK using finite element method could prove more accurate for predicting coalescence properties than the simple analytical methods undertaken in this study.

7.4.2 Future Work

This study has demonstrated that the temperatures which are occurring in the build chamber are both higher than the built in sensors suggest and contribute to the unique properties of used powder which currently render it unsuitable for re-use. Thus two directions present themselves; investigate build parameters in

an attempt to reduce the temperature required for successful sintering and thereby reduce degradation of powder leading to potential for its re-use, and more effectively control the temperature distribution within the build chamber in order to avoid the very high temperatures at the centre compared with the corners.

Given the high cost of HP3 PEK it is desirable to reduce the degradation which occurs in the material in order to improve its re-usability and identify how to re-use the material successfully. Thus, the logical direction of study is to investigate build parameters to identify if it is possible to reduce the temperature in the build chamber, thus improving the quality of used powder, and also to investigate build parameters in which refreshed powder can be used to build parts without detriment to the mechanical and physical properties of the components.

A stable sintering region has been identified for virgin HP3 PEK. Following on from the stable sintering region, Vasquez et al [102] presented a method which employs the Energy Melt Ratio (EMR) of a material to predict processing parameters which will lead to successful sintering with minimal degradation. EMR takes into account several processing parameters including bed temperature, laser power, scan spacing, scan count and layer thickness along with material properties such as melting temperature and enthalpy of melt. Multiple EMR values can be calculated based on different combinations of the parameters but can also be solved to find which EMR values will lead to degradation, thus allowing these to be avoided.

Vasquez et al [102] built tensile samples in PA12 using a range of EMR values both up to the value calculated to result in degradation and beyond. They found that the highest tensile properties achievable related to an EMR value slightly lower than that predicted to result in degradation. Berretta et al [8] investigated several values of EMR for PEEK 450PF and found that the highest tensile properties were found at EMR values higher than those predicted to cause degradation, however they concluded that EMR was still a useful starting point for prediction of processing parameters.

Ghita et al [12] investigated tensile properties of parts built using a mixture

of virgin and used powder. They reported a drop in tensile properties but did not systematically investigate the processing parameters used to build parts. By undertaking material characterisation on different ratios of virgin and used powder to find the properties required for EMR, this could be used to predict the processing parameters which would result in effective sintering of refreshed powder.

It has been estimated during this study that the stable sintering region of refreshed powder would be smaller than for virgin alone. Thus more effective control of the temperatures in the P800 would also be required in order for refreshed powder to be sintered effectively without detriment to the parts or the remaining powder. The temperatures of the heaters in the P800 can be set by an authorised operator, so it is suggest that the individual heaters be adjusted to try and even out the distribution.

It is not clear whether this will be effective; the reason for the uneven distribution may be that the heaters are spaced too far apart to effectively control temperature across the whole powder bed; research by Bourell et al [110] found that the traditional arrangement of process chamber dual-zone heaters positioned above the powder bed resulted in hot and cold spots, but installation of a new heater which was separated into several distinct zones which could be individually controlled evened out temperature distribution across the surface of the powder bed. A recommendation from the current study would be that temperature distribution needs to be more effectively controlled in the Z-direction as well at in the X-Y; this could be achieved using a greater number of heating bands in the exchangeable frame. Therefore an alternative direction of study would be to install hardware upgrades to more closely control the temperatures in the system.

To conclude, the research and results presented in this thesis have demonstrated the usefulness of material and process characterisation methods for understanding how and why a high temperature laser sintering material behaves in the way it does. The methods undertaken have potential to be applied to other high temperature polymers which have not yet been qualified for HT-LS and highlight the need for better understanding of the temperatures occurring inside HT-LS systems if

adoption of the system is to become more widespread.

Bibliography

[1] T. T. Wohlers, *Wohlers report 2010: additive manufacturing state of the industry annual worldwide progress report*, Wohlers Associates, 2010.

[2] R. D. Goodridge, C. J. Tuck, R. J. M. Hague, *Laser sintering of polyamides and other polymers*, Progress in Materials Science 57 (2) (2012) p. 229–267.

[3] N. Hopkinson, R. J. M. Hague, P. M. Dickens, *Rapid manufacturing: an industrial revolution for the digital age*, John Wiley, 2006.

[4] T. Rechtenwald, G. Esser, M. Schmidt, D. Pohle, *Comparison between Laser Sintering of PEEK and PA using design of experiment methods*, in: Advanced Research in Virtual and Rapid Prototyping, 2005, pp. 343–348.

[5] M. A. Beard, O. R. Ghita, K. E. Evans, *Using Raman spectroscopy to monitor surface finish and roughness of components manufactured by selective laser sintering*, Journal of Raman Spectroscopy 42 (4) (2011) p. 744–748.

[6] D. T. Pham, K. D. Dotchev, W. A. Y. Yusoff, *Deterioration of polyamide powder properties in the laser sintering process*, Proceedings of the Institution of Mechanical Engineers Part C-Journal of Mechanical Engineering Science 222 (11) (2008) p. 2163–2176.

[7] B. Wendel, D. Rietzel, F. Kuhnlein, R. Feulner, G. Hulder, E. Schmachtenberg, *Additive Processing of Polymers*, Macromolecular Materials and Engineering 293 (10) (2008) p. 799–809.

[8] S. Berretta, K. E. Evans, O. R. Ghita, *Predicting processing parameters in high temperature laser sintering (HT-LS) from powder properties*, Materials & Design 105 (2016) p. 301–314.

[9] N. Mys, R. Van De Sande, A. Verberckmoes, L. Cardon, *Processing of Polysulfone to Free Flowing Powder by Mechanical Milling and Spray Drying Techniques for Use in Selective Laser Sintering*, Polymers 8 (2016) p. 150.

[10] M. Vasquez, B. Haworth, N. Hopkinson, *Optimum sintering region for laser sintered nylon-12*, Proceedings of the Institution of Mechanical Engineers, Part B: Journal of Engineering Manufacture 225 (12) (2011) p. 2240–2248.

[11] M. Vasquez, *Analysis and Development of New Materials for Polymer Laser Sintering*, Ph.D. thesis, University of Loughborough (2012).

[12] O. R. Ghita, E. James, R. Trimble, K. E. Evans, *Physico-chemical behaviour of Poly (Ether Ketone) (PEK) in High Temperature Laser Sintering (HT-LS)*, Journal of Materials Processing Technology 214 (4) (2014) p. 969–978.

[13] D. I. Bower, *An Introduction to Polymer Physics*, Cambridge University Press, 2002.

[14] D. Campbell, R. A. Pethrick, J. R. White, *Polymer Characterization: Physical Techniques, 2nd Edition*, Taylor & Francis, 2000.

[15] C. L. Beyler, M. M. Hirschler, *Thermal decomposition of polymers*, SFPE handbook of fire protection engineering 2 (2002) p. 110–131.

[16] S. Kalpakjian, S. R. Schmid, *Manufacturing Processes for Engineering Materials*, Pearson Education, 2008.

[17] R.-M. Ho, S. Z. D. Cheng, B. S. Hsiao, K. H. Gardner, *Crystal Morphology and Phase Identifications in Poly(aryl ether ketone)s and Their Copolymers. 1. Polymorphism in PEKK*, Macromolecules 27 (8) (1994) p. 2136–2140.

[18] H. F. Mark, J. I. Kroschwitz, *Polyetheretherketones*, in: Encyclopedia of Polymer Science and Engineering, Volume 12, 2nd Edition, Wiley, 1990, pp. 313–320.

[19] J. A. Brydson, *Aromatic Polyether Ketones*, in: Plastics Materials, 5th Edition, Elsevier Science, 2013, Ch. 21.8, pp. 563–566.

[20] H. J. Zimmermann, K. Könnecke, *Crystallization of poly(aryl ether ketones): 3. The crystal structure of poly(ether ether ketone ketone) (PEEKK)*, Polymer 32 (17) (1991) p. 3162–3169.

[21] M. R. Reitman, D. Jaekel, R. Siskey, S. M. Kurtz, *Morphology and Crystalline Architecture of Polyaryletherketones*, in: S. M. Kurtz (Ed.), PEEK Biomaterials Handbook, Elsevier Science, 2011, Ch. 4, pp. 49–60.

[22] Y. Wang, M. Cakmak, *Ketone-Based Thermoplastics*, in: O. Olabisi, K. Adewale (Eds.), Handbook of Thermoplastics, 2nd Edition, Plastics Engineering, CRC Press, 2016, Ch. 15, pp. 461–484.

[23] S. M. Kurtz, J. N. Devine, *PEEK biomaterials in trauma, orthopedic, and spinal implants*, Biomaterials 28 (32) (2007) p. 4845–4869.

[24] W. Wang, J. M. Schultz, B. S. Hsiao, *Dynamic study of crystallization- and melting-induced phase separation in PEEK/PEKK blends*, Macromolecules 30 (16) (1997) p. 4544–4550.

[25] P. C. Dawson, D. J. Blundell, *X-ray data for poly(aryl ether ketones)*, Polymer 21 (5) (1980) p. 577–578.

[26] F. Herold, A. Schneller, *High-Performance Polymers*, Advanced Materials 4 (3) (1992) p. 143–152.

[27] K. H. Gardner, B. S. Hsiao, K. L. Faron, *Polymorphism in poly(aryl ether ketone)s*, Polymer 35 (11) (1994) p. 2290–2295.

[28] A. P. Harsha, U. S. Tewari, *Tribo performance of polyaryletherketone composites*, Polymer Testing 21 (6) (2002) p. 697–709.

[29] A. Jonas, R. Legras, *Thermal-stability and crystallization of poly(aryl ether ether ketone)*, Polymer 32 (15) (1991) p. 2691–2706.

[30] A. J. Lovinger, D. D. Davis, *Solution crystallization of poly(ether ether ketone)*, Macromolecules 19 (7) (1986) p. 1861–1867.

[31] S. Kumar, D. P. Anderson, W. W. Adams, *Crystallization And Morphology Of Poly(Aryl-Ether-Ether-Ketone)*, Polymer 27 (3) (1986) p. 329–336.

[32] Y. Lee, R. S. Porter, *Effects of thermal history on crystallization of poly(ether ether ketone) (PEEK)*, Macromolecules 21 (9) (1988) p. 2770–2776.

[33] T. Y. Ko, E. M. Woo, *Changes and distribution of lamellae in the spherulites of poly(ether ether ketone) upon stepwise crystallization*, Polymer 37 (7) (1996) p. 1167–1175.

[34] A. J. Lovinger, S. D. Hudson, D. D. Davis, *High-temperature crystallization and morphology of poly(aryl ether ether ketone)*, Macromolecules 25 (6) (1992) p. 1752–1758.

[35] A. J. Waddon, M. J. Hill, A. Keller, D. J. Blundell, *On the crystal texture of linear polyaryls (PEEK, PEK and PPS)*, Journal of Materials Science 22 (5) (1987) p. 1773–1784.

[36] H. X. Nguyen, H. Ishida, *Poly(aryl-ether-ether-ketone) and its advanced composites: A review*, Polymer Composites 8 (2) (1987) p. 57–73.

[37] H. X. Nguyen, H. Ishida, *Molecular analysis of the melting behaviour of poly(aryl-ether-ether-ketone)*, Polymer 27 (9) (1986) p. 1400–1405.

[38] D. C. Bassett, R. H. Olley, I. A. M. Al Raheil, *On crystallization phenomena in PEEK*, Polymer 29 (10) (1988) p. 1745–1754.

[39] R. A. Chivers, D. R. Moore, *The effect of molecular weight and crystallinity on the mechanical properties of injection moulded poly(aryl-ether-ether-ketone) resin*, Polymer 35 (1) (1994) p. 110–116.

[40] D. J. Blundell, B. N. Osborn, *The morphology of poly(aryl-ether-ether-ketone)*, Polymer 24 (8) (1983) p. 953–958.

[41] G. Reiter, G. R. Strobl, *Progress in Understanding of Polymer Crystallization*, Lecture Notes in Physics, Springer Berlin Heidelberg, 2007.

[42] Y. C. Lee, R. S. Porter, *Double-melting behavior of poly(ether ether ketone)*, Macromolecules 20 (6) (1987) p. 1336–1341.

[43] Y. Lee, R. S. Porter, J. S. Lin, *On the double-melting behavior of poly(ether ether ketone)*, Macromolecules 22 (4) (1989) p. 1756–1760.

[44] D. J. Blundell, *On the interpretation of multiple melting peaks in poly(ether ether ketone)*, Polymer 28 (13) (1987) p. 2248–2251.

[45] J. Wang, J. Cao, Y. Chen, Y. Ke, Z. Wu, Z. Mo, *Crystallization behavior of poly(ether ether ketone ketone)*, Journal of Applied Polymer Science 61 (11) (1996) p. 1999–2007.

[46] P. Cebe, S.-D. Hong, S. Chung, A. Gupta, *Mechanical properties and morphology of poly (etheretherketone)*, in: Toughened Composites, ASTM International, 1987, pp. 342–357.

[47] A. Tregub, H. Harel, G. Marom, C. Migliaresi, *The influence of thermal history on the mechanical properties of poly(ether ether ketone) matrix composite materials*, Composites Science and Technology 48 (14) (1993) p. 185–190.

[48] P. Cebe, S. Y. Chung, S.-D. Hong, *Effect of thermal history on mechanical properties of polyetheretherketone below the glass transition temperature*, Journal of Applied Polymer Science 33 (2) (1987) p. 487–503.

[49] J. N. Hay, D. J. Kemmish, *Thermal-decomposition of poly(aryl ether ketones)*, Polymer 28 (12) (1987) p. 2047–2051.

[50] S. Berretta, K. Evans, O. Ghita, *Processability of PEEK, a new polymer for High Temperature Laser Sintering (HT-LS)*, European Polymer Journal 68 (2015) p. 243–266.

[51] P. Cebe, *Annealing study of poly(ether ether ketone)*, Journal of Materials Science 23 (10) (1988) p. 3721–3731.

[52] M. Day, D. Sally, D. M. Wiles, *Thermal degradation of poly(aryl-ether-ether-ketone): Experimental evaluation of crosslinking reactions*, Journal of Applied Polymer Science 40 (9-10) (1990) p. 1615–1625.

[53] S. A. Thompson, R. J. Farris, *A novel method for crosslinking polyetheretherketone*, Journal of Applied Polymer Science 36 (5) (1988) p. 1113–1120.

[54] A. Banihashemi, B. Akhlaghinia, *Synthesis and cross-linking of poly(ether-ketone)s, and poly(ether-ketone-sulphone)s with pendant nitrile groups (II)*, Iranian Polymer Journal 11 (6) (2002) p. 365–371.

[55] C. M. Chan, S. Venkatraman, *Crosslinking of poly(arylene ether ketone)s 1. Rheological behavior of the melt and mechanical properties of cured resin*, Journal of Applied Polymer Science 32 (7) (1986) p. 5933–5943.

[56] C. M. Chan, S. Venkatraman, *Cross-linking of poly(arylene ether ketones) 2. Crystallization kinetics*, Journal of Polymer Science Part B-Polymer Physics 25 (8) (1987) p. 1655–1665.

[57] M. Day, T. Suprunchuk, J. D. Cooney, D. M. Wiles, *Thermal degradation of poly(aryl-etherether-ketone) (PEEK): A differential scanning calorimetry study*, Journal of Applied Polymer Science 36 (5) (1988) p. 1097–1106.

[58] M. Day, J. D. Cooney, D. M. Wiles, *The thermal degradation of poly(aryletheretherketone) (PEEK) as monitored by pyrolysisGC/MS and TG/MS*, Journal of Analytical and Applied Pyrolysis 18 (2) (1990) p. 163–173.

[59] Z. Zhang, H. Zeng, *Effects of thermal treatment on poly(ether ether ketone)*, Polymer 34 (17) (1993) p. 3648–3652.

[60] S. X. Lu, P. Cebe, M. Capel, *Thermal stability and thermal expansion studies of {PEEK} and related polyimides*, Polymer 37 (14) (1996) p. 2999–3009.

[61] F. Y. Yao, J. Zheng, M. B. Qi, W. Wang, Z. N. Qi, *The thermal-decomposition kinetics of poly(ether ether ketone) (PEEK) and its carbon-fiber composite*, Thermochimica Acta 183 (1991) p. 91–97.

[62] M. Day, J. D. Cooney, D. M. Wiles, *The thermal stability of poly(aryl-etherether-ketone) as assessed by thermogravimetry*, Journal of Applied Polymer Science 38 (2) (1989) p. 323–337.

[63] W. E. Moddeman, W. C. Bowling, E. E. Tibbitts, R. B. Whitaker, *Thermal stability and compatibility of polyetheretherketone (PEEK) with an oxidizer and pyrotechnic blend*, Polymer Engineering & Science 26 (21) (1986) p. 1469–1477.

[64] Y. N. Gupta, A. Chakraborty, G. D. Pandey, D. K. Setua, *Thermal and thermooxidative degradation of engineering thermoplastics and life estimation*, Journal of Applied Polymer Science 92 (3) (2004) p. 1737–1748.

[65] P. Patel, T. R. Hull, R. E. Lyon, S. I. Stoliarov, R. N. Walters, S. Crowley, N. Safronava, *Investigation of the thermal decomposition and flammability of PEEK and its carbon and glass-fibre composites*, Polymer Degradation and Stability 96 (1) (2011) p. 12–22.

[66] D. T. Pham, R. S. Gault, *A comparison of rapid prototyping technologies*, International Journal of Machine Tools and Manufacture 38 (1011) (1998) p. 1257–1287.

[67] S. P. Soe, *Quantitative analysis on SLS part curling using EOS P700 machine*, Journal of Materials Processing Technology 212 (11) (2012) p. 2433–2442.

[68] B. Caulfield, P. E. McHugh, S. Lohfeld, *Dependence of mechanical properties of polyamide components on build parameters in the SLS process*, Journal of Materials Processing Technology 182 (1-3) (2007) p. 477–488.

[69] K. Dotchev, W. Yusoff, *Recycling of polyamide 12 based powders in the laser sintering process*, Rapid Prototyping Journal 15 (3) (2009) p. 192–203.

[70] T. J. Gornet, K. R. Davis, T. L. Starr, K. M. Mulloy, *Characterization of Selective Laser Sintering Materials to Determine Process Stability*, in: Proceedings from the Solid Freeform Fabrication Symposium, 2002, pp. 546–553.

[71] P. K. Jain, K. Senthilkumaran, P. M. Pandey, P. V. M. Rao, *Advances in Materials for Powder Based Rapid Prototyping*, in: International Conference on Recent Advances in Materials and Processing, 2006.

[72] J. P. Kruth, G. Levy, R. Schindel, T. Craeghs, E. Yasa, *Consolidation of Polymer Powders by Selective Laser Sintering*, in: 3rd International Conference on Polymers and Moulds Innovations, 2008, pp. 15–30.

[73] M. Schmid, A. Amado, K. Wegener, *Polymer powders for selective laser sintering (SLS)*, in: AIP Conference Proceedings, Vol. 1664, AIP Publishing, 2015, pp. 160009–1–160009–5.

[74] I. Gibson, D. P. Shi, *Material properties and fabrication parameters in selective laser sintering process*, Rapid Prototyping Journal 3 (4) (1997) p. 129–136.

[75] D. Drummer, D. Rietzel, F. Kühnlein, *Development of a characterization approach for the sintering behavior of new thermoplastics for selective laser sintering*, Physics Procedia 5, Part B (2010) p. 533–542.

[76] R. S. Evans, D. L. Bourell, J. J. Beaman, M. I. Campbell, *SLS materials development method for rapid manufacturing*, in: Proceedings from the Solid Freeform Fabrication Symposium, 2005, pp. 184–196.

[77] J. P. Schultz, J. P. Martin, R. G. Kander, C. T. A. Suchicital, *Selective Laser Sintering of Nylon 12-PEEK Blends Formed by Cryogenic Mechanical Alloying*, in: Proceedings from the Solid Freeform Fabrication Symposium, 2000, pp. 119–124.

[78] S. Berretta, O. Ghita, K. Evans, *Morphology of polymeric powders in Laser Sintering (LS): From Polyamide to new PEEK powders*, European Polymer Journal 59 (2014) p. 218–229.

[79] J. H. Koo, S. Lao, W. Ho, K. Ngyuen, J. Cheng, L. Pilato, G. Wissler, M. Ervin, *Polyamide nanocomposites for selective laser sintering*, in: Proceedings from the Solid Freeform Fabrication Symposium, 2006, pp. 392–409.

[80] S. Haeri, Y. Wang, O. Ghita, J. Sun, *Discrete element simulation and experimental study of powder spreading process in additive manufacturing*, Powder Technology 306 (2016) p. 45–54.

[81] Y. Shi, Z. Li, H. Sun, S. Huang, F. Zeng, *Effect of the properties of the polymer materials on the quality of selective laser sintering parts*, Proceedings of the Institution of Mechanical Engineers Part L-Journal of Materials-Design and Applications 218 (L3) (2004) p. 247–252.

[82] S. Dupin, O. Lame, C. Barrès, J. Y. Charmeau, *Microstructural origin of physical and mechanical properties of polyamide 12 processed by laser sintering*, European Polymer Journal 48 (9) (2012) p. 1611–1621.

[83] S. Ziegelmeier, F. Wollecke, C. Tuck, R. Goodridge, R. Hague, *Characterizing the Bulk & Flow Behaviour of LS Polymer Powders Stefan Ziegelmeier*, in: Solid Freeform Fabrication Symposium, 2013, pp. 354–367.

[84] S. Ziegelmeier, P. Christou, F. Wöllecke, C. Tuck, R. Goodridge, R. Hague, E. Krampe, E. Wintermantel, *An experimental study into the effects of bulk and flow behaviour of laser sintering polymer powders on resulting part properties*, Journal of Materials Processing Technology 215 (2015) p. 239–250.

[85] S. Berretta, O. R. Ghita, K. E. Evans, A. Anderson, C. Newman, *Size, shape and flow of powders for use in Selective Laser Sintering (SLS)*, in: Proceedings of VRAP 2013, 6th International Conference on Advanced Research in Virtual and Rapid Prototyping, 2013, pp. 49–54.

[86] J. Prescott, R. Barnum, *On powder flowability*, Pharmaceutical technology 24 (2000) p. 60–84.

[87] D. Pohle, S. Ponader, T. Rechtenwald, M. Schmidt, K. A. Schlegel, H. Münstedt, F. W. Neukam, E. Nkenke, C. von Wilmowsky, *Processing of Three-Dimensional Laser Sintered Polyetheretherketone Composites and Testing of Osteoblast Proliferation in vitro*, Macromolecular Symposia 253 (1) (2007) p. 65–70.

[88] C. von Wilmowsky, E. Vairaktaris, D. Pohle, T. Rechtenwald, R. Lutz, H. Munstedt, G. Koller, M. Schmidt, F. W. Neukam, K. A. Schlegel, E. Nkenke, *Effects of bioactive glass and beta-TCP containing three-dimensional laser sintered polyetheretherketone composites on osteoblasts in vitro*, Journal of Biomedical Materials Research Part A 87A (4) (2008) p. 896–902.

[89] N. Woicke, M. Kroh, P. Eyerer, *Rapid Prototyping of PEEK Parts by Means of Laser-Sintering*, in: 22. Conference of Polymer Processings, 2006.

[90] S. Berretta, Y. Wang, R. Davies, O. R. Ghita, *Polymer viscosity, particle coalescence and mechanical performance in high-temperature laser sintering*, Journal of Materials Science 51 (10) (2016) p. 4778–4794.

[91] F. Muller, A. Pfister, M. Leuterer, *US Patent No. US 20120114848 A1* (2012).

[92] S. Haeri, *Optimisation of blade type spreaders for powder bed preparation in Additive Manufacturing using DEM simulations*, Powder Technology 321 (2017) p. 94–104.

[93] M. Dole, *The melting range of semicrystalline polymers and copolymers*, Journal of Polymer Science 19 (92) (1956) p. 347–352.

[94] J. P. Kruth, G. Levy, F. Klocke, T. H. C. Childs, *Consolidation phenomena in laser and powder-bed based layered manufacturing*, Cirp Annals-Manufacturing Technology 56 (2) (2007) p. 730–759.

[95] H. Zarringhalam, N. Hopkinson, N. F. Kamperman, J. J. de Vlieger, *Effects of processing on microstructure and properties of SLS Nylon 12*, Materials Science and Engineering a-Structural Materials Properties Microstructure and Processing 435 (2006) p. 172–180.

[96] B. Partee, S. J. Hollister, S. Das, *Selective Laser Sintering Process Optimization for Layered Manufacturing of CAPA[sup ®] 6501 Polycaprolactone Bone Tissue Engineering Scaffolds*, Journal of Manufacturing Science and Engineering 128 (2) (2006) p. 531.

[97] H. Zarringhalam, *Investigation into Crystallinity and Degree of Particle Melt in Selective Laser Sintering*, Ph.D. thesis, University of Loughborough (2007).

[98] A. Wegner, *New polymer materials for the laser sintering process: Polypropylene and others*, in: Physics Procedia, Vol. 83, 2016, pp. 1003–1012.

[99] C. Yan, Y. Shi, L. Hao, *Investigation into the differences in the selective laser sintering between amorphous and semi-crystalline polymers*, International Polymer Processing 26 (4) (2011) p. 416–423.

[100] Y. Shi, Y. Wang, J. Chen, S. Huang, *Experimental investigation into the selective laser sintering of high-impact polystyrene*, Journal of Applied Polymer Science 108 (1) (2008) p. 535–540.

[101] S. Dadbakhsh, L. Verbelen, T. Vandeputte, D. Strobbe, P. V. Puyvelde, J.-P. Kruth, *Effect of Powder Size and Shape on the SLS Processability and Mechanical Properties of a TPU Elastomer*, Physics Procedia 83 (2016) p. 971–980.

[102] M. Vasquez, B. Haworth, N. Hopkinson, *Methods for quantifying the stable sintering region in laser sintered polyamide-12*, Polymer Engineering & Science 53 (6) (2013) p. 1230–1240.

[103] A. J. Shaler, *The Kinetics of the Sintering Process*, Ph.D. thesis, Massachusetts Institute of Technology (1947).

[104] J. P. Kruth, X. Wang, T. Laoui, L. Froyen, *Lasers and materials in selective laser sintering*, Assembly Automation 23 (4) (2003) p. 357–371.

[105] A. Amado, M. Schmid, G. Levy, K. Wegener, *Advances in SLS Powder Characterization*, in: Proceedings from the Solid Freeform Fabrication Symposium, 2011, pp. 438–452.

[106] M. Khan, P. Dickens, *Selective laser melting (SLM) of gold (Au)*, Rapid Prototyping Journal 18 (1) (2012) p. 81–94.

[107] A. E. Tontowi, T. H. C. Childs, *Density prediction of crystalline polymer sintered parts at various powder bed temperatures*, Rapid Prototyping Journal 7 (3) (2001) p. 180–184.

[108] O. Ghita, E. James, R. Davies, S. Berretta, B. Singh, S. Flint, K. Evans, *High Temperature Laser Sintering (HT-LS): An investigation into mechanical properties and shrinkage characteristics of Poly (Ether Ketone) (PEK) structures*, Materials & Design 61 (2014) p. 124–132.

[109] W. Cooke, R. A. Tomlinson, R. Burguete, D. Johns, G. Vanard, *Anisotropy, homogeneity and ageing in an SLS polymer*, Rapid Prototyping Journal 17 (4) (2011) p. 269–279.

[110] D. L. Bourell, T. J. Watt, D. K. Leigh, B. Fulcher, *Performance limitations in polymer laser sintering*, in: Physics Procedia, Vol. 56, 2014, pp. 147–156.

[111] J. A. Nelson, A. Rennie, T. Abram, G. R. Bennett, A. Adiele, M. Tripp, M. Wood, G. Galloway, *Effect of Process Conditions on Temperature Distribution in the Powder Bed during Laser Sintering of Polyamide-12*, Journal of Thermal Engineering 1 (2015) p. 159–165.

[112] S. Josupeit, H.-J. Schmid, *Temperature history within laser sintered part cakes and its influence on process quality*, Rapid Prototyping Journal 22 (5) (2016) p. 788–793.

[113] A. Wegner, G. Witt, *Understanding the decisive thermal procebes in laser sintering of polyamide 12*, in: AIP Conference Proceedings, Vol. 1664, 2015, pp. 160004–1–160004–5.

[114] J. A. Benda, *Temperature-Controlled Selective Laser Sintering*, in: Proceedings from the Solid Freeform Fabrication Symposium, Vol. 5, 1994, pp. 277–284.

[115] J. D. Williams, C. R. Deckard, *Advances in modeling the effects of selected parameters on the SLS process*, Rapid Prototyping Journal 4 (2) (1998) p. 90–100.

[116] J. C. Nelson, *Selective Laser Sintering: A Definition of the Process and an Empirical Sintering Model*, Ph.D. thesis, University of Texas at Austin (1993).

[117] H. C. H. Ho, I. Gibson, W. L. Cheung, *Effects of energy density on morphology and properties of selective laser sintered polycarbonate*, Journal of Materials Processing Technology 8990 (1999) p. 204–210.

[118] V. E. Beal, R. A. Paggi, G. V. Salmoria, A. Lago, *Statistical Evaluation of Laser Energy Density Effect on Mechanical Properties of Polyamide Parts Manufactured by Selective Laser Sintering*, Journal of Applied Polymer Science 113 (5) (2009) p. 2910–2919.

[119] G. M. Vasquez, C. E. Majewski, B. Haworth, N. Hopkinson, *A targeted material selection process for polymers in laser sintering*, Additive Manufacturing 1 (2014) p. 127–138.

[120] T. L. Starr, T. J. Gornet, J. S. Usher, *The effect of process conditions on mechanical properties of laser-sintered nylon*, Rapid Prototyping Journal 17 (6) (2011) p. 418–423.

[121] M. Schmidt, D. Pohle, T. Rechtenwald, *Selective laser sintering of PEEK*, Cirp Annals-Manufacturing Technology 56 (1) (2007) p. 205–208.

[122] M. A. Beard, O. R. Ghita, J. Bradbury, S. Flint, K. E. Evans, *Material characterisation of Additive Manufacturing components made from a polyetherketone (PEK) high temperature thermoplastic polymer*, in: Innovative Developments in Virtual and Physical Prototyping, No. 2008, 2011, pp. 329–332.

[123] Y. Wang, J. D. Beard, K. E. Evans, O. Ghita, *Unusual crystalline morphology of Poly Aryl Ether Ketones (PAEKs)*, RSC Adv. 6 (4) (2016) p. 3198–3209.

[124] Y. Wang, E. James, O. R. Ghita, *Glass bead filled Polyetherketone (PEK) composite by High Temperature Laser Sintering (HT-LS)*, Materials & Design 83 (2015) p. 545–551.

[125] H. Zarringhalam, C. Majewski, N. Hopkinson, *Degree of particle melt in Nylon-12 selective laser-sintered parts*, Rapid Prototyping Journal 15 (2) (2009) p. 126–132.

[126] S. Berretta, *Poly Ether Ether Ketone (PEEK) polymers for High Temperature Laser Sintering (HT-LS)*, Ph.D. thesis, University of Exeter (2015).

[127] Y. Wang, D. Rouholamin, R. Davies, O. R. Ghita, *Powder characteristics, microstructure and properties of graphite platelet reinforced Poly Ether Ether Ketone composites in High Temperature Laser Sintering (HT-LS)*, Materials & Design 88 (2015) p. 1310–1320.

[128] B. Chen, Y. Wang, S. Berretta, O. Ghita, *Poly Aryl Ether Ketones (PAEKs) and carbon-reinforced PAEK powders for laser sintering*, Journal of Materials Science 52 (10) (2017) p. 6004–6019.

[129] O. E. Dictionary, *"sinter, v."*, Oxford University Press.

[130] S. Mazur, *Coalescence of Polymer Particles*, in: M. Narkis, N. Rosenzweig (Eds.), Polymer Powder Technology, J. Wiley, 1995, Ch. 8, pp. 157–173.

[131] C. T. Bellehumeur, M. K. Bisaria, J. Vlachopoulos, *An experimental study and model assessment of polymer sintering*, Polymer Engineering and Science 36 (17) (1996) p. 2198–2207.

[132] G. C. Kuczynski, I. Zaplatynskyj, *Sintering of Glass*, Journal of the American Ceramic Society 39 (10) (1956) p. 349–350.

[133] M. Narkis, *Sintering behavior of poly(methyl methacrylate) particles*, Polymer Engineering & Science 19 (13) (1979) p. 889–892.

[134] C. Bellehumeur, *Polymer sintering and its role in rotational molding*, Ph.D. thesis, McMaster University (1997).

[135] J. Frenkel, *Viscous flow of crystalline bodies under the action of surface tension*, J. Phys 9 (5) (1945) p. 385–391.

[136] G. C. Kuczynski, *Physics and chemistry of sintering*, Advances in Colloid and Interface Science 3 (3) (1972) p. 275–330.

[137] N. Rosenzweig, M. Narkis, *Coalescence phenomenology of spherical polymer particles by sintering*, Polymer 21 (9) (1980) p. 988–989.

[138] N. Rosenzweig, M. Narkis, *Sintering rheology of amorphous polymers*, Polymer Engineering & Science 21 (17) (1981) p. 1167–1170.

[139] P. R. Hornsby, A. S. Maxwell, *Mechanism of sintering between polypropylene beads*, Journal of Materials Science 27 (9) (1992) p. 2525–2533.

[140] B. Haworth, N. Hopkinson, D. Hitt, X. Zhong, *Shear viscosity measurements on Polyamide-12 polymers for laser sintering*, Rapid Prototyping Journal 19 (1) (2013) p. 28–36.

[141] G. C. Kuczynski, *Self-diffusion in sintering of metallic particles*, Transactions of the American Institute of Mining and Metallurgical Engineers 185 (2) (1949) p. 169–178.

[142] J. K. Mackenzie, R. Shuttleworth, *A Phenomenological Theory of Sintering*, Proceedings of the Physical Society. Section B 62 (12) (1949) p. 833.

[143] A. J. Shaler, *Seminar on the kinetics of sintering*, Transactions of the American Institute of Mining and Metallurgical Engineers 185 (11) (1949) p. 796–813.

[144] G. C. Kuczynski, *Study of the Sintering of Glass*, Journal of Applied Physics 20 (12) (1949) p. 1160–1163.

[145] A. Siegmann, I. Raiter, M. Narkis, P. Eyerer, *Effect of powder particle morphology on the sintering behaviour of polymers*, Journal of Materials Science 21 (4) (1986) p. 1180–1186.

[146] R. W. Truss, K. S. Han, J. F. Wallace, P. H. Geil, *Cold compaction molding and sintering of ultra high molecular-weight polyethylene*, Polymer Engineering and Science 20 (11) (1980) p. 747–755.

[147] I. B. Cutler, R. E. Henrichsen, *Effect of Particle Shape on the Kinetics of Sintering of Glass*, Journal of the American Ceramic Society 51 (10) (1968) p. 604.

[148] M. O. Prado, E. B. Ferreira, E. D. Zanotto, *Sintering Kinetics of Crystallizing Glass Particles. A Review*, in: Melt Chemistry, Relaxation, and Solidification Kinetics of Glasses, John Wiley & Sons, Inc., 2006, pp. 163–179.

[149] C. T. Bellehumeur, M. Kontopoulou, J. Vlachopoulos, *The role of viscoelasticity in polymer sintering*, Rheologica Acta 37 (3) (1998) p. 270–278.

[150] Y. Y. Lin, C. Y. Hui, A. Jagota, *The Role of Viscoelastic Adhesive Contact in the Sintering of Polymeric Particles*, Journal of Colloid and Interface Science 237 (2) (2001) p. 267–282.

[151] S. Mazur, D. J. Plazek, *Viscoelastic effects in the coalescence of polymer particles*, Progress in Organic Coatings 24 (14) (1994) p. 225–236.

[152] M. M. Ristic, S. D. Milosevic, *Frenkel's Theory of Sintering*, Science of Sintering 38 (1) (2006) p. 7–11.

[153] G. C. Kuczynski, B. Neuville, H. P. Toner, *Study of sintering of poly(methyl methacrylate)*, Journal of Applied Polymer Science 14 (8) (1970) p. 2069–2077.

[154] O. Pokluda, C. T. Bellehumeur, J. Vlachopoulos, *Modification of Frenkel's model for sintering*, AIChE Journal 43 (12) (1997) p. 3253–3256.

[155] J. D. Eshelby, *Seminar on the kinetics of sintering - discussion*, Transactions of the American Institute of Mining and Metallurgical Engineers 185 (11) (1949) p. 806–807.

[156] S. Hambir, J. P. Jog, *Sintering of ultra high molecular weight polyethylene*, Bulletin of Materials Science 23 (3) (2000) p. 221–226.

[157] N. Rosenzweig, M. Narkis, *Dimensional variations of two spherical polymeric particles during sintering*, Polymer Engineering & Science 21 (10) (1981) p. 582–585.

[158] N. Rosenzweig, M. Narkis, *Newtonian sintering simulator of two spherical particles*, Polymer Engineering & Science 23 (1) (1983) p. 32–35.

[159] M. Asgarpour, F. Bakir, S. Khelladi, A. Khavandi, A. Tcharkhtchi, *Characterization and modeling of sintering of polymer particles*, Journal of Applied Polymer Science 119 (5) (2011) p. 2784–2792.

[160] E. Perot, A. Maazouz, *Study of polymer sintering during rotational molding*, Journal of Polymer Engineering 27 (4) (2007) p. 267.

[161] J. D. Muller, K. Lamnawar, A. Maazouz, *Relationship between rheological and surface properties for the sintering process of polymers*, Journal of Materials Science 47 (1) (2012) p. 121–131.

[162] R. W. Hopper, *Coalescence of Two Equal Cylinders: Exact Results for Creeping Viscous Plane Flow Driven by Capillarity*, Journal of the American Ceramic Society 67 (12) (1984) p. C–262–C–264.

[163] R. W. Hopper, *Coalescence of two viscous cylinders by capillarity: Part I, Theory*, Journal of the American Ceramic Society 76 (12) (1993) p. 2947–2952.

[164] R. W. Hopper, *Coalescence of Two Viscous Cylinders by Capillarity: Part II, Shape Evolution*, Journal of the American Ceramic Society 76 (12) (1993) p. 2953–2960.

[165] V. H. Moll, *Special integrals of Gradshteyn and Ryzhik, the proofs. Volume II Volume II*, Chapman & Hall, 2015.

[166] A. Jagota, P. R. Dawson, *Simulation of the Viscous Sintering of Two Particles*, Journal of the American Ceramic Society 73 (1) (1990) p. 173–177.

[167] J. I. Martínez-Herrera, J. J. Derby, *Analysis of capillary-driven viscous flows during the sintering of ceramic powders*, AIChE Journal 40 (11) (1994) p. 1794–1803.

[168] J. I. Martínez-Herrera, J. J. Derby, *Viscous Sintering of Spherical Particles via Finite Element Analysis*, Journal of the American Ceramic Society 78 (3) (1995) p. 645–649.

[169] R. M. Tarafdar, T. L. Bergman, *Detailed Numerical and Experimental Investigation of Non-Isothermal Sintering of Amorphous Polymer Material*, Journal of Heat Transfer 124 (3) (2002) p. 553–563.

[170] B. Haworth, N. Hopkinson, D. Hitt, M. Vasquez, *Influence of molecular weight and viscosity on particle coalescence for laster sintering of Nylon-12*, in: PPS-27 Polymer Processing Society, 2011, pp. 7.1–7.7.

[171] M. Vasquez, N. Hopkinson, B. Haworth, *Laser Sintering Processes: Practical Verification of Particle Coalescence for Polyamides and Thermoplastic Elastomers*, in: ANTEC Society of Polymer Engineers, 2011.

[172] A. E. Brink, K. J. Jordens, J. S. Riffle, *Sintering high performance semicrystalline polymeric powders*, Polymer Engineering & Science 35 (24) (1995) p. 1923–1930.

[173] EOS GmbH, *EOS P 800 Basic Training Manual* (2017).

[174] EOS GmbH, *PEEK HP3 Datasheet* (2010).

[175] D. J. Blundell, D. R. Beckett, P. H. Willcocks, *Routine crystallinity measurements of polymers by d.s.c*, Polymer 22 (5) (1981) p. 704–707.

[176] A. Tregub, J. Kargerkocsis, K. Konnecke, H. J. Zimmermann, *Deformation and thermoelastic behavior of poly(aryl ether ketones)*, Macromolecules 28 (11) (1995) p. 3890–3893.

[177] Victrex PLC, *Victrex HTP22PF Datasheet* (2011).

[178] E. D. Dickens, B. L. Lee, G. A. Taylor, A. J. Magistro, H. Ng, K. McAlea, P. F. Forderhase, *US Patent No. US 5648450 A* (1996).

[179] B. Wunderlich, *Macromolecular Physics: Vol 3*, Macromolecular Physics Series, Academic Press, 1980.

[180] G. W. H. Höhne, *Another approach to the GibbsThomson equation and the melting point of polymers and oligomers*, Polymer 43 (17) (2002) p. 4689–4698.

[181] A. G. Al Lafi, *Cross linked sulphonated poly (ether ether ketone) for the development of polymer electrolyte membrane fuel cell*, Ph.D. thesis, University of Birmingham (2009).

[182] M. E. Yurchenko, J. Huang, A. Robisson, G. H. McKinley, P. T. Hammond, *Synthesis, mechanical properties and chemical/solvent resistance*

of crosslinked poly(aryl-ether-ether-ketones) at high temperatures, Polymer 51 (9) (2010) p. 1914–1920.

[183] N. S. Murthy, H. Minor, *General procedure for evaluating amorphous scattering and crystallinity from X-ray diffraction scans of semicrystalline polymers*, Polymer 31 (6) (1990) p. 996–1002.

[184] S. Park, J. O. Baker, M. E. Himmel, P. A. Parilla, D. K. Johnson, *Cellulose crystallinity index: measurement techniques and their impact on interpreting cellulase performance*, Biotechnology for Biofuels 3 (1) (2010) p. 1–10.

[185] A. McLauchlin, O. Ghita, L. Savage, *Studies on the reprocessability of poly(ether ether ketone) (PEEK)*, Journal of Materials Processing Technology 214 (1) (2014) p. 75–80.

[186] M. Buggy, A. Carew, *The effect of thermal ageing on carbon fibre-reinforced polyetheretherketone (PEEK)*, Journal of Materials Science 29 (8) (1994) p. 2255–2259.

[187] L. Shen, I. Y. Phang, T. Liu, K. Zeng, *Nanoindentation and morphological studies on nylon 66/organoclay nanocomposites. II. Effect of strain rate*, Polymer 45 (24) (2004) p. 8221–8229.

[188] I. Karacan, *An in depth study of crystallinity, crystallite size and orientation measurements of a selection of poly(ethylene terephthalate)fibers*, Fibers and Polymers 6 (3) (2005) p. 186–199.

[189] N. S. Murthy, Y. P. Khanna, A. J. Signorelli, *Crystallinities of poly(chlorotrifluoroethylene) and its copolymers by differential scanning calorimetry, X-ray diffraction, and density measurements*, Polymer Engineering & Science 34 (16) (1994) p. 1254–1259.

[190] P. Patel, T. R. Hull, R. W. McCabe, D. Flath, J. Grasmeder, M. Percy, *Mechanism of thermal decomposition of poly(ether ether ketone) (PEEK) from a review of decomposition studies*, Polymer Degradation and Stability 95 (5) (2010) p. 709–718.

[191] R. W. G. Hunt, M. R. Pointer, *Measuring Colour*, The Wiley-IS&T Series in Imaging Science and Technology, Wiley, 2011.

[192] J. P. Kruth, P. Mercelis, J. Van Vaerenbergh, L. Froyen, M. Rombouts, *Binding mechanisms in selective laser sintering and selective laser melting*, Rapid Prototyping Journal 11 (1) (2005) p. 26–36.

[193] B. Lautrup, *Surface Tension*, in: Physics of Continuous Matter: Exotic and Everyday Phenomena in the Macroscopic World, 1st Edition, Institute of Physics, 2011, Ch. 5, pp. 69–94.

[194] A. Jagota, C. Argento, S. Mazur, *Growth of adhesive contacts for Maxwell viscoelastic spheres*, Journal of Applied Physics 83 (1) (1998) p. 250–259.

[195] N. Sombatsompop, A. Wood, *Measurement of thermal conductivity of polymers using an improved Lee's Disc apparatus*, Polymer Testing 16 (3) (1997) p. 203–223.

[196] K. Jankova Atanasova, M. A. Islam, H. N. Hansen, P. T. Tang, *Surface tension of polymer melts - experimental investigations of its effect on polymer-polymer adhesion*, in: Nordic Polymer Days 2008, 2008.

[197] R. A. L. Jones, R. W. Richards, *The surface of a simple polymer melt*, in: Polymers at Surfaces and Interfaces, Cambridge University Press, 1999, Ch. 2, pp. 8–55.

[198] Surface-tension.de, *Solid surface energy data (SFE) for common polymers* (2007).

[199] W. A. LLC, *Wolfram Alpha Integral Calculator* (2013). https://www.wolframalpha.com/input/?i=integrate+1{%}2F(x*(sqrt(1{%}2Bx))*K(x))

[200] EOS GmbH, *EOS P8 Software Reference PSW 3.8* (2017).

[201] EOS GmbH, *EOS P 800 Basic Training Presentation* (2017).